Modelling Blood Flow and Oxygen Transport in the Human Cerebral Cortex

Shen-Wei Su
Keble College

Supervised by Dr. Stephen Payne



Physiological Understanding through Modelling, Monitoring and Analysis group

Institute of Biomedical Engineering

Department of Engineering Science

University of Oxford

Trinity Term 2011

This D.Phil. thesis is submitted to the Department of Engineering Science, University of Oxford. The thesis is entirely my own work, and, except where otherwise indicated, describes my own research.

Shen-Wei Su Keble College

D.Phil. Thesis Trinity Term 2011

Modelling Blood Flow and Oxygen Transport in the Human Cerebral Cortex

Abstract

Dementia, a stepwise deterioration of cognitive function, affects over 700,000 people in the UK, resulting in over 60,000 deaths and a cost of over £1.7 billion each year. It is believed to have a combination of vascular and degenerative origins and to have correlations with localised lesions, or infarctions, in the brains of affected patients. Mini-strokes are one of the causes for this disease as the presence of ischemia is highly related to the risk factors for dysfunction of the neurovascular unit. The underlying interacting mechanisms are, however, often very complex and they remain largely poorly understood.

The cerebral microvascular bed is highly irregular and localised variations in its structure are large. To capture these variations, statistical algorithms are required, rather than large volumes of expensive experimental data. Therefore, accurate modelling of blood flow and oxygen transport at the microvascular level is important in improving our understanding of the structure and function of the cerebral vasculature and hence of brain diseases.

A novel algorithm is proposed here to create artificial microvascular networks that match quantitatively experimental data previously obtained in human brain tissue. Blood flow and oxygen transport in the network and the tissue are analysed through both discretised and continuum transport models. By disabling flow sources, ischemic events can be simulated. Using multiple networks, the influence of individual network structures on the response to ischemia is analysed. The relationship between the discretised and continuum formulations of the model is quantified, providing a means for scaling up the model over multi length scales.

Finally, the phenomenon of microvessel collapse under ischemic conditions is examined and it is shown that this is fundamentally dependent upon the variability found at the network level, since it cannot be modelled by a continuum model. An initial infarction is also found to facilitate the occurrence of collapse events for most networks.

Acknowledgment

If life is just a short ride, this 4-year period of DPhil training is nothing but a glimpse, where many things come; few would last. This thesis would last, I suppose. Help from people around makes this work possible and a list of thank-you is thus inevitable.

My upmost gratitude should go to Stephen J. Payne for giving me a place in IBME. For that, I was able to dive into the sea of knowledge, drifting with my imagination, exploring something amazing but impractical, with full set of supports from many the best intellectuals. His profound knowledge, extremely patience and sarcastic sense of humour, has comforted my unsettling mind and guided me the way through this harsh voyage. The completions of this research work also relied on his never ending enthusiasm, encouragement and believe to truth. I am indebted to him so much that I could only partially pay back by expanding his limitation in reading through a painful process. In addition, I owe a lot to Prof. Hose and Prof. Ventikos not for the positive outcome of the viva, but for their constructive comments and profound knowledge during the viva, which puts a fair endnote to my D.Phil.

I also would like to thank my colleagues at the PUMMA and BSP group, with special thanks to Oliver Gibson, Mark Larssen, Hasan Abatay, Tingying Peng, Samira Kazan, Suresh, Chang Sub Park, David O'Neill, Queena Li, Claire Lucas, Yee Kai Tee, Amit Mehndiratta and other news and olds. They have collectively created a relaxing atmosphere through friendly day-to-day activities, and offered me sources for inspirations with their good advice and collaboration.

Last but not least, I owe my friends a lot, especially to Ieda, Gary, Owen, Guo, Winz, John and my flatmates, Lufei, Jason, Auther, Sibo, and Dongdong. Their support has flourished my life, whether in my good times and bad times.

I also want to thank many people in Taiwan for their support.

Finally, I would like to express my deepest gratitude to my family for the unconditional love over these years and the freedom when it came my time to go.

Acknowledgment 3

Nomenclature 8

Chapter 1 Introduction 13

1.1 Structure of brain 13

1.2 Function of cerebral cortex 14

1.3 Cerebral circulation 15

1.4 Cerebrovascular disease 18

1.5 Motivation 18

1.6 Summary of the thesis 20

Chapter 2 Literature review 22

2.1 Introduction 22

2.2 Geometric and topological structure of the cerebral microvasculature 23

2.3 Blood-oxygen transport in microvascular bed 27

2.3-1 Blood property 27

2.3-2 Blood flow in the microvasculature 29

2.3-3 Oxygen transport in the microvascular bed 31

2.3-4 Theoretical models for blood-oxygen transport 32

2.4 Network filtration and tissue interstitial pressure 36

2.4-1 Intracranial pressure 36

2.4-2 Network filtration 37

2.4-3 Blood brain barrier 43

2.5 Measurement techniques 44

2.5-1 Cerebral blood flow measurement 44

2.5-2 Oxygen concentration measurement in brain 45

2.5-3 Experimental studies about oxygen transport in network and tissue 52

2.6 Cerebrovascular diseases and dementia 57

2.7 Summary 60

Chapter 3. Network generation 61
3.1 Introduction 61
3.2 Network information 62
3.3 Network creation algorithms 64
3.3-1 Shortest arc method 66
3.3-2 Gamma distribution method 68
3.3-3 Spanning tree method 72
3.3-4 Modified spanning tree method 76
3.4 Discussion 80
3.5 Conclusion 87
Chapter 4. Discretised model for blood and oxygen transport. 88
4.1 Introduction 88
4.2 Blood flow in the network 88
4.3 Oxygen transport in the network 94
4.3-1 Mixture model 94
4.3-2 Oxygen saturation model 96
4.4 Tissue oxygen transport 99
4.5 Results 101
4.5-1 Simulation setup 101
4.5-2 Constant viscosity-single phase model 105
4.5-3 Sensitivity tests for the constant viscosity-single phase model 111
4.5-4 Variable viscosity- sigmoid approximation saturation model 113
4.6 Discussion 126
4.7 Conclusion 131
Chapter 5. Continuum model for blood and oxygen transport 132
5.1 Introduction 132
5.2 Porous media model for blood flow 133

5.3 Porous media model for oxygen transport 135
5.4 Analogy between discretised and continuum model 138
5.5 Results 141
5.5-1 Model comparisons on flow/oxygenation 142
5.5-2 Network variability test and model comparisons on flow 149
5.5-3 Network variability test and model comparisons on flow/oxygenation 164
5.6. Discussion 168
5.7 Conclusion 172
Chapter 6 Filtration and interstitial pressure 173
6.1 Introduction 173
6.2 Filtration equation 173
6.3 Filtration coupled interstitium equation 181
6.3-1 Lumped model 182
6.3-2 Discretised model 185
6.3-3 Continuum model 187
6.3-4 Summary 188
6.4 Model parameters and numerical procedures 189
6.4-1 Lumped model 189
6.4-2 Network based model 191
6.4-3 Continuum model 194
6.5 Results 195
6.5-1 Simulation results for lumped model 195
6.5-2 Simulation results for discretised model 202
6.5-3 Simulation results for continuum model 209
6.5 Discussion 214
6.6 Conclusion 218
Chapter 7 Conclusion 219

7.1 Summary 219
7.2 Future work 223
Appendix A: Discretisations and numerical solutions 226
Appendix B: Filtration 234
B-1 Solute transport across the capillary membrane 234
B-2 The parameters in pore theory 236
Appendix C: Publications 239
Journal papers: 239
Conference papers: 239

Nomenclature

Symbol	Unit	Name of variable or parameters
A_0	m^2	Initial cross sectional area for a capillary
A	m^2	Cross sectional area for a capillary
A_c	m^2	Exchange area for a capillary
A_d	m^2	Baseline cross sectional area for a capillary
A_e	1/m	Exchange area per unit volume tissue
a	nm	Solute radius
C_b	mM	Concentration of blood oxygen
C_{bw}	mM	Concentration of blood oxygen in near wall region
C_c	mM	Concentration of solute in a capillary
C_{Hb}	mM	Concentration of the binding site in haemoglobin
C_i	mM	Concentration of solute in the ISF
C_{ic}	m^5/N	Intracranial compliance
$C_{ic-tissue}$	m^5/N	Effective intracranial compliance for local volume tissue
C_t	mM	Concentration of tissue oxygen
$\overline{C}_{tissue}$	m^2/N	Intracranial compliance per unit volume tissue
D_{ion}	m^2/s	Tissue diffusion coefficient of ion
D_{pro}	m^2/s	Tissue diffusion coefficient of protein
D_t	m^2/s	Tissue diffusion coefficient of oxygen
D_w	m/s	Wall permeability of oxygen
E	mmHg	Capillary elastic constant
FQ_E	%	Volume fraction of RBC

FQ_B	%	Volume fraction of blood flow
G	m^2-s/kg	Flow conductance
G_{cross}	m/N-s	Effective cross conductance
G_D	cm^3/cmH_2O	Drainage conductance
G_{ex}	mM/s-m^3	Rate of oxygen extraction from network per unit volume tissue
G_{in}	m/N-s	Effective inlet conductance
G_{out}	m/N-s	Effective outlet conductance
G_S	mM/s-m^3	Rates of generation consumption
g_i	mM/s-m^3	Rate of oxygen extraction from network per unit voxel tissue
H_D	%	Discharge haematocrit
H_T	%	Tube haematocrit
h	m^4/N-s	Hydraulic conductivity of blood phase in tissue
h_i	m^4/N-s	Hydraulic conductivity of ISF phase in tissue
J_V	m^3/s	Transvascular flow rate
J_{VA}	s/m^2	Transvascular flow rate per unit exchange area
J_S	mol/s	Transvascular solute flow rate
$\bar{J}_{VA}$	m/s	Transvascular flow rate density per unit exchange area
$\mathbf{K}$	m^2	Permeability matrix of blood phase in tissue
k_e	1/m^3	Brain tissue elastance
L	m	Vessel length
L_p	cm/s-cmH_2O	Wall hydraulic permeability
L_{p-S}	cm/s-cmH_2O	Wall hydraulic permeability for the small pore system
L_{p-L}	cm/s-cmH_2O	Wall hydraulic permeability for the large pore system
M	mM/s-m^3	Rate of oxygen consumption from tissue per unit volume tissue

M_S	mM/s-m^3	Rates of generation consumption
M_0	mM/s-m^3	Baseline tissue consumption rate of oxygen per unit volume tissue
$N/\Delta x$	1/m	Number of pore density
n	3	Hill's constant
n_0	1/m^3	Number of vessels per unit volume tissue
P	Pa	Blood pressure
P_c	Pa	Hydraulic pressure in a capillary
P_{crit}	mmHg	Critical pressure for a capillary
P_d	m^2/s	Diffusion permeability of the solute in water
P_i	Pa	Hydraulic pressure in the ISF
P_{ic}	Pa	Intracranial pressure
P_{O2}	mmHg	Oxygen partial pressure
P_0	mmHg	Baseline oxygen partial pressure
P_{50}	mmHg	Oxygen partial pressure at 50% saturation
Q	m^3/s	Volume flow rate
r	μm	Vessel radius
r	nm	Pore radius (Appendix B)
$r_{(S)}$	nm	Radius of small pore system
$r_{(L)}$	nm	Radius of large pore system
S	%	Saturation of haemoglobin
S_D	1/s	Source term for Darcy equation
S_b	1/s	Pressure source density due to the local blood volume change
S_f	1/s	Pressure source density due to the net capillary filtration
$\mathbf{u}_D$	m/s	Darcy velocity

$\mathbf{V}$	m/s	Blood phase velocity
V	M^3/s	Tissue volume
X	m	Non-dimensional coordinate vector
x	m	Coordinate vector
y	m	Coordinate vector
z	m	Coordinate vector
α	mM/mmHg	Oxygen solubility
ΔG_{xy}	%	Fractional conductance difference between the x and the y directions
ΔG_{cross}	%	Fractional conductance difference between two cross directions
κ	m^2	Permeability constant of blood phase in tissue
κ_i	m^2	Permeability of ISF phase in tissue
κ_{rel}	%	Permeability ratio of the discretised to the continuum flow models
λ	1/m	Decaying constant
λ_p	%	Partition coefficient
μ_a	kg-m/s	Apparent viscosity of blood
μ_b	kg-m/s	Dynamic viscosity of blood
μ_p	kg-m/s	Dynamic viscosity of blood plasma
μ_i	kg-m/s	Dynamic viscosity of ISF
$\mu_{0.45}$	kg-m/s	Apparent viscosity with haematocrit at 0.45
Π_c	Pa	Osmotic pressure in a capillary
Π_{c-pro}	Pa	Osmotic pressure in a capillary for protein
Π_{c-ion}	Pa	Osmotic pressure in a capillary for ion
Π_i	Pa	Osmotic pressure in the ISF
σ	%	Reflection coefficient

σ_{pro-L}	%	Reflection coefficient for protein through large pores
σ_{pro-S}	%	Reflection coefficient for protein through small pores
σ_{ion-L}	%	Reflection coefficient for ion through large pores
σ_{ion-S}	%	Reflection coefficient for ion through small pores
Φ	mM	Concentration of a substance
ϕ_b	%	Volume fraction of blood (porosity)
ϕ_t	%	Volume fraction of tissue
Ω_b	m^3/s	Pressure source term due to the local blood volume change
Ω_f	m^3/s	Pressure source term due to the net capillary filtration
Ω_{in}	m^3/s	Pressure source term due to flow influx
Ω_{out}	m^3/s	Pressure source term due to flow efflux

Chapter 1 Introduction

The central nervous system (CNS) is essential in the maintenance of homeostasis through the control over the organs of the body. It receives vast amount of information (Mb/s) from sensory organs, integrates and process all the input signals, and determines the responses to stimuli by passing the output commands on to motor organs. As the centre of the central nervous system, the brain coordinate with other CNS compartments and body organs in the body through the neural signal processing in the nerve system (Guyton and Hall 2006). However, it can suffer from functional deficiency when localised metabolic demand and supply are not well matched. In particular, a shortage in blood supply may cause dysfunction or damage of tissue, which is known as ischemia. This blood deficient condition in brain tissue is believed to be a risk factor of many cerebral diseases including dementia, strokes and etc. (Bowler and Hachinski 2003). Therefore, understanding of the underlying interactions between haemodynamic deficiency and cerebral diseases is very crucial to improve the diagnosis methods and treatment interventions during clinical application. Like experimental studies, a theoretical modeling can provide analyse tools for further exploring this interaction if the model is physiologically relevant.

1.1 Structure of brain

The brain is protected by several layers. The skull and three thin layers, including the pia mater, arachnoid mater and dura mater, enclose the brain tissue and they provide a mechanical buffer to the brain tissue. In addition, in the subarachnoid space between the arachnoid and pia mater circulates the cerebrospinal fluid forming a water cushion. The brain is composed of three compartments, from bottom to top, the brain stem, cerebellum and

cerebrum. The brain stem is responsible for controlling the heart rate, breathing and any other autonomic processes whilst the cerebellum is related to body movement, posture control and balance. The cerebrum is responsible for high-level thinking, memory and recognition. The outer layer of the cerebral hemisphere is the cerebral cortex, with a highly folding structure containing most capillaries and neuronal cell bodies whilst the core region is white matter composed mainly by neuronal fibre tracts (Kandel, Schwartz, Jessell 2000).

1.2 Function of cerebral cortex

Brain functionally has been investigated for several decades but it is still far from being fully understood. In general, the brain can be divided into three functional categories, the primary sensory areas, primary motor areas, and association areas, which are located in different regions of the cortex. The primary sensory areas, including visual, auditory and somatosensory areas, receive the corresponding sensory signal inputs via a nerve fibre tract through the thalamus. Primary motor areas, sending off the signals via afferent axons, are located next to the somatosensory areas. The association areas cover the rest of the areas in the cortex. They do not have direct afferent or efferent nerve connections to the sensory-effector systems but are believed to mediate or modulate the inputs from other functional areas (Kandel, Schwartz, Jessell 2000). The map of these functional areas in human cortex is shown in the Fig.1.3(b)

(a)

Due to copyright issue, this figure is removed. Please refer to Figure B-6 in the reference.

(b)

Due to copyright issue, this figure is removed. Please refer to Figure 19-1 in the reference.

Figure 1.1 (a) The main structures of brain; (b) typical function areas of human brain cortex taken from (Kandel, Schwartz, Jessell 2000).

1.3 Cerebral circulation

Taking up only about 2% of the total weight of human body, the brain receives 12-15% of cardiac output and consumes 20% of oxygen supply of the whole body. Compared with other body tissues, this enormously high demand makes brain cells more vulnerable to blood shortage, thus a robust transport system for blood flow is necessary. The cerebral blood circulation is supplied by two pairs of arteries, namely the internal carotid arteries (ICAs) and vertebral arteries (VAs). The ICAs come from the common carotid artery, rising up to the surface of brain and dividing into the anterior and middle cerebral arteries. The anterior cerebral arteries provide blood for the medial surface of the parietal and frontal lobes and the opposite arteries are linked by the anterior communicating arteries. The middle cerebral arteries supply the majority of the lateral surfaces of frontal, parietal and temporal lobes (Kandel, Schwartz, Jessell 2000).

Due to copyright issue, this figure is removed. Please refer to Figure C-1 in the reference.

Figure1.2 The sketch of the Circle of the Willis, where the dark region represents the common sites for occlusion or atherosclerosis, taken from (Kandel, Schwartz, Jessell 2000)

The VAs enter the cranium cavity through the foremen magnum, giving rise to posterior and anterior spinal arteries and posterior inferior cerebellar arteries. They continue upwards and unite as the basilar artery, later giving off many branches such as the posterior cerebral and superior cerebellar arteries, which feed the occipital lobe of the cerebral cortex and most of the cerebellum. The internal carotid and vertebrobasilar artery system are connected by posterior communicating arteries, forming the circle of the Willis at the base of the brain. This topological arrangement can preserve reasonable perfusion even if the occlusion occurs at one of the main supplying arteries (Kandel, Schwartz, Jessell 2000).

The arteries (with diameters around few millimetres) would divide into smaller arteries (with diameter of order 0.7mm) at the surface of the cortex, and further branching and ramification in the cortex starts from precortical arteries to arterioles (pre-capillaries) with a change of diameter from around 50μm to 30μm. The arterioles are believed to play the key role in blood autoregulation by contracting or distending their vessel walls. The arterioles finally penetrate orthogonally into the cortical region and terminate at the level of the capillaries, where the nutrients and waste in the blood can exchange with the surrounding tissues.

Venules (post-capillaries) collect deoxygenated blood with metabolic waste products drained from the capillaries, converging to cerebral veins (Rodriguez-Baeza and others 1998).

The two kinds of veins, superficial cerebral veins and deep cerebral veins, are categorised by their relative locations. Originating from the subcortical white matter and cortex gray matter, small superficial cerebral veins join in the pia region to form large veins and drain into the dural sinuses. Deeper cerebral veins provide blood drainage from the deeper regions and gradually join the sigmoid sinus, finally carrying the venous blood toward the internal jugular veins in the neck.

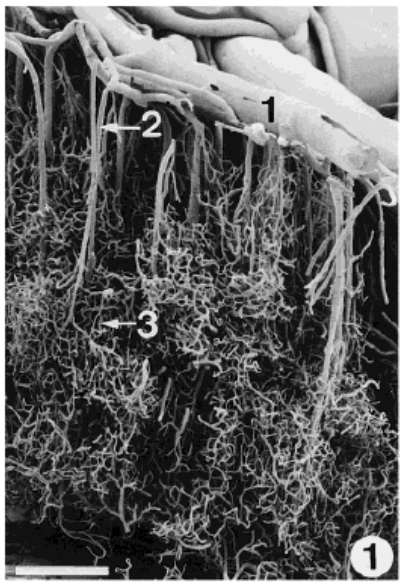


Figure1.3 Overview of a vascular cast of the occipital cerebral cortex for (1) the pial vessels, (2) the cortical arterioles, and (3) the cortical capillary network though the cerebral cortex; scale bar equivalent to 500 μm, taken from (Rodriguez-Baeza and others 1998).

1.4 Cerebrovascular disease

In the brain, the neurons, glia and vascular cells are functionally correlated with one another to form neurovascular units, which are believed to maintain the homeostasis of the cerebral cellular microenvironment by regulating blood flow and transvascular exchange, mediating immune surveillance at a local scale (Iadecola 2010). The adequate functioning of such neurovascular units relies on a stable blood supply and regular vascular filtration, the dysfunctions of or disturbances to which can lead to a pathological state for the neurovascular units, resulting in functional impairment of the brain or potentially dementia.

Dementia, a neurodegenerative disease, is a stepwise deterioration of recognition abilities resulting from brain damage, leading to symptoms of memory loss, confusion and changes in behavioural patterns. As a very common form of dementia, second only to Alzheimer's disease, Vascular Dementia (VaD), is believed to be associated with cerebrovascular diseases that damage neurological functions at specific cognition domains in the brain. In some patients with dementia syndromes, small damage sites can be observed in different functional regions of the brain. These multiple smaller lesions (<5mm) may result from local haemdynamic disturbances, like post ischemic infarctions, in small vessels in the cerebral microvasculature (Bowler and Hachinski 2003).

1.5 Motivation

There may be some lesions in the brain that are too small to cause noticeable cognitive impairment by the patients themselves or to be detected by modern imaging techniques such as MRI and CT, but they may evolve to more severe infarctions under certain haemodynamic conditions (Bowler and Hachinski 2003). Once the size or the number of these tiny infarctions grow enough to impair one specific functional area or to block a neural circuit

linking different functional areas, which is responsible for specific cognition functions, substantial mental deterioration is likely to become notable in clinical diagnosis.

In some cases, blood reperfusion can restore the haemodynamics and oxygen supply to the tissue near infarction after ischemic attacks, and shift their cellular states back to normal. However, it has been also found that such treatment can sometimes be compromised by the no flow phenomenon: blockage of some of the flow paths due to vessel collapse. This event is always accompanied by dysfunction of endothelium cells and detachment of enclosing astrocytes, which are involved in regulation of transvascular exchange of molecules. Abnormal functioning of these vascular cells can be found when no flow phenomenon occurs, however the underlying mechanisms of this event remain unclear (del Zoppo and Mabuchi 2003). Understanding the mechanisms behind such vessel collapse is crucial for improving the treatment for post ischemia stroke but the possible causes remain to be discovered.

Understanding the dynamics at this small scale can provide a detailed picture of blood perfusion and tissue oxygenation in the local microcirculation. For this purpose, experimental methods to monitor the haemodynamics at a microvascular level are always expensive and are nearly impossible for full domain recording. Therefore, modelling interplay between the small scale haemodynamics and oxygenation for brain microvasculature is, therefore, of considerable importance to offer an alternative analytic tool and is the aim of this thesis. Such a model can offer a picture of localised haemodynamics and oxygenation that cannot be resolved by the modern brain imaging techniques, to identify the flow or oxygenation conditions for infarction formation in their early stages. In addition, such a physiologically based model could also help to clarify the underlying mechanisms in post ischemic vessel collapse events. Through a better understanding of the haemodynamic conditions leading to

infarct expansion, or against the reperfusion treatment, the onset of the vascular dementia could then be potentially delayed.

1.6 Summary of the thesis

Chapter 2 gives an overview of the literature related to this thesis. It consists of reviews on the physiological background, related theoretical models and experimental techniques. The main focus of Chapter 3 is then to develop an algorithm generating statistically based networks to meet the statistical characteristics obtained from human brain tissue samples. Four different methods are tested and compared to the experimental data. The method along with an optimal set of parameters, which give the best match to the experimental statistics, are used to create networks required for the simulations performed in the following chapters.

Once the algorithm has been optimised in Chapter 3, a haemodynamic model for the resultant networks, with two different settings for viscosity (constant and variable viscosity) are proposed in Chapter 4 to test the interactions between flow and blood rheology. Later, this flow model, coupled to a network/tissue oxygen transport model, is used to predict the network and tissue oxygen level profiles. Ischemic conditions are simulated by disabling one flow source in the network, causing flow redistributions, leading to an alteration in the tissue oxygenation field. How the blood PO_2 approximations at the wall region and the values of model parameters, such as the wall permeability and maximum consumption rate, influence the resulting oxygenation field are also addressed in this Chapter.

Chapter 5 introduces a porous media model to approximate the network based model for the purpose of improving computational efficiency when a large scale simulation is required. Since the proposed network generation method is inherently random, variations in flow and

oxygen transport features due to the network variability are of considerable importance and are investigated in detail. Large length scale features of among a number of networks predicted by the discretised model are then compared to those predicted by the continuum model and through the comparisons, a method of characterising the overall flow features for each network are also presented.

In Chapter 6, the model is extended to replicate the vessel collapse events found in post ischemic reperfusion conditions. Two factors, over-filtration across the network and elevation of intracranial pressure, are thought to be responsible for the occurrence of buckling of vessel walls and are thus incorporated into the established discretised model. Conditions for the occurrence of collapse events are identified. Meanwhile a continuum approach is also tested for its capability to simulate vessel collapse. The model extension is carried out by including the same two factors above and corresponding results are presented. In the final chapter, all the findings in Chapters 3 to 6 are considered. The final conclusions are presented and possible directions for future work suggested.

Chapter 2 Literature review

2.1 Introduction

As discussed in Chapter 1, disturbances in blood flow and oxygen supply within the microcirculation can change the local metabolic status of brain tissue. For example, a blood shortage may cause irreversible damage to a region of tissue, leading to the formation of lesions or infarctions and thereby increasing the risk of the vascular dementia. In addition, pathological cerebral cellular states can also cause a departure from the normal states of haemodynamics by changing the vascular property. Just as the reperfusion treatment for ischemia may be compromised by vessel collapse, which is hypothesized to be attributed to two events: breakdown of the blood brain barrier and intracranial pressure elevation. The former event would cause over-filtration, through fluid accumulation in interstitial space, mediating the latter event and leading to vessel collapse.

Hence, normal neural function is closely associated to a stable flow supply and regular transvascular transport at the microvascular level to maintain the micro environment for vascular and neural cells within a haemostatic range. Gaining a better understanding of network-tissue interactions in terms of blood flow and oxygen transport at such a tiny scale is of importance and it cannot be achieved currently through most of the exsiting measurement techniques. A theoretical based model can thus open another alternative avenue to investigate the local dynamics of the network-tissue coupled system.

In order to construct a physiologically based model for blood and oxygen transport in brain microcirculation, basic knowledge regarding the structure of the microvasculature, blood flow, tissue oxygenation distribution and existing mathematical models are necessary and will thus now be reviewed in this chapter. Then the second part of this chapter will focus on vascular filtration and interstitial pressure dynamics. Techniques for monitoring blood flow

and oxygen transport including their basic principles and measurement results will then be introduced. Finally, literature about the possible causes and risk factors for vascular dementia will be addressed.

2.2 Geometric and topological structure of the cerebral microvasculature

Being able to characterize the response of the vascular system to micro infarcts would help to improve our understanding of how vascular dementia develops and evolves, which would be highly beneficial for better diagnosis and treatment of vascular dementia. A detailed knowledge of the morphometry of the cerebral microvessel network is necessary to provide information for physiologically realistic simulations of flow and mass transport (Secomb and others 2004) (Pries and Secomb 2005a). Accurate haemodynamic interpretations of functional imaging methods (Hyde, Biswal, Jesmanowicz 2001) (Logothetis and Wandell 2004) also rely on detailed anatomical maps of the microcirculation; likewise, flow regulation, remodelling (Carmeliet 2005) (Noble and others 2005) and the dynamic responses to varying physiological demands (Pries, Reglin, Secomb 2003) are also strongly influenced by the microvasculature architecture.

The microvascular structure, including its dimensions, topology and branching angles, is not, however, well understood due to its irregular anatomical features. One common feature is the heterogeneity widely found in different vascular architectures, such as coronary (Kassab and others 1993), mesentery (Ley, Pries, Gaehtgens 1986), retinal (Simoens, De Schaepdrijver, Lauwers 1992) and cerebral networks (Cassot and others 2006). Since the local haemodynamics are very closely influenced by the vessel network structure, tissue specific information in terms of topology and geometry is essential for network creation methods in numerical simulations of mass transport in either healthy or pathological states.

In comparison to other body organs, however, very limited anatomical information is available for the human cerebral network. Some researchers describe the microvasculature structure in the cerebral surface region or anatomical variations in large intra-cortical vessels (Lee 1995). Published material about morphological statistics and vessel distribution patterns has remained limited since Duvernoy and colleagues (Duvernoy, Delon, Vannson 1981) provided much information related to human cortical vessels. They described the anatomical features from the surface to the deep cortical and intra-cortical vessels according to penetration type, and found the relationships between these features and cellular layers. However, the lack of quantitative information about capillaries makes distinguishing between arteries and veins problematic and cannot help to identify the arterial-capillary junction locations in the micro-vessel bed.

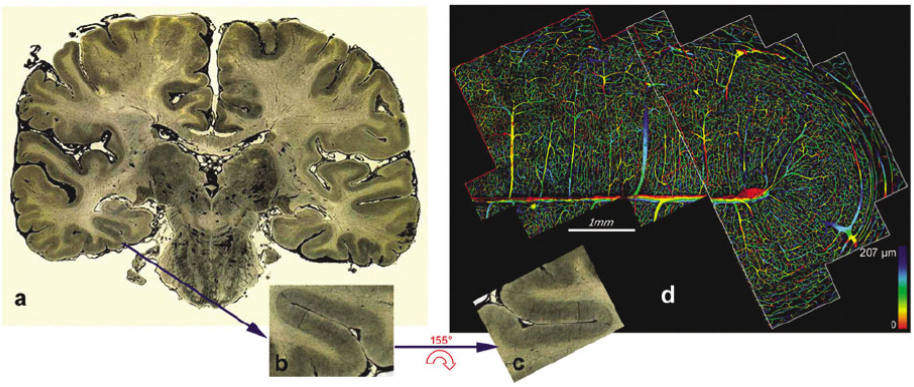
Duvernoy and co-workers suggested a central vein encircled by several arteries as being a functional unit in the brain. Other researchers (Reina-De La Torre, Rodriguez-Baeza, Sahuquillo-Barris 1998) also studied the human cortical network using scanned electron microscopy in cast corrosion samples. They described the artery and capillary branching distributions and suggested three blood flow regulation levels in the system, including pial arteries, cortical arteries and cortical capillaries. Peri-vascular structures in the cast such as ring-like furrows or plastic strips appearing at branching nodes were thought to be regulators for blood flow at the capillary level similar to smooth muscle cells in arteries or arterioles at the main vessel level (Peppiatt and others 2006). Pericytes, which are relatively undifferentiated cells, not only serve to support these vessels, but can also differentiate into smooth muscle cells (Sims 1991).

The morphometric data adopted in this work come from Cassot and co-workers (Cassot and others 2006), whose primary study was the first one to provide quantitative morphometric

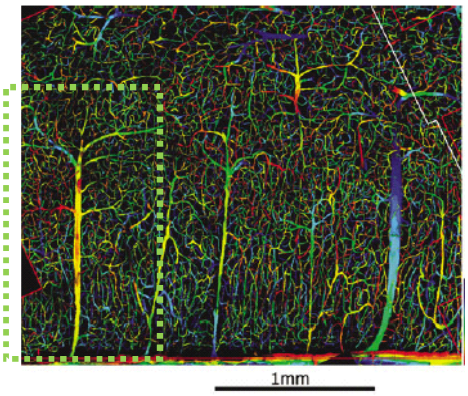
information regarding the human cerebral network. In their work, confocal laser microscopy was used to analyze sample sections, using Indian ink injected in the collateral sulcus in the right temporal lobe, due to the clear visual contrast, producing a detailed map of the cerebral vasculature and offering statistical geometric and topological data. The vessel length histogram reflects a left-shifted distribution in both zones studied. The vessel density (vessels per volume), average connectivity (branches per joint) and vessel orientation data provide enough information to quantify the network characteristics.

In their subsequent work, Cassot and co-workers (Lauwers and others 2008) extended their analysis to cover more sub-regions in the same area of the cerebral cortex. The vessel length and diameter histograms basically followed the result of the previous work while some of the characteristics (for example the skewness and kurtosis parameters) did not. They also found that the capillary volume density is higher in the middle third of the cortical depth while the larger vessels dominate the other parts (<42% and >86% of the depth) of the cortical layers. Alongside the values of statistics given in their primary work, they included the variations in venous and arterial-capillary density maps along the cortical depth and the cortical surface which were transferred to an averaged 2D power spectrum plot where discrepancies between venous and arterial-capillary distributions could be found in the high frequency (short length scale) components.

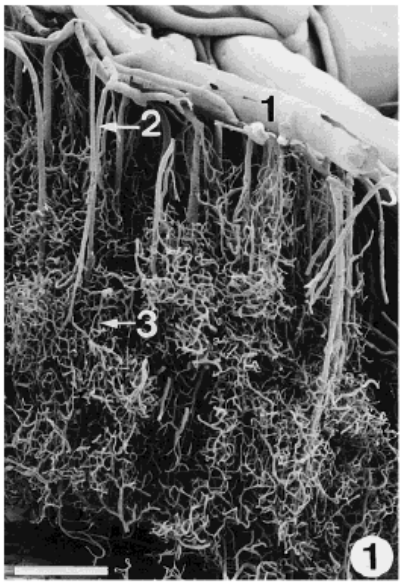
(a)



(b)



(d)



(c)

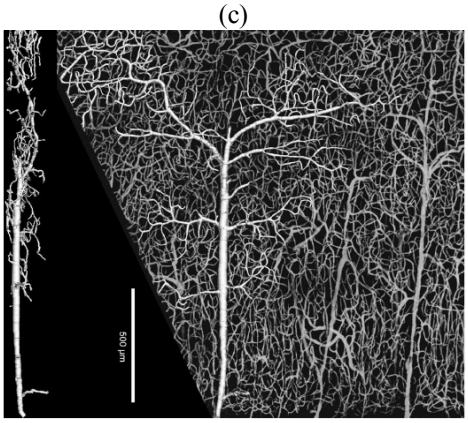


Figure 2.1: (a) Illustration of the sample region from human cortex (left region enclosed by red lines in block d and M2 (right region enclosed by white lines in block d). (b) A depth level map of the cerebral network (c) a large vein model reconstructed from the depth map for the network, taken from (Cassot and others 2006). (d) Overview of a vascular cast of the occipital cerebral cortex for though the cerebral cortex; scale bar equivalent to 500 µm, taken from (Rodriguez-Baeza and others 1998)

Variability of the microvascular structure in the same brain regions between different individuals is widely known, and the corresponding flow patterns are very likely to form diverse flow patterns. To consider variations occurring in clinical cases, blood flow predictions and thereby the vascular skeletons obtained from multiple cerebral tissue samples are required to give significant statistical power. This, however, cannot be easily achieved because reconstructing vascular maps merely based on a group of real brain tissues is extremely costly and time consuming.

One solution to the problem described above is to develop a numerical algorithm capable of regenerating a number of networks based purely on the experimental statistics for the human brain. Although there is only one experimental study for one individual at present, as larger databases of the vasculature become available in the future, this will offer a framework to characterise the microvasculature of humans in fuller detail.

A model with the capability to generate artificial networks with the correct statistics based on experimental data is thus of great importance in terms of the ability to produce a physiologically accurate vascular skeleton map. This accurate microvascular network model could be coupled with vessel/tissue oxygen transport models to help to improve our understanding of the mechanisms behind vascular dementia or other clinical brain diseases. A larger pool of comparisons between simulations and experiments thus becomes more feasible, providing a more solid ground for clinical applications.

2.3 Blood-oxygen transport in microvascular bed

2.3-1 Blood properties

Blood is a mixture of plasma and blood cells, including red blood cells (erythrocytes), white blood cells (leukocytes) and platelets. Plasma is an aqueous solution, made up of many

chemical species such as Na^+, K^+, Ca^{2+}, Cl^- and many other macromolecules, which can be regarded as being a incompressible Newtonian fluid with viscosity 1.8 mPa·s at 37ºC. Under normal conditions, human blood has such a high haematocrit (volume fraction of the red blood cells) about of 40-45%, with 0.16% and 0.125% of the total volume being taken up by white blood cells and platelets respectively, and its properties are highly dependent on the behaviour of blood cells. Since the diameters of vessels in the microvascular network are of the same order as those of the blood cells (10μm), understanding the behaviour of these cells is essential for analysis of the microvascular bed (Sugihara-Seki and Fu 2005).

A normal red blood cell is shaped like a biconcave disk, with approximate diameter 8 μm and thickness 2.8 μm. Its membrane is made up of a lipid bi-layer containing spectrin and actin protein networks, which results in a capsule-like mechanical structure. Such a thin walled structure is easily deformed in shear flow but is resistant to any surface area change (Shiga, Maeda, Kon 1990). The intra-cellular space of RBC is full of a haemoglobin solution, giving its capability for the exchange of gases such as oxygen and carbon dioxide. The oxygen carrying capability of RBC is usually influenced by several factors, such as blood pH value, body temperature and blood oxygen partial pressure.

White blood cells form an essential part of the immune system. According to their appearance under microscopy, they can be mainly categorized as polymorphonuclear leucocytes and mononuclear leucocytes, with different sizes and properties. Generally, WBCs are spherical with mean diameter 6-10 μm, with a hard nucleus and a thin membrane, and can be described as compound drops with three layers of viscoelastic fluid for plasma membrane, cytoplasm and nucleus respectively (Tran-Son-Tay and others 1998). Once the WBCs are activated (i.e. the onset of their interaction with endothelium cells via surface receptors), their

mechanical and biochemical properties undergo dramatic changes. In this way, the flow patterns may be changed as well, for example blocking the vessel.

2.3-2 Blood flow in the microvasculature

Due to the low velocity of the blood flow in the microcirculation (0.1-10mm/s), the dynamics of the flow are dominated by viscous effects. Thus, Poiseuille's assumptions concerning the steady state behaviour of the flow, implying that blood flow is laminar and Newtonian fluid passing through a rigid vessel, are usually adopted to simplify the Navier-Stokes equations for theoretical analysis (Popel and Johnson 2005). The pressure difference ΔP along one vessel is found to be proportional to the volume flow rate, giving the following theoretical basis for the relationship of the flow in a vessel:

$$\frac{\Delta P}{Q} = \frac{8\mu_a L}{\pi r^4}, \tag{2-1}$$

where the apparent viscosity is given by μ_a, resulting from the interaction between blood cells and plasma, the vessel length is given by L, and the lumen radius by r. From *in vitro* experiments with blood in a long glass tube followed by a discharge reservoir, Fahraeus (Fahraeus 1929), firstly discovered that the tube haematocrit (H_T) is smaller than that in the discharge (H_D), which is known as the Fahraeus effect, later confirmed empirically to provide a relationship between H_T and H_D (Pries and others 1990).

Later, Fahraeus and Lindqvist (Fahraeus and Lindqvist 1931) also found that the apparent viscosity decreases with decreasing tube diameter between 10-300μm, finally reaching a minimum at around 10μm (Fahraeus-Lindqvist effect). However, as the tube diameter decreases further, the apparent viscosity increases with decreasing diameter in a nearly linear manner (Gaehtgens 1980), which is known as the inversion of the Fahraeus-Lindqvist effect.

A comprehensive experimental database of viscosity dependence on diameter and haematocrit has thus been obtained from a collection of experimental results (Pries and others 1990) (Pries, Neuhaus, Gaehtgens 1992) (Pries and others 1994).

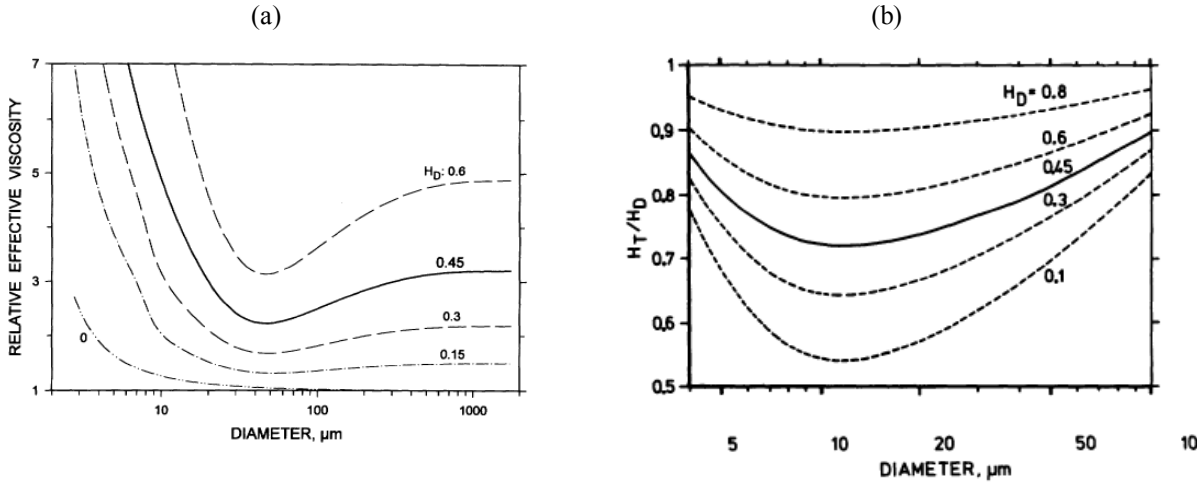


Figure 2.2 (a) Relative effective viscosity as a function of vessel diameter and discharge haematocrit, curves representing the empirical fitting of vivo experimental data (taken from (Pries and others 1994)); (b) Relationship between the tube haematocrit and discharge haematocrit (taken from (Pries and others 1990)).

The Fahraeus-Lindqvist effect is widely accepted to be the result of many processes in the flow system in microvascular bed (Pries and others 1994). Relevant factors like endothelium interactions with the blood cells, irregular configuration of inner lumen, and vessel haematocrit are very different from network to network and these factors can enlarge the differences between in vitro and in vivo observations. The effective viscosity-diameter relationship was later suggested to be mainly affected by the endothelium layer thickness, which is dependent on the vessel diameter (Pries and Secomb 2005b). In addition, inter-cell interaction can influence the blood rheology differently in different size of microvessels. As the tube diameter reduces below 10µm, the tube dimension becomes comparable with the RBC size. This makes the RBCs pass through the tube in single file. Many theoretical analyses have been proposed to explain the cause of both the Fahraeus-Lindqvist and the inverse Fahraeus-Lindqvist effects, from continuum models (i.e. a two layer model for core

and cell-deplete region), to discrete descriptions (i.e. a particle-flow model). These are summarized in two excellent review papers (Popel and Johnson 2005) (Sugihara-Seki and Fu 2005).

2.3-3 Oxygen transport in the microvascular bed

The main carrier of oxygen in blood is the haemoglobin on RBCs which loads and unloads oxygen molecules through the oxygen-haemoglobin binding process. This process can be regarded as a ligand-macromolecules reaction whose rate is highly influenced by the blood oxygen concentration. The molecular structure of haemoglobin binding site alters much to facilitate the binding process for the next oxygen molecule, resulting in a higher oxygen association rate in a high oxygen content environment. This cooperative binding of oxygen to haemoglobin can be visually described by a sigmoidal shape curve, as shown in Figure 2.3, and its shape varies in response to varying physiological conditions, such as body temperature, pH and BPG values. BPG (2,3-bisphosphoglycerate) is an organophosphate, created in RBC during glycolysis.

Due to copyright issue, this figure is removed.

Please refer to Figure 40-10 in the reference.

Figure 2.3 Typical saturation curve for human haemoglobin, taken from (Guyton and Hall 2006)

Given a value for local oxygen tension in blood, the saturation can be determined by the non-linear oxygen-haemoglobin binding relationship. The local oxygen flux across the capillary wall is dependent on the oxygen partial pressure (PO_2) drop across the wall and hence is

complicated by the discrete nature of the cell/plasma interaction. When the RBCs travel along a vessel, they are clustered with a random interval in the core region of the microvessel. The wall PO_2 level is higher when a RBC passes by. As a result, the oxygen efflux into tissue space is a function of the RBC position, saturation, and velocity.

Through the non-linear oxygen-haemoglobin binding relationship, the discrete nature of the cell/plasma mixture introduces extra complexity in the analysis of oxygen transport in the microcirculation. Modelling oxygen transport in a vessel network is very complex but it requires a huge computational expense since simulating hundred thousands of blood cells movement in a network with thousands of microvessels is not computationally feasible. In this work, the particulate nature of RBC on the transvascular oxygen efflux is simply assumed to be proportional to the concentration difference between tissue PO_2 and wall blood PO_2, the latter of which is approximated by either the area averaged blood oxygen level or the plasma oxygen level.

2.3-4 Theoretical models for blood-oxygen transport

The microvasculature plays an important role in oxygen transport in the coupled vessel-tissue system and many models based on different network morphologies and architectures have thus been proposed. In 1921, Krogh (Krogh 1921) suggested that the haemodynamic unit of the microvascular bed is like a bundle of tissue cylinders each with the same spatial arrangement. Each cylinder has a capillary located in the centre that supplies oxygen to the nearby concentric tissue area by diffusion as the blood is transported from the arteriole end to the venule end. This model is most likely to apply to tissue where the capillaries pass in nearly the same alignment, but may not be suitable for tissues perfused by curved vessels with an irregular geometric arrangement, as found in the cerebral microvasculature.

Hsu and Secomb (Hsu and Secomb 1989) investigated oxygen transport in skeletal muscle with nearly parallel spaced capillaries and transverse arterioles passing by. The governing equations for oxygen transport were solved using the Green's function method and a full three dimensional simulation for tissue oxygen transport was performed. The effects of setting different boundary conditions as well as the line source expression on the system oxygen transport were also discussed in later work focusing on oxygen delivery in tissue (Secomb and Hsu 1994).

A more realistic morphometric model with parallel evenly spaced capillaries having interconnections at random locations was proposed by Beard and Bassingthwaighte (Beard and Bassingthwaighte 2000) for analysis of cardiac tissue. The computational grids were hexagonally arranged and the vessel elements found at the same locations of certain tissue elements. Thus, the mass transport equations for vessels and tissues were solved together. An extension to this model was later proposed by Beard and co-workers (Beard, Schenkman, Feigl 2003) to interpret the experimental data of myocardial oxygen transport in pig heart tissue. It should be noted that, in these two models, the computation includes the individual influence of the plasma and red blood cells, and thereby the haemoglobin saturations in oxygen transport, but blood viscosity was assumed constant when performing the flow simulations.

Compared with other tissues, oxygen transport in cerebral tissue has been little investigated through theoretical models. This is partially due to the complexity of the network morphometry. In the cerebral cortex, the microvascular architecture in tissue varies from region to region, which affects the spatial distribution of blood supply. In addition, the regionally varying pattern of neuronal activities affects the consumption rate of oxygen. All

these factors are coupled together to contribute to the heterogeneity of oxygen levels in brain tissue, adding extra complexity to any investigations, whether theoretical or experimental.

On the basis of scanning electron micrographs of corrosion casts in rat brain, Secomb et al. reproduced a network with 50 segments (Secomb and others 2000). Haematocrit variations and the variable viscosity law were included in the flow calculation whilst haemoglobin saturation was also considered in the oxygen transport. The Green's function method was used to predict the oxygen level in the tissue surrounding the network, and the correlation between blood perfusion and oxygen consumption was also examined. They found that tissue hypoxia resulting from a perfusion shortage could be alleviated if the oxygen consumption rate in tissue was only moderately decreased.

Instead of reproducing a network from morphometric data, Beard directly used the network created by Secomb and co-workers (Secomb and others 2000), and performed a numerical simulation by solving the mass transport equation with an inhomogeneous volume method (Ivol method) (Beard 2001), which is a blending of the finite volume and finite difference methods. Unlike the previous method (Beard and Bassingthwaighte 2000), there is no restriction on the network geometry when using this method, where the vessels need not fit the computational grid arrangement. Thus, the oxygen transport in tissue with arbitrary scattered networks can be resolved with coarser grids and thereby fewer grids when the Ivol method is used. However, the flow and transport models are simple because only constant viscosity and a single phase mixture for blood were assumed in this method.

Recently, a single experimentally derived network based model (Reichold and others 2009) has been developed to simulate cerebral blood flow in animals. 3D flow simulations were performed based on the assumption of constant viscosity. Under specific pressure conditions,

the geometric data obtained from a 3D vascular skeleton provided the estimate of the dynamic resistance for resolving the flow patterns according to the mass and momentum balance in the whole network. The haemoglobin saturation effect on the network oxygen transport was ignored since the blood was treated as a single phase flow. Unlike their flow computation, only a 2D computation for tissue oxygenation field was performed by these authors.

Later, blood flow simulations based on the original cerebral vascular maps obtained from the studies mentioned above (Cassot and others 2006) (Lauwers and others 2008), were performed by Lorthois and co-workers (Lorthois, Cassot, Lauwers 2011b) to investigate the impact of three different boundary conditions on the flow/pressure distribution patterns and the upper/lower bounds for the baseline perfusion rate of model tissue. Flow territories were indentified within the simulation results, suggesting a complex combination of territories defined by flow feeding arterioles or collecting venules.

This model was later extended by incorporating the localised and global vasodilatation in the arteriole tree and venous tree compliance, and by retaining the structure of the capillary network (Lorthois, Cassot, Lauwers 2011a). In addition, a two resistor model, including a variable resistance in series with a constant resistance, to account for the arteriole tree and capillary-venous networks respectively, was also proposed to approximate global haemodynamics during vasodilation and some integrated parameters, such as mean capillary pressure, mean transit time network volume and region blood flow, were presented to show their correlations to flow condition variations. Meanwhile the authors also identified the flow effect (CBF vs CBV) on the brain functional map separately from the metabolic and neuron components, which previously were considered together. The corresponding flow patterns were found to give a good match to the available clinical observations.

2.4 Network filtration and tissue interstitial pressure

In the circulation system, the microvascular bed is the main venue for substance exchange between blood and tissue. Nutrients like glucose or oxygen are delivered by blood flow from arteries through branching arterioles to the local microvascular bed and waste substances including carbon dioxide and urea, produced through cellular metabolism, are transported by diffusion from the intracellular space through interstitial fluid, back to the lumen side of the capillary bed via transvascular exchange and are finally taken away by circulating blood (Guyton and Hall 2006). Thus adequate modulation of transvascular exchange is of crucial importance for homeostasis as the extracellular ion concentrations must be kept within certain levels for normal neural function.

2.4-1 Intracranial pressure

According to the Monro-Kellie doctrine, the total volume of the intracranial elements, i.e. the vascular volume, CSF space and brain tissue, must remain constant due to the rigidity of the cranium. Any change in one intracranial element will be accompanied by changes in others, and a change of the intracranial pressure. The artery tree in the brain is enclosed by the brain parenchyma; to keep the blood flowing, the mean arterial pressure (MAP) must be higher than the ICP. During pathological states, ICP can approach the same value as MAP, the vessel starting to contract due to reductions in the transmural pressure, leading to impairments in blood circulation. Therefore, the intracranial pressure (ICP) is a useful index for monitoring the haemodynamic conditions in the intracranial space since a rise in ICP is very common in neurosurgical and neurological patients, with possible causes being disorders in CSF circulation, intracranial mass lesions or more diffuse pathological processes (Steiner and Andrews 2006).

A number of mathematical models have been proposed to simulate the dynamics of ICP and other intracranial elements. For example, Ursino and Lodi (Ursino and Lodi 1997) used a multi-element model to consider the haemodynamics of the arterial cerebrovascular bed, CSF production and reabsorption processes, the nonlinear pressure-volume relationship of the craniospinal compartment and autoregulation.

In a subsequent paper (Ursino and Giannessi 2010), the simple element of the arterial-vascular bed in the original haemodynamics model was extended into a complex network formed by a number of hydraulic resistances and compliances, each of which represents either an artery or a vascular bed in the circle of Willis. In addition, two regulation mechanisms including autoregulation and CO_2 related reactivity were taken into account by modulating the arteriole compliance and resistance.

2.4-2 Network filtration

The structure of the capillary vessels determines the ease of material transport across the wall. On the luminal side, the vessel is covered by a matrix of fibres, known as the surface glycocalyx layer (100-500 nm thickness), which is formed by membrane-bound macromolecules from glycoproteins bearing acidic oligosaccharides and terminal sialic acids (SAs) to proteoglycans along with their associated glycosaminoglycan (GAG) side chains, and others (Weinbaum, Tarbell, Damiano 2007) (Vink and Duling 2000). The capillary, as shown in Figure 2.4, is composed of endothelium cells, which attach to one another to form a tube like structure. In the space between two adjacent endothelium cells lies a narrow cleft, where two cells fuse at the tight junction in the midway, termed the strand.

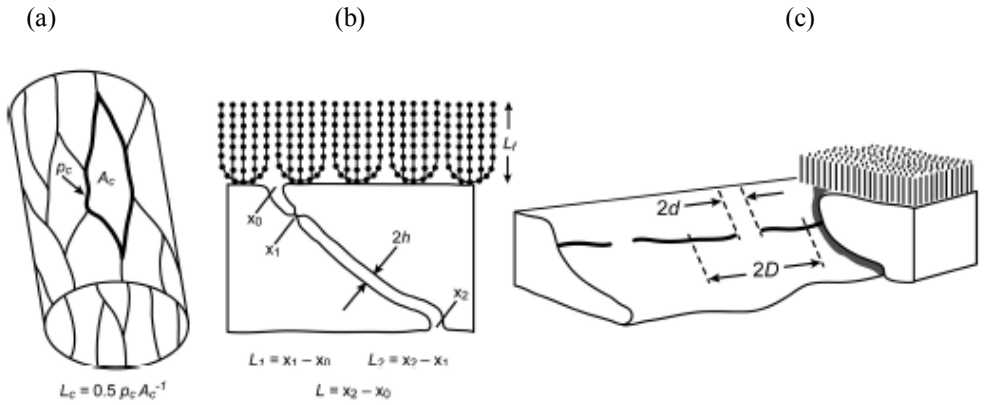


Figure 2.4. (a) Sketch of the cellular structure of the capillary vessels; (b) the SGL is the brush like layer whilst the strand is at $x = x_1$, the cleft runs from $x = x_0$ to $x = x_2$; (c) a strand containing the break with length 2d and a linear density 2d/2D in the strand; all taken from (Curry 2005).

Observations on frog mesenteries show that the junction strands are not perfect seals, but have a certain number of large breaks, with their length taking up about 10% of the junction strand length (Adamson and Michel 1993). In addition to the large breaks, there seem to be some slits on the junction strand allowing water passage, which give a extra water filtration term, which is found to be needed to match the numerical predictions to the experimental results (Fu and others 1994).

Material exchange across the capillary wall occurs in different ways depending on the particle size and its solubility to water or lipid. Gas particles like oxygen or carbon dioxide can easily pass through the cellular membrane of endothelium cells and enter the local tissue due to their good affinity to the lipid bi-layer at the cell membrane. Hydrophilic molecules, which are transported in the blood circulation, pass the vessel wall along the paracellular pathways, as shown in Figure 2.4, each of which is a narrow cleft between two endothelium cells (Curry 2005). The molecules firstly encounter the surface glycocalyx layer (SGL), whose fibre arrangement effectively retains the larger particles like albuminutes but allows smaller molecules to pass. Most of the small solutes and a few large molecules then enter the

paracellular spaces, passing the slits or large breaks in the strands, finally reaching the tissue space.

In addition to the paracellular pathways, trans-cellular pathways also play a role in the material exchange between blood and tissue. Generally, the solute flux should decrease monotonically with increased solute size. However, observations on transport of dextran between blood and lymph showed that solutes with sizes larger than serum albumin only change transport properties very slightly with change of the solute size, suggesting the existence of another transport mechanism. This form of exchange may occur in the endothelium cell itself, despite its minor contribution to total hydraulic permeability, and rely on the cellular transport mechanism (Grotte 1956). Some studies have revealed small vesicles, which pack and carry these molecules through the endothelium cells, the effect known as transcytosis, which is responsible for macromolecule trans-cellular transport (Michel and Curry 1999).

The first quantitative description of water and solute transport across the capillary wall was proposed by Starling, who postulated that the amount of fluid filtration is influenced by two driving forces exerting on both sides of the capillary: the hydraulic static pressure and the effective osmotic pressure (Starling 1896). The filtration rate is proportional to the net Starling force, being manipulated by a constant known as the hydraulic permeability of the capillary wall.

The Starling equation was later validated by experiments on single frog mesentery capillaries (Landis 1927), which provided two important findings. First, when the net plasma filtration rate approaches zero, the capillary pressure is close to the osmotic pressure of the frog plasma. Second, the diffusion patterns of low weight colour dyes across the capillary wall were very similar to their passage patterns across a collodion membrane tube, as this material is widely

used for osmotic pressure measurements. These findings are used as the basis of pore theory, which uses an analogy between the transvascular exchange of water and small solutes across the capillary wall to the passage across porous membranes (Curry 2005).

Pore theory treats the capillary wall as a porous membrane, with a number of water filled pores, allowing transvascular passage of the plasma and solutes. The flow resistance of these tiny pores can be estimated by a lumped term, the wall hydraulic permeability, which is mainly determined by geometric factors like the size (radius) and the density (number per area) of the pores. These transvascular pores can be characterised by two groups of porous pathways. For the model for skeletal muscle capillary vessels, the small pores of radius 4-5 nm are responsible for the paracellular pathways, contributing 95% of the total wall hydraulic permeability (Levick and Michel 2010).

The large pores correspond mainly to the transcellular pathways, with pore radius up to 20-30 nm and a density ratio to small pores of between 1/5,000 and 1/50,000 (Renkin and Curry 1982). Different microvascular beds tend to have different values of hydraulic permeability, this being explained by the differences in the total numbers of the small and large pores in the model. However, the dimensions of these small and large pores show little variation between different tissues (Rippe and Haraldsson 1994).

Although pore theory is straightforward, one drawback is the lack of inclusion of realistic information about the capillary structure. With subsequent advances in measurement techniques applied to the microvascular anatomy, the capillary structure, such as the endothelium glycocalyx layer, intercellular clefts and tight junction breaks, has become clearer, which has provided a foundation for the development of the glycocalyx junction break (GJB) models.

In this model, the paracellular pathway is divided into several regions in cascade, which have different flow resistances to the water and solute passage. If there is no strand in the cleft, the flow patterns, as shown in Figure 2.5(A), can be approximated by a 1D flow. However, there are always some breaks at junction strands, the break then becoming the bottle neck for the flow passage. The orifice-like break in the strand constrains the flow paths, creating a convergent-divergent flow pattern like 2.5(C). To consider this flow effect on the water solute passage, Phillips and co-workers (Phillips, Parker, Wang 1994) introduced a modification into the hydraulic permeability using a multiplying factor. This factor depends on the ratio of break length to cleft depth and the ratio of the strand depth to junction depth.

Due to copyright issue, this figure is removed.

Please refer to Figure 7 in the reference.

Figure 2.5. 1D or 2D flow pattern sketches through the intercellular cleft depending on the strand break dimension, taken from (Adamson and Michel 1993)

Furthermore, a bush like-fibre matrix occupies the glycocalyx layer and the water/solute passage is thus impaired by the matrix depending on the space between fibres, fibre radius and the thickness of the layer. The fibre arrangement determines the degree of movement of passage across the surface glycocalyx layer (SGL) in terms of the effective hydraulic permeability, similar to the pore theory (Curry and Michel 1980).

A more detailed model considering both the existence of the fibre matrix and the strand break in the cleft as the main flow pathway has been proposed and both flow convection and solute diffusion analysed in a multi-layer context (Fu and others 1994) (Fu and others 1997). It has been shown that 80% of the flow resistance through the cleft was found to be produced by the SGL. However, the small solute flux is only slightly affected by the thin matrix layer until the solute size becomes large. As the solute size approaches the fiber spacing (7 nm), for example serum albumin, the solute concentration drops rapidly across the SGL, suggesting the importance of its sieving function on large solutes and water movement along the paracellular pathways.

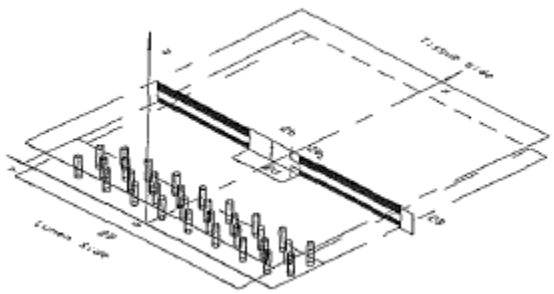


Figure 2.6. Sketch of the GJB model structure capillary vessel wall, with SGL and strand and cleft , taken from (Fu and others 1994)

Although the GJB type models have a more direct cellular structural basis, they still have some correlations with pore theory. For example, the dimensions of the small pores can be correlated to the spacing between the SGL fibers in the GJB model, defining the selectivity of the microvessel wall. Meanwhile, the pore density, dependent on the size and the frequency of the breaks in the cleft strands, can be used to give the effective area of the aqueous tunnels for material exchange (Michel and Curry 1999). The large pore system seems to be correlated

to a localized dysfunction of the molecule filter at SGL caused by damage or simply the onset of vesicle activity inside the endothelium cells (Curry 2005) (Curry and Adamson 2010).

2.4-3 Blood brain barrier

In the 19th century, experiments carried out by injection of acidic vital dye showed that injecting dye into the cerebrospinal fluid (CSF) would give clear staining patterns but not if it were injected into the blood stream, suggesting the existence of a special barrier separating the vascular and interstitial spaces of the brain tissue. In order to maintain homeostasis in the tissue environment for normal functioning of neurons and glial cells, the brain tissue is more isolated than any other body organ due to the highly selective nature of transvascular exchange between blood and tissue. This restricted transport is achieved by the blood-brain barrier (BBB), with a decrease in the effective area for the flow pathways, which permits only certain molecules like nutrients, amino acids and peptides to enter the parenchyma from blood, meanwhile toxins and some neurotransmitters are excluded by the BBB (Abbott and others 2010).

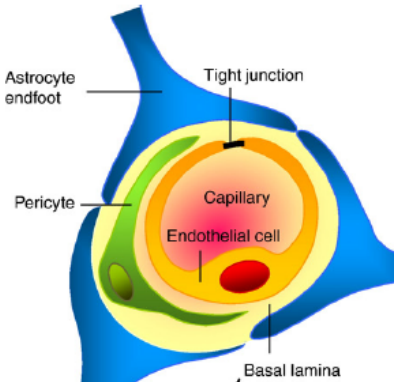


Figure 2.7 Typical structure of blood brain barrier (BBB) taken from (Abbott and others 2010).

Although the basic molecular structure of capillary vessels in the brain is similar to that found in other peripheral organs, other structural features make the BBB unique. As shown in Figure 2.7, the vessel, composed of endothelium cells, is enclosed by a matrix-like basement membrane, where more than 90% of the membrane area is covered by a number of feet originating from nearby astrocytes (Pardridge 1999). At certain locations on the cerebral capillaries, pericytes are found to enclose the vessel. These ring-like cells may play a role in local autoregulation. In addition, the tight junction strands in the intercellular space of endothelial cells have breaks with shorter lengths, offering less area for material exchange across wall. The trans-cellular transport is not efficient for most solutes due to the relative low activities of fluid-endocytosis and receptor mediated endocytosis in endothelium cells (Abbott and others 2010) .

As a result, the flow and solute exchange is greatly impaired across the BBB compared to that in the periphery capillaries in other organs. For example, the hydraulic permeability of cerebral capillary vessels (in cm/cmH2O-s) is of order 10^{-9} (Li, Yuan, Fu 2010), two orders smaller than typical values in other capillary vessels, which are $O(10^{-7})$ (Levick and Michel 2010).

2.5 Measurement techniques

2.5-1 Cerebral blood flow measurement

One popular device for blood flow measurement is the Laser Doppler Flowmetor (LDF), which generates a laser beam with specific light bandwidth penetrating through tissue to the region of interest. Since different materials have different absorption and reflection spectra, the reflection of light creates a very good contrast between plasma and red blood cells. Due to the Doppler effect, the moving blood cells reflect the light with a shifted frequency dependent

on the moving velocities, all reflected light being sampled in time and the flux in a sample volume being estimated from the total reflected light from the blood cells (Bolognese and others 1993) .

Other non-invasive techniques, such as Computerised Tomography (CT) or magnetic resonance imaging (MRI), can be used to measure blood perfusion in the brain in terms of the cerebral blood flow (CBF, ml/min/100g tissue). CBF is found to correlate with cerebral blood volume (CBV, ml blood/100g tissue) though the Central Volume Theorem (Stewart 1897) or through other theoretical models, i.e. (Buxton, Wong, Frank 1998) (Mandeville and others 1999). Blood perfusion can then be determined through CBV measurement, which can be dynamically detected by other CT or MRI measurements (Cenic and others 2000) (Speck and others 2000). For example, MRI based CBV measurements are carried out by injecting a paramagnetic contrast agent into the vascular space during an echo planar T_2^*-weighted gradient echo sequence and estimating the area under the tissue signal intensity vs. time curve, this being proportional to CBV (Speck and others 2000).

2.5-2 Oxygen concentration measurement in brain

Normal brain function relies on a constant supply of oxygen, whose reactive nature plays an essential role in the biochemical reactions in cell metabolism. In the presence of oxygen, glucose can be processed through oxidative metabolism to produce adenosine triphosphate (ATP), which is the main energy source for many cellular biochemical reactions. Unlike muscle tissue with myoglobin, the brain tissue lacks an efficient oxygen store. A low concentration of oxygen cannot be tolerated for a long time since the energy compensation from anaerobic respiration is not enough to cover the shortage (Acker and Acker 2004) .

However, extremely high oxygen tension can also be detrimental to brain tissue because it increases the risk of oxidative stress, which is correlated to cellular injury such as impairment of intracellular signaling, loss of cell function, and ultimately programmed cell death (Nordberg and Arner 2001). Therefore brain tissue is more vulnerable to oxygen disturbances and very tight regulation mechanisms are required. Understanding the optimal range of normal oxygen tension in the brain is of importance to assess cellular conditions. Due to its close correlation with neural activity, glucose consumption and blood flow distribution are all closely related to tissue oxygen level.

Techniques for oxygen concentration measurement can be categorised into direct and indirect methods according to the sources of the signals. In direct methods, such as polarography or the phosphorescence quenching method, oxygen is the signal extracted from the brain tissue and being processed and analysed. On the other hand, near infrared spectroscopy (NIRS), positron emission tomography (PET), and magnetic resonance imaging (MRI) non-invasively measure other oxygen related signals.

Polarographic microelectrodes

The majority of oxygen tension data of brain tissue are obtained by using polarographic microelectrodes, which are usually a noble metal or carbon fibre covered by a membrane cathode sensitive to the oxygen dissolved in the medium. The measurement is carried out by inserting the polarographic probe into in vitro prepared tissue slices. When a negative polarised cathode is exposed to the oxygen, a current signal is generated by electron transfer from the cathode to nearby oxygen. At certain voltage level, this current is linearly dependent on the tissue oxygen (Jiang, Agulian, Haddad 1991).

Although the polargraphic microelectrode has been widely used to measure tissue oxygenation, an accurate oxygen level reading is limited to the small region immediately close to the probe tip. Since the electrode consumes oxygen, this could also lead to signal disturbance during the measurement. In addition, this method is invasive and tissue can be damaged during the measurement (Kohling and others 1998).

Phosphorescence quenching method

Based on the correlation between oxygen tension and decay rate of light emission in the phosphorescence process, the phosphorescence quenching method can be used to monitor oxygen concentration in biological tissue (Lo, Koch, Wilson 1996). When exposed to light with a certain wave length, the phosphor molecules can be excited to triplet state, emit phosphorescence and go back to the ground state immediately. Oxygen is very likely to react with these excited molecules by forming oxidative radicals and thus quenches the phosphorescence emission process. The higher the oxygen tension, the greater the decay of the phosphorescence emission is. By measuring the intensity of the emission or the life time, oxygen partial pressure, P_{O_2}, can be determined according to a well defined Stern-Volmer equation:

$$I = I_0 / \left(1 + K_q P_{O_2}\right). \qquad (2\text{-}2)$$

where I_0 is the phosphorescence intensity (life time) in the absence of oxygen, I is the phosphorescence intensity (life time) with oxygen at a given level and K_q is the quenching constant.

Due to the blood/tissue exchange capability of albumin, the phosphors are bound to albumin as the oxygen probes, which in turn can be used as a tissue oxygenation indicter. The phosphors binding albumin may spend different times passing the vascular wall depending on

the local vascular architecture. For example, it is found that 20 minutes after injection, about 10% of the total albumin are tagged with the oxygen probes, which are well distributed in both vascular and interstitial spaces, providing sufficient spatial resolution for oxygen tension measurement (Tsai and others 1998).

Near infrared spectroscopy (NIRS)

Near infrared spectroscopy was developed to monitor the tissue oxygen content in terms of haemoglobin oxygen saturation and total haemoglobin concentrations (Cope and Delpy 1988) (Kurth and others 1993). Near infrared light sources with wavelengths from 600-900 nm are able to penetrate into tissue within a few centimetres. Many molecules in tissue, such as oxy and deoxy-haemoglobin, water, lipids can absorb light energy in this wavelength range but oxy and deoxy-haemoglobin have photon absorption rates one order larger than the rest. Based on the Modified Beer-Lambert Law, concentration changes in oxy and deoxy-haemoglobin are related to the changes in detected light intensity, which can be expressed by the empirical relationship:

$$\Delta OD = -\log \frac{I_{final}}{I_{initial}} = \varepsilon \Delta C L B, \tag{2-3}$$

where $\Delta OD = OD_{final} - OD_{initial}$ is the change in the optical intensity, I_{final} and $I_{initial}$ are the light intensity detected before and after the concentration change, ΔC, ε is the extinction coefficient of the chromophores, L is specified by the probe geometry and B is the differential path length factor, being responsible for the increase in photon path length by the light scattering effect in a medium. When accounting for the overall influence on the light intensity from oxy and deoxy-haemoglobin, the equation can be rewritten for two light sources with different wavelengths:

$$\Delta OD^{\lambda} = \left(\varepsilon_{Hb}^{\lambda}\Delta[\mathrm{d}Hb] + \varepsilon_{HbO}^{\lambda}\Delta[HbO]\right)LB^{\lambda}. \quad (2\text{-}4)$$

This forms a linear system with two unknowns and with the parameters $\varepsilon_{Hb}^{\lambda}, \varepsilon_{Hb}^{\lambda}, L, B^{\lambda}$ being known the concentration change in oxy and deoxy-haemoglobin $\Delta[\mathrm{d}Hb]$ and $\Delta[HbO]$ can be estimated by measuring the intensity changes ΔOD^{λ} at these two wavelengths. However, four wavelength systems are more often used in NIRS experiments for greater accuracy.

Electron paramagnetic resonance spectroscopy (EPR)

EPR has been used to detect the unpaired electrons in chemical species, like free radicals in many chemical or physical applications. The electron possess either the quantum state with magnetic moment of the anti-parallel and parallel alignment to the applied magnetic field with strength B_0.The energy gap ΔE between these two states is proportional to the magnetic field with a constant product of the electron g-factor g_e multiplied by the Bohr magnetron μ_B according to the formula $\Delta E = g_e \mu_B B_0$. The unpaired electrons are able to switch between these two levels depending on the absorption or emission of the electromagnetic waves with specific energy $\varepsilon = hv$. Combining these two formulations, one can obtain the following equation as the basic equation for EPR spectrometry:

$$g_e \mu_B B_0 = hv. \quad (2\text{-}5)$$

This implies that the switching of electron spin can only respond in a narrow band of external magnetic field corresponding to the microwave band at a specific frequency, v.

According to the Maxwell-Boltzmann distribution, there are more unpaired electrons in lower energy levels and thus a signal of net absorption of energy is monitored and recorded. In experiments, when the frequency is fixed, the external magnetic field is changed from low to high intensity, leading to a signal intensity change with the external magnetic field. This

magnetic field dependent signal known as the EPR spectra is recorded corresponding to the varying magnetic field.

EPR can also be applied to detect the tissue oxygen tension based on its spin-spin interaction with the electronic spin probe, usually Lithium phthalocyanine (LiPc). As the LiPc is very stable in biological environments, implantation does not cause damage to the tissue. The first derivative of the EPR signal has a specific value in line width, which is linearly dependent on the oxygen tension of the site near the LiPc probe (Dunn and Swartz 2003) (Liu and others 1993).

Magnetic resonance imaging (MRI)

Similar to the electrons, the nuclei have a resonant frequency, at which extra electromagnetic energy can change the spin state of the nuclei and trigger them to emit an detectable electromagnetic wave. In an extra magnetic field, each proton has its own spin with an axis aligning with the extra magnetic field, which is known as precession. This precession is found to have a angular velocity ω_0 (the Larmor frequency) that is linearly dependent on the strength of the magnetic field B, with a factor of γ_0 (gyromagnetic ratio):

$$\omega_0 = \gamma_0 B_0 . \qquad (2\text{-}6)$$

In the steady state, the overall effect of the precession of all protons in the nuclei is a net magnetisation in the direction parallel to the applied magnetic field (taken to be the *z* axis). When applying an electromagnetic pulse wave with the Larmor frequency, the protons are excited and the resulting net magnetization vector flips over 90 degrees and rotates in the *x*-*y* plane. Through the spin-lattice interaction and the spin-spin interactions, the net magnetization restore its precession and flips the net magnetization back towards the *z* direction. This restoration leads to an increase in the *z* direction (longitudinal relaxation),

corresponding to T_1 and a decay in the magnetization in the *x-y* direction (transverse relaxation), corresponding to T_2, both accompanied by electrical signal changes to be detected by the coils in a MRI machine (Weishaupt, Köchli, Marincek 2006).

Functional MRI techniques are based on the blood oxygen level dependent (BOLD) response to a cognition task to measure neural activities of the participant. Owing to the fact that deoxy-haemoglobin (d*Hb*) is paramagnetic whilst oxy-haemoglobin (*HbO*) is diamagnetic, a change in the blood d*Hb* concentration is associated with a change in the local magnetic susceptibility, altering the frequency of the local magnetization around the vessels and surrounding tissue. This frequency shift creates spin dephasing in a voxel and causes a decay in the resulting T2* signal (Ogawa and others 1990). In addition to the d*Hb* concentration, the vessel orientation is also known to play a role in the generation of the BOLD signal (Kwong and others 1992).

The BOLD signal is related to CBV, CBF and the cerebral metabolism rate of oxygen ($CMRO_2$), and is thus believed to be a good index for neural activity. Owing to the good temporal (1 s) and spatial (2-3 mm) resolution, fMRI has been widely used for brain mapping in cognition experiments (Sarty 2007). However, fMRI does not directly measure the tissue oxygenation, but a spatial average of the three variables above. In other words, the BOLD signal can be expressed by a lumped function of CBF, CBV and $CMRO_2$ according to curve fitting of the experimental data for one given monitoring voxel. The resolution is good enough for dynamic neural imaging, but may not be used to resolve the localised haemodynamics and oxygenations at microvascular level. The spatial resolution of the fMRI techniques can be refined with higher magnetic field strength, which however may cause potential damages to tissue samples and by far only applied to animal tests.

Positron emission tomography (PET)

Positron emission tomography is another monitoring technique for cellular metabolism in brain. The isotopes are unstable atoms, which have one more proton than neutrons in the nuclei and thus easily break down into a neutron and a positron. As the breakdown occurs, the positron leaves the nuclei and finally collides with an electron, causing a pair of gamma ray emission at 180 degrees which can be detected by a crystal. A 3D map for the tracer concentration can be created and a correlation with the tissue metabolism can be made and hence a map for metabolism.

After injecting the biological tracer tagged by radioactive isotopes, such as ^{18}F deoxyglucose, into the blood circulation, the neurons constantly take the glucose and tracer when doing neural firing, and the tracer remains in the neuron due to the restriction of the reactions on the isotope. In this way, the accumulation rate of the tracer is associated with cellular metabolism, which constantly supplies the energy required by the ion pumps to restore the membrane potential after neuron firing (Kandel, Schwartz, Jessell 2000).

2.5-3 Experimental studies about oxygen transport in network and tissue

In the last section, the principles of some techniques to measure cerebral oxygenation have been reviewed but the experimentally based oxygenation field distribution in the microvascular network and cerebral tissue will now be addressed in this section for ease of comparison to relevant results obtained from theoretical models.

As reviewed by Tsai (Tsai, Johnson, Intaglietta 2003), the oxygen distribution inside the vascular network differs from tissue to tissue and from species to species, the corresponding values varying also with the measurement technique used. In general, in the vascular network, the concentration drop across terminal junctions of the capillary and arteriolar network (20-50

mmHg) is larger than that of the venular tree (0-10 mmHg) for most tissues. The longitudinal O_2 gradient is also different from tissue to tissue, as the drop is lowest in the resting skeletal muscle and highest in the active brain or the myocardium.

In particular, Rubin and Bohlen (Rubin and Bohlen 1985) found that the average PO_2 in the rat cortex capillary bed is 13 mmHg and only 5% of sampled capillaries have a haemoglobin saturation higher than 30%. As found by Vovenko (Vovenko 1999), the PO_2 in the pial microcirculation in the rat cortex is about 58±11 mmHg at the arteriolar end of the capillary bed and 41±11 mmHg at the venule end of the capillary bed. Across the capillary bed, drops of haemoglobin saturation, *S*, is the greatest (23±14%) amongst other vessels compartments such as arterioles (10%) or venules, suggesting the importance of the capillary bed in the oxygen exchange with surrounding brain tissue.

Diversity is also found in the values for the tissue PO_2 measurement due to the variability in tissue samples, species and measurement techniques. In the experimental data reviewed by Tsai et al. (Tsai, Cabrales, Intaglietta 2010), three different tissue measurements in a hamster dorsal-window-chamber model were compared, as shown in Figure 2.8. The tissue PO_2 level distribution, obtained from multiwire polarographic electrode arrays placed on top of the tissue suffused with a heated buffer solution (Nolte and others 1997), has a peak below 20 mmHg and is close to zero for the values of oxygen tension higher than 40 mmHg.

However, the histogram obtained from a sealed window chamber with a random sampling of the tissue, showed a blunter peak at around 20-25 mmHg and a longer tail stretching further to about 65 mmHg. The oxygen distribution in terms of the volume fraction, based on the oxygen-dependent quenching of phosphorescence and signal analysis by the Maximal Entropy Method analysis (Wilson and others 2006), has a left shifted shape with a peak volume fraction of 0.013 at around 40 mmHg, with an average of all sampled volumes at

around 50 mmHg. The curve in the high PO_2 band might not be as accurate as the low level band since the uncertainty in determining phosphorescence lifetimes increases with decreasing signal to noise ratio.

Due to copyright issue, this figure is removed.

Please refer to Figure 1 in the reference.

Figure 2.8 Tissue PO_2 obtained from three different measurement techniques, white bar (Nolte and others 1997) ; black bar (Tsai, Johnson, Intaglietta 2003); and dashed line (Wilson and others 2006). This figure is removed for due to the concern of copyright .

For rat brain tissue, the tissue PO_2 level measurement data shows a large degree of heterogeneity in the local tissue PO_2 values. Grote and coworkers (Grote and others 1996) used surface and needle polarographic electrodes to evaluate the tissue PO_2 distribution in rat cortex. It was found that the tissue average oxygen level decays with the depth of the cortex, as shown in Figure 2.9 (a). The tissue PO_2 is 64±25 mmHg at the surface, dropping to 45±19 mmHg at a depth of 50μm and finally reaching a plateau of 29±9 mmHg at 200 μm. Figure 2.9 (b) shows the frequency histogram of PO_2 in the cerebral tissue in the surface region with a shape close to a normal distribution with a mean value of 27 mmHg, ranging from 0-80 mmHg.

(a) (b)

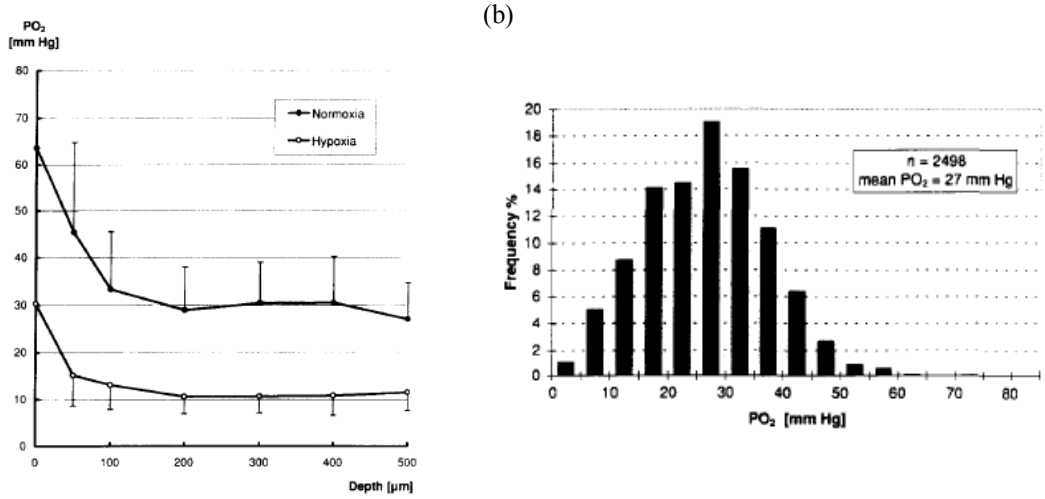


Figure 2.9 (a) Tissue PO_2 profile variations with depth from the rat cortex surface; (b) Oxygenation histogram in the surface rat cortex (Grote and others 1996).

Another set of PO_2 measurements (Sharan and others 2008) using a polarographic electrode on the rat cerebral cortex, gives a radial profile of tissue oxygen level next to the arteriole. As shown in Figure 2.10, the results are categorised by arteriole diameter into three groups (D: 10µm; E: 20µm; F: 30µm), where the PO_2 level is found to decay with the distance from the vessel wall, and the larger vessels tend to have higher values of near wall PO_2 levels. Since the capillary diameter is about 8-10µm, the profile in group D is the most relevant to the cerebral microvasculature, showing a PO_2 range of 10 to 75 mmHg).

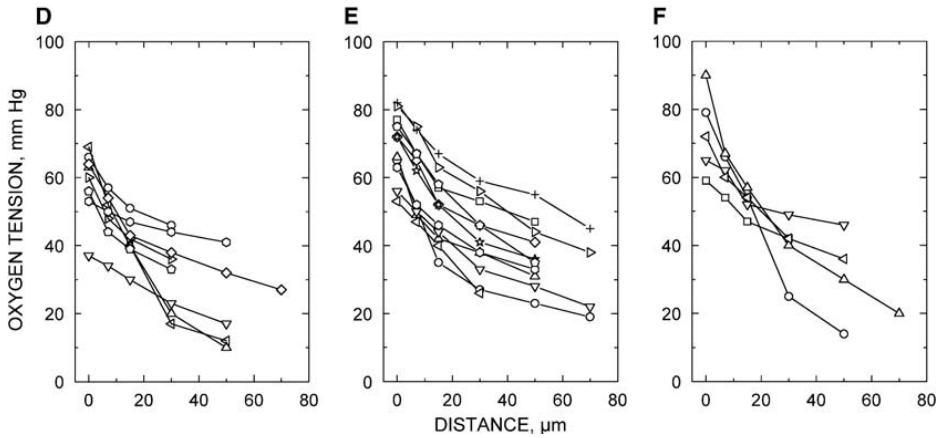


Figure 2.10 Tissue radial PO_2 profile near three different sizes of pial arteriole in the rat cortex, taken from (Sharan and others 2008).

Due to ethical constraints, the O_2 probe placement in normal human brain tissue is prohibited and direct brain tissue oxygenation measurements can only be performed in neurosurgery. Using single photon emission CT, Hoffman et al. (Hoffman, Charbel, Edelman 1996) reported an average value of 37 mmHg for the PO_2 level for 8 patients with uncompromised CBF. Assad et al (Assad and others 1984) utilized a surface polarographic electrode to measure the cortical PO_2, with values found between 33-36 mmHg during tumour section surgery. Higher values, with a mean PO_2 level of around 48 mmHg, were measured with surface Licox probes (polarographic electrode) by Meixensberger et al (Meixensberger and others 1993) when the patients underwent elective craniotomies.

Clearly, oxygenation measurements in human brain tissue offer only average values of a volume of tissue, and cannot offer detailed spatial profiles for direct comparison with simulation results. It is found that in the human brain cortex, the PO_2 values lie between around 33 mmHg and 48 mmHg. Based on the experimental observations for rat cortex (Sharan and others 2008), the tissue PO_2 level tends to decrease with distance to the arteriole, from a maximum of 80 mmHg to the minimum of 10 mmHg in the extreme case. If the oxygenation histogram of a volume of tissue is a normal distribution as shown in Figure 2.9(b), with these two extremes, the mean value is very likely to be around 50 mmHg, this

value being close to the value of 48 mmHg obtained from human brain. This closeness implies that the oxygenation field observed from rat could potentially be used to approximate that in humans, and will be used as the reference values for the simulations presented here.

2.6 Cerebrovascular diseases and dementia

Dementia, a neurodegenerative disease, is a stepwise deterioration of recognition abilities resulting from brain damage, leading to symptoms of memory loss, confusion and changes in behaviour patterns, and it affects mainly the elderly people, estimated prevalence rate increasing with age. It is estimated that in the UK alone in 2007, dementia affects over 700,000 people with a rate of 1/1400 at 40-64 years but with a much higher rate of 1/6 after 84 years. It results in over 60,000 deaths, at a cost over 1.7 billion pounds per year. Delaying the onset of dementia by five years is thought to have the potential to prevent nearly 30,000 deaths each year (King's College London, London School of Economics 2007).

Alzheimer's Disease (AD) and Vascular Dementia (VaD) are two leading subtypes of such a mental cognition impairment, taking up 62% and 17% of the total cases respectively (King's College London, London School of Economics 2007). For AD patients, a high density of amyloid plague is commonly found in the brain parenchyma (Tiraboschi and others 2004). Traditionally, it is accepted that AD is associated with accumulation of beta Amyloid (Aβ) peptides, which disrupt the cellular calcium ion homeostasis, leading to programmed cell death (apoptosis) (Yankner, Duffy, Kirschner 1990)

On the other hand, vascular dementia is believed to relate to cerebrovascular disease. According to (Bowler and Hachinski 2003), subtypes of ischemia related VaD can be divided depending on the location (cortical, white matter, thalamus), the size, the vascular distribution (small, large or microvessels), and the severity of the lesions. They may also be categorised

by their etiology (Chui and others 1992), such as embolism (embolus clotting), arteriolosclerosis (lipid-laden plaque obstruction), hypoperfusion (low blood perfusion), and amyloid angiopathy (deposition induced vessel wall failure). Some of VaD may result from small scale brain infarctions caused by local ischemia due to obstructions at the microvascular level (Jellinger 2008).

Although the origins of AD and VaD seem different (neurodegenerative and vascular respectively), increasing evidence suggests the existence of reciprocal interactions between these two neural diseases (Iadecola 2010) as Aβ has a potent cerebral vascular effect and ischemia-hypoxia is a significant regulator of amyloidogenesis (Iadecola 2004). In addition, coexistence of VaD and AD is found in the brain samples of a large number of patients with dementia, especially elderly subjects (Bowler and Hachinski 2003).

As mentioned in Chapter 1, neural and vascular units coordinate well with one another to maintain homeostasis of the cerebral cellular microenvironment. For example, both vascular and brain parenchyma cells can play a role in CBF regulation. Neural signals induced by neural activation can either transmit through synaptic connections (Paulson and others 2010) or be mediated by the astrocyte end-feet enclosement (Iadecola and Nedergaard 2007), and finally cause contraction or dilation of microvessels to regulate the local blood supply. On the other hand, mechanical (shear stress), chemical and cellular stimuli (immune cells) from blood flow can trigger specific receptors on the lumen side of the -endothelial membrane to initiate a signal cascade and to release potent molecules like protanoids, NO and endothelin to mediate the local flow control (Wolburg and others 2009).

If the regulation of blood flow becomes inefficient, the microenvironment in the cerebral cells cannot be well maintained. When a supplying blood vessel becomes blocked due to any disturbances from the neurovascular unit, CBF is impaired in the region of brain tissue

perfused by this vessel. Tissue will rapidly suffer from a varying degree of shortage of blood or oxygen supply depending on its distance to the supplying vessels and the new bypassed flow patterns (Heiss 2000).

Since brain tissue relies on aerobic metabolism and does not have an energy reservoir like other tissues, such a shortage will impair the generation of ATP in neural cells, and hence any energy dependent bio-reactions, such as ion pumps, or other membrane transporters will be affected. As a result, membrane transporter function, for example the glutamate transporter requiring the involvement of sodium ions, will stop. An abnormal increase in glutamate in the extracellular space, which is kept low under normal conditions, mediates the influx of calcium, leading to failure of mitochondria and further energy depletion (Deb, Sharma, Hassan 2010). In the worst case scenario, if the energy depletion lasts for more than a couple of minutes, cell death may be triggered via apoptosis (programmed death) or via necrosis (programmed death and to toxicise nearby cells) (Lipton 1999).

Several factors, such as the severity and duration of vessel occlusions, influence the size of infarctions in brain tissue, but the detailed correlations are not fully understood. These infarctions or lesions can be associated with cognition impairments; for instance, multiple small or micro-infarcts at strategic locations owing to co-occurrences of large or small vessel disease can damage the ganglia pathways in thalamocortical, striatocortical and prefrontal-basal ganglia pathways, which in turn impair the normal functions of recognition, memory and behaviour (Zekry and others 2003) (Szirmai and others 2002).

On the other hand, Lacunes lesions in basal grey or white matters, caused by disruptions to the subcortico-frontal circuit, are also believed to be correlated to VaD according to recent studies (Reed and others 2001) (Kovari and others 2004) (Gold and others 2005). These two kinds of morphometric features are commonly found in VaD brains, while large cystic

infarcts are less frequently found. However, the detailed relationships between the degree of cognition impairment and infarction related indices, such as the number, size, and location of the infarctions, are not yet fully understood (Jellinger 2008).

The idea of preventive treatment is to control the risk factors and causes of these cerebrovascular events before the cognitive deficit reaches the point of frank dementia. In addition, early detection is also of importance in order to offer suitable treatment intervention at the early clinical stage (Bowler and Hachinski 2003). Therefore, for some micro-ischemic events, which may not be detected by modern neural imagining tools, mathematical models can provide another window to further understand the interplay between the haemodynamics and oxygenation at the microcirculation level. This knowledge is crucial for future development of improved therapies for microcirculation related Vascular dementia or even Alzheimer's disease owing to their reciprocal interactions.

2.7 Summary

In addition to the literature about cerebral haemodynamics, tissue oxygenation and diseases, publications providing the topological and geometric information about human cerebral network have been reviewed in this Chapter, which will serve as a reference when reconstructing artificial networks mimicking the real microvasculature in the human brain. The foundation of the whole theoretical modeling work and the comparisons and optimisations of different algorithms for this attempt will be addressed in detail in Chapter 3.

Chapter 3. Network generation

3.1 Introduction

In all body organs, an adequate transport of waste and nutrients supplied via the circulation system is equipped to provide a stable environment for tissue to meet varying physiological demands. Vascular regulation provides a very tight supply between supply and demand. This delicate physiological balance may be destroyed if the haemodynamic regulation becomes impaired; for example in the cerebral vascular system, irreversible damage can be caused by changes to the blood supply bringing brain cells to a pathological state, which, when seen in brain tissue, can lead to some form of functional deteriorations. However, the tight balance between supply and demand can be well maintained by flow compensation of the highly interconnected microvasculature, which effectively restricts such deterioration inherently local in form. It is strongly dependent upon the regional properties of the microvasculature. Until recently there has been little information available to understand such flow patterns.

Very recently, the human cortex vasculature was finally studied and analysed in detail for the first time by Cassot et al. (Cassot and others 2006), and realistic cerebral morphometric information, such as the statistical distributions of lengths and diameters, vessel density and orientation, for the first time became available that reflects the fact that the microvascular network is a network-like rather than a tree-like structure.

Conducting models of these networks is, however not a simple task. A novel algorithm is proposed here to generate artificial microvascular networks based on quantitative experimental data obtained in human brain tissue. Vessel statistics are compared with experimental data to validate the artificial networks, showing a high level of agreement. Furthermore, the blood flow and oxygen transport in both the microvessels and the tissue can be analysed through flow and mass transport equations, to obtain a clearer picture of how the

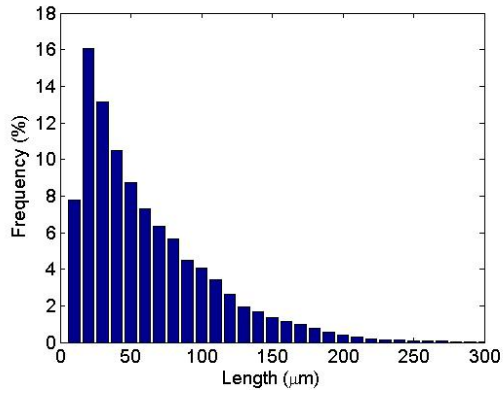
processes underlying and temporal changes in vascular dementia are influenced by the micro-scale haemodynamics.

3.2 Network information

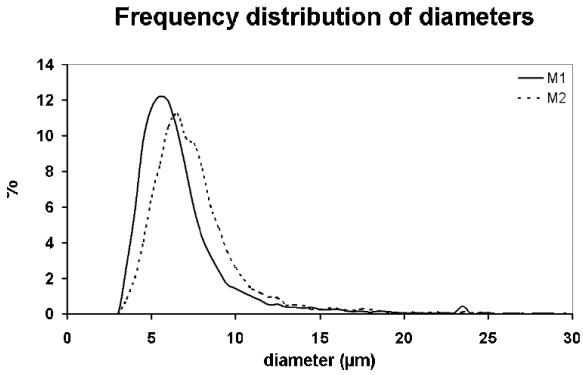
The aim of the present model is to create a set of networks which accurately mimic the cerebral microvasculature observed in experimental studies. It is widely accepted that the network topology and geometry strongly influence the patterns of blood flow circulating in the vessels and hence oxygen transport in the surrounding tissue (Harrison and others 2002). Since there are very limited topological data found in the literature concerning the cerebral microvasculature, the experimental study by Cassot et al. (Cassot and others 2006) is used here as the source of data. In their paper, they quantified all of the vessel segments in two different regions named M1, volume $(1.6\ \text{mm})^3$, and M2, volume $(2.15\ \text{mm})^3$, in the collateral sulcus in the right temporal lobe. Although this is only a small part of the cerebral vasculature, it serves as a representative sample and the algorithm proposed here for this specific case could easily be adjusted for other data sets.

The vessel length distribution plot, shown in Figure 3.1, is heavily shifted towards short lengths with a maximum at around 15 μm, decaying gradually to zero at lengths around 300 μm. The diameter distribution shows a nearly normal distribution in M1 and M2, both having a tiny peak at around 23-25 μm, which reflects the very small portion of the larger vessels included in the dataset. In addition, detailed characteristics of the networks are given: in particular, the average connectivity (neighbours per junction) and vessel density (number of vessels per unit volume) both of which reflect the topological features of the network. The vessel density provides a measure of the total number of the vessels in a given space, while the average connectivity allows for an assessment of how the network is constructed.

(a)



(b)



(c)

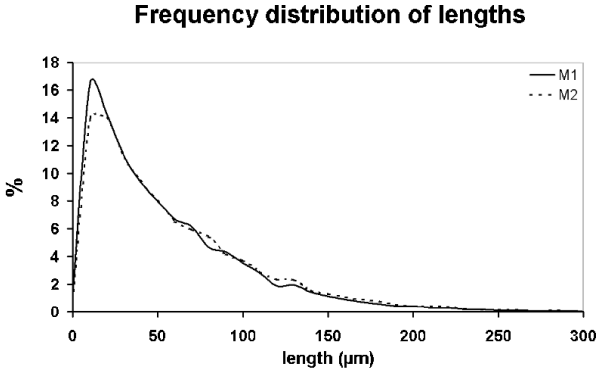


Figure 3.1 (a)Histogram of reproduced vessel length for the complete network, based on (Cassot and others 2006); original vessel diameter (b) and length distribution (c) of a human cerebral network taken from (Cassot and others 2006).

In addition to the length histogram of the entire network, the mean value, standard deviation, skewness and kurtosis of the length distribution, in two groups, classified as the complete network and the capillaries (the network excluding vessels with diameter larger than 9 μm), are also given. The average connectivity is calculated by summing up the branching of the vessels over the number of nodes giving an average values of 3.1.

Based on these data, it is possible to create physiologically realistic networks in order to get a more accurate picture of the system dynamics. Different methods will now be detailed for the vessel network generation and their performance compared. However, it should be noted that the length and diameter histograms give a continuous distribution. This will be difficult for

direct comparison with model simulations since the model vessel length distribution will inevitably be a discrete, rather than a continuous distribution. In order to facilitate this comparison, the experimental data have been converted into a discrete histogram, by creating several regions of length range 10 μm and calculating the interval area under the curve. After normalization, the reproduced length distribution histogram is shown in Figure 3.1.

3.3 Network creation algorithms

To present a network uniquely, only two matrices are needed: the node position vectors, **v**, and the connectivity matrix, **A**. The first is an $n \times m$ matrix which is an m-dimensional coordinate list for the n nodes of the network. The second one is an $n \times n$ matrix, where each element A_{ij} is equal to one if node i is connected to node j, and zero otherwise, leading to a symmetric matrix.

The connection between any two nodes is created by switching the relevant values in the connectivity matrix **A**, from 0 to 1, and this operation creates one "arc". One vessel can be composed by a number of arcs arranged in cascade or just by one arc. Vessel junctions are the nodes where the vessels are interconnected and hence a node may or may not be categorised as a vessel junction.

First, n sets of position vectors for nodes were produced by using a random number generator (Chandler and Northrop 2003) for a uniform distribution. These numbers are then used as the bases for the coordinate vectors for n nodes in three dimensions. Then the connections between nodes are added or removed through different network generating methods by consideration of a range of different factors, such as the node to node distance, the average connectivity or the vessel space density.

In the first step of the algorithm, a number of nodes are randomly located in a volume with a node density 3000-6400/mm^3 depending on the network generation method. This stochastic arrangement for the nodal locations attempts to reflect the spatial heterogeneity of the junction point distribution in real cerebral networks. It is very difficult to find a general trend regarding the junction distribution patterns due to the lack of sufficient human cerebral microvascular samples. The heterogeneity of the cerebral network structure is a common feature in the cerebral microvasculature and this includes the variations among different samples in terms of vessel diameters and length distribution, connectivity features as well as the junction locations. Although not all nodes are vessel junctions, the random nodal distribution in tissue space, usually leading to random location distribution of junctions, should be able to reflect the heterogeneous structure of the real brain network.

Several methods including the Shortest arc method (SAM), Gamma Distribution Method (GDM), Spanning Tree Method (STM) and the Modified Spanning Tree Method (MSTM) are now proposed here to generate artificial networks, giving corresponding statistical characteristics that will be compared with the available experimental data. Since the process is inherently random in nature, for each simulation there is always a variation in the nodal spatial distribution, and thereby geometric and topological variations will be found amongst the samples created from each kind of method. Therefore, a full statistical analysis is required to present the nature of the sample depending variability. One hundred networks are generated here based on each method to give reasonable statistical results, and mean and standard deviation values among these 100 samples are calculated accordingly for comparison.

After the lengths of all the vessels in the microvasculature are determined by one specific network generation method, a value for vessel diameter must be assigned to each vessel.

According to the experimental data (Cassot and others 2006), the diameter distribution of the networks roughly follows a Normal distribution with mean 6.23μm and standard deviation 1.3μm. Based on these data, the diameter of each vessel is set as a value obtained from a random number generated from this Normal distribution with mean and standard deviation values given above.

3.3-1 Shortest arc method

According to the length histogram obtained from experimental studies, there are many vessels with lengths under 100 μm. Therefore, it is logical to generate arcs with short lengths. In the shortest arc method, the algorithm builds up three connections for each node. During the procedure, three arcs are created from the first node to the final, creating a complex web-like structure. During this process, some connections may lead to unrealistic architectures in the network, such as closed loops. It is thus necessary to remove the redundant connections to keep the artificial network relative to the real one. To do this, an arc removing procedure is introduced to the method and the redundant arcs are tagged and cancelled in the existing network.

In addition, the arc removing procedure serves another function. After building three connections, some nodes may have more than three links to their neighbours. The extra connections are arbitrarily selected and removed by a "dicing procedure". In the procedure, the nodes with arcs are tagged and branching vessels are assigned a random number, in a range 0 to 1, which is produced from a uniform distribution number generator (Chandler and Northrop 2003). The probability of the removal then depends on the number of redundant arcs surrounding the given nodes. If the value of a tag for an arc is smaller than the removal probability for a given node, the arc will be removed and this repeats until the average connectivity for entire network converges to 3.1.

For example, all connections for a node with m neighbours, if m is larger than 4, are labelled and some of them (m-3) will be removed according to the procedure above. Such a process is also used in other network generation methods for cancelling of unwanted links in the network. Figure 3.2 gives the basic procedures for how this algorithm generates the network. The adding or removing of connections is simply carried out by setting the corresponding elements of the connecting matrix **A** from 1 to 0.

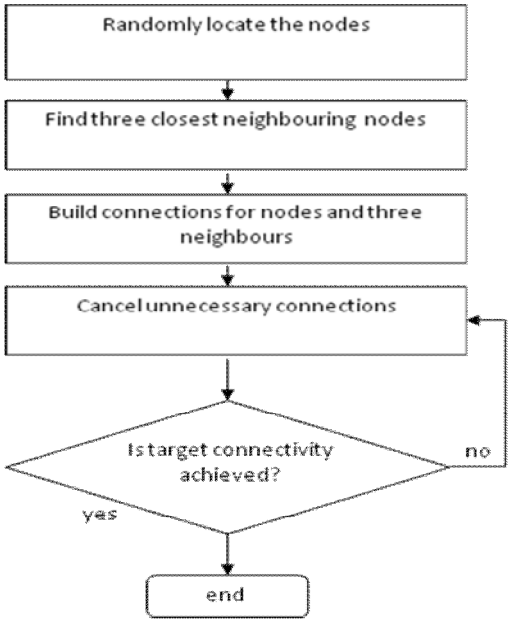


Figure 3.2 Flow chart for the shortest arc method

A typical artificial network is presented in Figure 3.3, where the vessel diameter is not shown to scale for plot clarity when vessels are densely clustered. This method produces a left shifted peak in length compared with the data based on experimental statistics, with average kurtosis 4.17 and skewness 0.32. A very high population of short vessels is produced by this method but the distribution otherwise shows a poor agreement with the experimental data; in particular, the distribution curve at large lengths is under-estimated. Furthermore, this method can sometimes generate isolated small webs connected to other webs through only one vessel

in the network, as shown in the top corner of Figure 3.3, which is very unlikely and not physiologically realistic.

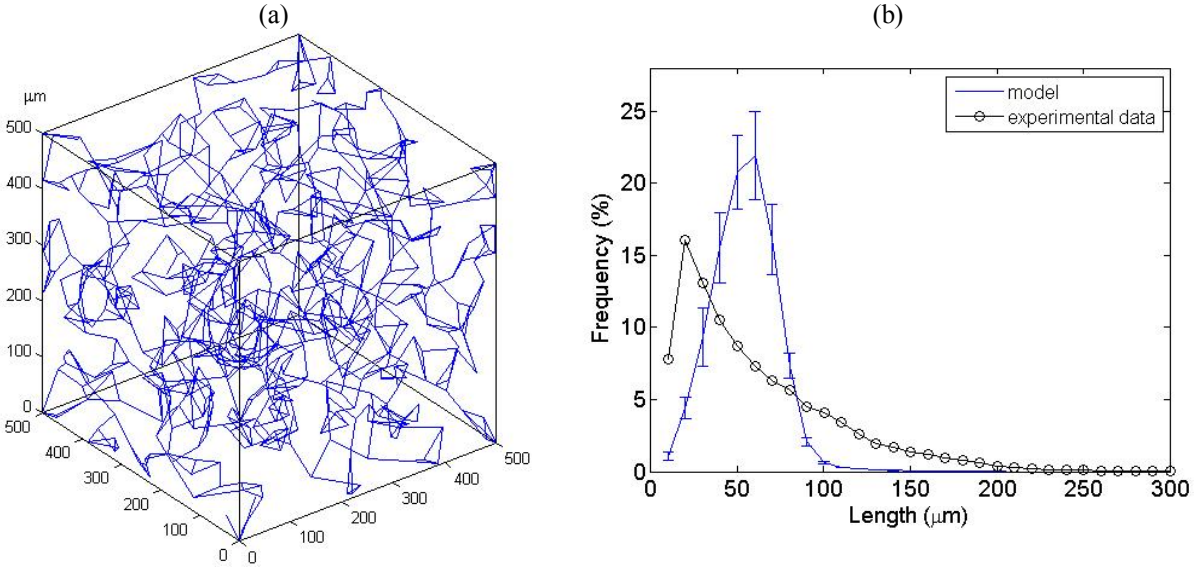


Figure 3.3 (a) Typical network created by the shortest arcs algorithm; (b) Length distribution histogram compared with the experimental data converted from (Cassot and others 2006)

3.3-2 Gamma distribution method

If the vessel lengths can be assigned directly, one possible way to create a network with desired length distribution is to choose a random number generator following the same distribution. In this way, the target random numbers, given by the specific distribution number generator, can be set as the values of the vessel lengths. The long tail of the length distribution in the experimental data suggests that the type of distribution characterised by the data is close to the gamma distribution. The probability distribution function of the gamma distribution can be expressed in terms of its scale parameter, a, and shape parameter, b (Hogg, R., Craig, A. 1978):

$$f(x;a,b) = a^b x^{b-1} \frac{e^{-ax}}{\Gamma(b)}. \quad (3\text{-}1)$$

A random number generator (Chandler and Northrop 2003) is adopted again for the gamma distribution. For each node, three random lengths are created by the Gamma distribution generator for the target lengths and the three arcs with lengths closest to the target lengths are built. Similar to the shortest arc method, the resulting average connectivity of the created network may be higher than 3.1 and the same arc removal procedure is adopted in this method as described above. Thus some of the arcs attached to a node having more than 4 neighbours are selected arbitrarily based on a uniform distribution and removed by setting the relevant elements in the connecting matrix to 0 until the average connectivity of the entire network converges at around 3.1.

Many trials have been made for this process with a wide range values for a and b, calculating the RMS error between actual and simulated length histogram. However, the most optimal values found here were still unable to create the desired long tail and enough arcs with short lengths. When generating the random numbers, directly applying the mean values and the variations obtained from the experimentally based statistics, b/a=59.57μm and b/a^2= $(29.41\mu m)^2$, is not able to generate a network giving the best match to the experimental statistics. Surprisingly, values of the scale a and shape number b of 0.05 and 1 respectively are found to be the optimal pair of values to best fit the target length distribution.

If arcs with lengths that were exactly the same as the values created by the gamma random number generator were used, the length distribution of the simulated networks should have been close to gamma distribution. This cannot be achieved by the settings of current method since the vessel lengths cannot be assigned directly. The nodal locations are determined in the

very beginning and in the algorithm, only three arcs, which are the closest matches to the random numbers among all available connections for each node, will be created. This length approximation in the selections of arcs, however, always creates arcs with length differences to the targets assigned by the random number generator. As a result, there is inevitably a discrepancy between the simulated and experimental based distribution curve for vessel lengths. The main steps of this method are demonstrated by Figure 3.4, which is similar to the shortest arc method except for the new arc selection criteria.

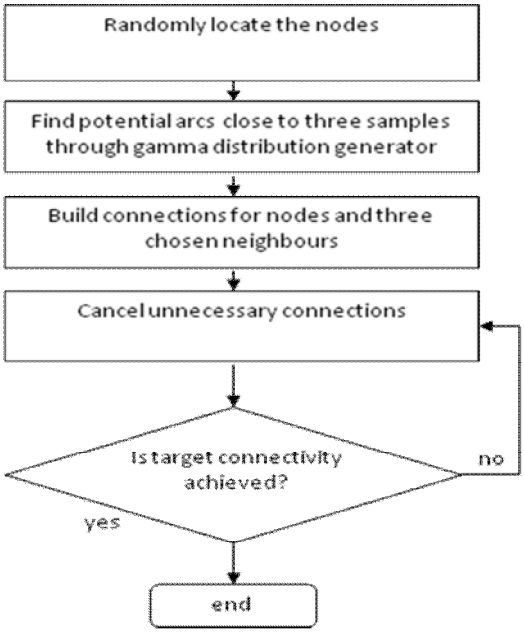


Figure 3.4 Flow chart for the gamma distribution method

One typical network is presented in Figure 3.5(a) where there are many arcs with similar lengths. The length histogram shows that over 55% of vessels have lengths ranged between 50μm and 80μm. Some regions are densely clustered by these similar vessels whilst others

are almost empty. This creates very non-homogenous vessel clustering patterns. In some cases, the vessel segments are nearly parallel to each other (some examples are shown in Figure 3.5(a). Many sharp angles between vessels and the non-even clustering pattern of the space resulting from this method are very unlikely to occur in a real vascular network.

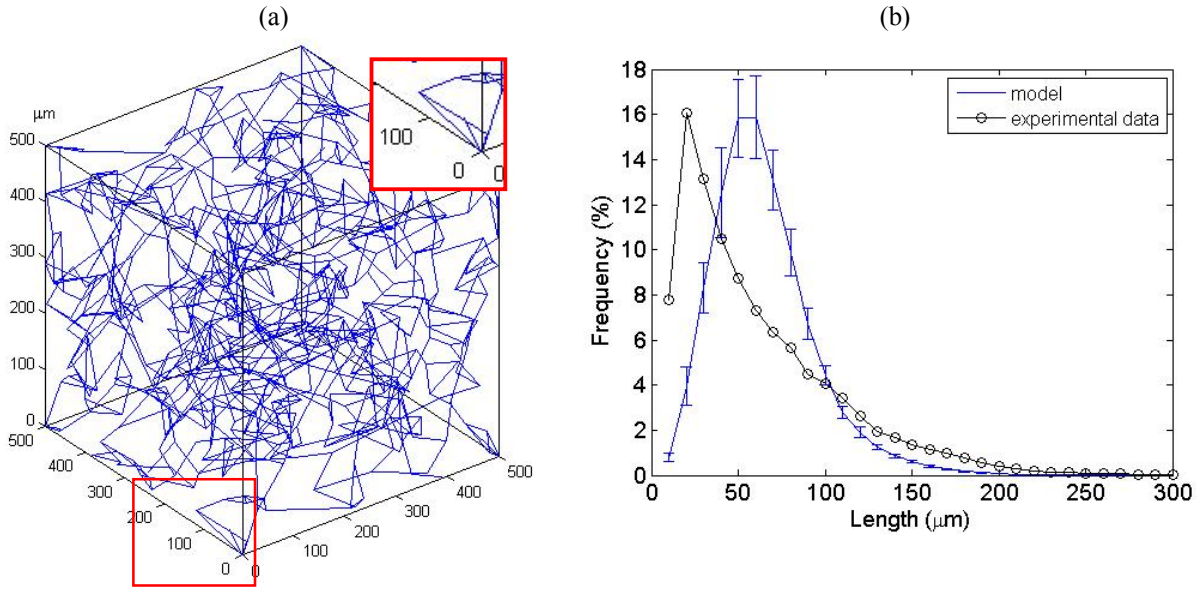


Figure 3.5 (a) Typical network created by the gamma distribution algorithm; (b) Length distribution histogram compared with the experimental data converted from (Cassot and others 2006)

Despite using the optimal set of parameter values for *a* and *b*, the resulting length histograms of the best fit networks still provide a poor comparison with the experimental data. As shown in Fig 3.5(b), it can be seen that the distribution curve is right shifted compared to the experimental length histogram. The GDM with the optimal setting of parameters generates a network with a tail longer than the SAM, but the tail is still not long enough. Meanwhile, the proportion of vessels at short lengths (30-70μm) is over-estimated and the peak in the distribution curve for the real networks is poorly estimated.

3.3-3 Spanning tree method

In the third method proposed here, the design strategy is to generate the branches from nodes in an existing small network to the closest node outside, node by node, expanding to a large network and then combining with another network created to form an interconnected 3D web. The algorithm is based on the minimum spanning tree method (Wallis 2007). The network is composed by two spanning trees merging together, each of which has a minimum total vessel length. This implies a minimum material cost when constructing the whole network. Longer vessels created by connecting several short vessel elements are commonly found in the network generated by the minimum spanning tree method.

In the algorithm, the first connection is built by searching for the shortest node-node distance in the space, then creating the initial tree which contains only two nodes. The next step adds a new node to the existing tree by building the shortest connection between the nodes of the tree itself and the nodes outside. Each time the new tree is formed, a search is made for a new node outside. To repeat this way, more and more arcs are added to the existing network, as if a new branching from the existing main part of a tree. As a result, the tree has many terminal nodes, each of which has only one neighbour arc.

In the second stage, similar connection procedures proceed on these terminal nodes only, building a second tree. In the end, these two trees merge together to form a web-like network through the connections at tip nodes. Interconnections of vessel elements are guaranteed so that creation of any isolated sub-networks is efficiently avoided. The flow chart, shown in Figure 3.6, summarises the main procedures of this method.

Many nodes in the network generated by this method are two-connected (one node with two arms), which allows the long, curved vessels observed in real cerebral network to be presented by a series of two-connected arcs. This creates more curved vessels in space than in

the two previous methods and the continuous bending feature of vessel configurations in real networks can easily be achieved.

In addition, this method reproduces the structure of real microvasculature in that arcs becoming parallel, even crossing over, are excluded. This can be explained by the fact that if two arcs with a very narrow angle are chosen as part of the tree, the third length opposite to the narrow angle should be the shortest one. In the current method, the shortest arc would be picked up by the shortest preference algorithm, and a triangle would be formed. Two long connected arcs with a narrow angle are thus absent in the resulting network.

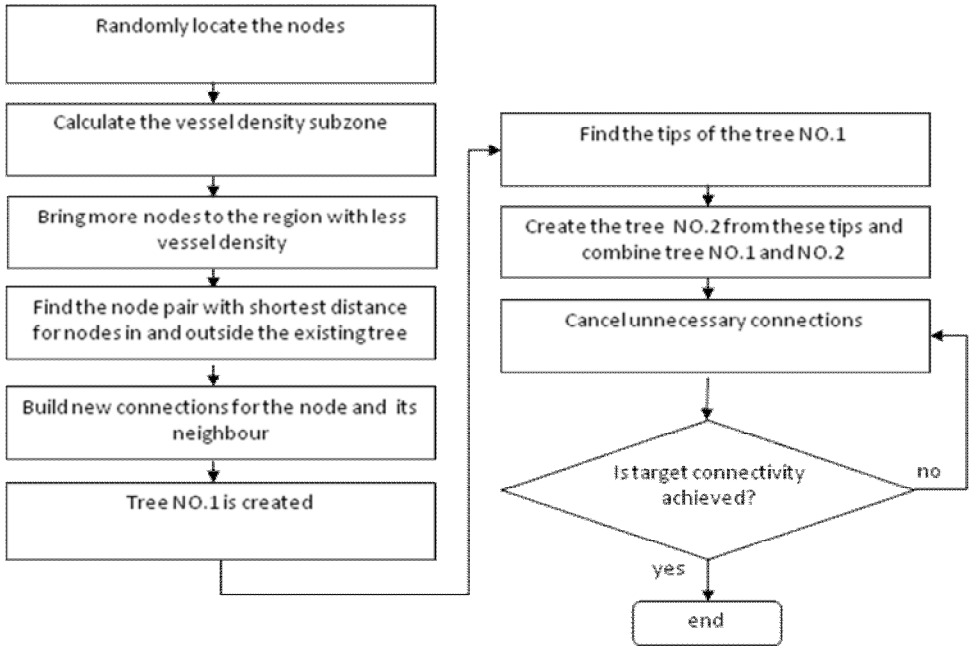


Figure 3.6 Flow chart for the spanning tree method

The basic trend of the distribution curve at long length modes is now well represented by the current method as shown in Figure 3.7. A more homogenous spatial distribution of vessels is achieved by the MST when visually compared to the network created from the SAM and the GDM. The network patterns have neither the high clustering of vessels in certain locations of

the space in the networks generated by the GDM, nor the isolated sub-networks found in those generated by the SAM. The desired long tail in the experimental based histogram is produced by the procedures of combining short vessel segments into longer vessels. However, the sharp peak at short lengths in the distribution curve cannot be produced by the simulated network; instead there is a broader peak in the range of the lengths 40-70µm.

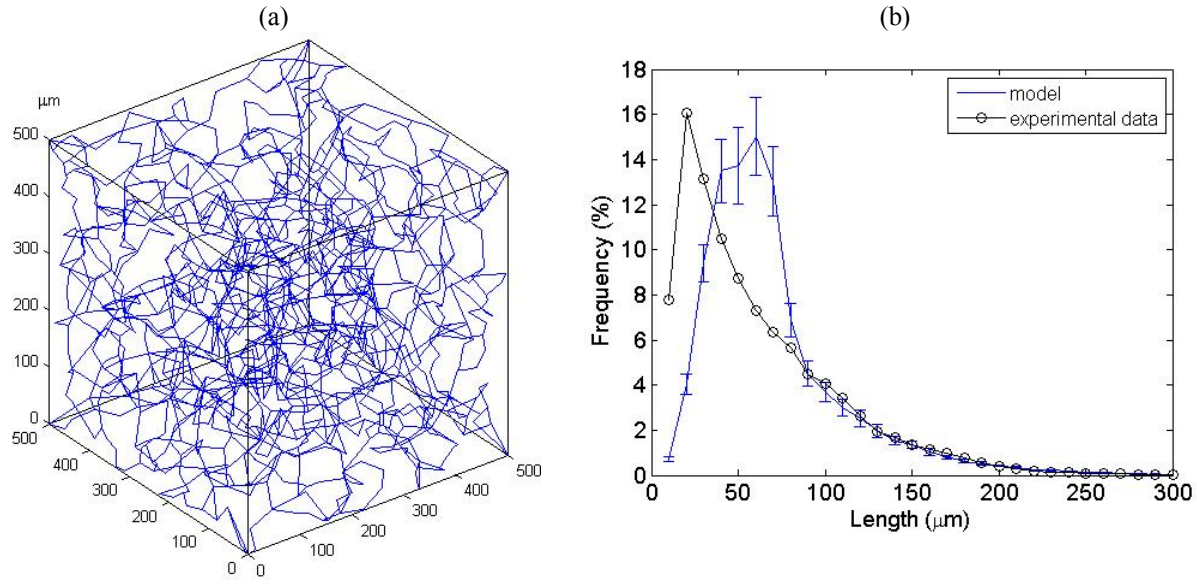


Figure 3.7 (a)Typical network created based on spanning tree method; (b) Length distribution histogram compared with the experimental data converted from (Cassot and others 2006)

To preserve the well fitted tail and to narrow down the peak in the histogram, a length filter is later introduced, in order to cancel some of the existing connections at lengths within the range 50-100 µm for adjusting the length distribution curve. The basic concept of the operation is similar to the arc removal procedure mentioned before but an arc length requirement for the operation is also included.

For each node, each potential arc to be removed is assigned a value tag from the random number generator and a comparison is made between this number and the given operation

probability. For each node, an existing neighbour arc will be removed if its length is within the filter range and the value tag is smaller than the operation probability. In this way, the number of vessels within the range of 40-100μm is effectively reduced, and the peak of the new distribution curve shifts to the left as expected.

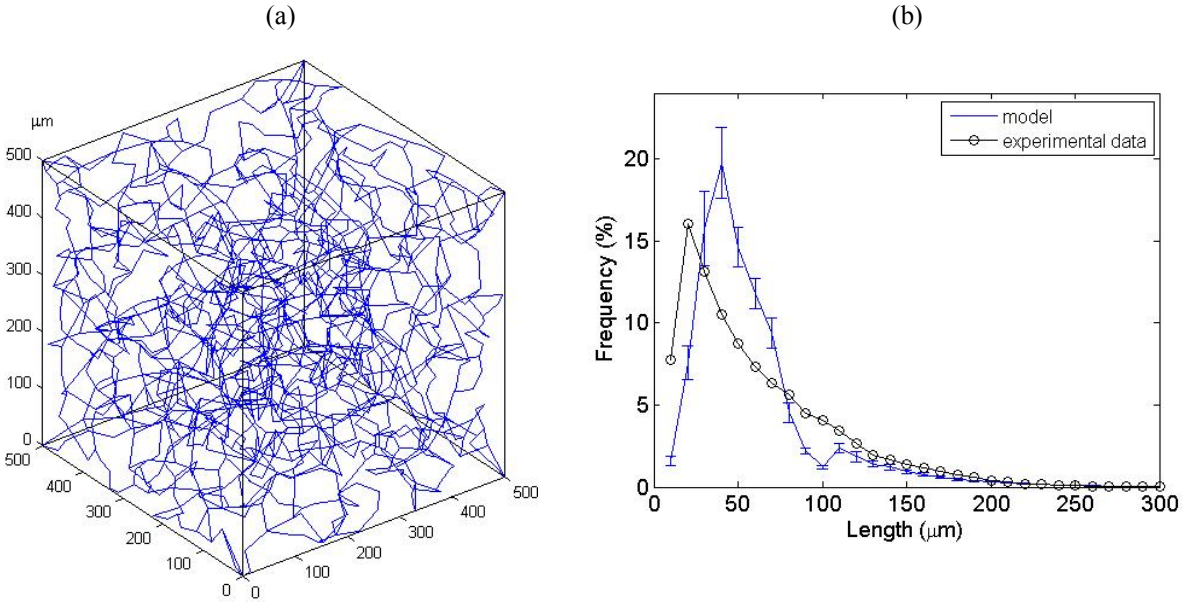


Figure 3.8 Typical network created by the spanning tree method with a length filter; (b) Length distribution histogram compared with the experimental data converted from (Cassot and others 2006)

When the length filter is introduced, the peak becomes narrower, shifting to smaller lengths; however, the peak length is still different from that of the target curve. The previous closely fitted long tail is destroyed and an undesired notch at around 100μm emerges, which is likely to be the trade off of introducing the filter. The third network generation method, like the first and the second, thus still does not generate networks with a proper length distribution. Incorporating a length filter is one possible way to regulate the length distribution, but it must be carefully tuned to avoid unexpected changes outside of the region of interest. Further

modifications for the spanning tree method are thus required to achieve a realistic network structure in the human brain.

3.3-4 Modified spanning tree method

The failure of the previous three methods to achieve the right distribution at the shortest lengths makes the direction of modification for the new STM very clear. The modified spanning tree method is still based on the STM but also contains other necessary modifications. The first modification is to increase the proportion of the arcs with lengths under 20μm, some very short arcs being created by introducing extra nodes arbitrarily. The number of the arcs is well regulated by the number of the new nodes. It is found that these arbitrarily located new nodes can only introduce a limited portion of the arcs with desired lengths (<20 μm). To patch this problem, new nodes are now intentionally located close to some existing nodes in the region where the node density is relatively lower.

The simulation domain was divided into 125 subzones of equal size and low node density regions where the new nodes were to be planted were tagged. In these low node density subzones, a certain number of nodes were chosen as targets depending on the degree of the node density deficiency and 4 extra nodes were introduced to the subzone, all at a distance less than 20μm from each target. The particular numbers given above were found to be the optimal combination to give the desired sharp peak found in the experimental data. Since the "shorter selection" is the basic strategy of the spanning tree method, many connections with lengths shorter than 20μm are built due to the introduction of extra nodes.

At this stage, the same arc creation algorithm is used as for the STM and a two tree combination web is formed. Then to refine the length distribution curve of the simulated network, some filters are introduced. As shown in the last section, incorporating a length

filter is one possible way to regulate the length distribution, but it must be carefully tuned to avoid unexpected changes outside the region of interest.

Adjustment of the length distribution curve can be carried out in the following ways. First, the lengths of the multi-arc vessels can be broken up by attaching the new branches to the internal nodes, leading to an increase in the population at small lengths and, at the same time, a decrease in those at large lengths. Second, the population can also be regulated in the opposite way by cancelling the branching vessels. As a result, mutual compensation of the population between the long and short lengths can be used to modify the shape of the length distribution curve. Unfortunately, there is no explicit way to express the quantitative effect of the population exchange between long and short length modes. Therefore, a number of tests must be performed to finalise the corresponding parameters used for length filters. Consequently, three vessel length filters are incorporated in the current method to create the connections within specific length ranges, adjusting the shape at different portions of the distribution curve in order to match the experimentally based statistics.

The first length filter is aimed at increasing the population in the length range 70-150μm by creating extra connections with arc lengths within the given range. The operation probability as introduced in the previous section was carefully selected to decay linearly from 10% to 0% within the range 70-150μm, which reflects the uneven demand to add arcs at different length modes. The second procedure is introduced here to reduce the over-populated vessels in the ranges of 30-50μm and 50-70μm, using constant operation probability of values 22% and 60% respectively. At the final stage, the third length filter targeting the vessels with lengths range 30-80μm, with chance parameter 100%, fully breaks down the long connected vessels having more than 2 intermediate nodes into shorter arcs, to increase the proportion of vessels with lengths shorter than 30μm. The procedures involved are fully listed in Figure 3.9.

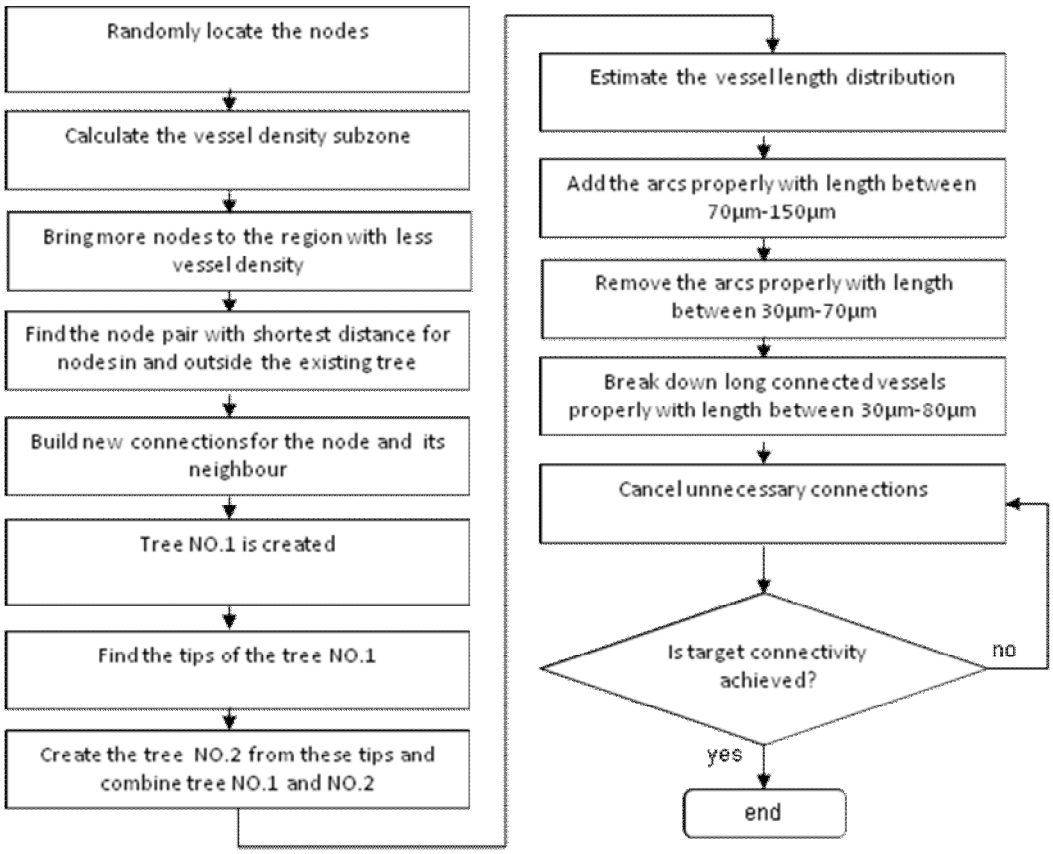


Figure 3.9 Flow chart for the modified spanning tree method

The distribution created by the modified spanning tree method is by far the best match to the experimental results, as shown in Figure 3.10. The introduction of extra nodes increases the proportion at the shortest lengths, and the regulator must be brought in at this step to keep the distribution correct.

A statistical comparison between the four methods presented above and the experimental data is given in Table 3.1. The modified spanning tree method gives the optimal length distribution, the L2 norm calculated from sample distributions and the target curve at each

mode having a value of 5.21%. All statistics lie within an acceptable range, apart from the skewness and kurtosis. These two values are different from these given by Cassot et al. (Cassot and others 2006) and the possible causes for this are addressed later.

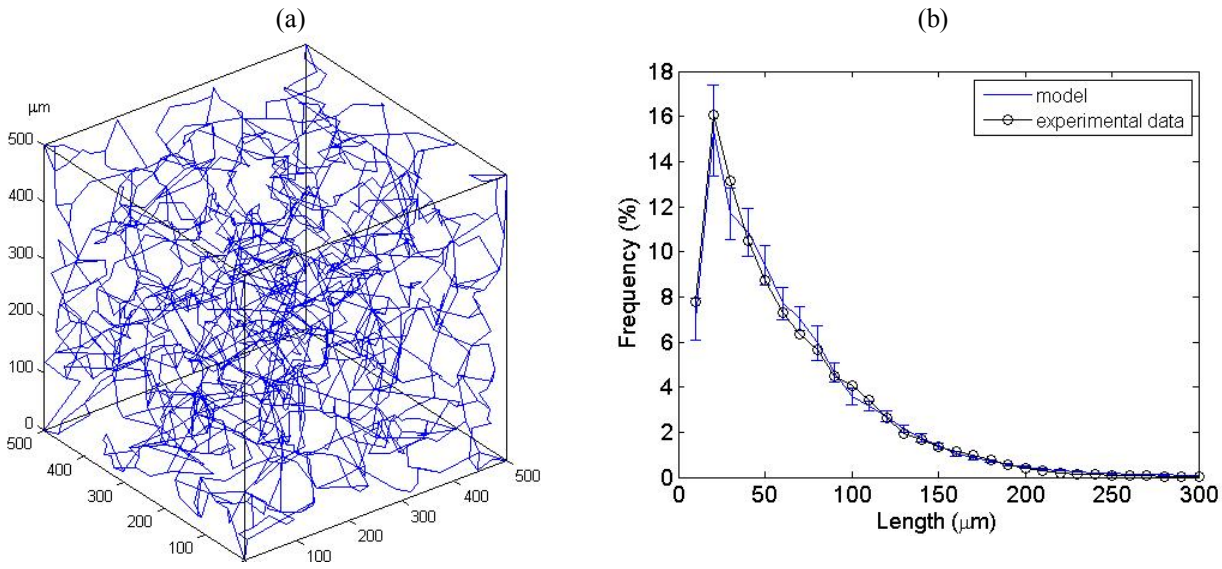


Figure 3.10 (a) Typical network created by the modified spanning tree method; (b) Length distribution histogram compared with the experimental data converted from (Cassot and others 2006)

It should be noted that the values of the parameters in the length filters are set before the simulation. Therefore, several tests, 100 networks for each, were performed to find the optimal parameters by choosing the minimum root mean square (RMS) errors in the length histogram between simulated and reproduced experimental data. The RMS error of one simulated network is obtained through calculating the L2 norm of the percentage difference from experimental data over all length intervals. The statistics suggest that the modified spanning tree method regulated by the specific settings is the best match in both the statistics as well as the length distribution curve to the experimental based data, and thus provides a very good starting point for future work.

Table 3.1 Comparison of the statistics of the simulated networks and the statistics from experimental studies

	Experimental data			Simulated data			
Name	M1*	M2*	**	SAM	GDM	STM	MSTM
RMS error				17.25	14.67	12.92	5.21
Connectivity	3.11	3.16		3.16	3.14	3.28	3.27
Vessel density	8817	7219	10129	8136	7424	8098	8584
Vessel length statistics							
Mean	57.37	63.26	52.95	49.14	59.57	65.58	58.69
Standard deviation	50.98	53.73	49.75	18.33	29.41	42.49	48.96
Skewness	2.68	2.2	1.97	0.32	1.18	1.96	1.62
Kurtosis	26.71	15.19	10.5	4.17	5.86	8.64	6.41

*(Cassot and others 2006); **(Lauwers and others 2008)

3.4 Discussion

The heterogeneity of the branching point distribution and the vessel geometry in the microvasculature is widely observed in a variety of different tissues. Even in the same type of tissue, it is hard to find a very similar microvascular architecture from one region to another. To represent this structural heterogeneity, in our model, many nodes are randomly located in the space, which mimics the diversity of connection patterns for junctions in real networks. Meanwhile, this assumption provides point to point distance distributions for nodes which cover a wide spectrum, facilitating the operation of a length filter and smoothing the vessel length distribution curve.

In reality, since some vessels must penetrate the system boundaries, the region of interest considered here can only include a limited and thus incomplete segment of the vessel network. In order to reflect this feature at the boundaries, some nodes are also randomly put on the

surface, building connections at boundary surfaces which aim to compensate for the otherwise underestimated vessel/tissue oxygen exchange due to the cutting of boundary vessels and the contributions of outside vessels.

The shortest arc method proposed here is a straightforward implementation of the need for a large proportion of short vessels. However, it fails to account for the other two ends of the length spectrum. The Gamma distribution method was then proposed to capture the values of mean and standard deviation given by the experimental data, but, similarly, the distribution is still far away from the target. The vessel distribution curves obtained from both of these methods can only mimic a small portion of the distribution curve, leaving a very weak tail and a left shifted peak in the distribution plot.

The spanning tree method developed here appears to be capable of capturing the long tail observed in the target vessel length histogram. The short arc picking strategy preserves the merit of the first method; meanwhile the spanning tree strategy creates longer vessels composed of one to one connected arcs. The combination of both these strategies fulfills the requirement of the long vessel population and also mimics the bending feature found in the real vessel configuration. To move the blunt peak of the curve to the left and to make it sharper, two measures were adopted here. One is to directly remove the connections of simple arcs in the over-populated length range. On the other hand, long connected vessels have been broken down into several shorter arcs in order to add a shorter arc proportion, compensating for the low population at shorter lengths by reducing the proportion of vessels at longer lengths. In the end, the peak could only be shifted to the left a little, requiring extra procedures to increase the proportion of very short arcs.

Among all methods proposed here, the shortest arc method can generate the highest population of short vessels, but still is not able to match the actual proportion. Thus, extra

nodes are planted closely to some nodes, making more very short arcs to increase the population of vessel length under 20μm. This is a necessary step to move the peak to the left and to make it narrower.

The modified spanning tree method, inheriting the advantage of the spanning tree method, is thus developed here along with certain tuning parameters, which try to alter the distribution populations in given frequency ranges by incorporating length filters to regulate two opposite operations: generation of long connected vessel and breakage of long connected vessels into branching arcs. This method thus does produce more realistic networks that give the smallest RMS error (5.21%) of all the other methods, and the statistics, except the skewness and kurtosis, are in good agreement with the experimental values.

As shown in Table 3.1, the skewness and kurtosis of the length distribution are larger than the values obtained in experimental studies. Such discrepancies may due to the conversion of the length distribution histogram to discretised form as the standard for comparison with network generation methods. In particular, there is a very small peak at very large lengths (450-500 μm) in the reference histogram of Cassot et al, which reflects the population of the large vessels. Despite the fact that it only takes up 1% of the total population, it would substantially increase the higher order moments, such as skewness and kurtosis. In the present capillary based models, these large vessels are not included in our algorithm, and hence our estimation of these two values are smaller.

Besides the length distribution statistics given by Cassot et al. (Cassot and others 2006) the distribution of vessel diameter is also an essential quantitative feature to represent the real network. The diameter distribution in the experimental studies is so similar to the normal distribution that the vessel diameter for each vessel is determined by one random number given by a normal distribution generator. This can be easily done by assigning a scaled

random number from the random number generator for normal distribution to the value of the diameter for each vessel. Unlike the case in Gamma distribution method, the random number generator can directly impose the diameter to the network, giving an accurate vessel diameter population as expected.

It should of course be noted that a novel algorithm for generating networks based on only one set of experimental data is proposed here. It is very likely that other regions in the human brain will have different statistics as will other tissues, which raises the question of how to get a more general model to describe the real cerebral network. The morphometric data obtained from experimental studies in one organ may not be suitable for other organs, or even for different locations in the same organ. Since our network generation algorithm is statistically based, however, it does open up the possibility of creating different type of networks to simulate regionally varying networks.

As more information about the topology and geometry of other networks in other regions of the human brain become available, a more convincing and general statistical database for the cerebral network is likely to emerges in the future. Experimental statistics such as vessel frequency in diameter and length, nodal distribution patterns and average connectivity, could simply be imported into the new algorithm to build artificial networks with specific vessel geometric distribution. In this work, four methods for four different base line curves along with three length filters for minor tunings greatly facilitate the creation of a variety of networks to fit different experimental statistics.

The algorithm proposed here is not an attempt to model the actual processes of the development or generation of the real cerebral microvasculature. Instead, it is purely an attempt to provide a means of generating artificial networks that share the same characteristics of real networks. It then becomes possible to study blood flow patterns for a

group of networks, based on available experimental data for regions of the human brain or any other organ. The question of what determines the blood vessel structure remains unresolved and the answer could be crucial to offer more detailed guidelines for creating physiologically relevant artificial networks. Both genetic and non-genetic factors work together on vascular cells, surrounding extracellular matrix and neural cells themselves to dynamically shape the configuration of the vasculature.

It is widely accepted that these rules can be categorized into many factors including genetic pre-specification and the haemodynamic response. In studies of vascular development (vasculogenesis), both factors have been found to play an important role at different stages in embryogenesis (Jones, le Noble, Eichmann 2006). In the early stage, the genetic specification is involved more in vessel identity and positioning in the vascular system while blood flow plays a crucial role in vessel identity and remodelling during the later stage. The flow driven mechanical forces are biologically active within the embryo, affecting gene expression, but the details of mutual interactions between haemodynamics and gene expression on network generation in embryogenesis remain unknown and no corresponding mathematical model is available for normal brain tissue.

After the vasculogenesis, the cerebral vasculature continuously undergoes changes in vessel structure and some physiological processes, termed angiogenesis or remodelling are involved in this later development stage. Vessel generation from pre-existing vessels is the general definition for angiogenesis, which is a physiological processes of endothelium cell migration, sprouting, proliferation and fusion (Risau 1997).

A number of mathematical models for angiogenesis (Mantzaris, Webb, Othmer 2004) (Chaplain, McDougall, Anderson 2006) have been developed but mostly for tumour induced development, which describes the endothelium cell migration and capillary formulations by a

set of transient diffusion equations for endothelium cell density, tumour mediated signals and the extracellular matrix. These models have been extended by including interactions between vascular structure (network topology and geometry) and haemodynamics (McDougall and others 2002) (Alarcon, Byrne, Maini 2003) where the haemodynamic stimulus vascular remodelling has been formulated by Pries and co-workers through interaction between vessel diameter change and a number of feedback mechanisms (Pries, Reglin, Secomb 2003) (Pries and Secomb 2005a) (Pries and Secomb 2008).

The brain microvasculature is the outcome of many physiological processes related to vessel generation such as embryogenesis, angiogenesis, remodelling, and other developmental process. The vasculature experiences different physiological process, from cellular, sub-cellular, to tissue level, for a long period of time. To formulate the remodelling and angiogenesis for the cerebral vasculature based on mathematical models above is possible, however it must involve multiscale modelling in space (vascular and cellular level) and time (vascular transport, cellular dynamics) and the modelling analogy between the brain tumor and normal tissue are also required. Even if the angiogenesis and remodelling can be well described, embryogenesis has yet to be done quantitatively.

Compared to this bottom up approach, the present statistically based algorithmcan provide a shortcut to generate an artificial network since it does not involve any multiscale modelling. The purpose of this work is not to resolve the detailed dynamics of each vascular and cellular elements in the network but merely to obtain a network whose statistical features are close to experimental observations.

From an engineering perspective, as design criteria, the concept of "minimum cost" proposed by Murray (Murray 1926) has been widely adopted and extended to help to explain the network structure (Painter, Eden, Bengtsson 2006) (Gafiychuk and Lubashevsky 2001). In

The first theorm by Murray, is based on the idea of finding a weighted minimum between the work needed to overcome the wall viscous stress and the building and maintenance costs of the vessel/blood flow system. The results suggest that a simple equation relating the cubic sum of the radii for all the downstream vessels and cubic of the radius for the parent vessel may quantify the geometric feature of one specific branching in the network. Murray's approach provides an insight into vascular design principles for large vessels, but further and more comprehensive experimental studies at the microcirculation level are still required to establish the processes.

Another way, being more practical, is to create a network based on the statistics inductively reasoned from real network samples (Dawant, Levin, Popel 1986) (Levin, Dawant, Popel 1986). Random perturbations in the vessel diameters and lengths are introduced to create artificial networks that faithfully mimic the vascular nature in terms of the morphometric diversity. However, the modelling level is restricted to the large vessels such as arteries or venous. Likewise, our algorithm is also based on a set of experimental statistics but it is able to mimic the real microvasculature. On the other hand, the spanning tree method, which can create a network with the minimum vessel total lengths when the nodal locations are fixed, is the frame work of the current algorithm. This minimum requirement, despite being compromised somewhat by the introduction of length filters, has similarilties to the design strategy stemming on "minimum material cost" and "minimum flow resistance" since the volume and resistance are all in proportion to the length of the vessel.

In general, the current network generation method stems on two design concepts: the minimum system cost and the randomness of the vessel distributions, representing the very complex nature of the microvasculature as a compromise between these two conflicting ideas: stochastic and organised features. It is found that the tuning parameters in the method create a

physiologically relevant network, giving a good match to the statistical data obtained from experiment. The artificial networks, therefore, are reasonable approximations to the real human networks, and thus can be used to analyse statistical features in the microvascular structures and the blood flow transport patterns for a number of networks.

The computation for network generation was executed, using around 1300 nodes, on a computer with Intel Core 2 6420 CPU, on a single core and with 2G bytes of memory. The execution time for generating one network was approximately 5 minutes for the STM and MSTM and less than one minute for the SAM and GAM in Windows XP environment.

3.5 Conclusion

Four methods for artificial network creation have been proposed here to mimic the real cerebral microvasculature. Among these methods, the modified spanning tree method produces artificial networks having characteristics closest to those of the real network in one tiny region of the human brain. Both length filters in this method for regulating arc adding or removing operations along with a planting procedure for new nodes have been shown to be necessary to help the spanning tree method to refine the population in certain length ranges, these three working together to give a very good agreement with the statistics taken from real cerebral networks. This network generation method could easily be extended in the future for creating artificial networks to mimic other tissues if their statistical characteristics become available. This model can give a valuable input to theoretical simulations, opening a window for further investigations into network properties for a range of organs if more microvasculature statistics become available.

Chapter 4. Discretised model for blood and oxygen transport.

4.1 Introduction

In this chapter, blood flow and oxygen transport patterns will be investigated for the artificial microvascular network using the Poiseuille's equation and 1D transport equation respectively. The simulations are used to mimic ischemia, as the most common cause of vascular dementia, by shutting down the blood supply of flow inlets. The influence of different models for blood viscosity and approximations for oxygen saturation are presented and analysed in terms of the flow and tissue concentration behaviours. Time courses for the tissue oxygen levels are also presented to monitor the system response to ischemia. The results are able to provide an alternative for understanding the behaviour of cerebral haemodynamics and their interaction with surrounding tissue in *in vivo* conditions when corresponding experiment is hard to conduct.

4.2 Blood flow in the network

Blood flow in the microvascular bed is very slow (Re = O(0.01)), so the blood stream is primarily driven by viscous forces (Popel and Johnson 2005). It can be further assumed that the capillary wall deformation is negligibly small and that the flow inside the vessel is fully developed. With the assumptions given above, Poiseuille's equation can be used to describe the flow of blood stream through each vessel in the network. This states that the flow rate through a vessel Q varies linearly with pressure drop along the vessel, ΔP :

$$\frac{\Delta P}{Q} = \frac{8\mu_a L}{\pi r^4} = R = \frac{1}{G}, \tag{4-1}$$

where the apparent viscosity is given by μ_a, resulting from the interaction between blood cells and plasma, the vessel length is given by L and the lumen radius by r. These determine

the flow resistance, R, which is the inverse of the flow conductance, G. The microvascular network can be treated as the inter-connections of many different flow resistances, each representing the flow in each vessel (Lipowsky and Zweifach 1974). Due to flow conservation at each node in the network, the net flow at each given node *i* should be zero except for flow source or sink nodes, giving *n* linear equations for a network with totally *n* nodes:

$$\sum_{i}^{n}(P_i - P_j)G_{ij} = S_i \ , \tag{4-2}$$

where G_{ij} is the flow conductance of vessel connecting node *i* to all other nodes *j*, with nodal pressures P_i and P_i respectively. The flow conductance is zero unless the connectivity is equal to unity. Eq.4-2 can be further expressed in matrix form for a network of vessels, with conductance matrix $\mathbf{B}$, node pressure vector $\mathbf{P}$ and source vector $\mathbf{S}$, leading to a linear system, $\mathbf{BP} = \mathbf{S}$:

$$\begin{bmatrix} \sum_n G_{1k} & -G_{12} & \cdots & -G_{1n} \\ -G_{21} & \sum_n G_{2k} & \cdots & \vdots \\ \vdots & \vdots & \ddots & \vdots \\ -G_{n1} & \cdots & \cdots & \sum_n G_{nn} \end{bmatrix} \begin{bmatrix} P_1 \\ \vdots \\ \vdots \\ P_n \end{bmatrix} = \begin{bmatrix} S_1 \\ \vdots \\ \vdots \\ S_n \end{bmatrix}. \tag{4-3}$$

The matrix $\mathbf{B}$ is symmetric and positive definite, and this matrix inversion can be solved by many linear solvers. The conjugate gradient (CG) method (Vandervorst 1992) is adopted here to solve the *n*-unknown linear system due to its efficiency.

In Eq.4-1, the flow conductance can be determined if the vessel dimensions and the effective blood viscosity are known. The dimensions of each vessel are determined directly by the network, but the apparent viscosity, in practice, is not known a priori for each vessel. As the vessel diameter approaches that of the blood cells, the particulate effect of the blood cells

must be taken into account to estimate the blood rheology. At this length scale, the viscosity is highly coupled with the local haemodynamics due to the inhomogeneous migration patterns of blood cells in the microvasculature.

The flow conductance can be estimated by dividing the pressure drop by the flow rate, both measured experimentally, and calculation of the apparent viscosity in each vessel is simply the product of the conductance and a factor $\pi r^4 / 8L$ (Pries and others 1990). According to experiments conducted by Pries and co-workers (Pries and others 1990) (Pries and others 1994), the apparent viscosity is found to be dependent on both the vessel diameter and the discharge haematocrit, H_D, according to the following empirical formulations:

$$\frac{\mu_a}{\mu_{plasma}} = \left[1 + (\mu_{0.45} - 1)\frac{(1-H_D)^C - 1}{(1-0.45)^C - 1}\left(\frac{D}{D-1.1}\right)^2\right]\left(\frac{D}{D-1.1}\right)^2, \tag{4-4}$$

$$\mu_{0.45} = 220\exp(-1.3D) + 3.2 - 2.44\exp(-0.06D^{0.645}), \tag{4-5}$$

$$C = (0.8 + e^{-0.075D})(-1 + \frac{1}{1+10^{-11}D^{12}}) + \frac{1}{1+10^{-11}D^{12}}. \tag{4-6}$$

The strong interconnectivity of the microvascular bed, however, makes estimation of the haematocrit in each vessel very difficult, especially at flow bifurcations. The blood cell distribution pattern (phase separation) at these places has been characterised by an empirical relation derived from rat mesentery experiments (Pries and others 1989) (Pries and Secomb 2005b). The relative volume flow rate of red blood cells in a daughter vessel to that in the parent vessel $FQ_E = (Q_d / Q_p)_{RBC}$, and the volume fraction of total blood flow, $FQ_B = (Q_d / Q_p)_{blood}$, can be related by the following equations, which is demonstrated in Figure 4.1.

$$\ln\left[\frac{FQ_E}{(1\text{-}FQ_E)}\right] = A + B\ln\left[\frac{(FQ_B - X_0)/(1-2X_0)}{1-(FQ_B - X_0)/(1-2X_0)}\right], \tag{4-7}$$

where:

$$A = -13.29\cdot\left[((D_\alpha / D_\beta)^2 - 1))/((D_\alpha / D_\beta)^2 + 1)\right]\cdot(1 - H_D)/D_P, \tag{4-8}$$

$$B = 1 + 6.98\cdot(1 - H_D)/D_P, \tag{4-9}$$

$$X_0 = 0.964\cdot(1 - H_D)/D_P, \tag{4-10}$$

where A, B and X_0 are the parameters obtained from linear fitting of data from the experimental study related to the parent vessel diameter, D_P, the diameter of daughter vessels D_α and D_β, and the discharge haematocrit of the parent vessel, H_D.

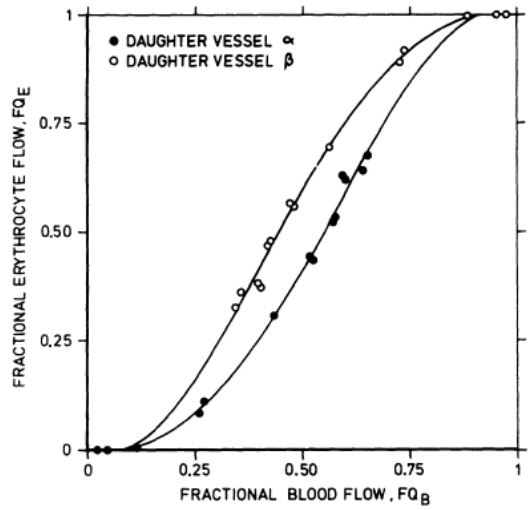


Figure 4.1 Logit fitting curve for phase separation effect as a relationship between the fractional erythrocyte flow and fractional blood flow, taken from (Pries and others 1990)

However, there are not always 3 branches (one parent and two daughter vessels or two parent and one daughter vessels) at each node since the average connectivity is known to be greater than 3. An experimentally based relationship is, however, only available for cell partition at bifurcations and another formulation is required for junctions with more than three branches.

The volume fraction occupied by the blood cells at these locations is assumed here to be in proportion to the velocities of all of the daughter vessels, which is a modified form of the theoretical partition law for blood cells (Wu and others 2008):

$$(H_D)_1 : (H_D)_2 : (H_D)_3 = V_1 : V_2 : V_3 . \tag{4-11}$$

In the simulations presented here, either pressure or flow boundary conditions can be applied to the inlet and outlet nodes. In this chapter, some outlet and inlet junctions, mimicking the venule-capillary and arteriole-capillary junctions, are imposed with given pressures. Since the inlet pressures are then assumed known, the linear equations (Eq.4-2) need to be rearranged. For example, if nodes 1 and 2 are the terminal points, the corresponding pressures P_1 and P_2 are replaced by the flow rate at these two points S_1 and S_2 in the modified pressure vector. Hence:

$$\mathbf{B}_0 \mathbf{P}_0 = \mathbf{S}_0 , \tag{4-12}$$

where:

$$\mathbf{S}_0 = \begin{bmatrix} \sum_n G_{1,k} P_1 + G_{1,2} P_2 \\ G_{2,1} P_1 + \sum_n G_{2,k} P_2 \\ G_{n-1,1} P_1 + G_{n-1,2} P_2 \\ G_{n,1} P_1 + G_{n,2} P_2 \end{bmatrix}, \tag{4-13}$$

$$\mathbf{B}_0 = \begin{bmatrix} -1 & 0 & -G_{1,3} & -G_{1,n} \\ 0 & -1 & -G_{2,3} & : \\ : & 0 & \ddots & : \\ 0 & 0 & .. & \sum_n G_{n,n} \end{bmatrix}. \tag{4-14}$$

In general, the blood pressures at terminal junctions in the microvascular bed lie within a range of approximately 1333-4000Pa (10-30 mmHg) (Guyton and Hall 2006). The pressures

at venule-capillary junction nodes are taken to be 1000Pa and 3000Pa at arteriole-capillary junction nodes in current simulations presented here.

To explore the influence of the rheology model on the blood flow patterns, two kinds of viscosity laws are used in the simulations. One setting assumes that blood viscosity in the microvasculature is affected only by the geometry of the network (μ_a in Eq. 4-1), where discharge haematocrit H_D is taken as 0.5 through Eq.4-4 – Eq.4-6, i.e. blood viscosity is independent of the flow patterns. In the second set of simulations, the influences of both flow and geometry on the viscosity are considered, thus solving all the equations (Eq.4-1 to 4-11).

For the latter model, accounting for flow-geometry dependent viscosity, since the haemodynamics and rheology of the network are highly coupled, the equations of these two parts are solved iteratively until a set precision for nodal pressures is achieved. Initially, the apparent viscosity is set to be equal to the geometric dependent viscosity with constant haematocrit ($H_D = 0.5$) throughout all vessels in the network.

The first part of the computation solves Eq.4-1 to estimate the blood flow rate in each vessel and the second part updates the blood rheology in each vessel according to the flow rate. In this second part, the blood cell partition at branching points can be estimated by the relationship between fractional blood cell flow and fractional blood flow at bifurcation nodes as well as the cell partition law for other branching conditions (Eq.4-8 – Eq.4-11). A list for all nodes in a descending order of pressure is generated to label the parent-daughter vessel hierarchy. The haematocrit values in daughter vessels are updated following the order in the list and finally the apparent viscosity at each vessel is determined according to the viscosity relationship (Eq.4-4 to Eq.4-6). This process continues until a suitable accuracy is achieved ($\left\| (\mathbf{P}^n - \mathbf{P}^{n+1}) / \mathbf{P}^n \right\|_\infty < 10^{-3}$ where $\mathbf{P}^n$ is the node pressure vector at iteration step *n*). The flow

model above is valid only for steady state simulations, which is however, a good approximation since the dynamics of tissue oxygen transport are much slower than those for flow.

4.3 Oxygen transport in the network

Once the map of the perfusion in the microvasculature has been calculated in the above section, the oxygen concentration map can be described by the 1D transport equation. In the first stage, blood is treated as a perfect mixture of blood cells and plasma, which ignores the oxygen dissociation effect of the haemoglobin to oxygen in red blood cells. In the second stage, the oxygen binding effect of the RBC on the oxygen transport will be considered by adopting two different approximations for the saturation curve.

4.3-1 Mixture model

In the microvasculature, due to the small values of Peclet number (the ratio of diffusion to convection for mass transfer) oxygen transport is dominated by flow advection. It takes quite a short time (of order 50 ms) to transport blood from one end to the other of one specific vessel, suggesting that a quasi-steady state assumption can be made for the oxygen transport in the network. If the concentration is averaged over the cross sectional area, the oxygen transport along the vessel can be described by the 1D equation:

$$Q\frac{dC_b}{dx} = -D_w 2\pi\, r(C_{bw} - C_t), \tag{4-15}$$

where Q is the volume flow rate of the vessel, C_b, C_{bw} and C_t are the average blood oxygen concentration, the blood concentration around the vessel wall and the tissue oxygen concentration respectively (mM), r is the vessel radius and D_w is the oxygen permeability

across the vessel wall. The average blood oxygen concentration is related to the wall oxygen concentration through radial oxygen transport, which is very complex due to the RBC-plasma interactions. Here, they are treated as the same for this simple model, similar to the literature (Beard 2001), giving:

$$Q\frac{dC_b}{dx} = -D_w 2\pi\, r(C_b - C_t)\,. \tag{4-16}$$

The LHS of Eq.4-16 is the convection term whilst the RHS represents trans-vascular exchange related to the driving concentration difference. This equation describes the balance between the change of oxygen along the flow direction and the trans-vascular flux through the vessel wall. Since the vessel is generally short compared to the characteristic dimension of the tissue, it is further assumed that the tissue oxygen level, C_t, varies linearly to first order along the direction of the arc axis, from C_{ts} to C_{te}:

$$C_t = \left(C_{ts} + (C_{te} - C_{ts})\frac{x}{L} \right). \tag{4-17}$$

The tissue oxygen level at these locations close to two terminal points of the given vessel is carried out by spatial linear interpolation of the concentration field of the tissue. In addition, the blood oxygen level at the inlet node of the vessel, C_{bs}, needs to be given since Eq.4-16 is first order. Solving Eq.4-16 gives the full solution:

$$C_b = (C_{bs} - C_{ts} + \frac{\Delta C}{\lambda L})e^{-\lambda x} + \frac{\Delta C}{L}x + C_{ts} - \frac{\Delta C}{\lambda L}. \tag{4-18}$$

where $\Delta C = C_{ts} - C_{te}$, and $\lambda = 2\pi\, rD_w / Q$. The solution implies that the oxygen level at any given point is affected by the boundary value, C_b, the tissue oxygen drop outside the tube,

ΔC, and the constant λ which characterises the exponential decay of the blood oxygen level along the vessel.

The analysis in the last part is valid only for one vessel if the boundary condition is given. In the microvascular bed, oxygen is carried by the blood stream and the blood oxygen level is re-adjusted when the blood flow mixes at nodes. The convection mixing process can give an estimation of the blood oxygen at a junction node *i*, as a flow rate weighted combination of the *m* sets of values from all incoming neighbouring vessels *j*:

$$C_{bi} = \sum_{j}^{m} C_{bj} Q_{ij} / \sum_{j}^{m} Q_{ij} \ . \tag{4-19}$$

4.3-2 Oxygen saturation model

Despite the mixture model greatly simplifying the analysis by lumping the plasma with blood cells into one variable in the 1D transport equation, this may not be a suitable approximation for oxygen transport in the real microcirculation system. This section shows how to take into account the haemoglobin induced effect in the blood oxygen transport analysis.

In reality, the blood is not a perfect mixture of blood cells and plasma, but is closer to a two phase system, with suspended blood cells immersed in plasma. The blood oxygen level is thus a weighted sum of the levels in the plasma and RBC, where the oxygen binding with haemoglobin takes up the majority of the fraction of the oxygen in blood. The blood oxygen level can be expressed as follows:

$$C_b = (1 - H_T)C + C_{Hb} H_T S(C) + H_T C\,, \tag{4-20}$$

where C, C_{Hb}, and S are the plasma oxygen concentration, RBC haemoglobin concentration, and the saturation of the haemoglobin respectively. The first term of the RHS in Eq.4-20 represents the oxygen concentration in the plasma and the other terms represent the oxygen content retained by haemoglobin and by the RBC plasma respectively, at approximately the same oxygen level as the blood plasma. The saturation represents the oxygen binding rate of the haemoglobin and it depends mainly on the plasma oxygen level. The curve is found to be of a sigmoidal shape, as shown in Figure 4.2, and its shape varies in response to varying physiological conditions.

To incorporate the dissociation curve into the oxygen transport equation, an approximation is made for the saturation curve based on Hill's equation:

$$S = \frac{P_{O2}^n}{P_{50}^n + P_{O2}^n}\,, \tag{4-21}$$

where n is Hill's constant, and P_{50} is the partial pressure measured in tissue when haemoglobin is 50% saturated. In the simulations here, these values are set to be equal to 3 and 38 mmHg respectively (Secomb and others 2000). The amount of oxygen dissolving in the blood is proportional to the oxygen partial pressure in the blood plasma according to Henry's Law, $C = \alpha P_{O2}$, where α is the oxygen solubility.

(a) (b)

Due to copyright issue, this figure is removed. Please refer to Figure 40-10 in the reference.

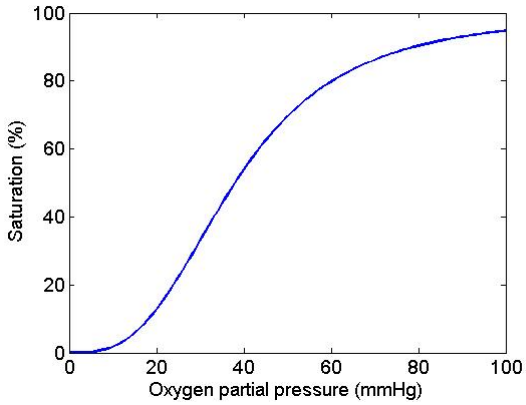


Figure 4.2(a) Typical saturation curve of human haemoglobin, taken from (Guyton and Hall 2006); (b) sigmoidal curve approximation to the haemoglobin saturation according to Eq.4-21.

To consider the total contribution of oxygen content from both the RBC and the plasma, the 1D transport equation must be modified accordingly. By substituting Eq.4-20 into Eq.4-16 and replacing the blood oxygen concentration at the wall, C_{bw}, in the RHS with the plasma oxygen concentration, C, based on equations from the literature (Secomb and others 2000; Secomb and others 2004), the equation for plasma oxygen concentration, C, can be written as:

$$Q\frac{d(C+C_{Hb}HS)}{dx}=-D_w 2\pi\, r(C-C_t)\,. \tag{4-22}$$

The numerical procedure for solving this equation is thus not identical to that used previously due to the nonlinear shape of the saturation function. In this way, Eq.4-22 has no analytical solution, and it can only be solved numerically. Here, this equation is discretised by the finite volume method (Patankar 1980) and solved iteratively (see Appendix A for details). The plasma concentration is initially set as a known, leading to a known saturation. The concentration can then be solved numerically, this procedure repeats until the updated plasma concentration satisfies the convergence criteria $\left\|(C^n-C^{n+1})/C^n\right\|_\infty<10^{-6}$. The network is discretised by the boundaries of the tissue computational unit (voxel), which creates over

10,000 sub-vessel elements scattering in every tissue voxel, for the standard case $\Delta x = 12.5 \mu m$. To solve the vessel oxygen transport equation, the number of grid arrangements in the network has to be carefully chosen. It is found that 10 meshes for each sub-vessel element are sufficient to give satisfactory results with a balance between accuracy and efficiency.

4.4 Tissue oxygen transport

Oxygen transport in brain tissue can be treated as a diffusion problem for a porous medium (Nicholson 2001). This process is thus governed by the following equation:

$$\frac{\partial C_t}{\partial t} = D_t \nabla^2 C_t + G_{ex} - M \,, \tag{4-23}$$

where C_t is the spatially and temporally varying concentration in tissue (mM), D_t is the oxygen diffusivity in tissue (m^2/s), which is taken to be a constant since at this small scale, the tissue oxygen transport is assumed homogenous and isotropic, G_{ex} is the oxygen generation rate (mM/s) due to the tissue /vessel exchange and M is the tissue oxygen consumption associated with brain function (mM/s). It should be noted here that the oxygen diffusivity is always a function of space, reflecting the variations in oxygen diffusion capability influenced by the difference local cellular or extracellular structures. The modeling size here is so small, however, that the spatial variations in cerebral cortex are ignored and the tissue is taken as a homogeneous and isotropic medium.

Oxygen diffuses to the tissue from the network through the vessel wall, so mass transport in the tissue is thus directly linked with the mass transport in the nearby vessels. Since the oxygen distribution along each vessel can be calculated first, the oxygen extracted from one particular vessel is the integral of the flow flux over the area for exchange. In other words, based on mass conservation, the total oxygen input for tissue can easily be obtained by

calculating the blood oxygen concentration drop between the terminal points x_s to x_e for any given vessel segment (the part of the element enclosed by the voxel):

$$g_i = \int_{x_s}^{x_e} D_w 2\pi\, r(C - C_t)dx = -Q\left[(C + C_{Hb}HS)\right]_{x_S}^{x_e} . \tag{4-24}$$

To estimate the oxygen generation rate in the tissue space, G_{ex}, numerically, the sum of all the oxygen generation rates from each vessel segment in the given voxel needs to be calculated:

$$G_{ex} = \sum_{1}^{m} g_i . \tag{4-25}$$

The oxygen metabolism can be described to first order accuracy by a Michaelis-Menten model, which relates the tissue oxygen consumption rate M (mM/s) to the tissue oxygen partial pressure P_{O2} as follows:

$$M = M_0 \frac{P_{O2}}{P_{O2} + P_0} . \tag{4-26}$$

where M_0 is the consumption rate for un-restricted metabolism and P_0 is the reference pressure at which metabolism drops to half of this value (Secomb and others 2000). The same 3D diffusion equation used for both vascular transport models in this chapter is discretised by Finite Volume Method, with concentration gradient term approximated by central difference method. The metabolism and oxygen input terms are treated as source terms first then we then solve the symmetric matrix via Conjugate Gradient Method. After that, updated metabolism and oxygen input terms are obtained accordingly. In each time step, the iterations repeats until the tissue oxygen concentration converges. The discretisation procedures and grid refinement test are presented in Appendix A.

4.5 Results

The first case for the simulation is the combination of the simple models for flow and oxygen transport. In this simplest case, the RBC and plasma are perfectly mixed, so that blood is assumed to be a single phase fluid and viscosity is set as a constant. Then a test for parameters is performed as for the first case but with settings of different wall permeability and maximum consumption rates. Finally, the third case for the simulations treats blood as a mixture of blood and plasma, which allows the effects of RBC partition and the varying apparent viscosity to be modelled. The effects of the plasma saturation on the haemoglobin, with sigmoidal approximations to the curve are also introduced into the network mass transport equations in the third set of simulations.

4.5-1 Simulation setup

There are two flow sources and two flow sinks in the network, as shown in Figure 4.3(a), labelled S1 to S4 and located at points S1 (100,100,100), S2 (400,100,400), S3 (100,400,100), S4 (400,400,400) all units in micrometres. This simple arrangement does not necessarily faithfully replicate the flow input conditions in a cerebral network since the statistical information about the location and the number for the terminal points in the capillary network to arterioles and venules is not available. The intention here is rather to provide acceptable matches to the boundary conditions in the blood flow in real microvasculature. The arteriole-capillary and venule-capillary junctions in the microvasculature are mimicked by terminal points, which are applied with boundary conditions with inlet pressure 3000 Pa and outlet pressure 1000 Pa. This pressure condition at terminal nodes of network is applied for two different flow-transport models in this chapter.

After a steady state is reached, the flow source S2 is suddenly shut off. The flow patterns adjust accordingly and thereby the oxygen transport in the network, leading to a change in the trans-vascular oxygen exchange with the surrounding tissue and a new steady state. A time of 200s is found to be sufficient for the system to reach equilibrium, which is measured by the criteria $\left\|(C^n - C^{n+1})/C^n\right\|_\infty < 10^{-3}$ for the tissue oxygen level.

The purpose of removing one of the flow sources is to simulate the tissue response to a flow blockage induced ischemic condition, which is an underlying cause of vascular dementia. To check the system response at different locations, the oxygen levels at four monitoring points, as shown in Figure 4.3(b), located at M1 (100,125,100), M2 (400,125,400), M3 (100,375,100), and M4 (400,375,400) (all measured in micrometres) respectively, are recorded.

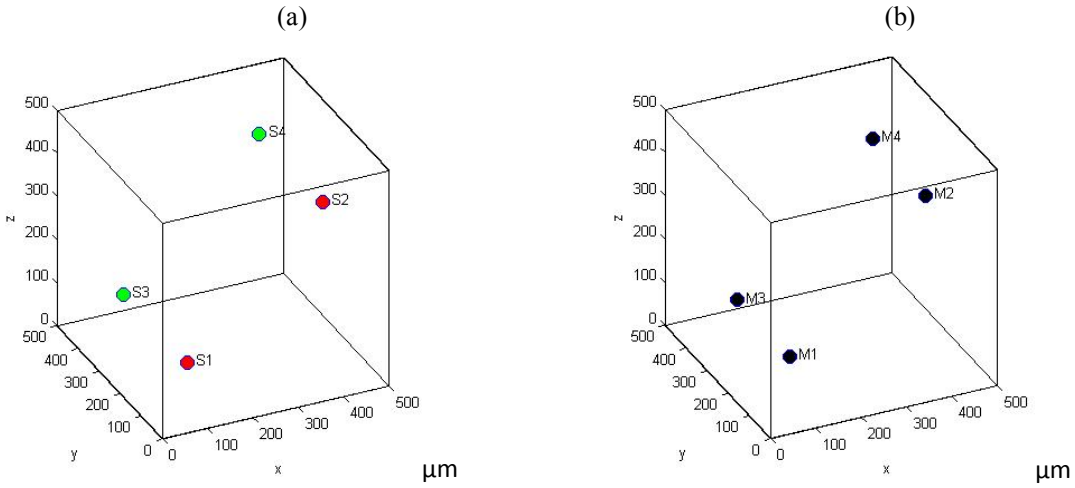


Figure 4.3 Spatial arrangements of: (a) four terminal nodes S1-S4; (b) four monitoring points, M1-M4 (all dimensions in µm).

The 1st order ODE used in the oxygen transport model (Eq.4-16) requires one boundary condition, which is the inlet blood oxygen level for the mixture model. Likewise, the inlet plasma oxygen level is required as a boundary condition for the later models accounting for

the saturation curve. The inlet tube haematocrit is estimated with the discharge haematocrit set at 0.5 from the empirical relationship between the tube haematocrit and discharge haematocrit (Pries and Secomb 2005b). The inlet P_{O2} is assumed to be 100mmHg (0.136mM), being slightly higher than typical PO2 level (90mmHg) in the precapillary arterioles found clinically (Nemani and Manley 2004). This gives an estimate for the inlet blood oxygen level according to Eq.4-20, of about 7.3mM.

For the tissue, the mass transport equation is a second order elliptic differential equation. Therefore two boundary conditions for each dimension are required to solve the partial differential equations. Ideally, the concentration field would be directly imposed on the six boundary surfaces of our computational domain based on experimental observations. However, it is currently infeasible even for leading-edge imaging techniques to obtain real-time measurements of either the oxygen concentration or the oxygen flux all over all surfaces of a volume of living brain simultaneously.

One possible setting for the boundary condition is thus to set isolated surfaces, which may not be realistic, but which would simplify the system considerably. In this case, no concentration flux would be allowed to pass through any of the boundaries of the computational domain. Under the no flux condition (Neumann type), the spatial distribution of consumption function in tissues can be determined directly since the oxygen consumption and flow carrying input must be exactly balanced.

On the other hand, the oxygen level at the boundary can also be fixed as a constant, this being known as Dirichlet boundary conditions. To focus on how oxygen exchange takes place at two boundaries and to check how the system responds to the no flux conditions at the other four surfaces at the same time, a mixed approach is used here with Neumann boundary condition at the boundaries in the *y* and *z* dimensions, and Dirichlet boundary conditions in

the *x* dimension. All of the parameters used in the models of this chapter are listed as below in Table 4.1. The summary of the boundary condition is outlined in Table 4-2

Table 4.1 Model parameters

Parameter	Symbol	Value	Reference
Tissue diffusion coefficient of oxygen	D_t	$1.0\times10^{-9}m^2/s$	(Hsu and Secomb 1989)
Wall permeability of oxygen	D_w	$5.0\times10^{-5}m/s$	(Secomb and others 2000)
Baseline tissue consumption rate of oxygen	M_0	$0.004mM/s\text{-}m^3$	(Kudomi and others 2009)
Dynamic viscosity of blood	μ_b	$3.0\times10^{-3}m\text{-}kg/s$	(Guyton and Hall 2006)
Dynamic viscosity of blood plasma	μ_p	$1.8\times10^{-3}m\text{-}kg/s$	(Guyton and Hall 2006)
Concentration of the oxygen binding site in haemoglobin	C_{Hb}	0.0204M	(Beard, Schenkman, Feigl 2003)
Hill's constant	n	3	(Secomb and others 2004)
Oxygen partial pressure at 50% saturation	P_{50}	38mmHg	(Secomb and others 2004)
Baseline oxygen partial pressure	P_0	1mmHg	(Secomb and others 2000)
Oxygen solubility	α	0.00136mM/mmHg	(Hsu and Secomb 1989)

Table 4-2 The boundary condition for the 3D mass transport equation

Direction	Boundary condition
x	$C(x,y,z) = C(L,y,z) = C_{tb}$
y	$\frac{\partial C(x,0,z)}{\partial y} = \frac{\partial C(x,L,z)}{\partial y} = 0$
z	$\frac{\partial C(x,y,0)}{\partial z} = \frac{\partial C(x,y,L)}{\partial z} = 0$

4.5-2 Constant viscosity-single phase model

As shown in Figure 4.4 (a), blood flows through every vessel in the network, forming a very complex pattern. The flow starts from the inlets, marked by red, further down to daughter vessels, through complex connections made by many tortuous 3D web like pathways in the core region. After this region, blood flow gradually converges through different collecting capillaries and exits through two flow outlets, marked in green.

In Figure 4.4(a), there seem to be two flow territories sustained by two flow source-sink pairs S1-S3 and S2-S4. When one of the flow inputs is disabled, as seen in Figure 4.4(b), the flow rate in the source removal region greatly drops, some vessels, especially around the source removal region, even reducing to 1% of their original flow rate. The even flow distribution, maintained by the two source sink pairs, is destroyed now, creating a flow-depleted zone around node S_2. On the contrary, some vessels around the upstream region receive more flow, as shown by the fact that the inlet S1 flow rate increases from 2.0×10^{-13} m^3/s to 2.7×10^{-13} m^3/s between two flow states.

(a) (b)

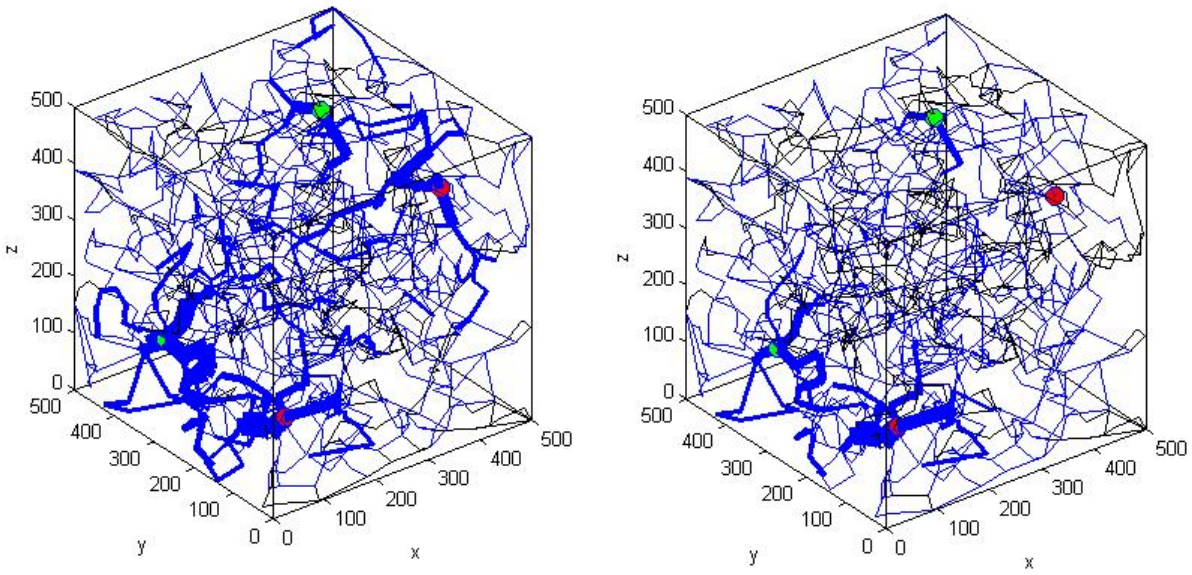


Figure 4.4 Typical flow patterns for the constant viscosity-single phase model: (a) before S2 removal; (b) after S2 removal. The thickness of each line represents the non-dimensional flow rate normalised by the maximum flow rate, lines in black representing the vessels with flow rate less than 1% of the maximum (all dimensions in μm).

At 200 seconds, the distribution of blood oxygen concentration, as seen in Figure 4.5, is found to be consistent with the flow patterns shown above. The oxygen level is higher in the vessels in the upstream region, and gradually decays from the upstream region to the downstream region. From the source region to the centre region, the oxygen level drops about 80% of its input value, suggesting that a great amount of oxygen is extracted by the tissue near the source region. For vessels in the regions distant to the inlets, the oxygen level is even lower than 0.07mM, marked in black, presenting an oxygen decaying pattern in the network under this flow condition.

An unbalanced pattern of oxygen distribution now emerges when one of the sources becomes disabled after 200 seconds. Without a direct supply, vessels around S2 can only receive limited oxygen since the oxygen is delivered gradually through many flow paths before S2.

Compared to the first steady state, more vessels, especially in the regions distant to the only flow source, are not supplied with sufficient oxygen at 400s.

It should be noted that not all vessels exhibit decreases in oxygen level after source removal. For instance, when examining the middle bottom region of Figure 4.5(b), more oxygen is found to pass through vessels around S1. There is no other flow source counterbalancing the influence made by S1, so more blood enters the vessels around S1. Mathematically, the increasing flow input for these vessels creates a smaller decay constant in Eq.4-18 ($\lambda \propto 1/Q$), restricting the concentration drop along the vessel, and thus resulting in a higher concentration in the inlet region of the network.

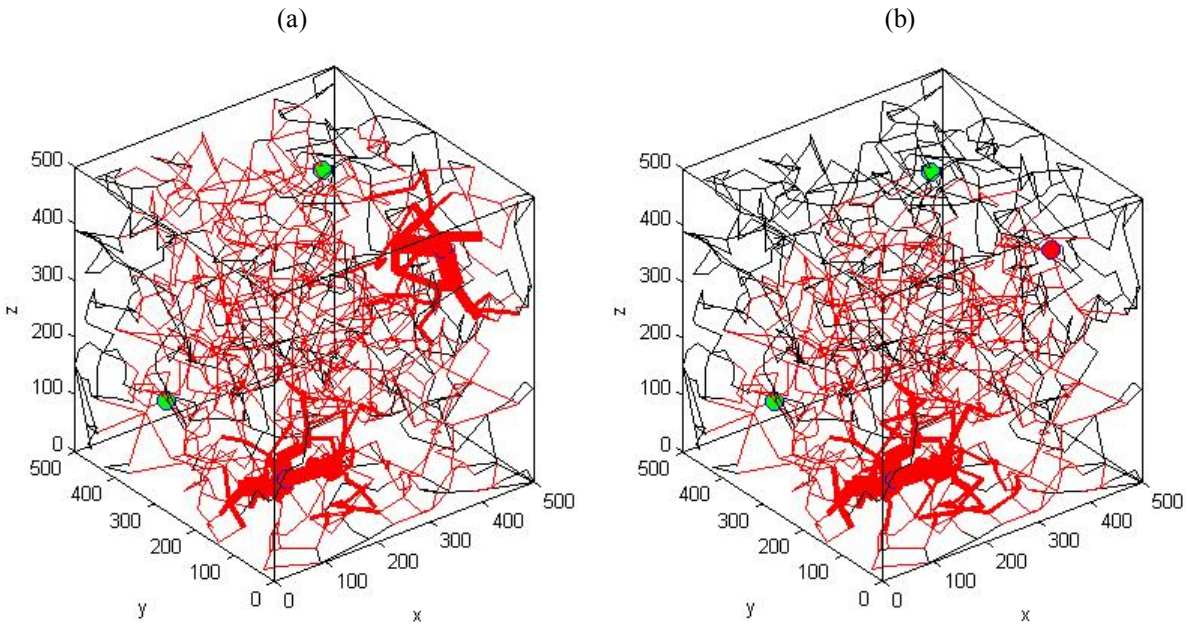


Figure 4.5 Typical distribution of blood oxygen level for the constant viscosity-single phase model: (a) at 200s; (b) at 400s (all dimensions in μm). The thickness of each line represents the non-dimensional flow rate normalised by the maximum flow rate, lines in black representing the vessels with flow rate less than 1% of the maximum

The resulting oxygen transport patterns in the tissue are shown in Figure 4.6. At 200s, there are two contour lobes of the high oxygen levels with similar strength, located nearly

symmetrically and stretching mainly along the y-direction in the tissue space. The tissue oxygen diffusion is fairly symmetric despite the irregular vessel distribution. The tissue oxygen level near the two flow sources has the highest value, about 4.3mM, decaying with distance. The tissue near source S1 develops a slightly larger contour lobe than does S2, which is seen in Figure 4.6(a) that, at the middle section, the S1 lobe has a highest oxygen level of 1.5mM compared to 1.3mM for the S2 lobe.

The net oxygen flux entering the tissue space is simply a product of the flow rate and oxygen drops in each vessel segment. Since the tissue around the flow inputs can receive the full flow supply of the first order bifurcations, which equals to flow inputs, the net oxygen efflux across the vessel walls around S1 or S2 is the highest in the tissue space. Such a maximum oxygen input from vessels to tissue, therefore, creates a maximum oxygen concentration at points very close to flow input nodes.

The high level contour lobe sustained by source S2 disappears in the new steady state, as shown in Figure 4.6(b) and Fig4.6(d), once S2 is removed. The remaining flow source S1 is the only supply for the cube of tissue and the resulting lobe has a similar stretching axis, due to the y-directional flow convection. The maximum tissue oxygen concentration in the tissue space is 3.5mM, even higher than the maximum in the old steady state, because of the increase in flow input at S1. On the other hand, remote sites in the downstream region can have oxygen levels lower than 0.1mM. This large variation in tissue oxygen levels over the cube, suggests that there may be a limiting distance for oxygen transport in tissue, even at such a small scale.

(a) (b)

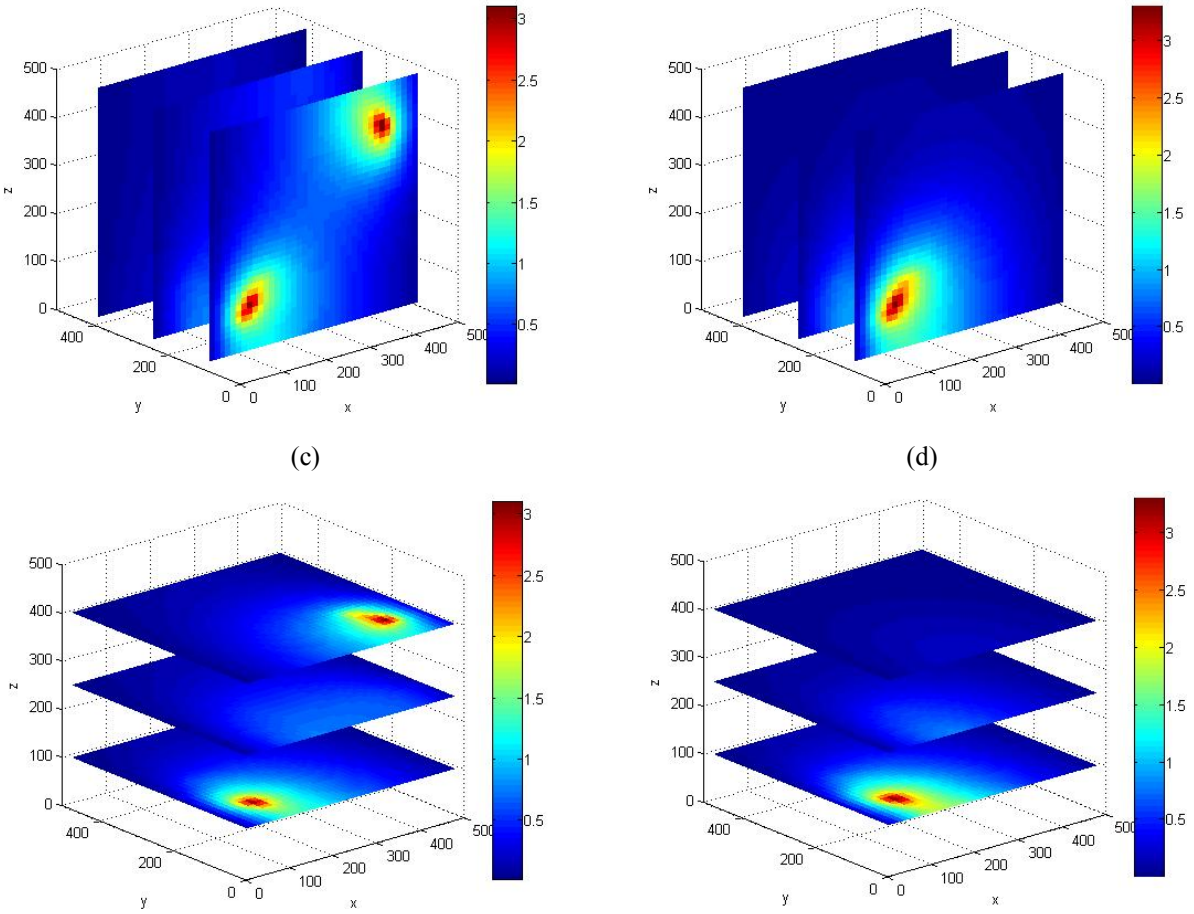


Figure 4.6 Typical distribution of tissue oxygen concentration for the constant viscosity-single phase model presented in three slices in the y direction: (a) at 200s; (b) at 400s; and presented in three slices in *z* direction: (c) at 200s; (d) at 400s (all dimensions in μm).

Figure 4.7 shows how the tissue oxygen level at different locations responds to the source removal. The oxygen concentration at M1 reaches its steady state concentration, 1.75mM, in 50s, from its initial value of 0.0136mM. After S2 is disabled, the oxygen level in some places undergoes a further increase, reaching a value of 2.1mM. Similar temporal behaviour can be found in the time course for S3 since M1 and M3 are in the same flow territory covered by the S1-S3 source-sink pair. The oxygen level at M3 rises up to 0.4mM and has a further increase of 0.1mM.

Before S2 is removed, vessels between S1 and S2 rarely get a large flow due to a rather small pressure difference between them. Without the counterbalance of S2, more flow can pass into these vessels between S1 and S2 after 200s. This drives more oxygen passing the vessels close to S1, leading to more oxygen entering the tissue space across the vessel wall. As a result, tissue near S1 receives more oxygen from surrounding vessels. This is why the S1 flow territory can get more blood and oxygenation after S2 removal.

Likewise, the time courses for M2 and M4 (C_2 and C_4 in the Figure respectively) are quite similar in a qualitative sense. The tissue around M2 undergoes a initial increase of oxygen level, having a steady state oxygen concentration of 2.1mM; it then experiences a dramatic decay of 1.8mM around 200-250s, finally settling down to 0.25mM in the new steady state. The drop in oxygen level at around 200s is directly caused by the shortage of the blood supply due to the removal of S2. The oxygen level at M4 also has a similar decaying transition, from the first steady state concentration 0.3mM to the final value of 0.07mM. These diverse patterns of the tissue dynamic suggest that the spatial variations in tissue oxygen field are apparent even at such a small length scale.

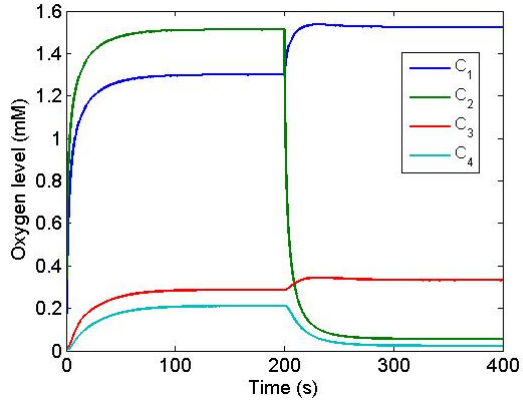


Figure 4.7 Time courses of tissue oxygen concentrations at different monitoring points (M1-M4) for the constant viscosity-single phase model

4.5-3 Sensitivity tests for the constant viscosity-single phase model

In this section, although most of the parameters used here are set based on the values found in literature, where there are value variations for some of the parameters used in this model. It is thus of interest to test what influences these parameters have on transport patterns in the tissues. Here, different values of maximum oxygen consumption and wall permeability are tested and the time courses of the tissue oxygen level are presented.

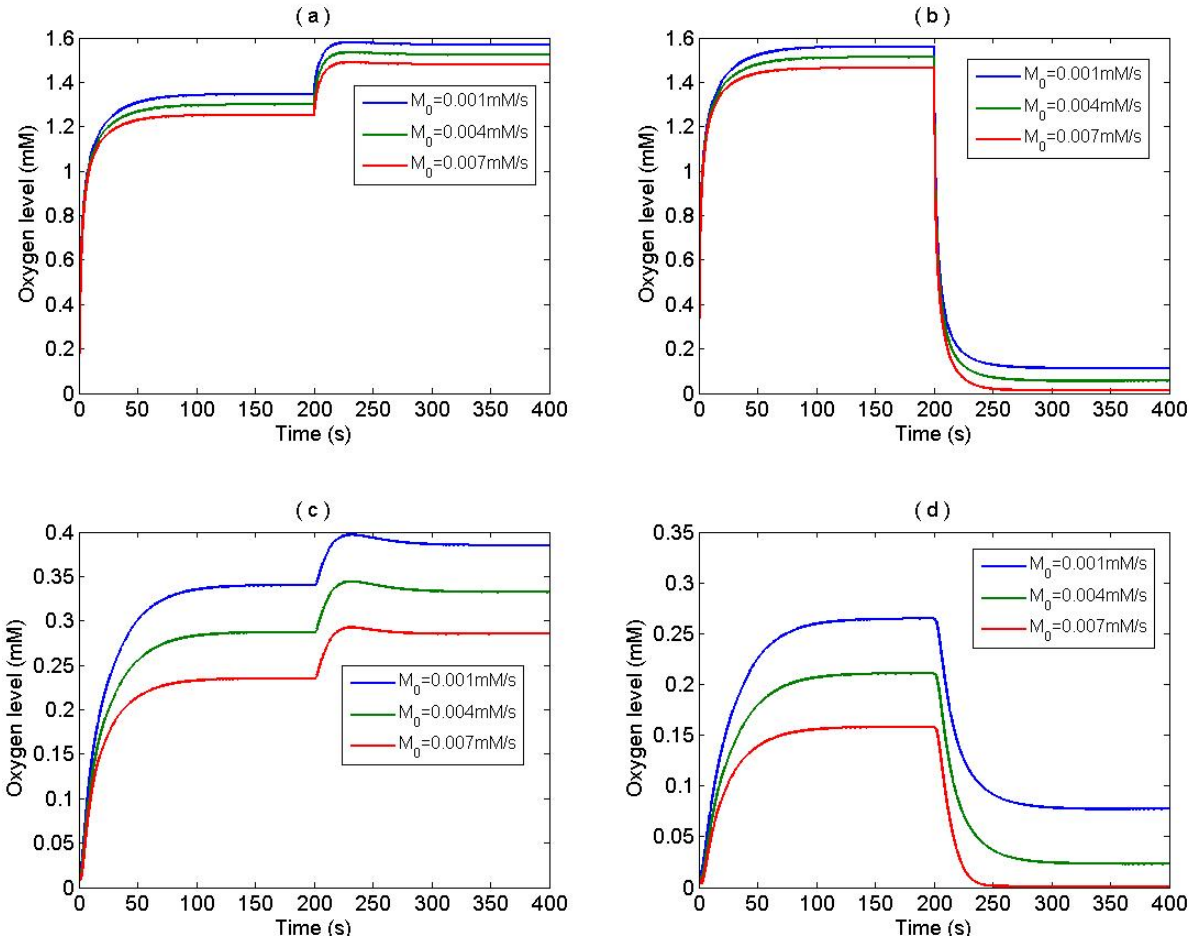


Figure 4.8 Time courses for tissue oxygen level at monitor points (a) M1; (b) M2; (c) M3; (d) M4 with different values of maximum tissue consumptions.

In the transport equation, the oxygen consumption is the term acting like a sink for the concentration field. In other words, this term is one of the factors which brings down the oxygen level in the tissue. The consumption would be counterbalanced by the amount of

oxygen extracted from the vessels or diffused from nearby tissues. As shown in Figure 4.8, the tissue oxygen level at all four monitoring sites becomes lower with an increase in the maximum consumption, and hence the effective consumption, as outlined in Eq.4-26. Although the oxygen consumption is oxygen level dependent, it remains very close to constant (the maximum consumption rate) until the level drops below the critical PO_2 value. At the oxygen levels presented in this case, the nearly constant consumption would lead to a homogenous oxygen level change. Tissue oxygenation decreases uniformly in space with an increase in maximum metabolism rates as the reduction (0.007-0.001mM/s) in M_0 produces a PO_2 level increase of about 0.1mmHg at the four monitoring sites.

The wall permeability is the constant that regulates the oxygen flux from vessel to tissue. An increase in this value means that more blood oxygen is allowed to enter the local tissue space when oxygen level drop across the wall is fixed. The time courses shown in Figure 4.9 are not as regular as in Figure 4.8 since the wall oxygen efflux is not nearly constant like the oxygen consumption but a product of the wall permeability and other terms, such as exchange area and concentration drop across vessel wall. In fact, an increase in the wall permeability can only raise the oxygen tension in some of the upstream regions, as shown in 4.9(a), but not in the downstream regions, such as M3 as shown in Figure 4.9(c). Due to mass conservation of oxygen in blood, with the same oxygen input in the network, the more the upstream wall flux is, the less is the downstream wall flux. This explains the fact that an increase in the wall permeability does not always create a higher oxygen level in tissue, especially in the downstream region.

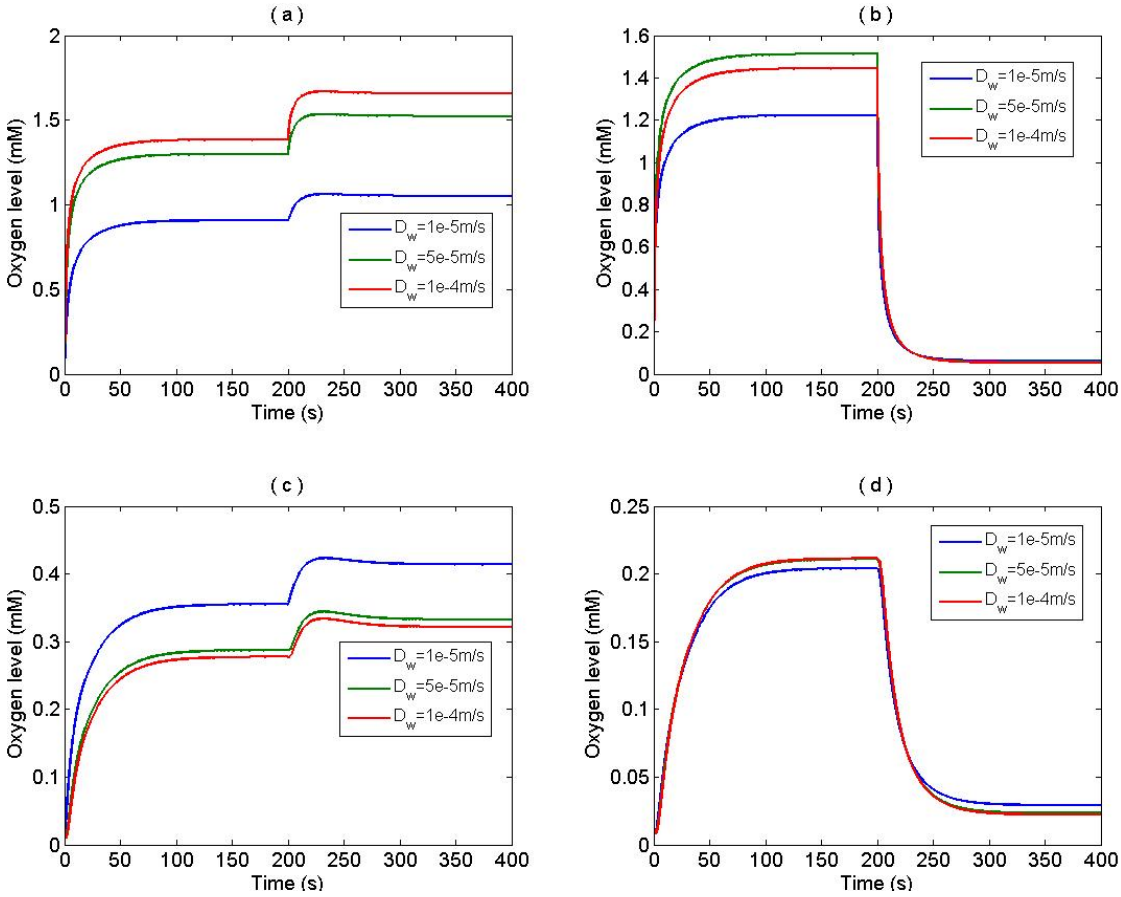


Figure 4.9 Time courses for tissue oxygen at monitoring points (a) M1; (b) M2; (c) M3; (d) M4 with different values of wall permeability.

4.5-4 Variable viscosity- sigmoid approximation saturation model

When the influences of plasma and RBC on oxygen transport are approximated by a two phase model, the system dynamics are very different from those for a single phase model. In particular, the more realistic RBC division at branches and the flow dependent viscosity law are now included in the flow model, whilst the plasma oxygen dependent haemoglobin binding ability is coupled with the transport equation. Except for the choice of models, all other settings, such as the pressure conditions and the inlet-outlet locations are set to be the same as in the previous simulations.

Before S2 removal, source pairs S1-S3 and S2-S4 seem to create flow territories as in the previous model, as shown in Figure 4.4. When S2 is shut down, the vessels in the flow territory covered by S2 can rely on the distant supply from S1 and hence corresponding flow is greatly reduced. Some of the vessels in the S2-S4 flow territory can get more flow but in general, most vessel flow rates reduce after S2 is shut down.

The flow patterns of the two steady states share very similar features with the constant viscosity model, and a direct comparison of flow rates in each vessel in the network shows that in general, the vessel flow rates calculated from the variable viscosity model are, as seen in Figure 4.10, smaller by a factor of about 20% from those that in the constant viscosity model. This pattern of a lower flow rate in the variable viscosity model results from higher estimations of the apparent viscosity in most of the vessels, due to the usage of the more complicated viscosity law. The irregular haematocrit partition at flow bifurcations and the vessel dimension related cell-plasma interactions create large variations in the vessel apparent viscosities but their values in most vessels are larger than the constant set for the first case.

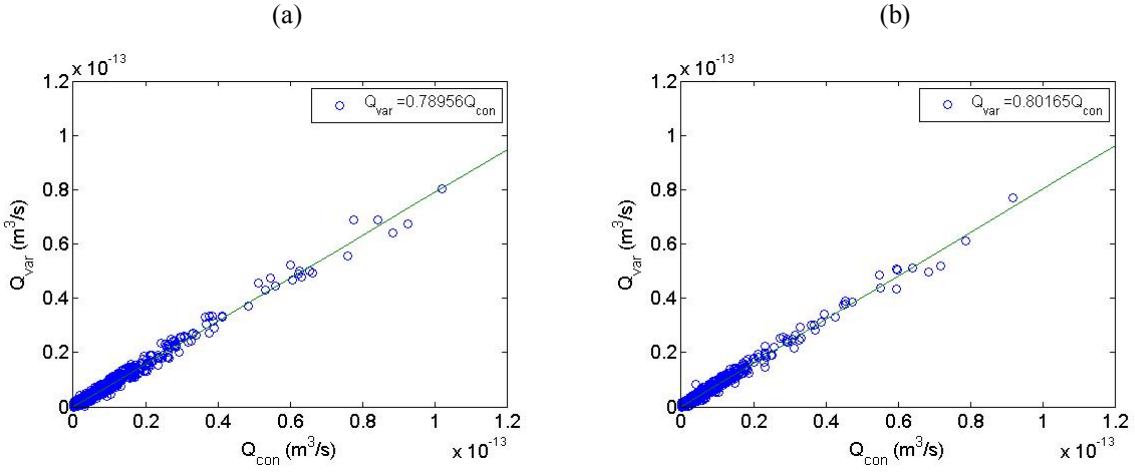


Figure 4.10 Comparison of the vessel flow rates between the flow model with the constant viscosity and with variable viscosity laws: (a) before S2 removal; (b) after S2 removal.

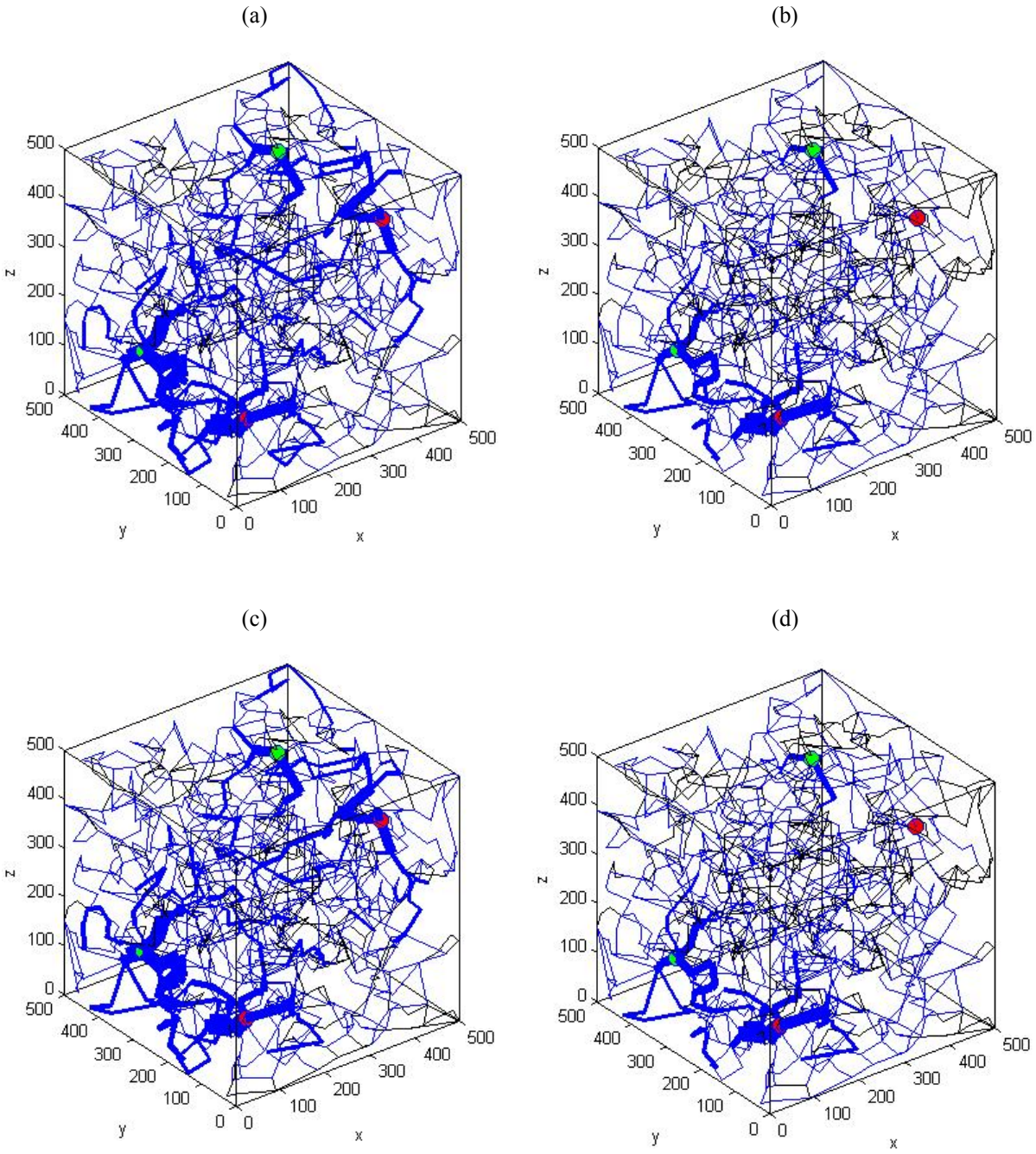


Figure 4.11 Typical flow patterns for the non-constant viscosity-oxygen dissociation model:(a) before S2 removal; (b) after S2 removal. The corresponding results for the constant viscosity-single phase model are presented here for comparison: (c) before S2 removal; (d) after S2 removal (all dimensions in μm). The thickness of each line represents the non-dimensional flow rate normalised by the maximum flow rate, lines in black representing the vessels with flow rate less than 1% of the maximum

For these two flow models, the differences visually between Figure 4.11 (a)-(c) and (b)-(d) are not apparent. As a result, the flow strengths of S1, S2 are $1.64\times10^{-13}m^3/s$ and $1.36\times10^{-13}m^3/s$ respectively for the current model and $2.0\times10^{-13}m^3/s$ and $1.8\times10^{-13}m^3/s$ respectively for the constant viscosity model. Despite the lower flow rate predicted by the current model, the flow predictions, in general, show no significant qualitative differences from the constant viscosity model in terms of non-dimensional flow distribution patterns, as shown in Figure 4.11.

The flow rates predicted by this model for vessels in the network are in general uniformly reduced with a drop of 20% of the values in the constant viscosity case, suggesting that the constant viscosity law may be a good approximation to the variable viscosity model in terms of the fractional flow distribution patterns. On the other hand, the transport models with approximations for oxygen dissociation curve are now coupled with the flow model with the non-constant viscosity law. Despite no significant differences being shown in these two different flow models, the oxygen distributions in the network have very distinct features when compared to the previous one.

As shown in Figure 4.12, the network blood oxygen is in general much higher than in the previous model and the oxygen level decays bluntly along the flow directions, suggesting that less oxygen enters the tissue compared with the single phase model. The reduced oxygen extraction in the present model results from the replacement of C_b by C to approximate the near wall oxygen concentration C_{bw} in Eq.4-22. Some vessels around the boundary between the two flow territories have a relatively low oxygen content since their flow rates are very small, which indicates the oxygen dependence on the flow patterns.

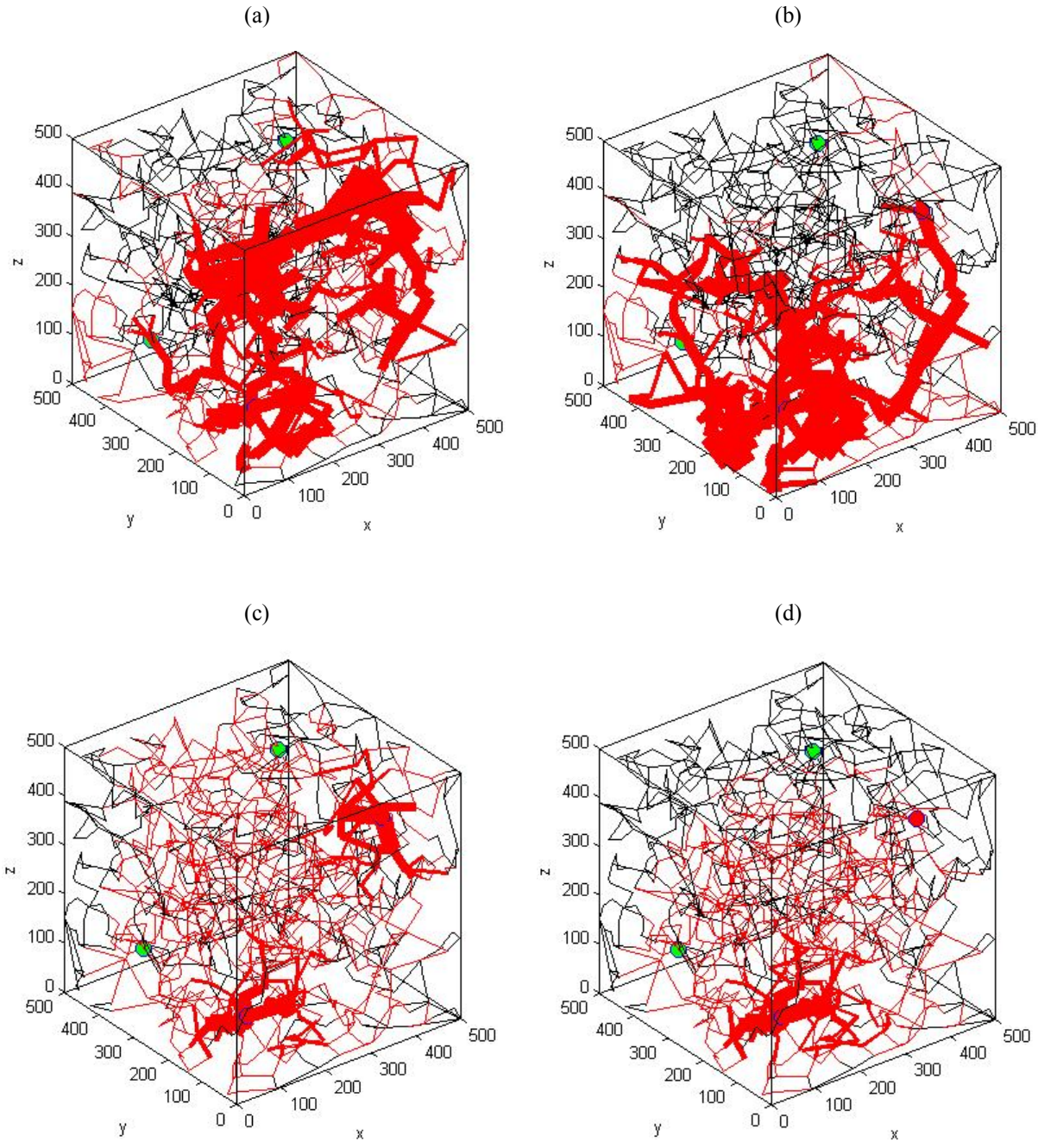


Figure 4.12 Typical blood oxygen distributions for the non-constant viscosity-oxygen dissociation model:(a) before S2 removal; (b) after S2 removal. The corresponding results for the constant viscosity-single phase model are presented here for comparison: (c) before S2 removal; (d) after S2 removal (all dimensions in μm). The thickness of each line represents the non-dimensional flow rate normalised by the maximum flow rate, lines in black representing the vessels with flow rate less than 1% of the maximum

After the flow source S2 is cut at 200 s, the flow is redistributed in the network and a new network oxygen distribution pattern is formed accordingly. As seen in Figure 4.12(b), the oxygen level in the S1 flow territory, in general, has an increase and this corresponds to the increase of oxygen inflow at S1 due to flow increase. However, after the transition time, many vessels around the downstream region receives less oxygen (<0.07mM) than before. In both states, some vessels tend to possess much more oxygen, passing more oxygen into nearby tissue than others, which can lead to highly heterogeneous oxygen extraction patterns and thereby the spatially inhomogeneous tissue oxygen field.

On the contrary, in the single phase model, the near wall oxygen concentration in the network, approximated by higher values of C_b, creates very large vessel oxygen efflux around the inlets, causing network oxygen levels to decay very rapidly and to reach a plateau in the rest of the region, as most of the vessels have oxygen levels above 0.07mM. This inlet dominating distribution implies a great oxygen flux into tissue in the upstream region, creating a very high oxygen level at the places around the sources. In the downstream region, the vessel blood oxygen is much lower and homogeneously distributed, leading to an even distribution pattern in oxygen extraction.

Figure 4.13 clearly illustrates how the blood oxygenation composition in the network changes under two flow conditions for both discretised models. In the variable viscosity and oxygen dissociation model, the vascular oxygenation distribution has a peak frequency at the first mode, which decays gradually with RBC fraction before S2 removal, Fig.4.13(a). After flow inlet S2 is disabled, Fig.4.13(b), the population of the first mode increases considerably, from 13% to 31%, indicating that the vessel oxygen shortage becomes more severe during flow shortage. The number of high oxygenation vessels decreases more than low oxygenation vessels, and the region with greatest drop is in the vessels near S2, as shown in Fig.4.12(b).

For the simple model, changes in vessel oxygenation due to flow condition alternations share a similar transition with the non-constant viscosity-oxygen dissociation model. Under normal condition, Fig.4.13(c), a great population of vessels are found at low oxygenation levels, with 70% of vessels at the first mode, 18%, 6% and 2% at the 2^{nd}, 3^{rd} and 4^{th}. The flow shortage makes the situation worse, leading to 83% of vessels being under 1.48mM, as shown in Fig.4.13(d). This can also be seen in Fig.4.12(d), where vessels near S2 receive less oxygen than before. It is found that the blood oxygen distribution is highly influenced by the flow condition, given the predictions by two different models presented here.

Distinctions can also be made using Fig.4.13 for the use of different models. The simple model predictions give a lower oxygenation in the network, suggesting that oxygen tends to enter tissue space rather than vascular space. Since, in this model, the oxygen input is assumed to be proportional to the oxygen difference across the vessel wall, $C_b - C_t$, the oxygen is extracted by tissue primarily in the upstream network and less oxygen is retained in the downstream region. On the other hand, the oxygen drop across the wall, $C - C_t$, for the variable viscosity – oxygen dissociation model is much smaller in magnitude, which retains more oxygen in the network and hence downstream vessels receive more oxygen.

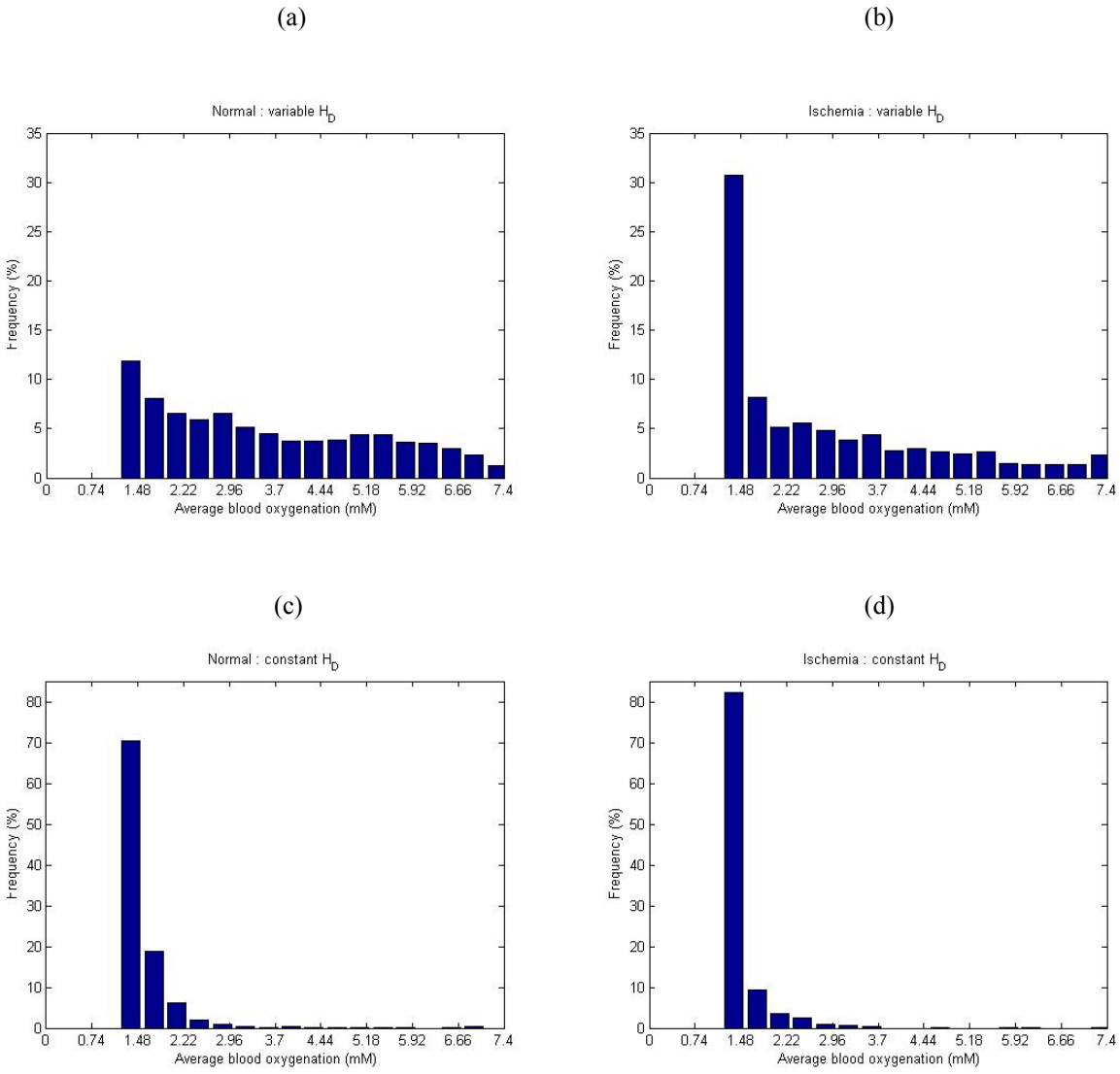


Figure 4.13 Typical blood oxygen histograms for the non-constant viscosity-oxygen dissociation model:(a) before S2 removal; (b) after S2 removal. The corresponding results for the constant viscosity-single phase model are presented here for comparison: (c) before S2 removal; (d) after S2 removal .

When the sigmoid approximation for the saturation curve is used, the tissue oxygen field, as shown in Figure 4.14, is quite different to that in the previous transport model in many ways. First, the oxygen level becomes much lower, about 1/30 of the values predicted by the single phase model. Since the local oxygen extraction, which used to be proportional to $(C_b - C_t)$, is now replaced by $(C - C_t)$, the extraction is highly reduced in this two phase transport model, leading to a prediction with lower PO_2 levels.

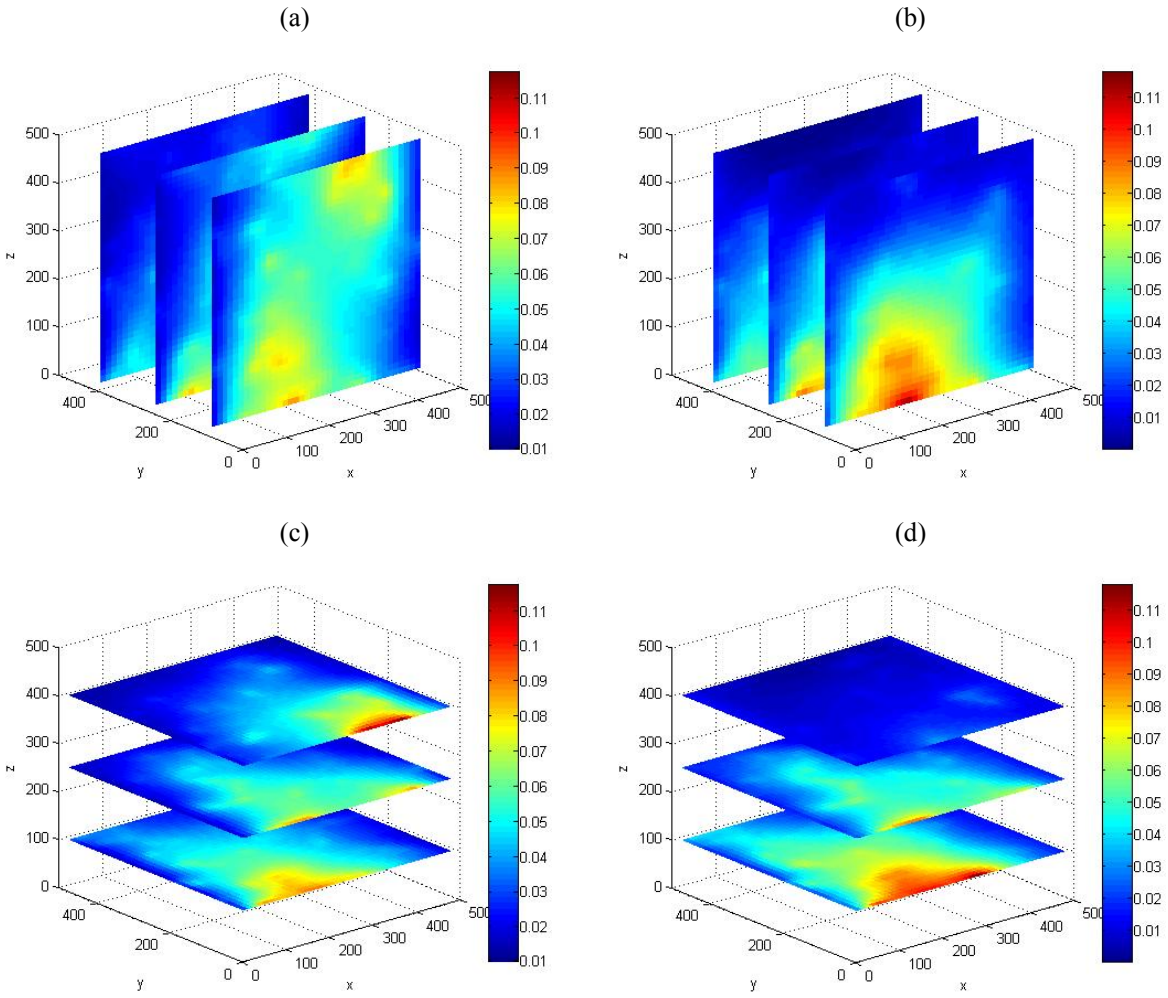


Figure 4.14 Typical distribution of tissue oxygen concentration for the variable viscosity-oxygen dissociation model is presented on three slices in y direction: (a) at 200s; (b) at 400s; and on three slices in z direction: (c) at 200s ; (d) at 400s (all dimensions in μm).

As shown in Figure 4.14(a) and 4.14(c) the high concentration spots, with concentration levels of about 0.11mM, shift to the points near the boundaries, at a distance about 100-140 μm from the flow inlets. At the plane of y=100 μm, the two high concentration zones supplied by S1 and S2 are of similar sizes, but the latter contour lobe shrinks more severely in the y direction as the contour lobe supplied by S1 covers a larger area in the plane y=250 μm. At y=400 μm, the oxygen distribution pattern is completely dominated by the contour lobe supplied by S1.

In the new steady state, as shown in Figure 4.14(b) and (d), the new local maximum sites have a higher oxygen concentration than before. The influence of the S1 supply zone decays steeper in the *z* than in the *y* direction due to the flow stretching effect. The contour plot is more irregular than that of the constant viscosity-single phase model as many sites with local maxima in tissue can easily be spotted. The spatial fluctuations in the oxygenation field may be attributed to the local variations in oxygen extraction from blood, which are not seen in the constant viscosity-single phase model.

On the contrary, the transport model, considering blood and RBC as a single phase, gives a predicted oxygenation map with high oxygen gradients in the inlet region of the tissue. This strong local diffusion will smooth out the oxygenation field in the upstream regions whilst the evenly distributed oxygen extraction in the rest of the tissue also leads to a smoothly distributed oxygen field. This may be the reason why the tissue oxygen contour is more regular than that in the non-constant viscosity- sigmoid approximation saturation models.

The discrepancies in tissue oxygenation patterns between these two discretised models, seem to be counter-intuitive at the first glance, but this can be explained by the following paragraphs. The constant viscosity- single phase model (DM1) over-estimates the oxygen input from network to tissue because the wall oxygen level in the vascular space is approximated by average blood oxygenation (oxygen in RBC and in plasma), being much higher than that in the tissue space and oxygen input is proportional to the oxygen level drops across the vessel wall. The spatial distribution of the vascular-tissue exchange has sharp foci, as shown in Fig.1(a) and (b) for two flow conditions (without and with source removal respectively). The oxygen input is dominated by the inlet regions, with extremely high magnitude compared to other nearby voxels (more than 10 times as large). This highly concentrated pattern suggests that there is a very large gradient around flow inlets, leading to

oxygenation distribution with foci being located very close to the flow inlets. The oxygenation profile is more regular and symmetrical than those predicted by the second discretised model (DM2).

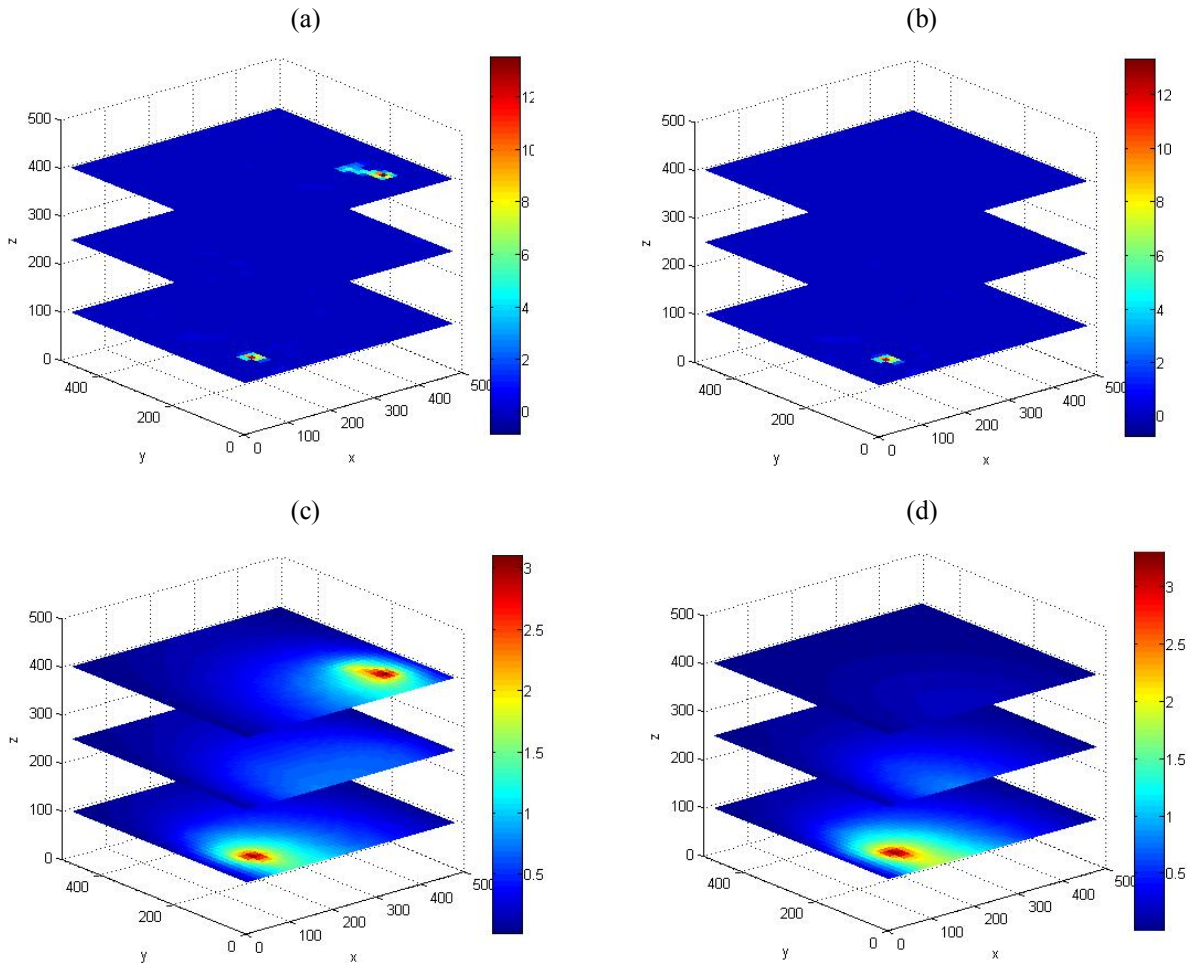


Figure 4.15 Oxygen input field from vascular space to tissue space for the constant viscosity- single phase model (DM1) is presented: (a) at 200s; (b) at 400s; resulting oxygenation patterns for the constant viscosity-single phase model (DM1) is presented on three slices in y direction: (c) at 200s ; (d) at 400s (all dimensions in μm).

When considering the variable viscosity-oxygen dissociation model (DM2), the oxygen input patterns are very different. Several oxygen input foci can be found irregularly located in the space. Since the plasma oxygen profile is an exponential decay with space, the vascular oxygen input ($\propto C - C_t$) for each vessel would has a much higher value in the upstream

region. In this way, vascular input appears at diverging vessel junctions. As a result, multi-focus pattern for oxygen input is created. The ratio of maximum to mean value in the oxygen input pattern is smaller (0.2) than those for DM1 (>10). As a result, there is no clear direction gradient for the oxygenation and the magnitude of this gradient is smaller in this oxygenation field, which tends to compromise the smearing effect. Along with non-uniform oxygen consumption patterns, the weak diffusion contributes to a more irregular spatial oxygenation distribution, with several local foci.

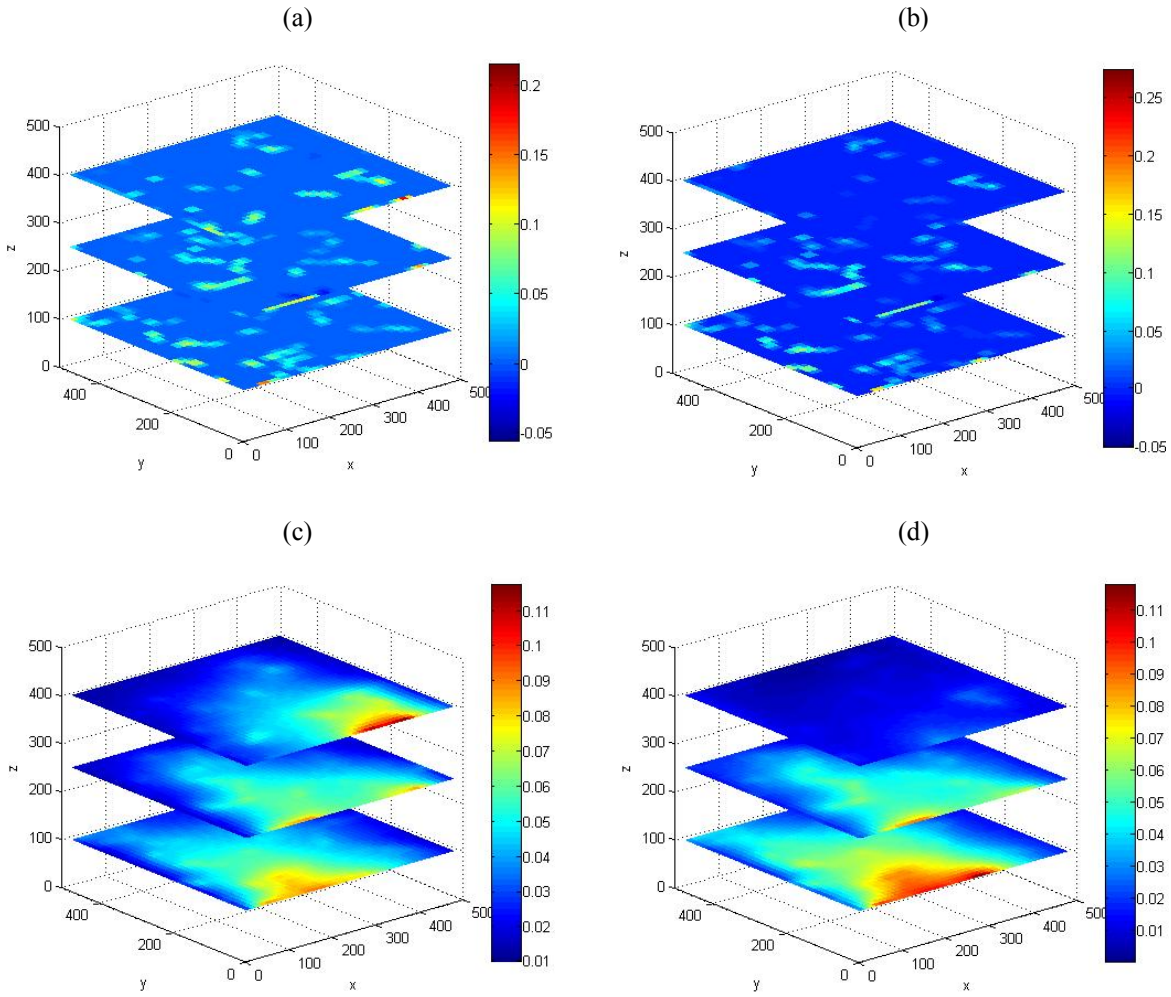


Figure 4.16 Oxygen input field from vascular space to tissue space for the variable viscosity-oxygen dissociation model (DM2) is presented: (a) at 200s; (b) at 400s; resulting oxygenation patterns for the variable viscosity-oxygen dissociation model (DM2) is presented on three slices in y direction: (c) at 200s; (d) at 400s

(all dimensions in μm).

As shown in Figure 4.17, the tissue at M1 undergoes two stages of increase in oxygen level, with increments of 0.02mM and 0.01mM respectively. On the contrary, the tissue at M2 experiences an initial rise up to 0.034mM, then experiences an oxygen level drop of 0.023mM, finally reaching an the oxygen level of 0.01mM.

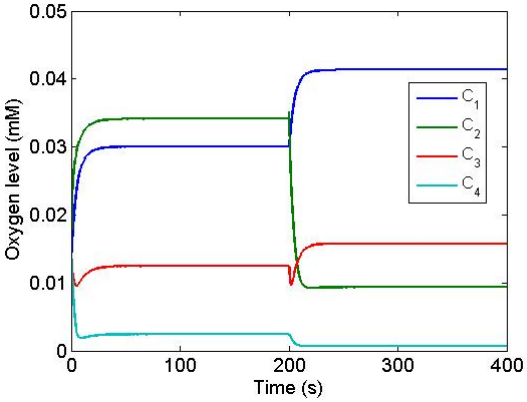


Figure 4.15 Time courses of tissue oxygen concentration at different monitoring points for the non-constant viscosity-dissociation model with sigmoid approximations

The oxygen level at M3 has an initial drop, then an increase to 0.138mM after S2 removal, the oxygen level drops again but rises rapidly to 0.16mM. Since M3 belongs to the flow territory S1-S3, the M3 curve should have been composed of two monotonically increasing sub-curves, if the tissue did not have localised maxima in oxygen field. But, in fact, each part of the curve has an initial drop and followed by a late increase before reaching steady states.

This two phase feature in the time course for M3 may be explained as follows. The oxygen source into the voxel where M3 is located is very weak for both the steady states in current model. According to the transport equation, the change of the oxygen level depends mainly on two competing terms: the diffusion and the consumption terms. The former relies on exchange with the surroundings, usually taking a longer time to react than does the

consumption. The initial drop seen in Figure 4.15 is induced by the consumption initially, but gradually becomes counterbalanced by the oxygen input by other higher level spots. Since the oxygen transfer is diffusion based, it takes a time for the oxygen diffusion from nearby local maximums of oxygen level to reach the local voxel. The local maximum sites in tissue act like diffusion sources, each of which creates a localised oxygen flux due to its concentration gradient. The farther or weaker the diffusion source, the slower is the reaction. After the removal of S2, the initial dip is caused by an imbalance between the local consumption and diffusion and the increase is caused by more input diffusion due to the general increase in flow in S1 territory.

For the model that considers a variable haematocrit distribution, the resulting oxygen field becomes less homogeneous; therefore, a shut down source does not always cause a oxygen flux shortage for vessels far away. A source removal in the same territory, on the contrary, might cause an increase in oxygen supply for a few vessels near the monitoring point, and this scenario could be used to explain the strange time courses of M2 and M3 in Figure 4.15. Since there is insufficient oxygen network influx to M4, the time course in Figure 4.15 has an initial dip, the raising up slightly due to the input from flow convection and boundary diffusion. As S2 is completely shut down, the network input is reduced and thus a further decay is expected.

4.6 Discussion

In the flow simulations presented here, two viscosity laws, constant and flow-geometry dependent, have been adopted to mimic blood flow in the heterogeneous microvasculature. In the first case, the overall flow rate passing through the cube of tissue is $3.8\times10^{-13}m^3/s$ whilst the net flow rate estimated in the later model is $3.0\times10^{-13}m^3/s$, about 80% of that of the

constant viscosity model. Such an increase in the flow resistance is the outcome of a more realistic rheology model, which accounts for the non-even haematocrit distribution and the geometry-haematocrit dependent viscosity.

The flow plots have shown that, for both flow models, the network can generally be divided into two territories, each containing one source and one sink. For example, the blood in the S1 territory runs through the microvascular tree, from one bifurcation to the next, most of it being finally collected by S3. A smaller portion of the blood, mixed with the blood driven by S2 in the middle region of the network, is finally collected by S4. There is only limited flow exchange across the boundary of the flow territory in the upstream region due to the counterbalance of the two flow sources with the same blood pressures.

When S2 is blocked, a majority of vessels in the S1 territory can get more blood than before, for both flow models. Considering the simple flow model firstly, the new pressure drop built between S1 and S2 tends to drive more flow through the vessels in between, which must be achieved by an increase of flow input at S1. Such an increase of the inflow, leading to the S1 source becoming stronger, explains why S1 can cover a larger flow territory after S2 removal. Although the refining of the viscosity law brings complexity in the flow patterns by allowing haematocrit variations between vessels, the resulting flow pattern change very little in terms of the flow distribution.

The oxygen field is largely homogenous in the constant viscosity-single phase model, where two contour lobes sustained by two source-sink pairs are located evenly in the tissue before the S2 removal. After S2 is shut down, the corresponding contour lobe disappears and the other seems to expand due to the increase in the flow input at S1. The tissue oxygen level is higher than the other transport model because it treats the blood/cell mixture as a single phase and ignores the possible variations in network RBC distribution.

When the oxygen saturation and refined viscosity law are applied, despite the similarities in the flow distribution patterns, the oxygen fields are very different from the simple model. The non-homogenous spatial transition and the rather low estimated oxygen level (3.3% of the values in the single phase model) are the features that distinguish the results from those from the simple one. The former is very likely to be the consequence of the variation of the haematocrit, creating an uneven blood oxygen distribution among daughter vessels. As a result, some vessels in the network retain fairly high oxygen levels, and hence a high oxygen efflux. The oxygen extraction is found to be confined to certain regions near these flux dominating vessels.

The latter is simply the outcome of different ways to approach the saturation curve. In the simple model, concentration drops across the wall are, in general, larger than in the two phase model and hence also the oxygen efflux, since the average blood oxygen level is much higher (up to 100 fold) that of the plasma level, which is used to approximate the near wall blood oxygen in the single phase and two phase vessel transport models respectively. Consequently, less network oxygen entering the tissue in the two phase model leads to a lower oxygen profile in tissue.

In the constant viscosity-single phase model, a large amount of the oxygen flux enters the tissue space, being 10 times larger than the consumption in total, so 90% of oxygen from the network becomes the source term, and is available to be re-distributed via diffusion in the tissue space. However, the resulting tissue extraction in the variable viscosity-two phase model is lower, being the same order of the consumption, so less oxygen is free to diffuse in the tissue space.

The net oxygen accumulation in a tissue voxel, which determines the dynamic of local oxygenation, is simply the sum of the source term and the local diffusion. Since the

imbalance between oxygen extraction and consumption is very close, compared to the single phase model, the resulting net source can be positive around some vessels with sufficient oxygen or be negative in some oxygen deprived vessels. The spatial variations in the blood oxygen distribution in the network are thus correlated to the spatial heterogeneity found in tissue oxygen field.

In addition, this tight match between two source terms makes the local tissue oxygen level very sensitive to diffusion because the net oxygen accumulation in a tissue voxel defines the local tissue dynamics. A number of sites with local maxima in oxygen level are found to be located separately in the space, which would diffuse oxygen into the regions with lower oxygen levels. In a voxel, these multiple diffusions from nearby local maxima can individually regulate the small source term, and bring different dynamic impacts on the local tissue oxygen concentration. This spatial heterogeneity in diffusion can, in some cases, create overshoots or undershoots in the time courses of the local tissue oxygen level.

The tissue oxygen field depends mainly on the trans-vascular oxygen exchange across the walls of the microvasculature. The estimation of oxygen level at the lumen side is critical because it directly determines the oxygen flux for a given vessel, and thereby the tissue oxygen level. Considering the blood flow along a vessel, the RBCs, as the main carriers of the oxygen, are embedded by the plasma. The near wall PO_2 level is a function of the RBC position and the mean plasma oxygen level, as the wall PO_2 level is higher at the places around the RBC and plasma PO_2 determines the RBC oxygenation. It is then logical to set a maximum of lumen oxygen concentration as the average blood oxygen level and to set the minimum as the average plasma oxygen level. Our models would, in other words, provide a theoretical estimation of the extremes for the oxygen levels in the brain tissue, with an upper bound set by the mixture model and a lower bound set by the saturation models.

Typical flow entering into the tissue region is $4.0\times10^{-13}m^3/s$, roughly corresponding to 22ml/100g-min, which is found to be as small as the one part of simulation results by Lorthois and co-workers (Lorthois, Cassot, Lauwers 2011b), but under-estimating the physiological values of the typical human brain perfusion rate (60ml/100g tissue-min) (Buxton 2005) by a factor of about 3. This mismatch can be easily remedied by increasing the pressure difference between the flow inlets and outlets, or by introducing more flow-sources into the network.

In addition, the maximum oxygen consumption rate used in the simulations here, set to have a value of 0.004mM/s (0.6 ml/100g-min), is smaller than the typical rate of 2-3ml/100g-min, obtained from O^{15} PET measurement on $CMRO_2$ (Kudomi and others 2009). The setting of a lower value in the model here is aimed to avoid the negative tissue oxygen during calculation, under the flow conditions described above. If the prediction can be made more physiologically relevant by increasing the flow input in the simulation, the tissue oxygen consumption rate can also be elevated to a value close to the experimentally measured data based on the basis of mass conservation of oxygen between network and tissue.

Despite the model providing two simulations for tissue oxygen level with two different magnitudes using different near wall oxygen level approximations in blood, it is found that the lower oxygen field, predicted by the model accounting for the non-constant viscosity and sigmoid approximation for the oxygen saturation curve, gives an oxygen content variation from 0.001-0.11mM, corresponding to 0.7-88mmHg, in the tissue space. This estimation offers a good match to the brain oxygen level in physiological relevant condition, 0-80 mmHg, as mentioned in Chapter 2.5-3 (Ndubuizu and LaManna 2007).

It should be noted that the results have been shown in this section are based on one particular network generated by the modified spanning tree method. In fact, the network structure has a

strong influence on change the blood flow and oxygen transport patterns and the effect of network variability on these flow and transport features given by the stochastic network generation method, is of great interest and hence will be further explored in the next chapter.

It should be noted here the blood flow computation was executed, using around 1300 nodes for the network and the computation time is within 1 min for the case considering linear viscosity and within 3minutes for the case considering nonlinear viscosity, respectively. As for the tissue oxygenation, the computation for both models was executed, using a grid of 40×40×40 elements, for 40,000 timesteps ($\Delta t = 0.01$s). The executionS for both models were both completed in 8 hours in Windows XP environment. All computation are run on a computer with Intel Core 2 6420 CPU, on a single core and with 2G bytes of memory.

4.7 Conclusion

A set of simulations regarding flow and oxygen transport in an artificial network and surrounding tissue have been presented to mimic the tissue response to the micro-stroke in cerebral microvasculature. Different settings in blood viscosity and the near wall blood PO_2 approximation have been tested. The variable viscosity law seems to increase the flow resistance of the network by tuning the viscosity according to haematocrit and vessel size. However, this change in viscosity does not cause a significant change in the flow distribution patterns. Introducing the oxygen binding effect of haemoglobin in the oxygen transport equation in the network changes the distributions of oxygen exchange with tissue, so that the tissue oxygen field is changed accordingly in terms of its distribution patterns. The resulting values of flow and tissue oxygen lie in a satisfactory region, being 35% and 110% for the experimental flow and oxygen tension data, suggesting that this flow and transport coupled model is capable of replicating the complex patterns shown in brain networks.

Chapter 5. Continuum model for blood and oxygen transport

5.1 Introduction

As shown in the last two chapters, the network generation algorithm presented here can statistically capture the geometric and topological features of the human cerebral microvasculature. The resulting flow and oxygen transport patterns, obtained from model predictions, provide reasonable approximations when compared with corresponding values in experimental studies, suggesting the feasibility of the current discretised model at such a small length scale. There are, however, some drawbacks of this model, such as the computational cost due to the detailed modelling of the individual impact of each microvessel in the network. This accuracy would inevitably reduce the computational efficiency, and would not be feasible at larger length scales.

In particular, in our computations, a domain having about 1,000 vessels (1300 nodes) only occupies a cube of length 500μm. A standard voxel in fMRI imaging is, however, about $(5\text{mm})^3$: this contains approximately 1,300,000 nodes in the network, which would require an extremely large computational cost and memory loading, especially when coupled with the mass transport equation through tissue. Scaling the model up to the size of the whole brain to provide a more comprehensive picture of the interplay between blood flow and mass transport for potential clinical uses would be totally impractical.

To remedy this, it is necessary to develop an efficient model that can capture the overall flow and the oxygen transport features of the network-tissue system for the microvasculature. Since blood flow in the microvasculature is somewhat like the flow in voids or small channels in rocks or soils, a porous media model based on the continuum assumption is proposed here to replicate the general flow patterns and a two phase transport model is used

to describe the oxygen transport in both the blood and tissue in a manner that can be scaled up for larger volumes of tissue.

5.2 Porous media model for blood flow

Porous media are very common in nature and can be described by a two phase system including a fluid and a structure phase. They have interconnected voids, cavities or tiny channels, with a wide variety of geometric and topological features, allowing fluid to pass through the internal pathways. The main idea of the model is to find a proper volume integral representation of the flow field in the void space rather than to account for the flow patterns in individual flow pathways.

When the length scale of the problem is much larger than the size of the flow channels or cavities, the volume averaged equations resulting from the porous media model can be a very good approximation for the behaviour of the discretised flow system. Hence, the size for the region of the interest in the porous media model needs to be large enough to smear out the structural variability of the random flow paths. Meanwhile it also needs be small enough to give a desired resolution for the flow field (Kolev 2007). In other words, this gives the lower and upper limits for the element of the calculation element for the porous media problem.

Tissue with fluid moving through an interstitial space (Khanafer, Vafai, Kangarlu 2003) (Linninger and others 2008) or a capillary bed (Chen and others 2007) can also be treated as a porous medium flow due to the analogy with a typical porous medium.The embedded networks are randomly arranged and the structure of the extra-vascular space can together be treated as a porous medium with isotropic and homogeneous flow pathways. Taken together with the slow flow condition, the blood flow in microvasculature can be taken to be governed by Darcy's flow equation:

$$\mathbf{u}_D = -\frac{\mathbf{K}}{\mu}\nabla P = \phi_b \mathbf{V}, \tag{5-1}$$

where $\mathbf{u}_D$ and ∇P are the Darcy velocity and the pressure gradient respectively. $\mathbf{V}$ is the flow field for the blood and ϕ_b is the porosity. The volume averaged velocity, Darcy velocity, is found to be proportional to the pressure gradient. Since only a fraction of the total formation volume is available for blood, the blood velocity $\mathbf{V}$ is thus estimated according to Eq.5-1. Although the permeability $\mathbf{K}$ is a second order symmetric tensor, representing the directional transport preferences, here it is assumed to be a constant, κ, under the assumption of an isotropic medium. By taking the divergence of Eq.5-1, it becomes the Poisson equation for pressure, based on mass conservation:

$$\frac{\kappa}{\mu}\nabla^2 P = S. \tag{5-2}$$

The source field, S, is equal to zero except at the flow sources and sinks. This can be solved numerically in a number of ways, here by the Conjugate Gradient method (Vandervorst 1992). The blood velocity can then be estimated according to Eq.5-1.

In the simulations here, the blood viscosity is taken as 3.6×10^{-3} Pa·s, which is calculated with haematocrit 0.5 and mean diameter 6.23 μm, being used in the normal distribution random number generator) using Eq.4.4-4.6. The porosity is taken as 1.63%, which is taken as the ratio of the tissue volume to the mean values of the vascular volume obtained from 100 artificial networks generated by the MSTM. The permeability κ (3.6×10^{-15} m^2) is converted from the flow hydraulic conductivity (h=1×10^{-12}m^4/N·s) according to the relationship ($\kappa/\mu = h$) (Kolev 2007).

5.3 Porous media model for oxygen transport

Since local oxygen extraction in tissue is affected by the flow patterns of the blood, the oxygen transport in blood and tissue must be analysed in a coupled manner. Here we consider the vessel/tissue system as a two phase flow system, including the blood phase representing the flow perfusion with a volume fraction of ϕ_b and the tissue phase representing a static fluid at a volume fraction of ϕ_t, where $\phi_t + \phi_b = 1$.

By analogy with other two phase flow models, (Nicholson 2001), (Khaled and Vafai 2003), (Wang, Wang, Chen 2001) oxygen transport in the fluid phase (blood) and the structure phase (tissue) can be taken to be described by the coupled equations Eq.5-3 and Eq.5-5 respectively.

$$\phi_b\left(\frac{\partial C_b}{\partial t} + (\mathbf{V}\cdot\nabla)C_b\right) = G_{ex}, \tag{5-3}$$

$$G_{ex} = -A_e \times (C_{bw} - C_t), \tag{5-4}$$

Instead of modeling blood oxygen transport individually, the present model treats the blood as a phase with corresponding blood velocity, $\mathbf{V}$, the transvascular exchange area per unit volume tissue, A_e, and a locally volume averaged oxygen concentration, C_b. This continuum model transfers the problem of the network blood flow from sets of 1D ODE into one 3D PDE, allowing blood oxygen transport patterns to be investigated in a continuum manner.

In the blood phase, the oxygen is mainly transported by flow convection, whereas tissue oxygen transport is dominated by molecular diffusion. The transvascular exchange of oxygen, G_{ex}, which links equations Eq.5-3 and Eq.5-5 together, is assumed to be linearly proportional to the difference across the vessel wall with a factor, A_e, which is the effective

area of the blood-tissue interface for the substance exchange per volume tissue. The blood oxygen level at the vessel wall, C_{bw}, in Eq.5.4, is approximated by the plasma oxygen level, C, as in the discretised model presented in the last chapter.

Similarly, the tissue oxygen concentration field is represented by the volume averaged variable, C_t. The rate of change in tissue oxygen tension depends on the local exchange at blood-tissue inter-surface G_{ex} and the local oxygen consumption M :

$$\phi_t \frac{\partial C_t}{\partial t} = \phi_t D_t \nabla^2 C_t - G_{ex} - M \quad . \tag{5-5}$$

The oxygen consumption of the tissue, like the approximation used in the discretised model earlier, is assumed here to follow the Michaelis-Menten kinetic model, which relates the tissue oxygen consumption rate M (mM/s) to the consumption rate for un-restricted metabolism, M_0 and the reference oxygen partial pressure, P_0, at which metabolism drops to the half of the value (Secomb and others 2000):

$$M = M_0 \frac{P_{O2}}{P_{O2} + P_0} \tag{5-6}$$

The plasma oxygen level, C, is related to the average blood oxygen level, C_b, through the following equation by using Hill's equation $S = \left(\frac{C^3}{C_{50}^3 + C^3} \right)$ for the saturation curve (Secomb and others 2000):

$$C_b = (1 - H)C + C_{Hb} H_T S(C) + H_T C \,, \tag{5-7}$$

where C, C_{Hb}, S are the plasma oxygen concentration, haemoglobin concentration in RBC, and the saturation of the haemoglobin respectively. At a given blood oxygen level, the plasma oxygen level can be determined by solving Eq.5-7. Since this equation is nonlinear, iteration is used here to obtain the plasma oxygen level and thereby the wall oxygen flux. The transport equations for blood and the tissue phases are all discretised by the finite volume method, which has been widely used in dealing with heat and mass transfer equations (see Appendix A). The boundary conditions for the 3D transport equations used in this chapter are outline in the Table 5-0.

Table 5-0 The boundary condition for the 3D mass transport equations

Direction	Boundary condition for oxygen transport at blood phase for the continuum model
x	$\frac{\partial C_b(0,y,z)}{\partial x} = \frac{\partial C_b(L,y,z)}{\partial x} = 0$
y	$\frac{\partial C_b(x,0,z)}{\partial y} = \frac{\partial C_b(x,L,z)}{\partial y} = 0$
z	$\frac{\partial C_b(x,y,0)}{\partial z} = \frac{\partial C_b(x,y,L)}{\partial z} = 0$
Direction	Boundary condition for oxygen transport at tissue for both continuum and discretised models
x	$C(0,y,z) = C(L,y,z) = C_{tb}$
y	$\frac{\partial C(x,0,z)}{\partial y} = \frac{\partial C(x,L,z)}{\partial y} = 0$
z	$\frac{\partial C(x,y,0)}{\partial z} = \frac{\partial C(x,y,L)}{\partial z} = 0$

5.4 Analogy between discretised and continuum model

Instead of treating the network as discrete, here it is considered to be the void space in a porous medium. In this way, the network tissue system can be converted into a two phase system using the continuum model to further explore the potential link between the discretised flow transport model and the porous media model, or more precisely, to characterize the overall flow conductance of a network in terms of the permeability of the flow/medium system. In addition, how the variability of the network affects the flow patterns and resulting tissue oxygen profile is the other question addressed here. A simple test problem is presented here to explore the analogy and a set of simulations for 100 sample networks is performed to quantify the variations induced by the randomness of the network generation method.

A uniform pressure field at four surfaces is applied to form a pressure drop in both the x and y directions. The pressure drops are set at values from -3000Pa to 3000Pa, with an increment of 1000Pa, in both x and y directions. Pressures at upstream surfaces change accordingly while pressures at downstream surfaces are fixed as 1000Pa. The total flow rates across four surfaces, driven by corresponding pressure conditions, are then estimated, as shown schematically in Figure 5.1.

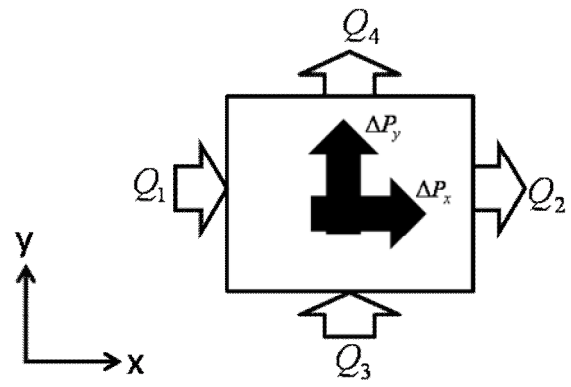


Figure 5.1. Schematic for the flow fluxes and the coordinate system

In the *z* direction, no blood flow can pass through the two surfaces. These 7×7 combinations for the pressure drops are used to define the relationship between the pressure drops and the flow rates at the four surfaces. This can be expressed in matrix form if the flow system is individually influenced by the two driven pressures, i.e. the pressure flow system is linear:

$$\begin{bmatrix} G_{x1} & G_{y1} \\ G_{x2} & G_{y2} \\ G_{x3} & G_{y3} \\ G_{x4} & G_{y4} \end{bmatrix} \begin{bmatrix} \Delta P_x \\ \Delta P_y \end{bmatrix} = \begin{bmatrix} Q_1 \\ Q_2 \\ Q_3 \\ Q_4 \end{bmatrix}. \tag{5-8}$$

Since there is no flow flux in the *z* direction, the net blood flow across surfaces can be decomposed into the flows driven by the pressure drops in *x* and *y* directions individually. The conductance matrix represents the impact of the pressure drops on the surface flow fluxes: for instance, G_{x3} is the flow conductance at surface 3 contributed by the *x* direction pressure drop and Q_1 is the total flow passing through the surface 1, according to the schematic presented in Figure 5.1.

This matrix form allows for direct comparison between the flow pressure correlations in both the discretised and continuum models on the same basis. For the continuum model, a computation is initially performed to simulate the blood flow transport in a isotropic and homogeneous medium with a size of $(400\mu m)^3$. The four surface flows are then estimated according to Eq.5-1 once the pressure field has been determined.

Due to flow conservation, in the case of the continuum model, the estimated conductance matrix can also be reduced from 8 to 6 independent elements. Further simplification to 3 elements can be made resulting from the spatial symmetry between *x* and *y*. The original 8 elements in conductance matrix in Eq.16 are thus reduced to 3 elements.

$$\begin{bmatrix} G_{in} & -G_{cross} \\ G_{out} & G_{cross} \\ -G_{cross} & G_{in} \\ G_{cross} & G_{out} \end{bmatrix} \begin{bmatrix} \Delta P_x \\ \Delta P_y \end{bmatrix} = \begin{bmatrix} Q_1 \\ Q_2 \\ Q_3 \\ Q_4 \end{bmatrix}. \tag{5-9}$$

The inlet surface flow is found to have a large correlation with the pressure drop in the same direction, whereas the most distant flux is very weakly dependent on the pressure drop, being even smaller than the other cross surface flows. In other words, along the direction of a given pressure gradient, the flow conductance of the inlet surface, G_{in}, at the high pressure side is the largest, followed by two cross flow conductance, G_{cross}, and finally the conductance at the outlet surface, G_{out}. This is due to the fact that the mean flow paths to the cross surfaces are shorter than those to the outlet and conductance is inversely proportional to the length of mean flow path in an isotropic and homogenous medium.

In order to test the variations in flow patterns for different network structures in the discretised model, 100 networks were created, each with about 1000 vessels, generated by the modified spanning tree method embedded in a $(500\mu m)^3$ cube. To mimic the vessels crossing the real system boundaries, a smaller cube in the centre was extracted as a test sample of brain tissue, and the same set of boundary conditions used in the continuum model applied. Many vessels constructed from the $(500\mu m)^3$ cube penetrate the boundaries of the small box. Hence, in order to impose the pressure condition properly, vessels intersecting these boundaries were labelled, and the given pressure directly applied at these intersection points.

One straightforward way to set a no flux condition in the network flow is to make the flow conductance equal to zero for the vessels passing through a boundary. However, setting zero flow conductance value for a given vessel makes all elements in the corresponding row of the coefficient matrix of the linear system (Eq.4-3) zero, leading to an ill-posed matrix. To

implement no-flow conditions at z direction, the vessel flow conductance across boundaries can only be set as a tiny value but not zero. This is due to the limitation of the flow solver when a great number of vessels need to be blocked. Through a series of tests we found that 10^{-10} is the smallest value that can robustly maintain the convergence of the flow calculation. Using a value of 10^{-9} instead gives a maximum relative error for the surface fluxes of less than 0.1% using a sample of 10 networks. Since the main focus of this part of the simulation is to investigate the collective flow feature (net surface flux) rather than individual vessel flow rates, we thus regulate the flow conductance by a factor of 10^{-10} and take this value as a good approximation for the vessel no flow condition.

For the discretised model, simulations with the two viscosity settings with different network sizes $(200\mu m)^3$, $(300\mu m)^3$ and $(400\mu m)^3$ of volume centred in the basic network are extracted from the same 100 networks of volume $(500\mu m)^3$. Since the dependence of the conductance matrix on the sampled network size and the impact of variable haematocrit in the blood rheology on the flow patterns in the network are both far from fully understood, these issues are addressed separately.

5.5 Results

The main purposes of this chapter are two folds: to construct a continuum model as close as possible to the discretised one and to demonstrate the variations in the flow and oxygenation patterns induced by the stochastic nature of the artificial networks. Firstly, the analogy between the continuum and the discretised model is presented and discussed in the first section for one particular network. In addition, flow features due to the network variability is well characterised thorough a statistic analysis for 100 networks and a sufficient condition for analogy to the porous media flow is well illustrated. Followed by the flow features, the analogy in oxygenation pattern between these two models is addressed as well.

5.5-1 Model comparisons on flow/oxygenation

Comparisons of the flow features are made here between the network model and the porous media model under the same conditions. In both models, two flow sources and two flow sinks are put in a $(0.5\text{mm})^3$ cube at the following locations, as shown in Figure 5.2. They are labelled as S1 to S4, and located at S1 (100,100,100), S2 (400,100,400), S3 (100,400,100), S4 (400,400,400) with all units in micrometres, to represent the arteriolar and venule-capillary junctions in the microvascular bed.

Two flow sources and sinks, S1-S2 and S3-S4, with flow rates of 1.8×10^{-13} m^3/s and -1.8×10^{-13} m^3/s respectively, where the flow rate 3.6×10^{-13} m^3/s is the mean flow rate input estimated in the previous chapter, are placed at the vessel junctions in the network for the discretised model. For the continuum model, flow sources and sinks are put in the same locations as in the blood phase. The boundary conditions for the porous flow required when solving the pressure Poisson equations is a no flux condition at all boundaries.

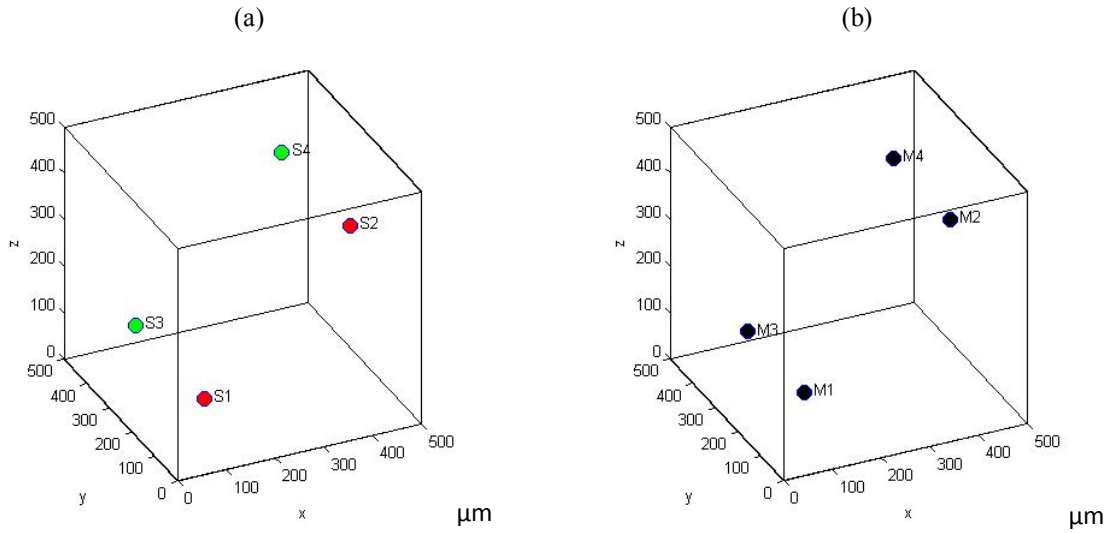


Figure 5.2 Spatial arrangements of: (a) four terminal nodes S1-S4; (b) four monitoring points, M1-M4 (all dimensions in μm).

The inlet oxygen concentration for both models is set to be 0.73mM, corresponding to a plasma oxygen tension of 100mmHg. For the discretised model, the settings and procedures for solving the blood oxygen transport problem are the same as those outlined in the last chapter. On the other hand, boundary conditions for the continuum model are required and the no flux condition is thus applied to mimic oxygen transport in a closed flow system.

For the tissue phase, the initial and boundary conditions are exactly the same. The initial condition is set at 0.0136mM for both models. The mixed boundary conditions for oxygen concentration in the tissue are the same as the previous chapter: in the y and z directions there is no flux whilst in the x direction concentration is set to be a constant. To simulate a mini-infarct caused by a blood flow shortage, a vascular blockage is mimicked by disabling one flow source S2 at 200s. Four symmetrically arranged points, M1-M4, as shown in Figure 5.2, are chosen in this comparison to monitor the temporal behaviour of tissue oxygenation in response to this reduction.

The concentration contours for the blood and tissue phases are shown in Figure 5.3 at two different times, 200s and 400s. The contours in Figure 5.3(a) have two large regions with an oxygen tension of 7mM, symmetrically located in the inlet regions, stretching out mainly in the y direction and dominating the transport of the conduction of blood oxygen here. These two oxygen contours in the blood phase are caused by symmetric flow condition in terms of the geometric and strength arrangement and correspond to the flow territories fed by the two equal sources S1 and S2.

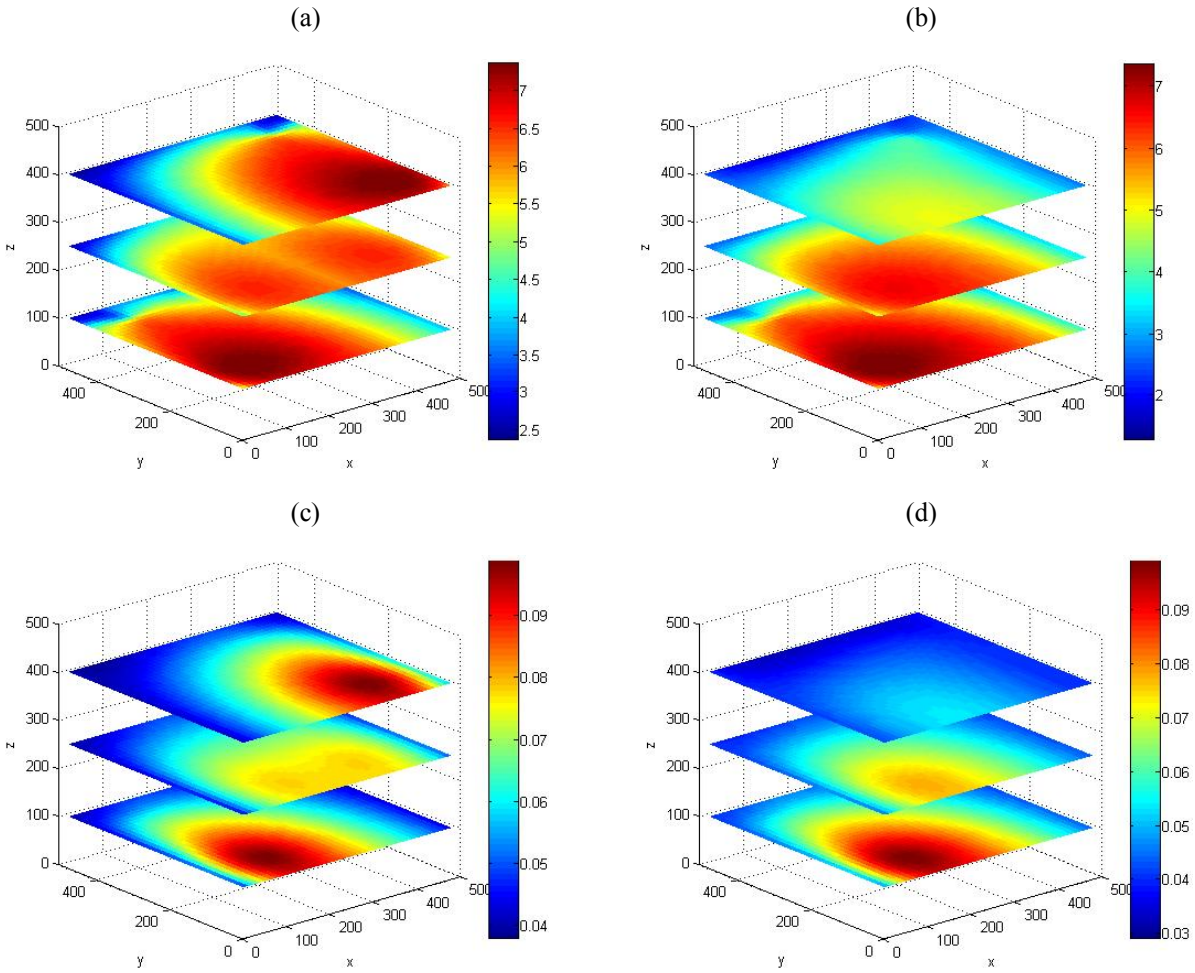


Figure 5.3 Typical distribution of blood oxygen concentration in three slices in x-y plane: (a) at 200s ; (b) at 400s and tissue oxygen concentration in three slices in x-y plane: (c) at 200s ; (d) at 400s; all for the continuum model (all dimensions in μm).

The oxygen level distribution in the network is mainly determined by blood perfusion. According to Poisson's equation for pressure, the blood flow has a higher velocity near the inlet region, and this strong convection drives the oxygen further away. This creates a larger zone with a high level close to inlet oxygen level. The stronger is the blood perfusion, the further the high oxygen contour that can be reached. This may be the reason why the blood oxygen profile is relatively flat in the inlet region

After S2 is disabled, the high oxygen level region sustained by S2 shrinks greatly, and is

finally taken over by S1 as shown in Figure 5.3(b). Tissue oxygen shows similar distribution patterns, but with smaller values in both steady states. As shown in Figure 5.3(c), the tissue oxygen level has a maximum value of 0.136mM at the two inlets, decaying mainly in the *y* direction, reaching a minimum value of 0.04mM. After S2 removal, oxygen exchange is shut off around S2 territory, leaving the tissue very dependent on S1.

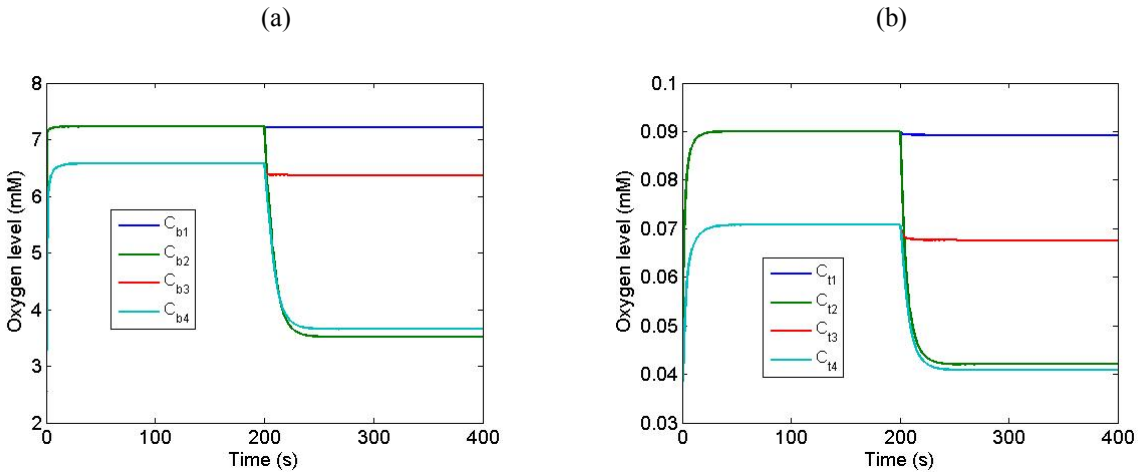


Figure 5.4 Time courses of the oxygen level (a) (C_{b1}-C_{b4}) at M1-M4 in the blood phase; (b) (C_{t1}-C_{t4}) at M1-M4 in the tissue phase, all for the continuum model.

As shown in Figure 5.4, for both phases, the oxygen levels at symmetric monitoring points have the same time courses before the source removal and their courses bifurcate afterwards. The blood oxygen level at M1 shows a slight decrease, with a drop of about 0.06mM after the S2 removal, and so does M3, but with a larger drop of about 0.2mM. However, the blood oxygen level at points in the S2 territory undergoes a dramatic drop in response to the S2 shut off. For instance, the oxygen tension at M2 decreases within 25s, from 7.3mM to 3.5mM, whilst the drop at M4 is only slightly smaller, being from 6.5mM to 3.6mM. The tissue oxygen levels at the same monitoring points share similar shapes of the transition patterns but with much smaller changes in magnitude.

The tissue oxygen distributions for the discrete and continuum models in the two steady states are shown in subplots (a) (c) and (b) (d) of Figure 5.5 respectively. Compared to the continuum model, the tissue oxygen tension for the discretised model is very non-homogeneous, as the contours are located separately in the space and the shapes are very irregular. The oxygen level is generally lower in the discrete model, with a spatial average of about 1/2 that in the continuum model, implying that less oxygen is extracted in the discretised model under the settings shared with the continuum model.

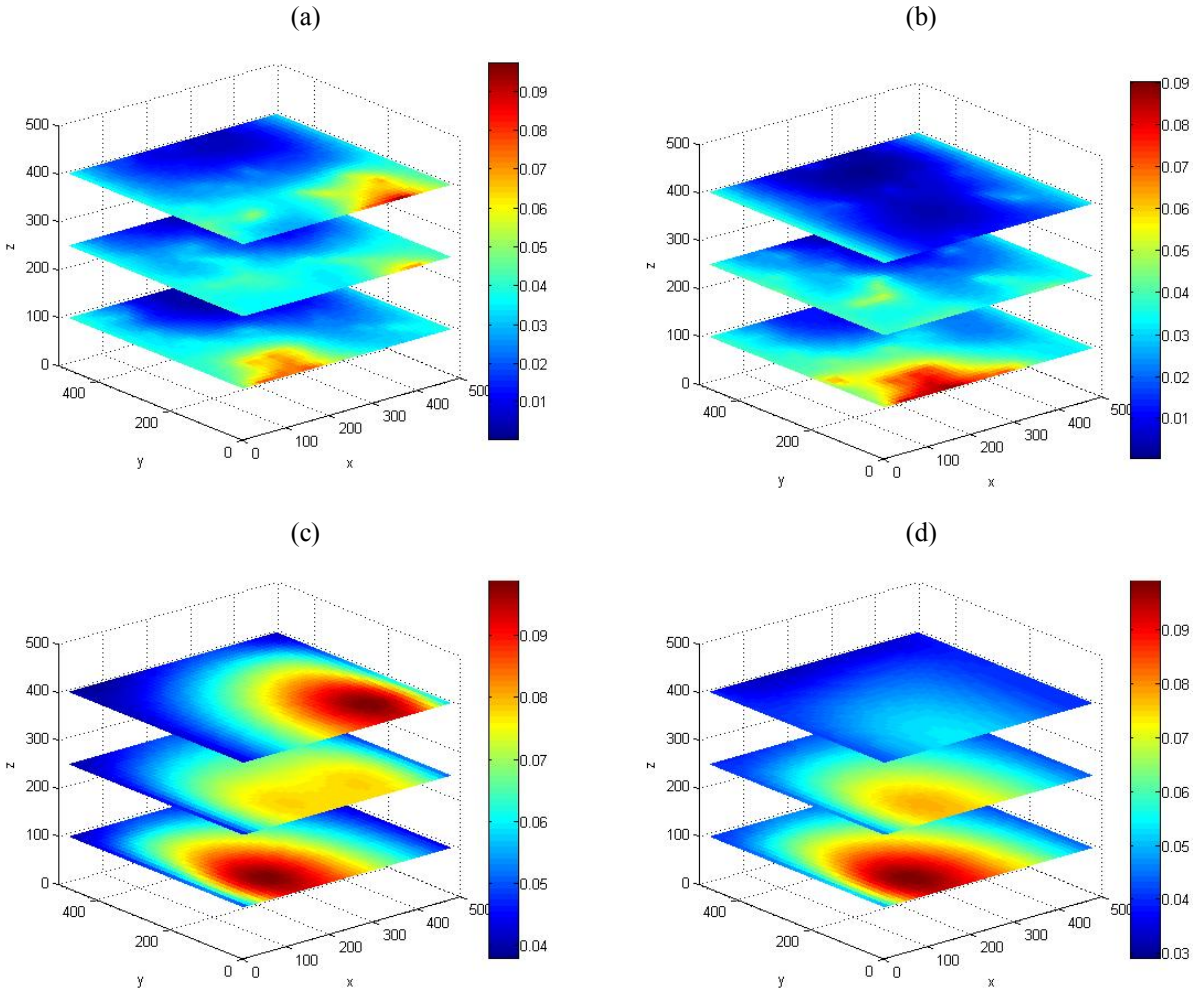


Figure 5.5 Typical distribution of tissue oxygen concentration for the discretised model in three slices in x-y plane (a) at 200s; (b) at 400s and tissue oxygen concentration for the continuum model presented in three slices in x-y plane (c) at 200s; (d) at 400s (all dimensions in μm).

As seen in Figure 5.5(a), the locations of the two maxima do not coincide with the flow inlets, but are located near the boundary of x=0. The unbalance in location between the flow inlets and oxygenation maximum is mainly caused by the anisotropic oxygen extraction as well as the no flux condition boundary at x=0. In the discretised model, given the same longitudinal plasma oxygen gradient for a vessel, oxygen extraction is higher in the vessel with the higher haematocrit due to the unloading effect of the haemoglobin.

Unlike the constant haematocrit setting in the continuum model, the haematocrit in the vessels are distributed in a very irregular manner. In fact, some of the vessels in the network can have discharge haematocrit values higher than 50%, and consequently, pour more oxygen into the surrounding tissue, becoming the main oxygen sources to the nearby tissue, and thus making the oxygen tissue contours fairly heterogeneous. If the high oxygen extraction from vessel occurs at sites near the no flux boundary, as in this case, oxygen will be accumulated, creating a local maximum away from the flow inlets, and it will end up with an oxygen distribution pattern as shown in Figure 5.5(a) and (b).

From the oxygenation time course comparison between the two models, shown in Figure 5.6, the tissue oxygenation is generally found to be higher in the continuum model. For both models, curves for C2 rise up rapidly to reach an equilibrium state, dropping sharply as the flow blockage occurs, finally settling down to a new steady state. Apart from that, the tissue time courses at other monitoring points for the discretised model are very different from the continuum model.

For the discretised model, as shown in Figure 5.6(a), the oxygen level at M1 can show a increase, from 0.04 to 0.05mM after the S2 removal. At a higher oxygen level (in red), the corresponding contour, shown in Figure 5.5(b), covers a larger region than the previous one,

as shown in Figure 5.5(a), due to the flow redistribution after one source is removed. This implies that there is some local concentration increase in specific regions that benefit from the flow path and that there is haematocrit rearrangement in the vessel network even if the net oxygen input is reduced. Tissue oxygenation at M3 undergoes a transitional drop at around 40s, but the level rises up from 0.025 to 0.032mM, again after 200s. A similar time course for M4 can be found, apart from the drop from 0.018mM to 0.012mM at the second stage.

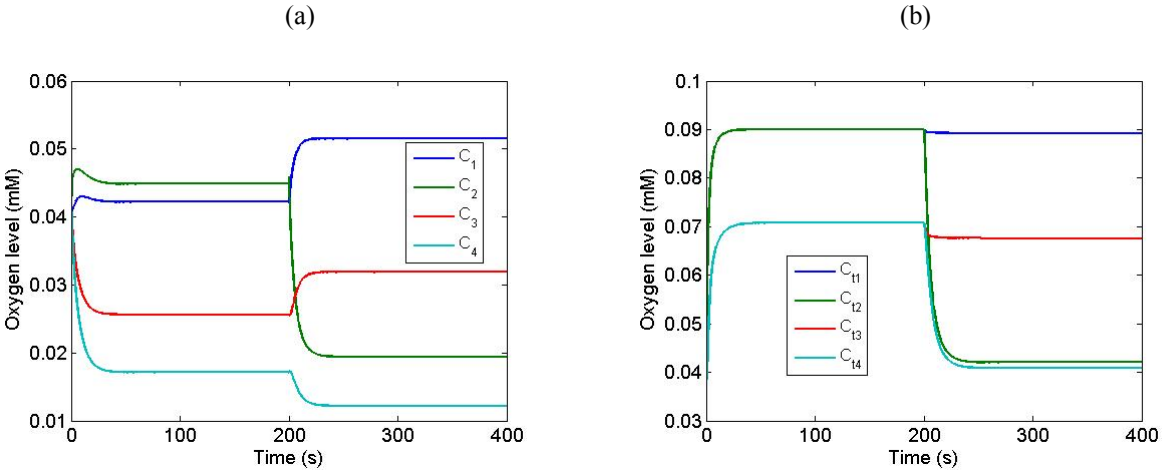


Figure 5.6 Time courses of the tissue oxygen level (C_1-C_4) at M1-M4 (a) for the discretised model; (b) for the continuum model.

Interestingly, like M2, the time course for M1 has an instant overshoot, which is due to the complex combinations of different time responses from the diffusion, the oxygen input from network and local consumption. This complex dynamic is explained as follows. The wall oxygen input around S1 and S2 increases immediately but consumption does not. At this moment, the oxygen tension is lifted up because the input overcomes the net efflux from diffusion and consumption. Later, the imbalance made by oxygen diffusion and consumption over the oxygen input tends to pull down the local oxygen, and hence creates the overshoot in the time courses.

In the oxygenation field predicted by the discretised model, it is commonly found that the inhomogeneous haematocrit distribution in the network causes oxygen spatial input pattern to tissues. The isolated distribution of the higher concentration lobes in the tissue oxygen field makes such diffusion responses more complicated in time as there may be more than one high level spot and the distances involved are likely to all be different.

5.5-2 Network variability test and model comparisons on flow

In the previous chapter, the influences of the constant and variable viscosity laws on flow pattern are investigated for a one particular network. However, the flow pattern variability amongst a set of networks is of very importance for clinical applications and will be addressed here. In addition, overall flow features predicted by the discretised flow model for 100 networks with two viscosity settings (geometric dependent viscosity as well as flow and geometric dependent viscosity laws) are compared to those predicted by a continuum model to check the degree of analogy. The influence of the network size on the overall flow behaviour will also be investigated since it is very important to know at what scale the continuum model can successfully be used to mimic the discretised models.

Flow features for the continuum model is presented first. Simulation results based on constant or variable haematocrit assumptions in the discretised models are introduced afterwards. Finally, the size effect on the flow pattern will be addressed. All of the three sets of simulations are run under the same conditions.

The simulations of continuum model are performed and the variations in flow across the four boundaries are illustrated in Figure 5.1. The pressure-flow relationship at boundary 1 is a 3D surface composed by 4 pure flat sub-planes corresponding to 4 groups of pressure conditions (positive and negative for both x and y). This surface is symmetrical for y pressure conditions

but not for *x* pressure conditions. Due to the isotropic assumption in the continuum model, there should be no difference in the flow between positive or negative gradients in *y*. Any change in *x* pressure drops just provide a different baseline for the total flow rate and the net flow is the superposition of the *x* and *y* pressure contributions. On the other hand, the *x* pressure drop is parallel to the flow at surface 1 and the flow rate baseline changes more sharply for a negative gradient than for a positive gradient in *x*. This means that the flow conductance varies according to its location, i.e. whether it is an inlet or outlet boundary relative to the corresponding pressure drop.

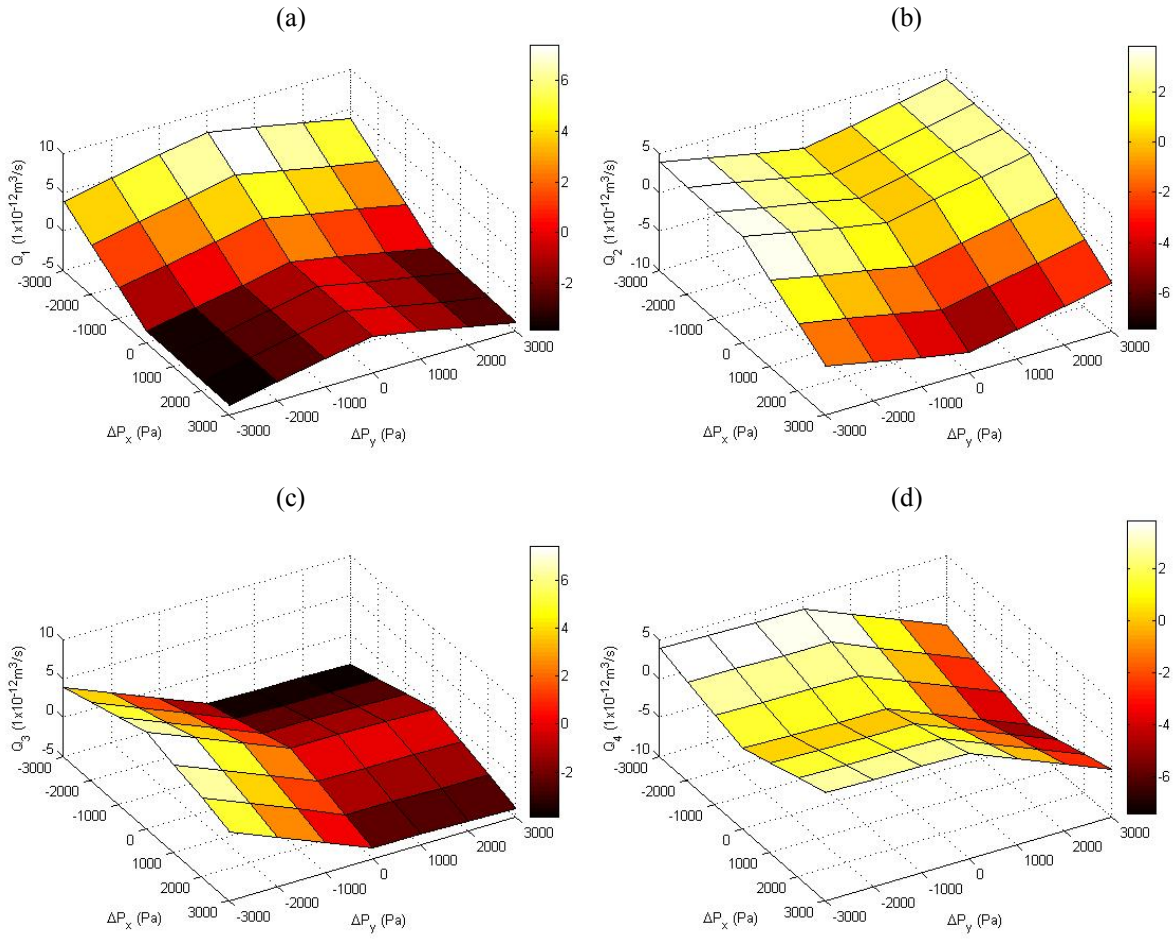


Figure 5.7. Flow-pressure plots in the continuum model for pressure drop in both *x* and *y* directions, showing total flow rate across surfaces: (a) surface 1; (b) surface 2; (c) surface 3; (d) surface 4.

The 3D surface in Figure 5.7(b) is simply a symmetrical version of the 3D surface in 5.7(a) due to the isotropic assumption of the medium when relative arrangements between the boundary locations and the pressure gradients of Q_2 are similar to Q_1. For instance, the fractional flow across surface 3 contributed by the positive *x* pressure drop should be equal to that at surface 4 contributed by the same pressure drop, but in the negative direction. The *x* pressure gradient provides the baseline patterns, along with the *y* gradient contribution, finally ending up with a set of symmetrical 3D surfaces related to those shown in Figure 5.7(a).

When the streamwise pressure drops are considered (i.e. $\Delta P_x < 0$), surface 1 becomes the inlet and the flow rate is thus the sum of the total flow passage. As pressure becomes positive, boundary 1 becomes the outlet, leading to a weak correlation with applied pressure. In the transverse directions, the sign of the *y* pressure gradients does not change the flow conductance, which means that the two cross conductance values are equally affected by the pressure conditions.

Figure 5.7(c) and (d) form a symmetrical pair just as do Figure 5.7(a) and (b) and the surface shown in 5.7(c) is simply replicated by twice mirroring the 3D surface in 5.6(d) through $\Delta P_x = 0$ and $\Delta P_y = 0$. This symmetric feature is due to the isotropic nature of the continuum model. The values of streamwise conductance and cross conductance can be obtained by taking the gradient of projection lines with respect to $\Delta P_y = 0$ and $\Delta P_x = 0$. For instance, the 3D surface is split into 2 sub-surfaces by the plane $\Delta P_y = 0$ and the average of the gradient of the left sub-surface is taken in Figure 5.7(c) and right sub-surface in Figure 5.7(d) to estimate the inlet conductance.

Outlet conductance is estimated from the other sub-surfaces in the same figure and likewise for the two cross conductance values in Figure 5.7(a) and (b). Data projections on $\Delta P_y = 0$ are also carried out for all four sub-plots in Figure 5.7 by splitting the surfaces at $\Delta P_x = 0$ to estimate the flow response to pressure conditions in *x* and the elements of the resulting flow conductance matrix are listed in Table 5.2. As a result, the flow can be decomposed into two elementary flow fields driven individually by its streamwise and transverse pressure drops.

Table 5.2. Values of flow conductance matrices for continuum models with dimension of $(400\mu m)^3$

Conductance	G_{in}	G_{out}	G_{cross}
$(10^{-15}$m/N-s)	2.476	0.088	1.194

A linear relationship between pressure drops and boundary flows is seen, just as in the continuum model. In this way, each element in the conductance matrix *G* can again be estimated by calculating the average slope of the lines obtained from projections of the pressure – flow plot. When the viscosity law dependence on the vessel dimensions is introduced into the discretised model, the overall flow behaviour becomes even more complex. Figure 5.8 shows in the same way as Figure 5.7 how the flow rate changes with the applied pressure drops for a discretised model under the assumption of constant discharge haematocrit. Each element in the conductance matrix for the discretised model is found to be independent of the pressure conditions, which means that the linear relationship is capable of approximating the flow dynamics even with the model accounting for a very complex network structure.

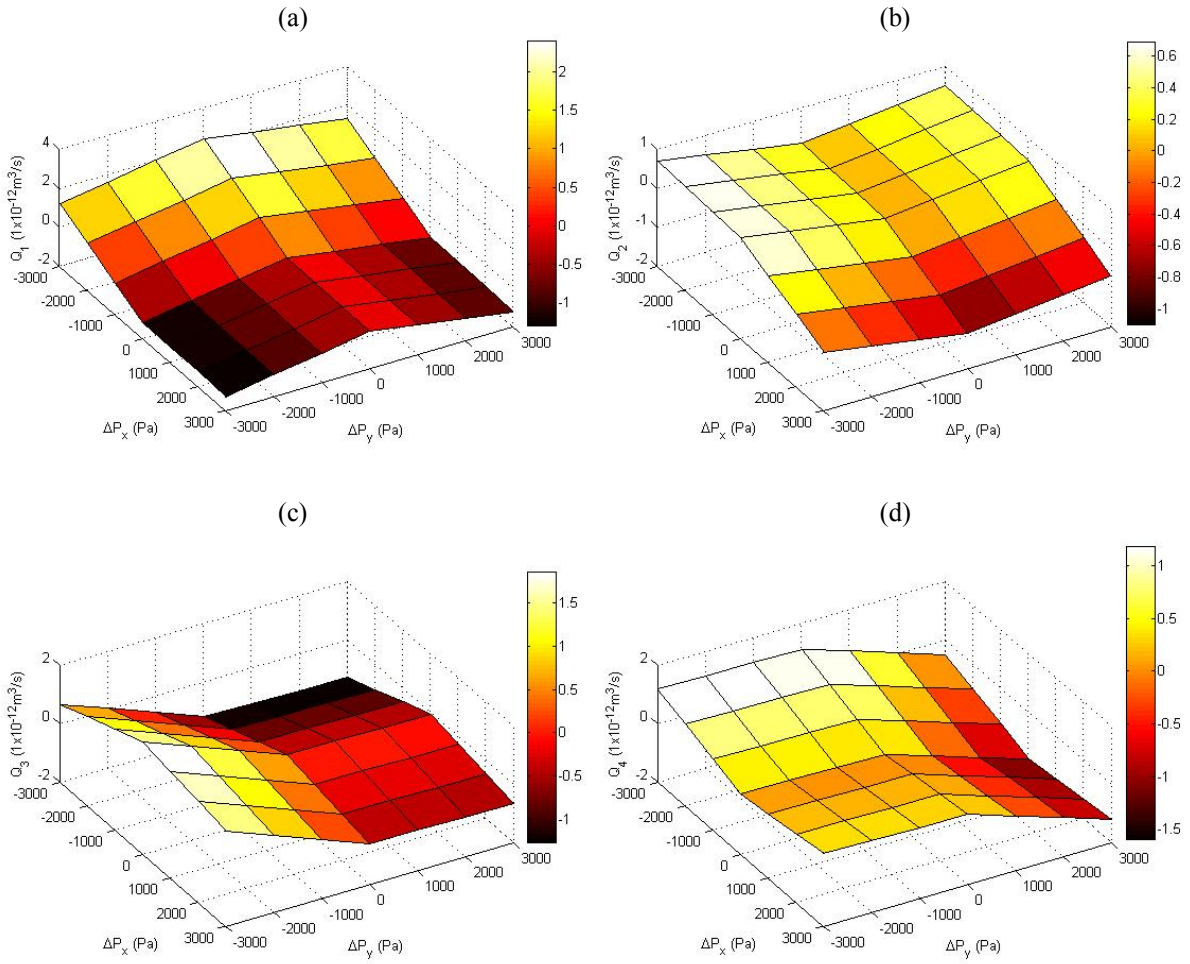


Figure 5.8. Flow-pressure plots in the discretised model with geometric dependent viscosity law for pressure drops in both *x* and *y* directions, showing total flow rate across surfaces: (a) surface 1; (b) surface 2; (c) surface 3; (d) surface 4.

However the flow symmetries found in the continuum model no longer exist in the network based flow model, as shown in Figure 5.8. For instance, the two sub-surfaces divided by plane $\Delta P_y = 0$ in Figure 5.8(a) are not quite symmetrical, suggesting that the *y* pressure gradient has a different contribution on flow rate at boundary 2 as the direction alters. Furthermore, the *z* scale in Figure 5.8(a) covers a larger range (2.4×10^{-12} m^3/s) than that in 5.8(b) (1.8×10^{-12} m^3/s), suggesting that the flow passages across these two boundaries are not necessarily similar when the symmetric pressure condition is applied. Furthermore, two opposite transverse pressure gradients no longer produce the same flow rates across a

boundary. This departure from symmetry is a common feature of the global flow patterns found in the discretised models.

Data projection to the plane $\Delta P_x = 0$ can also be made for Figure 5.8(c) and (d). In the isotropic case, the average slope of lines for the positive *y* gradient in Figure 5.7(c) is the same as that for the negative *y* gradient in Figure 5.7(d). As seen in Figure 5.8(c), the two slopes obtained from two sub-planes separated by $\Delta P_y = 0$ have different magnitudes. The flow conductance is then obtained by taking the average of the two different gradients from the corresponding parts of the sub-planes. As a result, the statistics for flow conductance values among 100 network flow patterns are shown in Table 5.3 in terms of the mean and standard deviation values.

As impact of both flow and geometry on the viscosity are now considered, the haematocrit partition is allowed to vary according to the local flow conditions at branches. During computations, the flow alters the haematocrit in most of the vessels, creating different flow patterns in the network compared with the case that only considers the network geometry. The haematocrit re-distribution in the network changes the flow patterns so much that, in most networks, some resulting data points in the pressure–flow plots no longer show a linear relationship.

The flow-pressure plots for the model with variable haematocrit, as shown in Figure 5.9, no longer exhibits the symmetric patterns seen in the continuum model case. As for the results in Figure 5.7 and Figure 5.8, the cross flow rate changes as the pressure gradient changes sign. In addition, the influences of the pressure gradients in *x* and *y* directions on the flow are sometimes quite different even if the boundaries and the pressure gradients have the same relative arrangement in space.

Despite the general similarities between both discretised models, the variable haematocrit case does introduce some degree of non-linearity to the global flow patterns. For instance, the sub-planes in 3D surfaces are not quite flat. As shown in Figure 5.9(a), there is a deviation from a perfect plane at around $(\Delta P_x, \Delta P_y) = (-3000, -1000)$ and these small perturbations are shown in most networks. The local flow field can change the blood cell flow patterns in daughter vessels, creating a diverse haematocrit distribution in the whole microvasculature, which can lead to higher or lower flow conductance values depending on the precise topology and geometry of the network.

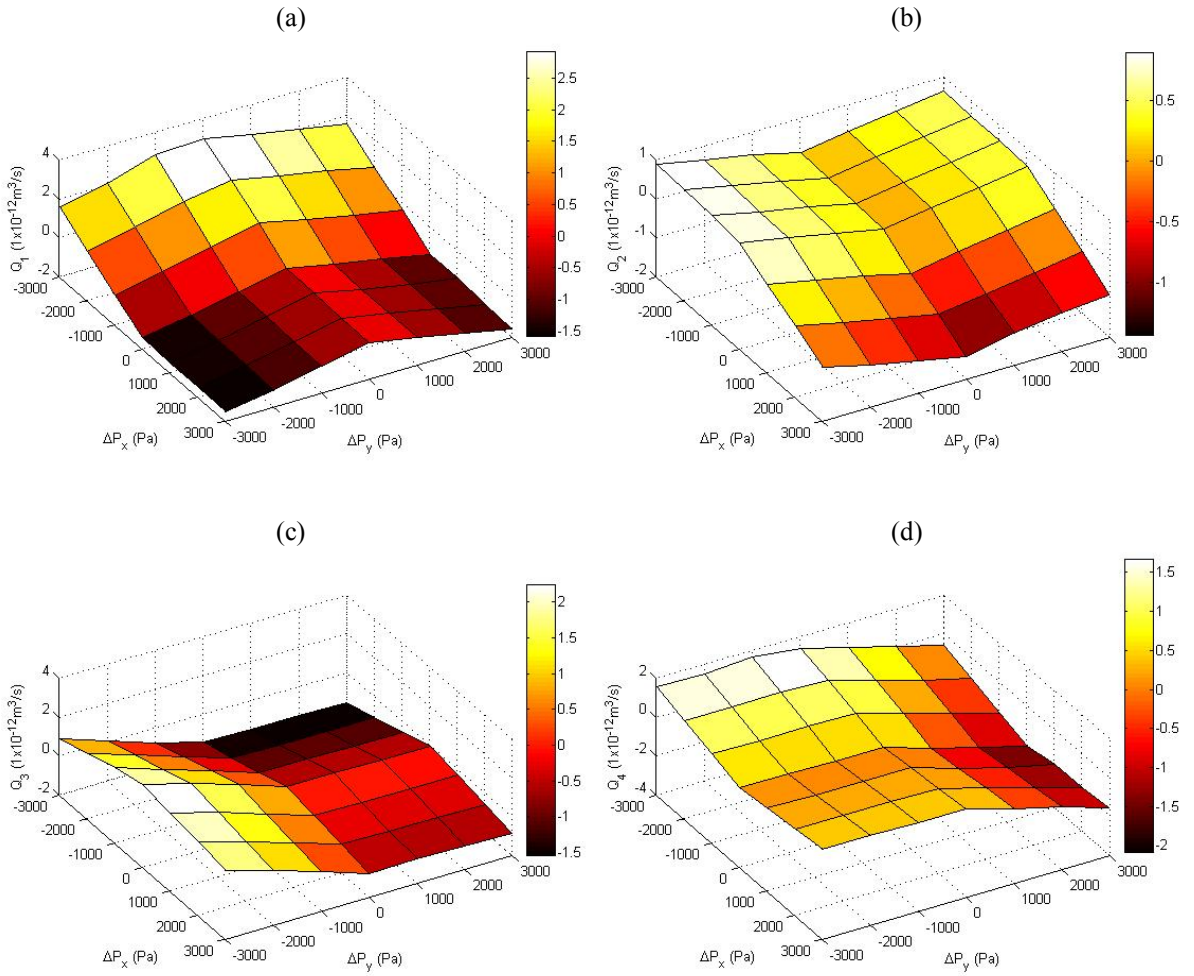


Figure 5.9 Flow-pressure plots in the discretised model with both flow and geometry dependent viscosity law for pressure drops in both *x* and *y* directions, showing total flow rate across surfaces: (a) surface 1; (b) surface 2; (c) surface 3; (d) surface 4.

As shown in Table 5.3, in the direction of the pressure gradient, the conductance element at the high pressure surface is the largest, followed by the two transverse elements, and the element at the low pressure surfaces is the smallest. For constant haematocrit cases, the mean values give almost symmetrical patterns in cross conductance values $G_{cross1} \cong G_{cross2}$, and there is almost no difference between the corresponding values in the column vector for *x* and *y* (i.e. $G_{xin} \cong G_{yin}$ and $G_{xcross1} \cong G_{ycross1}$). The standard deviation is quite large, with values ranging from about 30%-90% of the mean values for G_{xout} and G_{xcross} respectively, suggesting that the flow conductance values at the surfaces show a high degree of variation from one network to another.

Table 5.3 Statistics for flow conductance matrices of discretised models of size $(400\mu m)^3$

	Constant haematocrit (10^{-15}m/Ns)	Variable haematocrit (10^{-15} m/Ns)
G_{xin}	0.978±0.536	1.354±0.786
G_{xout}	0.032±0.015	0.044±0.029
$G_{xcross1}$	0.448±0.315	0.666±0.608
$G_{xcross2}$	0.499±0.449	0.650±0.566
$G_{ycross1}$	0.448±0.315	0.669±0.607
$G_{ycross2}$	0.499±0.449	0.654±0.574
G_{yin}	0.979±0.538	1.353±0.796
G_{yout}	0.032±0.012	0.032±0.018

In the model accounting for the haematocrit variations, the flow conductances are similar to the constant haematocrit case, but their values are larger by a factor of 1.3-1.6. However, the mean cross conductance values among the 100 samples are very similar in both the *x* and *y* directions and the same similarities in the mean values of corresponding elements in *x* and *y* columns are also found. Such *x*-*y* symmetries are common statistical features for both cases despite the discrepancy between G_{xout} and G_{yout} in the variable haematocrit cases. This departure from the symmetry may caused by the non-linearity introduced by the viscosity law as the flow-pressure relationship cannot be characterised simply by a constant matrix.

For both discretised models, if the data in table 5.3 are further processed by taking the average of corresponding mean values of inlet, outlet, and cross conductances, the resulting values can be directly compared to those obtained from the continuum model. As shown in table 5.4, the fractions of the conductance between the two discretised models are fairly close, whose differences are only 0.1% and 0.4% for the cross and outlet conductances respectively. The relative differences between the discretised and continuum models are small enough (0.5% by maximum). Taken together, these results imply that the network flow passage can be decomposed into a mean flow field due to an isotropic porous medium flow, and a random flow field with local large variations.

Table 5.4 Averaged values of flow conductance matrices for continuum models and two discretised model with dimension of $(400\mu m)^3$

Conductance $(10^{-15}$m/N-s)	G_{in} (fraction)	G_{out} (fraction)	G_{cross} (fraction)
Continuum model $\mu = \mu_b$	2.476 (100%)	0.088 (3.4%)	1.194 (48.2%)
Discretised model $\mu = f(D)$	0.978 (100%)	0.032 (3.3%)	0.475 (48.5%)
Discretised model $\mu = f(H, D)$	1.354 (100%)	0.038 (2.9%)	0.669 (48.6%)

The values in the conductance matrix in the variable haematocrit setting are about 1.3-1.5 fold higher than those in the constant haematocrit case, implying that the blood, in general, passes more easily in the network with variable haematocrit. Since haematocrit plays a crucial role in the flow patterns, the distribution of discharge haematocrit is a simple way to show the flow variability caused by the network structure differences. The distribution curve, shown in Figure 5.10, has a local peak with a value of about 15% in the region with values of haematocrit less than 0.1 and a plateau ranged from 0.1-0.4 at about 10%. As the haematocrit increases, the fraction rises up again at 0.4-0.5 and finally decays with increasing haematocrit. In fact, the discharge haematocrit for 65% of vessels is less than 0.5, and about 15% of vessels have a discharge haematocrit less than 0.1. This two-peaked distribution with a lower average haematocrit gives higher average flow conductance values than in the cases where vessel haematocrit is uniformly set at 0.5.

In Fig.5.10 (b is the new figure taken from other simulation study; see p.158), the frequency distribution of the haematocrit is qualitatively to that obtained by other simulation as both share a two peaked curve. The mismatch lies in the high haematocrit modes where these frequencies in our prediction is higher, which is likely to be caused by the use of two haematocrit distribution relationships for different branch geometries at nodes. The network model based on observations of primate cerebral tissue used in other simulation has only bifurcations and hence only one cell partition relationship (Eq.4-7-4-10) is used. Our artificial network has few trifurcations and thus a second cell partition relationship (Eq.4-11) is required, leading to the discrepancy. If a new empirical relationship becomes available, the over-estimation at high haematocrit mode will then be improved

(a) (b)

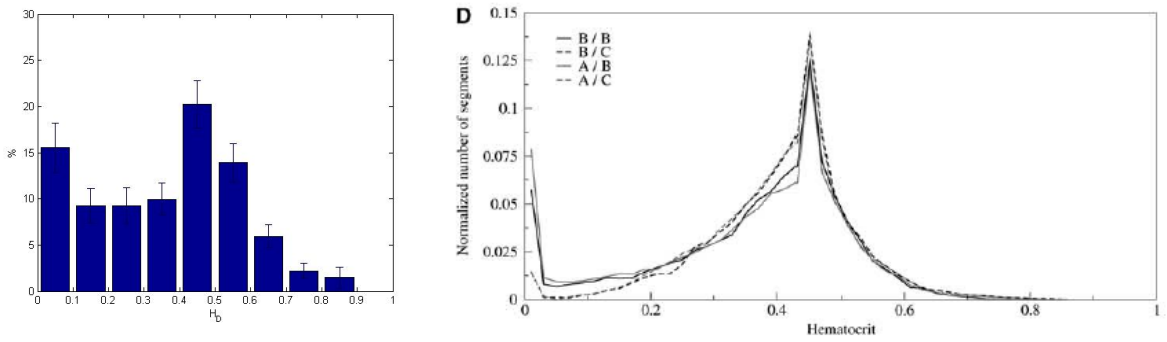


Figure 5.10. Histograms of the discharge haematocrit distribution;(a) in the 100 microvascular networks in variable haematocrit cases; (b) in other blood flow simulations in the primate cerebral network model (Guibert, Fonta, Plouraboue 2010).

Unlike in the continuum model, the influences of the *x* and *y* pressure gradients on the flow patterns are not always identical for flow patterns in individual networks. In the flow conductance matrix, the elements in column for *x* should be very close to their counterparts in the column related to *y* pressure conditions and the two cross conductance values should be very close if the flow patterns show little preference for any particular direction. In each network, it appears that for both discretised models, the two cross conductance values are not close and the elements in conductance related to *x* are not always similar to their counterparts related to *y*. These anisotropic flow patterns seem to be mainly caused by the occasional creation of very short vessels connecting high pressure surfaces with a nearby transverse surface, thus substantially enhancing the flow transport.

Since the proposed network creation method is statistically based, the flow pattern show randomness due to the potentially high dependence on the individual network structure. The size of the sample network, in addition, is found to play a role on the overall flow variations. As shown in Figure 5.11, the fractional conductance difference ($\Delta G_{xy} = 2\left|G_{xin} - G_{yin}\right| / \left|G_{xin} + G_{yin}\right|$) provides a quantitative measure of the flow pattern deviations from symmetrical flow, caused by directional preferences between the *x* and *y*

pressure drops. The 95% data scatter band for the network size $(200\mu m)^3$ is about 0.2 and 0.17 but it tends to decay as the networks become larger, finally narrowing down to the width valued less than 0.07 and 0.07 for the constant and variable haematocrit cases respectively. Based on these results, the enlargement of the network appears to reduce the fractional conductance differences between *x* and *y* directions. In other words, the net flow passage into the network would be indistinguishable whether it is driven by *x* and *y* pressure drops as long as the network is large enough

(a) (b)

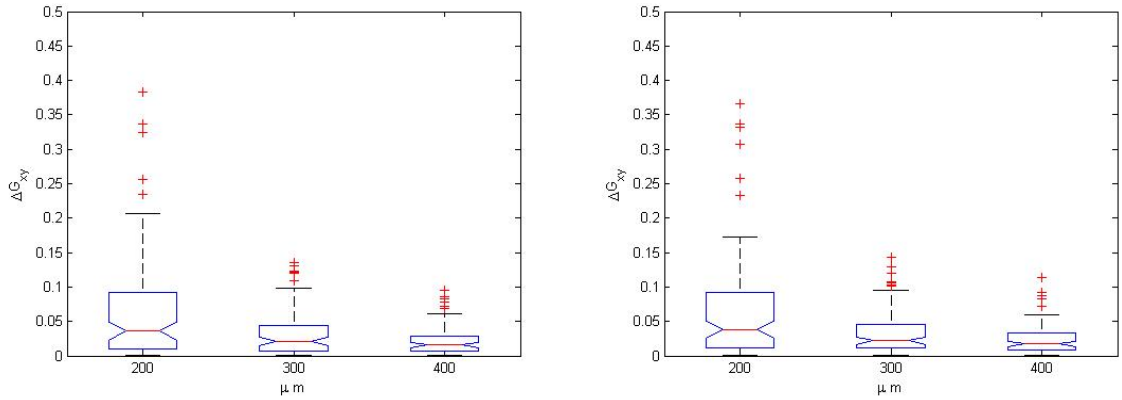


Figure 5.11. Differences between *x* and *y* gradient influences on flow patterns in varying sizes of networks for the viscosity settings (a) constant haematocrit (geometry dependent); (b) variable haematocrit (geometry and flow dependent).

A variety of asymmetries in cross conductance values are observed among the 100 sample networks. In Figure 5.12, the fractional differences for cross conductance values, defined by $\Delta G_{cross} = \left| G_{cross1} - G_{cross2} \right| / G_{in}$, for both the *x* and *y* pressure gradients as shown in Figure 5.12(a) and 5.12(c) for the fixed haematocrit case; both having values of less than 0.6 for most sample networks in the size of $(200\mu m)^3$ with a median value at around 0.35. For both viscosity settings, as the network size increases, for both *x* and *y* directions, the median fractional difference drops from around 0.35 through 0.27 to 0.23, showing a decreasing

trend with the network size. Again the average differences in fractional cross conductance values between the two discretised models are small.

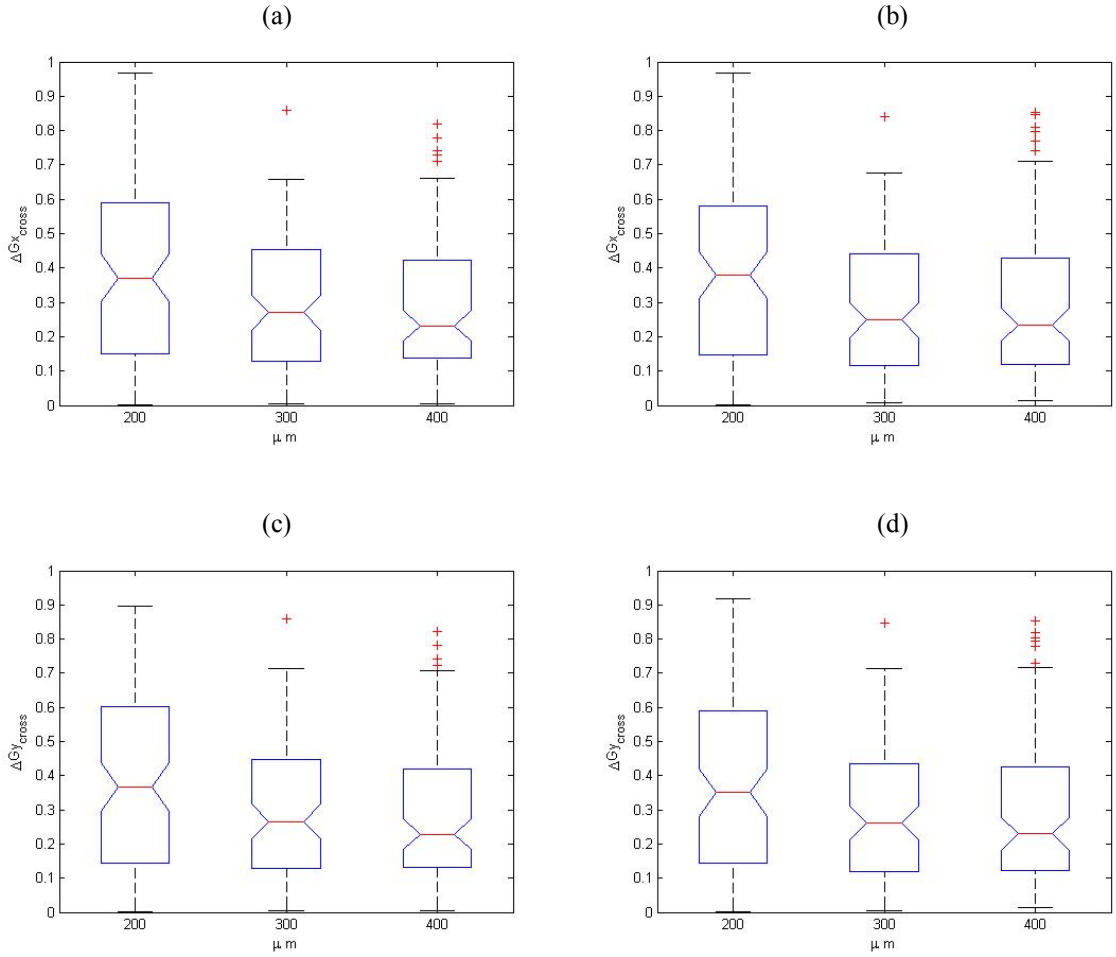


Figure 5.12. Differences in cross conductance from *x* and *y* pressure gradients (1st and 2nd rows respectively) in varying sizes of networks for two viscosity settings (1st and 2nd columns respectively): (a) (c) constant haematocrit (geometry dependent); (b) (d) variable haematocrit (geometry and flow dependent).

The randomly directed flow preferences exist differently in different networks, but both asymmetric indicators, the differences in cross conductance values and in inlet conductance values, are found to decrease with the network size. This suggests that the anisotropic nature of the flow behaviours in complex vessel networks is a key feature. The flow in a discretised

model can approach an isotropic medium flow only if the sample network size is much larger than the size of the network considered here. All of these asymmetric flow features are caused by the heterogeneous structures of the network, reflecting the strong flow dependence on the network architecture at this small length scale.

To link the two network-based transport models directly to the continuum model, an effective permeability is now introduced. The effective permeability κ_{DM} for a flow embedded in the network is estimated by finding the optimal scaling parameter s which minimizes the L2 norm error $\| \mathbf{G}_{CM} - s\mathbf{G}_{DM} \|$ between the conductance matrices of the continuum and the discretised models. The effective permeability is estimated according to $\kappa_{DM} = \kappa_{CM} / s$ and the relative permeability κ_{rel} $(\kappa_{DM} / \kappa_{CM})$ then obtained for comparison.

Figure 5.13 shows the distribution of the relative permeability of the media in both viscosity settings with different network sizes. Generally, the relative permeability is found to be less than 2, except for a very few extreme examples, which are not shown here for plot clarity. For the model with variable haematocrit, the statistical variations are larger than those in the model where the haematocrit is held constant. When the network size expands from a $(200\mu m)^3$ to $(300\mu m)^3$ cube, the data points seem to concentrate in a narrower range of the effective permeability. As the network size expands further to the $(400\mu m)^3$ cubes, the distribution of data points, however, remains close to that of the $(300\mu m)^3$ cubes.

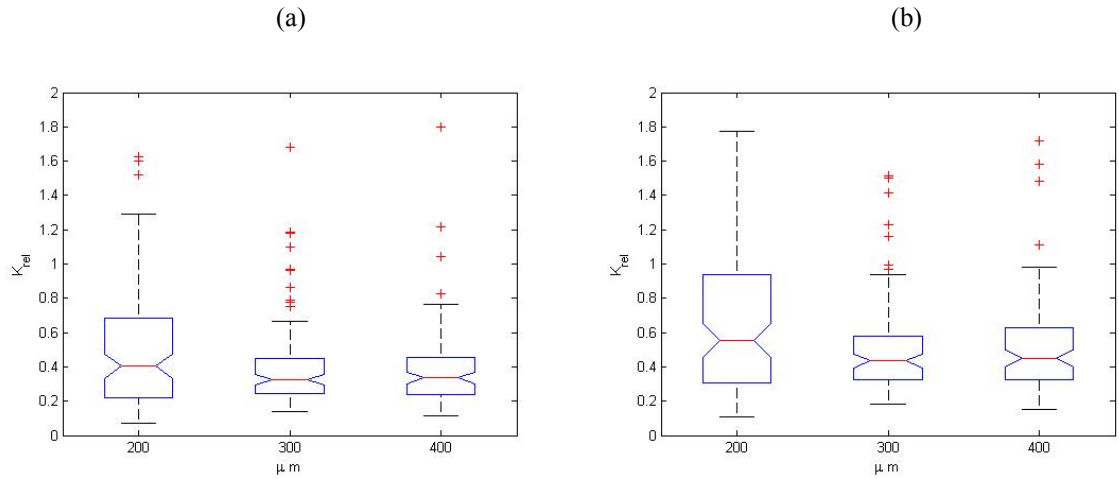


Figure 5.13. Relative permeability in the network with sizes of $(200\mu m)^3$, $(300\mu m)^3$ and $(400\mu m)^3$ for the two viscosity law: (a) constant haematocrit (geometry) and (b) variable haematocrit (geometry and flow).

For the model with variable haematocrit, the 95% data scatter bands are wider than those in constant haematocrit cases, with ratio ranges of (0.11-1.78), (0.21-0.96) and (0.17-1.02) respectively in their respective magnitudes for the three different network sizes. In the constant haematocrit cases, the ratio bands are (0.83-1.36), (0.15-0.68) and (0.13-0.78) for the network size $(200\mu m)^3$, $(300\mu m)^3$ and $(400\mu m)^3$ respectively. Compared to the variable haematocrit case, the scattering bands are narrower, indicating the dependence of the flow variations on the haematocrit distributions. The wider data scatter bands in the variable haematocrit cases may be affected by two factors. It can be attributed to the higher flow heterogeneities in different sample networks caused by the nonlinear viscosity settings. On the other hand, most of the high relative permeability values for flow in individual networks may also amplify the data scatter effects.

The stochastic network creation introduces heterogeneities in topological and geometrical structures for the flow paths, as expected, leading to deviations from the isotropic flow patterns found in the continuum case. The flow patterns in the models with the two viscosity settings are similar in terms of asymmetrical behaviour. However, flow passage in the

network seems to be easier in the variable haematocrit cases because of the larger effective tissue permeability. The interactions between the local flow and vessel viscosity lead to the two peaked distribution for haematocrit, and most vessels are populated in the region with values less than 0.5. As a result, the sample averaged relative permeability in the variable haematocrit case is generally higher than that found in the constant haematocrit cases.

5.5-3 Network variability test and model comparisons on flow/oxygenation

In the previous section, the impact of network variability on the flow patterns has been investigated, and the simulation results show that the flow patterns vary from one network to another in terms of the detailed flow maps and the overall flow features. Whether the variability of the network structure has a similar influence on the oxygen transport, through the interaction between the tissue oxygen extraction and network oxygen distribution is also of importance. Flow and oxygen transport simulations are thus performed for a set of random networks with assumptions of variable haematocrit and sigmoid saturation curve. Here, flow/mass transport simulations for only 10 different networks are performed because the computation time of oxygen transport calculation is much longer than the flow calculation. Two flow sources and sinks located at the same sites as in Chapter 4 are applied with pressures 3000Pa and 1000Pa respectively and simulations are run using the same settings for initial and boundary conditions used in Chapter 4.3-3.

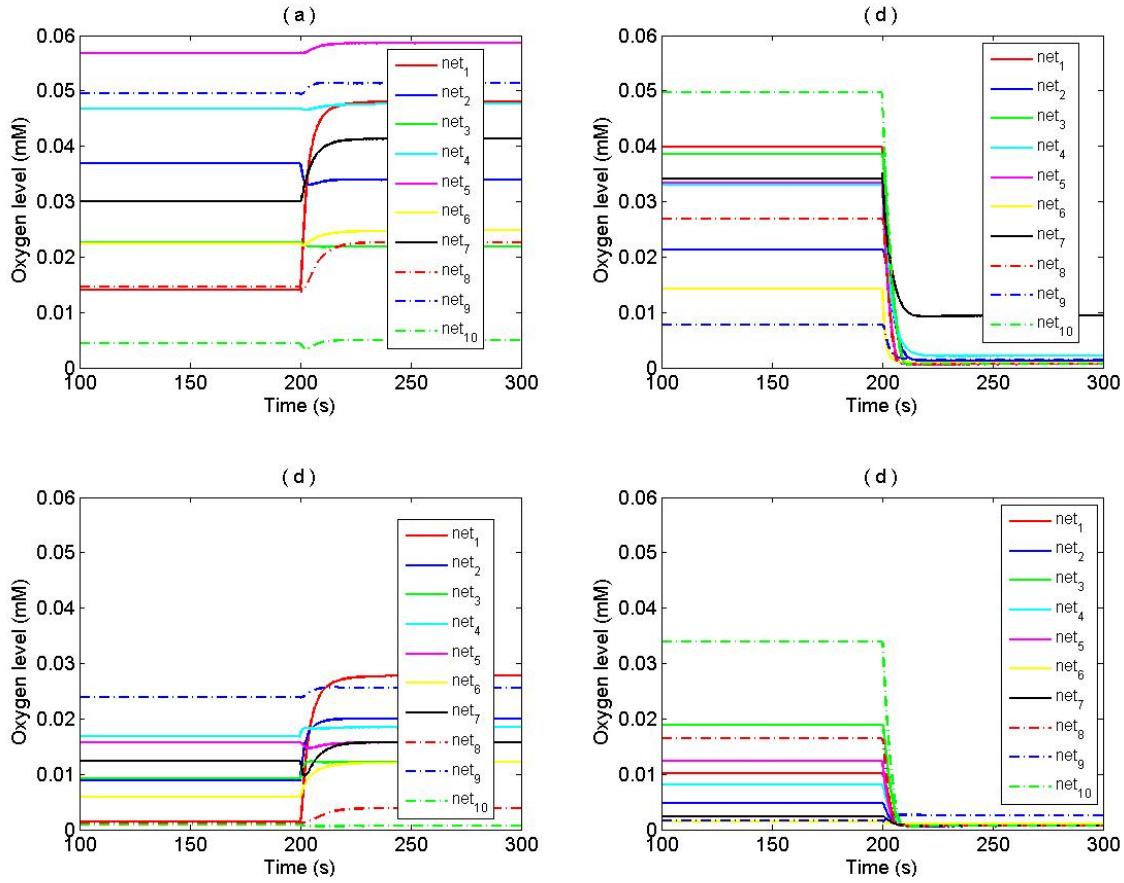


Figure 5.14 The time courses of tissue oxygen concentration for 10 networks are recorded at different monitor sites (a) at M1; (b) M2; (c) M3; (d) M4.

Although M1 and M2 have the same spatial arrangements relative to S1 and S2, and the inlet/outlet conditions are set to be the same before S2 removal, their time courses turn out to be very different. In Figure 5.14(a) and (b), the difference in the first part of the time course for each network is large, ranging from 0.08 to 0.45mM, and this asymmetry can also seen in the time courses before 200s for M3 and M4. The flow patterns are strongly affected by the irregular network distributions even when the flow conditions are applied symmetrically. For each network, the resulting spatial variations in local oxygen extraction from vessels create very asymmetric contours of oxygen level in tissue space, and hence very different time courses are found at two symmetrically located monitoring sites in the tissue.

The time courses vary a great deal between different networks, but a common trend during the transition at around 200s is easily spotted. There is, in general, an oxygen level increase at M1 and M3, despite the decreases shown in networks 2 and 3, and the fact that not all transitions are monotonic rises. On the other hand, the time courses at M2 and M4, in most cases, have a decrease in response to the source turn-off. The oxygen responses at different sites are influenced by the flow territory being sustained by the relevant source-sink pairs.

The spatial averages of the tissue oxygen tension for those tissue samples are illustrated in Figure 5.15, which aims to characterise the overall dynamics of tissue oxygen transport in a simple manner. In Figure 5-15(a), a variety of time courses are expected since the information here is the sum of the dynamic responses of all voxels in the tissue cube, four of which have been proved to be highly affected by the network variations in terms of the geometric and topological structures.

(a) (b)

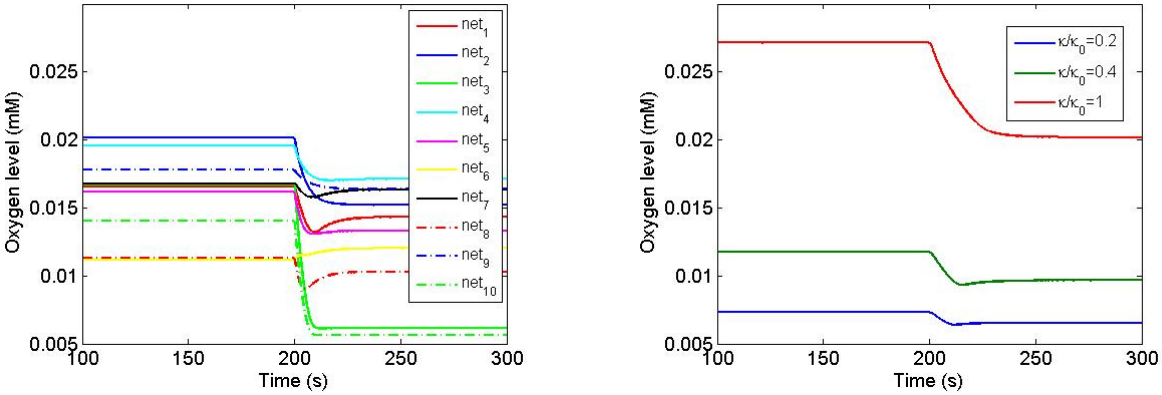


Figure 5.15 The time courses of spatial averaged tissue oxygen concentration: (a) for 10 networks; (b) for 3 media with different values of effective hydraulic conductivity.

The flow shortage, although resulting in local oxygen rises at some sites, overall reduces the total oxygen flux from network to tissue, leading to a drop in the tissue oxygenation. This transition due to the source removal is not necessarily monotonic and sometimes a slight

undershoot can be found in the time courses, e.g. networks 1, 6 and 8, depending on the network distribution patterns. Despite these variations in transient dynamics, the tissue oxygen level in general has an increase, and then a rapid drop to a lower oxygen level due to the flow shortage. This gives a general pattern for overall oxygen responses to the flow shortage when the discretised model is applied to describe the network/tissue interactions in flow and oxygen transport.

For comparison, three continuum models, with different values of effective permeability, are tested to check their capability to mimic the network based model in the overall scale oxygen transport dynamics. Based on the results shown in both the first section and here it is found that the continuum model, with the baseline value of effective permeability used so far, would over-estimate the tissue oxygen level. As shown in Figure 5.15(b), if the effective permeability is set lower, with values ranged from 0.2 and 1 of the baseline value, most of the time courses obtained from the discretised models are found to lie in the band formed by these two curves. In other words, the band provides a match to the overall tissue time responses to most of the networks presented here. The continuum model appears to give very good estimations for the lower and upper bound curves to the time courses predicted by the discretised models.

As discussed earlier, for the overall flow features a match can also be made between the continuum and discretised models if the effective permeability is adjusted. As shown in Figure 5.13 (b), 95% of networks have an effective permeability with values ranged between 0.15 and 0.93 relative to the baseline values used in the continuum model. This band is quite comparable to the values of 0.2-1.0 estimated from the comparisons for the tissue oxygen responses, implying that the overall oxygen transport is highly flow dependent. Once the

network flow is well characterised through the porous model, dynamics of the tissue oxygen transport can be resolved properly.

This comparison further implies that the continuum model is able to approximate the discretised model not only in terms of the flow behaviour but also the oxygen transport dynamics obtained as long as the effective hydraulic conductivity for the networks is well estimated. However, the discretised model can resolve the detailed variations in tissue dynamics due to network variability, which cannot be resolved by the continuum approximation.

5.6. Discussion

A discrete model and a continuum model are both presented here to simulate flow and oxygen transport in a small volume of brain tissue. The discrete model considers the detailed network information, capturing the individual flow patterns, and creates a non-homogenous oxygen flux input pattern to the tissue. Some oxygen transport features, such as local maxima in the oxygen levels caused by flow heterogeneity can only be identified by this model. This is due to its capability to model the individual flow patterns and their influence on the tissue. A detailed pattern for oxygen transvascular exchange can thus be obtained, and hence localised oxygenation can be resolved in detail.

On the other hand, with a better resolution in the oxygen extraction patterns, some subtle changes in the time courses , e.g. overshoot or undershoot, can therefore be captured by the discretised model. In particular, the local oxygen input from the network, diffusion from surrounding tissue, and the local consumption may have different time characteristics in response to the flow shut off, and all these differences can be larger if their spatial distribution patterns have locally high gradients. Unlike the geometric symmetry of contours

found in the continuum model, due to the irregular oxygen transport in the vessel networks, there is only weak symmetry seen in the oxygen contours in the discrete model. This flow induced asymmetry may result from spatial variations in the network structure, which also affect the flow and haematocrit distribution in the network and thereby the mass transport patterns in both blood and tissue.

The significance of the flow source can be found in the present models for mass transport in brain tissue. In both models, it can be found that blood convection is unable to sustain the tissue demand after S2 removal, and this creates an oxygen deprived zone in the downstream region. The continuum model can capture this transition, although the resulting oxygen field has higher values than those in the discretised model. The oxygen level distribution is fairly homogenous whilst some irregular, even isolated, contours can be found in the oxygen field predicted by the discretised model. This homogenous distribution pattern is one of the common features for the continuum model, since vessel variability has been smoothed out.

In all, the continuum model can capture basic mass transport patterns as does the discrete model as steady state time profiles at four monitoring sites are similar for these two models. The tissue oxygenation distributions for both models are qualitatively close as the oxygenation change after the S2 removal, from having two major contours to only one, can be fairly captured. It can be anticipated that the predictions of both models will become closer if the network used in the discretised model is in a regular connection pattern. Localised features such as asymmetry of the contours and perturbations of the tissue dynamics, which are due to network variability, cannot be resolved through the continuum model.

To further investigate the effects of network viability on flow patterns, two viscosity laws, geometry dependent and both flow and geometry dependent laws, are adopted in the

discretised flow model. Flow features at a global scale are measured by summing up all flow at vessels across boundaries. Despite some small perturbations in the pressure–flow isoplots for the model with flow-geometry dependent setting, these global flow characteristics show that the flow field usually behaves as a linear system for both viscosity laws. Small differences between these two viscosity settings are found in the overall pressure-flow relationship, suggesting that the nonlinearities still play a role in the global flow behaviour in terms of increasing the effect of the network variability.

The asymmetries have been measured by two indicators, the *x*-*y* conductance differences and the cross conductance differences. They both exhibit a certain level of statistical variation within different networks, indicating heterogeneity in flow patterns. However, as the network size expands, these differences resulting from the network structure asymmetry gradually reduce. A fundamental question is how large a network is required to smear out the local flow variations to give a roughly isotropic flow in a global sense. Further flow computations in larger networks will be required to check if the flow in the network approaches an isotropic porous media as the network size is increased.

For grey matter, no direct experimental measurement of the hydraulic conductivity has been made, relevant values ranging from $1\times10^{-14}m^4/N\cdot s$ to $1\times10^{-12}m^4/N\cdot s$, have been adopted by other theoretical studies (Netti and others 1995) (Linninger and others 2008) (Chen and Sarntinoranont 2007). The hydraulic conductivity is used to estimate the interstitial fluid passage through flow channels in the interstitial space but not the blood flow in brain tissue.

The hydraulic conductivity for the microvascular network, used in the continuum model, is taken to be the upper limit value of the tissue hydraulic conductivity ($1\times10^{-12}m^4/N\cdot s$) for interstitial flow channels, which is not based on a physiological evidence but a rough estimation. On the other hand, through the flow model analysis for 100 networks, the

resulting effective permeability κ of each network (estimated through $h = \kappa / \mu$), the minimum and maximum of the effective permeability ratios (κ_{rel} ($\kappa_{DM} / \kappa_{CM}$)) are found to be 0.1 to1.8 respectively. This however, suggests that the current estimation of the baseline values for effective permeability and hence for hydraulic conductivity used in present continuum model, is a reasonable estimate.

For one network, the vessel distribution can produce asymmetric local flow patterns even if the flow conditions are applied at symmetric locations. In addition, this heterogeneity brings unevenness in the oxygen distributions in the network, creating irregular oxygen extraction patterns for tissue. As a result, the tissue oxygen level does not present a smooth contour but several high level spots are found to be located separately in the tissue, suggesting that the tissue oxygen may have a non-monotonic distribution at such a small length scale.

Variability amongst networks resulting in variations of network structure, of flow pattern and thereby of the oxygen distribution, which in turn lead to unevenly distributed oxygen extractions in tissue and the resulting tissue oxygen fields. The discretised model can faithfully demonstrate how the individual vessel influences the flow and oxygen transport patterns in the tissue and the variations amongst each different network.

The local features in flow or transport patterns being predicted by the discretised model cannot be replicated by the continuum model presented here. However, the overall distribution features can still be captured by the continuum model. In particular, the time response for the whole cube, predicted by both models, can also be well matched when the effective hydraulic conductivity for flow passage in the microvascular network is well estimated.

Consequently, the continuum model presented here can easily be scaled up for larger sized simulations for blood and oxygen transport in the brain microvascular bed, since some crucial parameters required in this model, such as the effective wall area of transvascular exchange, tissue porosity, and the effective hydraulic conductivity, can be obtained by the analysis of the network structure.

It should be noted here the tissue oxygenation computation by the continuum model was executed, using a grid of 40×40×40 elements, for 40,000 timesteps ($\Delta t = 0.01$s), on a computer with Intel Core 2 6420 CPU, on a single core and with 2G bytes of memory. The execution was completed in 20 hours in Windows XP environment.

5.7 Conclusion

A porous media model is proposed here to describe the network blood flow and oxygen transport in a continuum manner. Tissue oxygenation in the continuum model is found to exhibit more regular and symmetric patterns in space than in the discretised model. Statistical comparisons in flow behaviour between the continuum model and discretised models show that an isotropic and homogenous porous media flow model can be used to replicate the flow pattern inside complex vessel network systems if the network size is large enough. Variations in the oxygen distributions patterns for the discretised model are also notable in the local and the global scale but the overall scale differences can be captured by the continuum model through tuning of the value of hydraulic conductivity. Conversion of the network information into some lumped parameters required in the continuum model is feasible, allowing for scale-up of the network model to a tissue level. In addition, this scale-up can characterise the network variability through adjustment of these lumped parameters.

Chapter 6 Filtration and interstitial pressure

6.1 Introduction

As postulated by the Monro-Kellie doctrine, the cranium is essentially rigid so that the total volume of the brain should be a constant, hence the sum of volume in the vasculature, tissue and cerebrospinal fluid (CSF) should remain constant. Any increases in the volumes of these compartments will cause compression in the rest, building up the pressure in the interstitial space which is known as intracranial pressure (ICP) in the intracranial space of brain. Inadequate volume expansion of the intracranial element is usually accompanied by an enormous increase in the vessel filtration rate in many pathological states of brain tissue, one of which is known as vasogenic edema after traumatic brain injury (Unterberg and others 2004).

Therefore, fluid exchange between blood and interstitial fluid (ISF) plays an important role in regulating fluid volume in the interstitial space and hence the intracranial pressure. Once the interstitial pressure is elevated to a higher level, the transmural pressure across the capillary wall may become negative, leading to a condition in favour of vessel collapse.

The filtration model will be introduced first and coupled to three sets of interstitium equations for pressure. In this way, three resultant models, namely the lumped, network based and continuum models will be proposed here to investigate the interaction between the abnormal filtration and the elevation of interstitial pressure, and to find a possible mechanism underlying the vessel collapse events found in post ischemia reperfusion experiments.

6.2 Filtration equation

Fluid exchange between blood and interstitial fluid (ISF) was described by the Starling equation, which originated from the thermodynamic analysis of transport across a thin

membrane under conditions of minimum Gibbs energy in the thin film system. This equation states that the transvascular flow flux is influenced by two driving forces, the capillary hydraulic pressure drop across the vessel wall and the osmotic pressure offset caused by the transvascular concentration difference of the osmotic active solutes. Transvascular water exchange thus follows Starling's equation:

$$J_{VA} = L_P\left[\Delta P - \sigma\Delta\Pi\right], \tag{6-1}$$

where J_{VA} is the filtration flux of the capillary wall (m/s), L_P is the wall hydraulic permeability of the capillary and ΔP is the hydraulic pressure difference between plasma and ISF. The solute concentrations in the blood and ISF affect the osmotic pressure drop, $\Delta\Pi$, across the vessel wall regulated by reflection coefficient σ. An increase in the transmural pressure or a decrease in the osmotic pressure drop tends to pump more water into the interstitial space. Under physiological conditions, this flux is quite small because these two opposite terms are tightly balanced.

For most tissues, the capillary wall cannot completely filtrate certain molecules and the leakage tendency for one particular solute into the ISF is expressed by the osmotic reflection coefficient, σ, which ranges between 0 and 1. For example, $\sigma = 1$ stands for 100% wall reflection for the solute, in other words, no solute can enter the tissue space whereas a solute with coefficient $\sigma = 0$ can freely pass the membrane and is not osmotically active.

Since there is a variety of water soluble molecules, such as Na^+, K^+ and other ions in blood plasma and the ISF, the osmotic pressure force is thus the summation of all contributions of osmotic active solutes ($\sigma < 1$). Eq.6-1 is thus re-written as:

$$J_{VA} = L_p \left[\Delta P - \sum_n (\sigma \Delta \Pi)_n \right]. \tag{6-2}$$

In general, the vessel wall is relatively permeable to small molecules (σ <0.1) but impermeable to large molecules, which creates significant concentration drops across the microvessel wall. Since the majority of the hydrophilic macromolecules are plasma proteins, the osmotic pressures are mainly induced by the difference in plasma protein concentration across the vessel membrane. Eq.6-2 can be further expressed as:

$$J_{VA} = L_p \left[(P_c - P_i) - \sum_n (\sigma (\Pi_c - \Pi_i))_n \right], \tag{6-3}$$

where P_c and P_i are the hydrostatic pressures in the capillary and interstitial space respectively and similarly for osmotic pressure at both sides. The osmotic pressure is a function of the protein concentration. The ISF protein concentration C_i is not a fixed value, but is dynamically and locally adjusted depending on the ratio of solute flow to water flow ($C_i = J_S / J_V$) (Levick and Michel 2010). This condition holds when steady state has been reached and the concentration is very close to the ratio of volume flow rate between solute and water. With such a direct link between ISF interstitial protein concentration, C_i, and plasma protein concentration, C_c, this can be used to generate an expression for osmotic pressure, Π_i, in terms of Π_c, the detailed derivation of which is presented in Appendix B:

$$(\Pi_c - \Pi_i) = \sigma \Pi_c \frac{1 - e^{-(Pe)}}{1 - \sigma\, e^{-(Pe)}}. \tag{6-4}$$

By using this relationship, Eq.6-3 can be expressed as:

$$J_{VA} = L_p \left[\left(P_c - P_i \right) - \sum_{n}^{N} \Pi_{c,n} \left(\sigma^2 \frac{1 - e^{-(Pe)}}{1 - \sigma\, e^{-(Pe)}} \right)_n \right], \tag{6-5}$$

where *n* refers to the individual solute, such as proteins or ions. $Pe = J_{VA}(1-\sigma)/P_d$, the modified Peclet number, is the ratio of the solute convection to diffusion, P_d being the diffusion permeability, a function of solute and pore size as well as the solute diffusion coefficient (see Appendix B-12 – B-16). The equation is not an explicit form for the flow flux because the modified Peclet number in RHS of Eq.6-4 is a function of the flow flux J_{VA}. To obtain the flow flux, the nonlinear equation must be solved numerically.

As explained in a review of pore theory by Rippe and Haraldsson (Rippe and Haraldsson 1994), deduced from experimental observations, there may be many tiny water filled flow channels penetrating across the vessel wall, with diameters comparable to those of ions or plasma proteins. The rest of the wall is impermeable to these molecules and thus those pores are the main pathways for transvascular exchange. There are two main flow and solute pathways across the capillary wall, including the large pore and small pore pathways as well as the low conductive pathways. Accompanied by water flux, the smaller solutes can pass through both small and large pore pathways whilst large solutes are mainly transported through the large pore system. For instance, the small pore pathways take up more than 95% of the fluid passage and the large pore pathways take almost 5% in the muscle capillary. The aquaporin pathways were considered negligible compared to large and small pore transport system at capillary membranes (Levick and Michel 2010) .

When using pore theory, the reflection coefficient, σ, the diffusion permeability of solute, P_d, and the wall permeability, L_P, must be defined for both small pore and large pore pathways. The nonlinear equation for each pore pathway then needs to be solved individually.

The total water flux across the capillary wall is the summation of the flux via the large pore and small pore transport systems, each of which is related to the osmotic pressure due to transvascular transport of ions and proteins:

$$J_{VA} = L_{p-S}\left[(P_c - P_i) - \Pi_{c-pro}\left(\sigma^2 \frac{1-e^{-(Pe)}}{1-\sigma\, e^{-(Pe)}}\right)_{pro-S} - \Pi_{c-ion}\left(\sigma^2 \frac{1-e^{-(Pe)}}{1-\sigma\, e^{-(Pe)}}\right)_{ion-S}\right] + L_{p-L}\left[(P_c - P_i) - \Pi_{c-pro}\left(\sigma^2 \frac{1-e^{-(Pe)}}{1-\sigma\, e^{-(Pe)}}\right)_{pro-L} - \Pi_{c-ion}\left(\sigma^2 \frac{1-e^{-(Pe)}}{1-\sigma\, e^{-(Pe)}}\right)_{ion-L}\right]. \quad (6\text{-}6)$$

where Π_{c-pro} is the protein osmotic pressure at capillary side and the term,

$\left(\sigma^2 \frac{1-e^{-(Pe)}}{1-\sigma\, e^{-(Pe)}}\right)_{pro-S}$, is a function of σ_{pro-S} and Pe_{pro-S}, being used to estimate osmotic pressure drop caused by the passage of proteins through the small pore system and similarly for the others. In all, there are two pathways for two solutes involving the regulation of the osmotic Starling forces, which creates four osmotic pressure terms in Eq.6-6.

The brain is unique in its regulation mechanism of water and solute exchange. Unlike other organs in the body, intact brain capillary vessels do constrain the passage of small ions or proteins. Endothelial cells are attached to one another with tight junctions which are composed of a variety of complex structures know as zonulae occludens (Rapoport 2000). For other systemic peripheral capillaries, there appear to be some breaks in these junction strands, allowing the water and solutes to move from blood to tissue. The endothelial cells at these peripheral capillaries permit free passage for these ions, indicating that the reflection coefficient for salt is equal to zero. Among all solutes on both sides of the capillary wall, only proteins create an osmotic pressure due to a concentration difference.

However, it has been found that there is a substantial restriction on water and solute passage across the capillary vessel wall in the brain due to the function of the BBB. The ultrastructure

of the brain capillaries, such as the astrocytes and basal lamina, increases resistance to the material passage. When applying the present filtration model to the transvascular transport, this higher resistance at the BBB can still be modelled as the value of capillary wall hydraulic permeability is reduced by O(10^{-2}) from its baseline value.

The less frequent breaks and the more solid tight junctions are the main structural features of the BBB, which makes the vessel wall largely impermeable to small molecules. Moreover, experimental studies suggest that the contribution of the large pore pathways of the BBB seems to be negligible because the pore size for the BBB is thought to be around 1nm (Sarin 2010). In this way, only the small pore pathways are considered in the model proposed here for material exchange of the intact cerebral capillary.

In addition to the plasma proteins, ions such as Na^+ and K^+ can also exert an osmotic pressure due to their impermeability across the intact BBB ($\sigma \approx 1$) if there is a concentration difference across the vessel wall. In physiological conditions, the influences of both colloid (proteins) and the crystalloid (ions) osmotic pressures on water filtration must be considered when modeling the transvascular transport for the BBB. Thus, Starling's equation should include the osmotic pressure term caused by the ions. In the CNS, however, almost no salts and protein can pass the capillary membrane, implying that the reflection coefficient for salt is nearly equal to 1 (Kimelberg 2004). Since the large pore transport in intact BBB is fairly small, it is ignored in the calculation. Based on Eq.6-6, by setting L_{p-L} to be zero, the total wall flux is thus dominated by the small pore system, giving the following equation:

$$J_{VA} = L_{p-S}\left[(P_c - P_i) - \sigma_{pro-S}^2 \Pi_{c,pro}\left(\frac{1-e^{-(Pe)}}{1-\sigma\, e^{-(Pe)}}\right)_{pro-S} - \sigma_{ion-S}^2 \Pi_{c,ion}\left(\frac{1-e^{-(Pe)}}{1-\sigma\, e^{-(Pe)}}\right)_{ion-S}\right]. \quad (6\text{-}7)$$

In Eq.6-7, to approach the condition of $\sigma \approx 1$ due to the nearly total rejection of these solutes, both the reflection coefficients for protein σ_{pro-S} and the salt σ_{ion-S} are set as 99.99%. In addition, the strands in intact cerebral capillary vessels are almost continuous, and only a tiny slit found at the tight junction seal allows limited transport of water and solute through the small pore pathways. This is equivalent to the small pore pathway with diameter less than 1nm for water and solute transport (Sarin 2010).

When the cerebral capillary is in pathological conditions such as inflammation or post-ischemic attack, the selectivity capability of the blood brain barrier tends to break down due to cellular structure adaption. The ions in plasma, which were once kept on the lumen side of the intact vessel, are now allowed freely to enter the tissue space when tissue is inflamed. The plasma proteins can pass the capillary; however, still under restriction.

These changes during pathological conditions can be reflected by a modification to the filtration model and can be presented in terms of the reflection coefficient of protein, σ_{pro}, and ions(or salt), σ_{ion}, as being 0.93 and 0 respectively for both pore systems (Kimelberg 2004). In addition, to replicate the inflammation conditions in the capillary bed, the large pore system needs to be re-introduced to the Starling equation since observations in rat BBB under ischemic conditions shows its participation in the transvascular material exchange (Preston and Foster 1997). Since σ_{ion} is set to 0, the equation for the transvascular flux under abnormal conditions, accounting for the influence of protein, is expressed as follows:

$$J_{VA} = L_{p-S}\left[(P_c - P_i) - \sigma^2_{pro-S}\Pi_{c,pro}\left(\frac{1-e^{-(Pe)}}{1-\sigma\, e^{-(Pe)}}\right)_{pro-S}\right] + L_{p-L}\left[(P_c - P_i) - \sigma^2_{pro-L}\Pi_{c,pro}\left(\frac{1-e^{-(Pe)}}{1-\sigma\, e^{-(Pe)}}\right)_{pro-L}\right] \quad (6\text{-}8)$$

In addition, under some ischemic attack conditions, it was found that the wall hydraulic permeability could become up to 100 times larger than its normal value (Hakamata and others 1995). The wall hydraulic permeability is then set to be 2.9×10^{-7}cm/s/H_2O, being about 150 times larger than the baseline values 2.0×10^{-9}cm/s/H_2O (Fraser, Dallas, Davies 1990) (Li, Yuan, Fu 2010) and all the other parameter values are taken to be identical to those in the previous theoretical studies of the mildly inflamed capillaries (Levick and Michel 2010). All these changes in the filtration property of the BBB cause a significant increase in the water and solute filtration into the interstitial space.

Since the values of hydraulic permeability and the protein reflection coefficient in abnormal conditions are close to those for the peripheral capillaries, the endothelial cells are assumed to have a transport pathway system similar to that of the peripheral capillaries in other organs when undergoing ischemic attacks. The same parameters, including P_d , L_p, and etc used in the previous theoretical study (Levick and Michel 2010) have been applied to predict the flow filtration in an inflammatory capillary in the current model.

In summary, the filtration flux, J_{VA}, has very different behaviours in models of the transvascular exchange for physiological and pathological states. For normal capillaries, the flux is estimated by Eq. 6-7 where refection coefficients for ions and protein are set very close to 1, representing the nearly perfect selective function of normal BBB. The large pore system, meanwhile, is ignored due to its weak influence on transvascular exchange in intact capillaries.

Conversely, the filtration flux is expressed by Eq.6-8 when accounting for the abnormal functioning of the BBB. Reflection coefficients are reduced as well, with values of 0.93 and 0 for proteins and ions respectively; filtration through the large pore system will now be added.

The wall permeability is set to be about 150 times of that in the normal state by increasing the density of small pore about 100 fold and opening a number of large pores, as previously done in (Levick and Michel 2010).

Table 6.1 Parameters used in the water filtration model for cerebral capillary vessels			
Albumin radius	a	3.5 nm	(Levick and Michel 2010)
Albumin diffusion coefficient	D_{pro}	9.29×10^{-7} cm^2/s	(Zhang and others 2006)
Salt diffusion coefficient	D_{ion}	5.62×10^{-6} cm^2/s	(Fu, Curry, Weinbaum 1995)
Crystalloid osmotic pressure	Π_{ion}	5100 mmHg	(Kimelberg 2004)
Colloid osmotic pressure	Π_{pro}	25 cmH_2O	(Levick and Michel 2010)
Hydraulic permeability (normal)	L_{p-S}	2×10^{-9} $cm/s/cmH_2O$	(Li, Yuan, Fu 2010)
Hydraulic permeability (abnormal)	L_{p-S}	1.9×10^{-7} $cm/s/cmH_2O$	(Levick and Michel 2010)
	L_{p-L}	1.0×10^{-7} $cm/s/cmH_2O$	
Small pore radii (normal)	$r_{(S)}$	4 nm	(Levick and Michel 2010)
Small pore radius(abnormal)	$r_{(S)}$	0.5 nm	(Sarin 2010)
Large pore radii (abnormal)	$r_{(L)}$	22.5 nm	(Levick and Michel 2010)

6.3 Filtration coupled interstitium equation

As the transvascular filtration in the BBB in the physiological and pathological states has been previously expressed in Ch.6.2 qualitatively, it can then be combined with three different interstitial pressure equations to form three corresponding theoretical models accounting for the effects of filtration induced ICP elevation on vascular deformation. Here, all the sets of equations used by these three models, namely the lumped model, the network based model and the continuum model, are outlined.

6.3-1 Lumped model

The dynamic intracranial pressure is related to the volume changes in blood and CSF spaces (Ursino and Lodi 1997), where the net volume change of the vascular volume, CSF accumulation, and extra CSF manipulation, all contribute to the regulation of intracranial pressure:

$$C_{ic}\frac{dP_{ic}}{dt}=\frac{dV_a}{dt}+\frac{P_c-P_{ic}}{R_f}+\frac{P_{ic}-P_{vs}}{R_o}+I_i, \tag{6-9}$$

where $C_{ic}=1/k_eP_{ic}$ is the compliance of whole brain and the compliance is inversely proportional to the intracranial pressure with a factor of k_e (Ursino and Giannessi 2010). V_a is the blood volume in the vascular bed. P_c, P_i and P_{vs} are the capillary, intracranial and the venous sinus pressures respectively. R_f is the filtration resistance whilst R_o is the resistance of the CSF absorption. I_i denotes CSF injection. The terms in Eq.6-9 can also be re-written as follows:

$$C_{ic}\frac{dP_{ic}}{dt}=q_b+q_{in}-q_{out}+I_i, \tag{6-10}$$

where the terms q_b, q_{in}, q_{out}, refer to blood volume change, the CSF input and output, respectively, forming a net accumulation in the CSF space due to fluid passage. Following a similar rationale, the intracranial pressure dynamics can also be determined by the tissue and vascular spatial changes under the constraint of the Monro-Kellie doctrine. In this way, a similar equation can also be applied to link the intracranial pressure dynamics to the local volume changes in both the interstitial and vascular spaces in a small volume of brain tissue.

The tissue size, V_{tissue}, is simply the ratio of the vessel number density to the total number of vessels in the tissue, and intracranial pressure, P_{ic} in Eq.6-10, is equal to the interstitial pressure, P_i, giving:

$$C_{ic-tissue}\frac{dP_i}{dt} = \Omega_b + \Omega_{in} - \Omega_{out}, \tag{6-11}$$

where the term $C_{ic-tissue} = f_c \cdot 1/k_e P_i$ is the effective ICP compliance, being modulated by the factor of $f_c = V_{tissue}/V_{brain}$ and the term $\Omega_{in} - \Omega_{out}$ refers to the net flow accumulation rate in the tissue (interstitial space). Tissue fluid input is attributed to capillary filtration:

$$\Omega_{in} = \sum_{m}^{N_m} (J_{VA} \cdot A_c)_m, \tag{6-12}$$

where Ω_{in} stands for the net water filtration of N_m capillary vessels in the region of interest, each of which is just the product of flux J_{VA} and its exchange area S. In this model, the exchange area remains equal to the circumferential area for any vessel, as a constant, until the vessel collapses. On the other hand, the cross sectional area of a given capillary may change due to wall deformation. The total area for water exchange $(A_c)_m$ for capillary *m* is just the perimeter $2\sqrt{\pi A_{0m}}$, where A_{0m} is the cross sectional area, multiplied by the length, L_m, of a given vessel:

$$(A_c)_m = 2\sqrt{\pi A_{0m}} \cdot L_m. \tag{6-13}$$

A proper drainage term is required to mimic the flow drainage through the tissue interstitium in the brain, which is proportional to the pressure drop between the interstitial pressure and the baseline pressure, P_B, set here to be 5mmHg (Kimelberg 2004):

$$\Omega_{out} = (P_i - P_B) \cdot G_D , \tag{6-14}$$

where G_D is the fluid drainage conductance, which was taken here to be approximately equal to 2.25×10^{-10} cm^3/cmH_2O based on the normal brain drainage rate per volume tissue in the brain interstitial space with a rate of 0.11-0.29 μL/g brain/min (Weller and others 2009).

The configuration of the capillary is closely related to the pressures on both sides of the vessel wall. A change in the vessel dimensions is always accompanied by a change in transmural pressure. As excess fluid enters the brain tissue, the interstitial pressure builds up locally due to the imbalance between the fluid production and drainage rates in the local tissue space. The capillary walls deform with the changes in transmural pressure (capillary pressure P_c minus interstitial pressure P_i), causing a reduction in the cross section area, A, of the capillary, which can be approximated by the tube law for microvessels (Baish, Netti, Jain 1997):

$$(P_c - P_i)_m = E\left(\frac{A}{A_d}\right)_m^5 - P_{crit} , \tag{6-15}$$

where E is the elastic constant, set here to be 6.5 mmHg (Baish, Netti, Jain 1997). A_d is the baseline cross section area and P_{crit} is the critical pressure at which vessel collapse occurs, set to be 3.5 mmHg (Baish, Netti, Jain 1997). Since the cross sectional area changes with time, the rate of blood volume deformation, dV_a / dt, is obtained from:

$$\Omega_b = \sum_m^{N_m} L_m \left(\frac{dA}{dt}\right)_m . \tag{6-16}$$

6.3-2 Discretised model

Darcy's equation has been widely used for modeling steady flow in the interstitial space of biological tissue, as mentioned in Chapter 5. It relates the Darcy velocity $\mathbf{u}_D$ to the pressure gradient ∇P in a linear manner:

$$\mathbf{u}_D = -\frac{\kappa_i}{\mu_i}\nabla P_i, \tag{6-17}$$

where κ_i and μ_i are the tissue permeability and the ISF viscosity respectively, being linked by the tissue hydraulic conductivity ($\kappa_i / \mu_i = h_i$). By taking the divergence of Eq.6-17, the Poisson equation for pressure with vessel wall filtration as the source term $S_D = \nabla \cdot \mathbf{u}_D$ (Wu and others 2008) takes the form of Eq.6-18, which shows that the steady state flow patterns are just the result of the volume balance between the flow across the boundary $\frac{\kappa_i}{\mu_i}\nabla^2 P_i$ and the local generation term S:

$$\frac{\kappa_i}{\mu_i}\nabla^2 P_i + S_D = 0. \tag{6-18}$$

Eq.6-18 is used to describe the spatial distribution of interstitial pressure in the steady state, which shows that the pressure field disperses with space in a diffusive manner. Similarly, the transient pressure equation for interstitial fluid (Eq.6-11) can be extended by including pressure dispersion in space if filtration coupled ICP dynamics are analysed. The units in Eq.6-11 are m^3/s whilst in Eq. 6-18 they are 1/s. Therefore, Eq.6-11 is divided by the local tissue volume unit, ΔV, and the pressure diffusion term $\frac{\kappa_i}{\mu_i}\nabla^2 P_i$ is then added in, giving a temporal-spatial dependent P.D.E. for the interstitial pressure field:

$$\overline{C}_{tissue}\frac{\partial P_i}{\partial t}=\frac{\kappa_i}{\mu_i}\nabla^2 P_i+S_b+S_f, \tag{6-19}$$

where $\overline{C}_{tissue}$ is the effective tissue compliance per unit volume tissue. The term S_f is the pressure source density (1/s) due to the net capillary filtration whilst S_b is the pressure source density due to a change in the vascular volume. The effective compliance per unit volume tissue, $\overline{C}_{tissue}$, can be estimated by dividing whole brain compliance C_{ic} by the whole brain volume $\overline{C}_{tissue}=C_{ic}/V_{brain}=1/(k_e\ P_i\ V_{brain})$.

The local water filtration into the interstitial space is estimated by summation of flow from each vessel enclosed by the unit volume, which is simply the wall flux $(J_{VA})_m$ multiplied by its wall area for fluid exchange $(A_c)_m$. The filtration source density, S_f, is equal to the ratio of filtration rate (m^3/s) to local tissue volume (m^3):

$$S_f=\sum_m^{N_m}(J_{VA})_m\cdot(A_c)_m/\Delta V. \tag{6-20}$$

Similarly, the vessel cross sectional area can be calculated individually from the tube law:

$$(P_c-P_i)_m=E\left(\frac{A}{A_d}\right)_m^5-P_{crit}. \tag{6-21}$$

The volume occupied by the blood undergoes a change depending on the pressure condition, and can be expressed as a pressure source. S_b is thus obtained from:

$$S_b=\sum_m^{N_m}L_m\left(\frac{\partial A}{\partial t}\right)_m/\Delta V. \tag{6-22}$$

6.3-3 Continuum model

Since the continuum model can be applied to replicate the overall flow and oxygen transport features for a small volume of microvasculature, it is natural to extend this model in order to check its capability to model filtration induced stenosis. The purpose of this section is thus to test the capability of the continuum approach when modelling the collapse phenomenon due to over-filtration.

For simplicity, the capillary pressure is set as a constant throughout the blood phase and spherical symmetry is assumed. The interstitial pressure and the filtration source density are only functions of the radius, r. Equation 6-19 becomes:

$$\overline{C}_{tissue}\frac{\partial P_i}{\partial t}=\frac{\kappa_i}{\mu_i}\frac{1}{r^2}\frac{\partial}{\partial r}\left(r^2\frac{\partial P_i}{\partial r}\right)+S_b+S_f\,. \tag{6-23}$$

The transmural pressure and the plasma filtration into the interstitial space are no longer estimated vessel by vessel, but is purely a function of radius, being estimated by solving the Starling's equation with local values of transmural pressure.

The source densities, S_b and S_f, for the interstitial pressure equation result from wall filtration and blood volume deformation respectively. The dimension of all the vessels in the network must be properly described in the continuum because their information is necessary to estimate S_b and S_f. To avoid model complexity in the calculation, the vessels at a certain location are assumed to have uniform behaviour; in other words, at certain radius, this small portion of the network is assumed to be composed of a number of identical vessels, with the same cross sectional area, A, vessel surface area, A_c, both thus being functions of r and t. With a specific vessel number density, n_0, the filtration density is thus computed as following:

$$S_f = \bar{J}_{VA} \cdot A_c \cdot n_0 . \tag{6-24}$$

Since the vessel cross sectional area is purely a function of its location, at certain radius vessels a are assumed to react in the same manner, the tube law being directly used to predict the cross sectional area:

$$(P_c - P_i) = E\left(\frac{A}{A_d}\right)^5 - P_{crit} . \tag{6-25}$$

The source density, resulting from the vascular space volume change, is thus obtained from:

$$S_b = n_0 \frac{\partial A}{\partial t} L . \tag{6-26}$$

where n_0 is the number of vessels per unit volume of tissue, and L is the vessel length in this local region of the network.

6.3-4 Summary

In this section, three different sets of pressure equations for the interstitial fluid are introduced, which can then be combined with the filtration equations outlined in Chapter 6.2. These models based on the filtration interstitium coupled equations will now be applied to investigate the interactions between the ISF accumulation and ICP elevation, and thereby the diverse patterns of vessel responses in the microvasculature. The lumped model ignores the spatial variations in interstitial pressure and focuses on investigation of the effect of the parameters in the filtration equation on the vessel dynamics. Later, the artificial networks created in Chapter 3 are introduced into 3D interstitial pressure equation, which accounts for both the spatial variations in the vascular filtration and interstitial pressure. Finally, a 1D continuum model is proposed here to test how the idea of the porous media analogy works for the prediction of vessel collapse events due to filtration induced pressure increase.

Whichever model is involved in the simulation, three groups of equations, namely the filtration, filtration coupled interstitium and other equations must be solved simultaneously. The relevant equations for the different models are outlined in Table 6.2 for clarity.

Table 6.2 the equations used in different models

	Lumped model	Network based model	Continuum model
Filtration equations	Eq.6-7&Eq.6-8	Eq.6-7&Eq.6-8	Eq.6-7&Eq.6-8
Filtration coupled interstitium equation	Eq.6-11	Eq.6-19	Eq.6-23
Other equations	Eq.6-12 - Eq.6-16	Eq.6-20 - Eq.6-22	Eq.6-24 - Eq.6-26

6.4 Model parameters and numerical procedures

In this section, simulation settings for three models, namely the lumped model, the 3D discretised model and the 1D continuum model, are presented to show the interactions between network filtration and vessel collapse, under conditions which are designed to simulate the brain tissue response to both physiological and pathological states. For each model, the simulation is carried out by simultaneously solving three groups of equations, namely the filtration equation, the filtration coupled intersitium equations and the tube law. In addition, settings for each model may be different and will be introduced accordingly in the following sections.

6.4-1 Lumped model

Analysis starts from a simple case, where there are only two vessels in the region of interest. Since the vessel number density of the brain tissue is about 8000/mm^3, the equivalent volume

for the two vessel model is about 1/4000 mm^3. The effective compliance and the fluid drainage conductance are adjusted accordingly for the local tissue size. The detailed dimensions of these two vessels are listed in Table 6.3. The vessel dimensions adopted here are based on the statistics in the experimental study by Cassot et al (Cassot and others 2006).

Table 6.3 Parameter values in the lumped model

	Vessel 1	Vessel 2
Initial blood pressure	30mmHg	20mmHg
Initial vessel radius	5 μm	5 μm
Vessel length *L*	50 μm	50μm

The initial pressure in the interstitial space is set at 5mmHg (Kimelberg 2004). Along with the initial pressure conditions for the two vessels given above, the reference areas can be determined individually according to the tube law outlined in Eq.6-15. As the interstitial pressure builds up due to the imbalance between flow filtration, drainage and blood volume variations, altering the transmural pressures in the two vessels, this immediately leads to changes in the vessel volume, the filtration fluxes for both vessels and the flow drainage and thereby the interstitial pressure. The coupled equations are solved numerically rather than analytically since the filtration equation is strongly nonlinear.

In one time step, iterations are performed several times. Each term in the filtration-interstitium equation (Eq.6-11) is calculated first. For example, the water filtration is determined by Eq.6-7 or 6-8, depending on the vascular condition, local filtration in a unit volume of tissue can then estimated via Eq.6-12 and similarly the drainage by Eq.6-14 and the vascular volume change by Eq.6-16. This gives a new estimate for interstitial pressure

and the terms in Eq.6-11 are updated. This iteration continues until satisfactory convergence is reached for the value of interstitial pressure. The calculation is then advanced to the next time step and the dynamics of all variables can thus be fully resolved. During computation, the circumferential area of one particular vessel remains equal to its initial value unless its transmural pressure, ΔP_m, reaches the collapse threshold pressure, P_{crit}. When the vessel fully collapses, the circumferential area is then set to be zero for all subsequent time.

6.4-2 Network based model

After gaining a basic understanding of the vessel response to tissue pressure in a simple system, a system with a small network of around 1000 vessels is considered. The interaction between the haemodynamics in the microvasculature and the transvascular transport patterns are highly complex. Since the capillary pressure distribution is very irregular in the network, the local flow accumulation in the interstitial space is expected to exhibit a degree of spatial heterogeneity. The Laplace term in the interstitial pressure equation, however, acts to smear out local variations in the pressure field. These two opposing effects on the interstitial pressure field contribute towards potentially very complicated distributions.

These vessel collapse events have been widely found in post-ischemic attacks but theoretical analysis is very limited. In particular, the aim of this section is to investigate the correlations between haemodynamic conditions and the localised dynamics of vessel collapse in more realistic networks. An artificial network embedded in a cube of brain tissue $(500\mu m)^3$ is generated by the modified spanning tree method, as presented in Chapter 3, with full geometric and topological information regarding each node and each microvessel.

Two sources and sinks are assigned at the same locations as the previous simulations with pressures set at 4000Pa and 1000Pa respectively for normal conditions. Average blood

pressure in the capillary bed during inflammation, accompanied by increased blood flow and vasodilatation, is much higher than that in normal states, possibly rising up to 3922 Pa (40 cmH_2O) (Levick and Michel 2010). To make a comparable setting for this increase in average capillary pressure, 7000Pa and 1000Pa are set as values for the flow inlets and outlets representing for mimicking the arterial pressure increase due to tissue inflammation. The vessel flow and pressure distribution for the whole artificial network are then solved following the procedures outlined in Chapter 3.

In the current model, the capillary pressure for one particular vessel is set to be the mean value of the two terminal pressures of a vessel and the pressure for each node in the network is then assumed constant over time for simplicity. Given the pressure in each capillary in the network, the filtration flux is then estimated according to the local interstitial pressure. Based on the filtration distribution in space, the local flow accumulation and vessel deformations are calculated, these acting as a source term in the transient pressure equations.

In simulations, the filtration equation (Eq.6-7 or Eq.6-8) needs to be solved iteratively due to its non-linearity. First, the solution to filtration equation becomes the input for computation of the transient pressures (Eq.6-19). Along with the given vascular change terms, the source terms in Eq.6-19 are determined and a new solution is obtained by solving the transient pressure Poisson's equation. The new solution then becomes the input for the filtration equation and other terms to be used in the next iteration for the interstitial pressure. In this way, both of the equations are solved alternatively until required precision is achieved. After that, the time step is marched and the nest iteration begins. These numerical procedures are implemented as loops; the inner loop for filtration calculation and the outer loop for interstitial pressure calculation.

Extra procedures are necessary when the 3D computation is performed. First, the non-dimensional compliance requires a re-scaling according to the model dimension; here, this is done by dividing it by the volume of brain. The drainage term in the lumped model, which represents the flow exchange at the system boundary, is now replaced by the pressure dispersion term. Dirichlet boundary conditions, constant pressures being set at the baseline tissue pressure 5mmHg (Kimelberg 2004) for the six boundaries are applied according to the assumption that the surfaces of the model tissue is in direct contact with a pressure reservoir.

In the 3D simulation, the spatial influence of the interstitial pressure field is represented by the Laplace term in the filtration coupled intersitium equations, accounting for the ease of flow movement in the interstitial space. Hence the hydraulic conductivity for the fluid movement through the extracellular matrix is of crucial importance in modulating the system response. The impact of this parameter on the dynamics of blood filtration, pressure elevation in the interstitium and vessel collapse in the network will be addressed in below.

Two simulations with two different values for hydraulic conductivity for the interstitium matrix are presented here: h=1.3×10^{-13} m^4/N·s and h=1.3×10^{-16} m^4/N·s, which are close to the extremes of the values found in the literature for biological tissues (Levick 1987). For both cases, the whole microvasculature in the cube is assumed to be either inflamed or intact, implemented with the settings for physiological pathological states.

Table 6-4 The summary of boundary condition for the pressure equation for 3D discretised model

Direction	Boundary conditions
x	$p(0,y,z) = p(L,y,z) = 667Pa$
y	$p(x,0,z) = p(x,L,z) = 667Pa$

z	$p(x,y,0) = p(x,y,L) = 667Pa$

6.4-3 Continuum model

As shown in Chapter 5, a continuum model is capable of capturing some of the flow and oxygen features found in the discretised model, which can potentially provide an efficient approximation for simulation of the microcirculation at a larger length scale. Following the same rationale, a 1D continuum is proposed here to test its ability to model filtration induced vessel collapse.

For the interstitial fluid phase, the initial condition is set to be the baseline pressure 667 Pa (5mmHg), which is a typical value for interstitial pressure. The pressure boundary condition at the origin is of Neumann type ($\frac{\partial p_i}{\partial r} = 0$) due to symmetry. The baseline value of pressure is applied at the edge of the sphere $r = R_0$, at the same constant pressure boundary condition set in the last section. Two simulation cases are presented to investigate the influences of tissue size and the hydraulic conductivity on the dynamics of the vessel/tissue system.

In the first set of simulations, the effective radius for the spherical tissue is set to be 337μm, with a volume equal to $(500\mu m)^3$, and a larger sphere with radius of 33.7mm; both cases being tested under the setting of intact capillaries with the very low value of hydraulic conductivity (h=1.3×10^{-16} m^4/N·s). In the latter simulations, three different values of tissue hydraulic conductivity are then tested for a sphere of tissue with a radius of 337μm.

Table 6-5 The summary of boundary condition for the pressure equations for 1D continuum model	
Direction	Boundary conditions
r	$\frac{\partial p(0)}{\partial r} = 0, \quad p(R_0) = 667Pa$

6.5 Results

6.5-1 Simulation results for lumped model

Figure 6-1(a) illustrates how the vessel cross sectional area responds to the change in interstitial pressure (ICP) when the capillary is intact. The cross sectional areas for both vessels remain unchanged, reflecting the fact that the transmural pressure is time independent, since the area is just a function of transmural pressure. The vessel shapes remain constant during 3000s, showing that the system is stationary in the physiological condition.

As shown in Figure 6.1(b), the filtration flux across vessel 1 is about twice (5.7×10^{-12}cm/s) that of vessel 2 (3.4×10^{-12}cm/s). Since the volume change of vascular space is fixed, filtration flux is the only way to modulate the total volume of the intracranial elements (blood and tissue), and hence the intracranial pressure. The net filtration flux, and of course the volume expansion, is not sufficient, however, to create a significant change in interstitial pressure (Figure 6-1(c)), leading to a stationary system.

Figure 6.1(c) shows the time courses for all Starling forces for these two vessels, whose osmotic pressures induced by across wall differences in ion concentrations (33 and 20 cmH_2O for vessels 1 and 2 respectively) are far greater than those caused by transvascular protein transport (nearly 0.5 and 0.5 cmH_2O respectively) due to the high value of capillary ionic osmotic pressure (6396 cmH_2O). The ionic dominating Starling forces counter-balance

the hydraulic Starling forces under these physiological conditions. The very small ion and water passage across the vessel wall is relevant to the settings for the reflection coefficient, being set at nearly 100%. This restriction for the material exchange across capillary wall is one of the important features for the intact BBB.

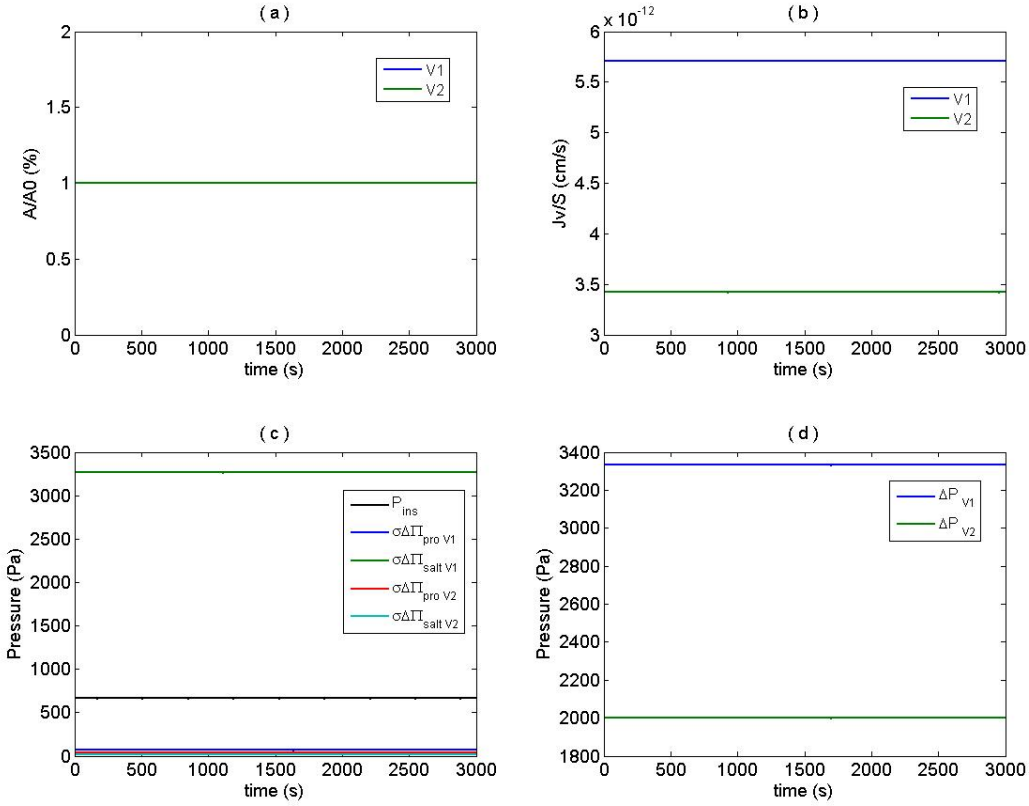


Figure 6.1 Time courses for vessel behaviours: (a) cross sectional areas; (b) flow fluxes; (c) Starling forces; (d) transmural pressures under physiological conditions.

Although the dynamics of most of the variables, shown in Figure 6.1, is stationary under physiological conditions, the system changes when only the vessel condition switches to the pathological state defined above and other settings remain unchanged. The lost of the restriction in the BBB creates tremendous changes in many aspects of the system behaviour.

In this state, both of the curves in Figure 6.2(a) indicate the narrowing down of both vessels in the system, as the interstitial pressures (see Figure 6.2(c)) are elevated.

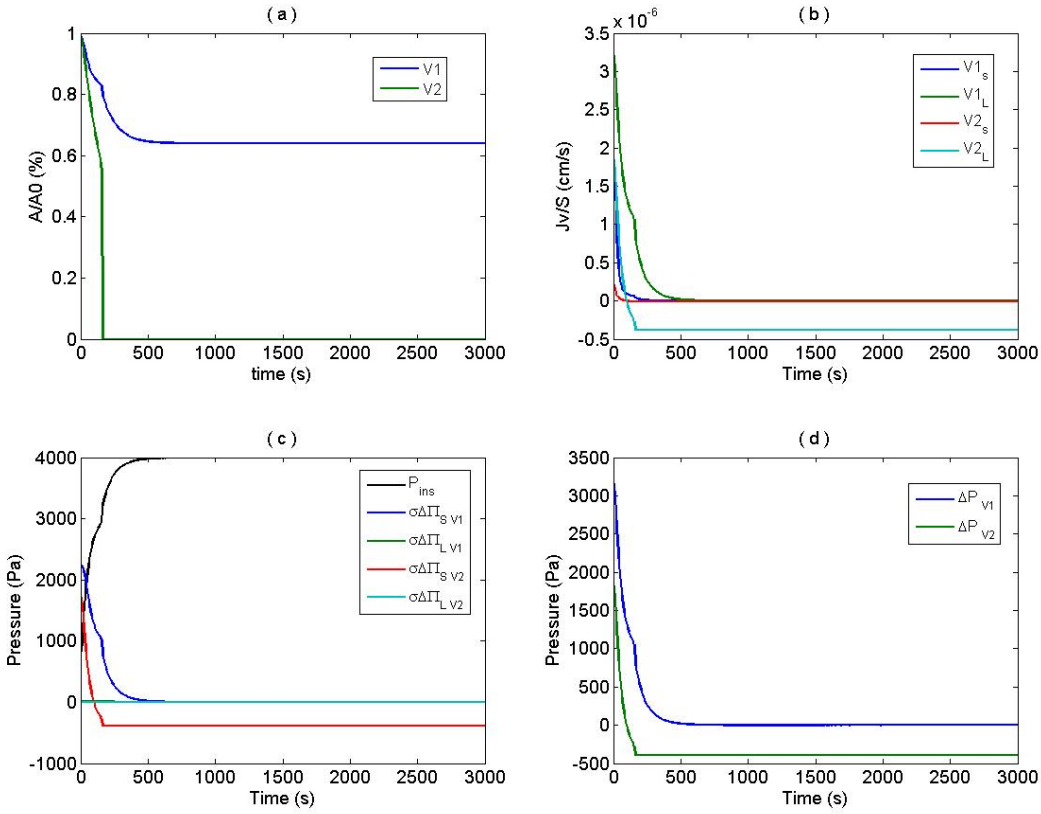


Figure 6.2 Time courses for vessel behaviours: (a) cross sectional areas; (b) flow fluxes; (c) Starling forces; (d) transmural pressures under pathological conditions.

Vessel 2 starts to collapse within about 160s as interstitial pressure gradually elevates. It undergoes a dramatic contraction, and completely collapses. During the period 140-160s, the vessel deforms very rapidly, due to the 5^{th} order tube law (Baish, Netti, Jain 1997) when ΔP_2 becomes negative (see Figure 6.2(d)). This sharply decreasing pattern captures the tube buckling effect due to the net compression loading on the vessel wall approaching its material limit.

At the same time, the effective cross sectional area (CSA) of vessel 1 reduces to about 83% of its initial value and further narrowing continues until a steady state is reached at 65%. The time course of vessel 1 resembles a combination of two decay curves. The value of its cross sectional area reaches a plateau at around 160s, but is then interrupted by the collapse event of vessel 2, leading to a further sharp decrease in CSA.

When simulating pathological conditions, the large pore path way, although only taking up 40% of the initial contribution to the total wall hydraulic permeability, appears to dominate the transvascular exchange in the system, as shown in Figure 6.2(b). In the beginning, the large pore system in vessel 1 generates a flux of 3.4×10^{-6}cm/s (about 75% of the total water flux), which undergoes a monotonic steep decrease, ending up close to zero. The flux across the vessel wall of vessel 1 via the small pore system has a similar two stage decay pattern but with a smaller drop with time. The transvascular flux for vessel 1 stop at 160s, and the resultant flow accumulation slows down, creating a slower decay in interstitial pressure and thereby the two stage change in the time courses for the Starling forces, transmural pressures and vessel CSA.

As shown in Figure 6.2(c), the osmotic Starling forces across the large pore system are smaller than those across the small pore system for both vessels since the flux simply depends upon the imbalance between the hydraulic pressure and osmotic pressure when transmural pressure holds constant. The osmotic pressure difference across vessel 2 decays with time and finally settles down. The time course of the osmotic Starling's force for vessel 2 has a similar two stage decaying pattern, being driven by the collapse of vessel 1.

The transmural pressure of vessel 2 decreases with time, finally settling down at the value of -3.5mmHg, that is negative critical pressure. The transmural pressure of vessel 1, on the contrary, behaves differently after the vessel collapse event, as shown in Figure 6.2(d).

During the time 150-160s, the sharp decrease in the CSA of vessel 2 generates a negative blood volume change for the interstitial pressure equation Eq.6-11. Since the blood volume change, vessel filtration and system drainage forms the source term for Eq.6-11, negative blood volume change compromises the remaining vessel fluxes, as the filtration and blood volume change terms are all in the RHS of filtration-interstitium coupled equation. Therefore, the interstitial pressure increase slows down and thereby the degree of vessel deformation and transmural pressure in vessel 2.

As vessel 2 completely collapses, due to the setting of zero effective area for transvascular exchange, the flux passing through the wall of vessel 1 becomes zero and the transmural pressure remains stationary afterwards. Without the strong blood volume decrease, the flux from vessel 1 is less compromised, so the interstitial pressure rises up sharply again. By the end, the flow source density due to both the vessel flux and vessel deformation is thus very small and is counter-balanced by the boundary drainage. In this way, the RHS of the interstitial pressure equation, Eq.6-11, becomes zero, and the pressure and hence all other variables reach steady state conditions.

The results show great differences in the system response between the two conditions. In an intact capillary, the filtration to tissue is so small that a negligible change in interstitial pressure is found, and hence there is no change in the effective area for filtration. However, the vessel/tissue coupled system changes significantly under pathological conditions,

As shown above, the vessel contraction event in the lumped system is associated with the increase in interstitial pressure, which regulates the dynamics of transmural pressure and hence the cross sectional area in the vessel through the tube law. Interstitial pressure can thus control the vessel contraction events via changes in the corresponding terms on both sides of the pressure equation, Eq.6-11. For instance, the collapse events can be delayed by either

reducing fluid accumulation (RHS in Eq.6.11) or by increasing the effective intracranial compliance. Four parameters, L_p, k_e, Π_c, and G_D are now tuned to test their impacts on the vessel contractions when the other three parameters are set at their baseline values. For intact capillaries, the most extreme cases among the simulations with those parameters can only cause a 0.001% deformation in the cross sectional area, so the system is taken to be in equilibrium throughout the modeling period and the results are not shown here.

The wall hydraulic permeability, L_p, modulates the filtration flux, so reducing the value can effectively delay the occurrence of the vessel collapse, as seen in Figure 6.3(a). There is a significant delay of around 1000s when the value drops by a factor of 0.1 from its baseline value. On the other hand, the time response of the vessel can be adjusted by the modification of the effective tissue compliance through the resulting change in elastance ($C_{ic-tissue} \propto 1/k_e$). Figure 6.3(b) illustrates that the time to collapse increases with a reduction in the elastance, k_e, or in other words, an increase in the effective tissue intracranial compliance. If the elastance is set to be 10 times its baseline value, the interstitial pressure increases very rapidly, and hence so does the transmural pressure, leading to collapse events in vessels.

Regulation of the wall filtration flux can also be achieved by increasing the capillary osmotic pressure, Π_c, however, within the same tuning range, only small changes are seen in the time courses shown in Figure 6.3(c). An increase in the draining conductance, G_D, reduces the fluid accumulation and thereby the interstitial pressure, but the effect is also limited, as shown in Figure 6.3(d), although it is worth noting that at 10 times the baseline value the time course of the CSA of vessel 1 shows an undershoot when vessel 2 fully collapses. This temporary area increase is due to the net negative source term in the pressure equation,

caused by the over-drainage. Since it is very unlikely to happen in reality, it can thus serves as the upper limit of the drainage term.

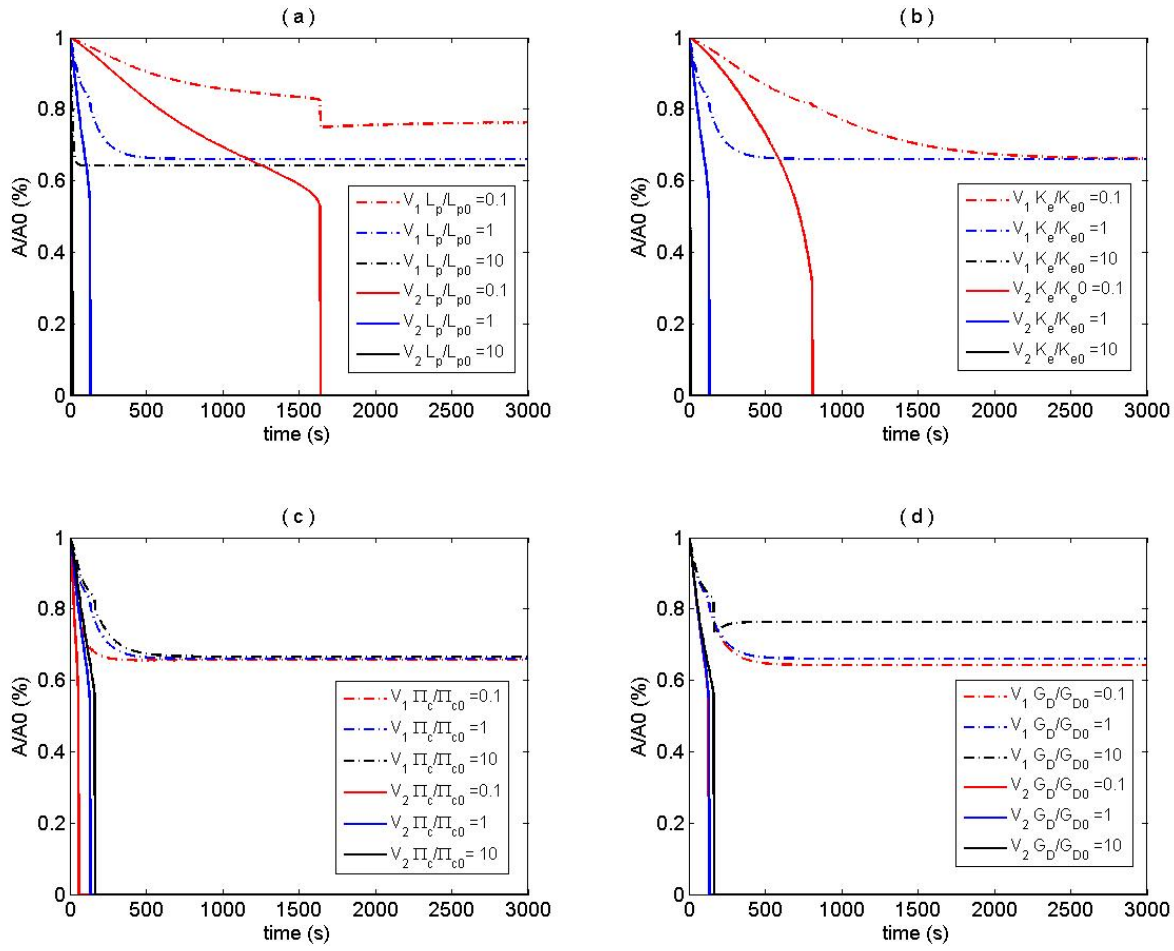


Figure 6.3 Time courses of the vessel cross sectional areas for four parameter tuning cases: (a) wall hydraulic permeability, L_p; (b) elastance, k_e; (c) capillary osmotic pressure Π_c; (d) drained conductance, G_D, under pathological conditions

Of the four parameters examined in the sensitivity test above, only two parameters, wall hydraulic permeability, L_p, and elastance, k_e, can substantially modulate the collapse time. Since the typical time for vessel collapse events observed in ischemic experiments, is about 1-2 hours, significantly longer than the predicted values (160 seconds) calculating using baseline model parameters, it would be possible to fit the experimental values by adjusting those two parameters to increase the accuracy of the simulations.

In this section, simulations are only shown for a small volume of tissue with two vessels, or equivalently for any scaled lumped system with two groups of identical vessels. Information regarding the spatial distribution of the pressure field, and its interactions with vessel constriction patterns in the microvasculature is of importance for gaining the detailed picture of vessel collapse events. To understand the interplay between the spatial variations of the vessel collapse, this lumped model is now extended into a 3D version by incorporating the Starling equation to each vessel in a network of vessels in the next section.

6.5-2 Simulation results for discretised model

Firstly, the physiological state settings are adopted in the simulations. It is found that the intact vessels hold constant cross sectional areas during the simulation time as the filtration flux into interstitial space is not sufficient to cause a significant pressure increment (less than 0.2%), and likewise for other variables. As predicted by the lumped model, the time courses for the variables are stationary so the results are not shown here.

In the pathological state, four vessels are chosen in the network as example vessels, as shown in Figure 6.4(a), all sample vessel cross sectional areas remaining unaffected under the conditions set here. The ratios of the cross section area to the initial values are very close to unity, in the range 0.9973 to 0.9997. Despite there being a large filtration flux (3.4×10^{-5}cm/s on average per vessel) across the capillary network, no large amount of fluid accumulates in the interstitial space and hence there is only a limited increase, from 666.7Pa to 699.2Pa on average, in interstitial pressure.

It should be noted as well that the area ratio for those four vessels are all initially 100%, but that each shows a sudden drop after the first time step (0.01s). This is because the initial flow

flux across each vessel wall is set to be zero, the flux then rising to a value of $O(10^{-5}\text{-}10^{-6})$ at the first time step. This very rapid increase in flux creates a sudden rise of the interstitial pressure and thereby a small drop in area fraction.

Figure 6.4(b) presents a histogram of the cross sectional area ratio of all vessels in the network. It can be seen that all of the vessels have an area contraction of less than 5%, actually or precisely less than 1% according to the raw data. In an inflamed network, the vessel transmural pressure may experience a small drop, and the contractions of the vessels are negligible when the tissue hydraulic conductivity is set at the baseline value, 1.3×10^{-13} $m^4/N\cdot s$.

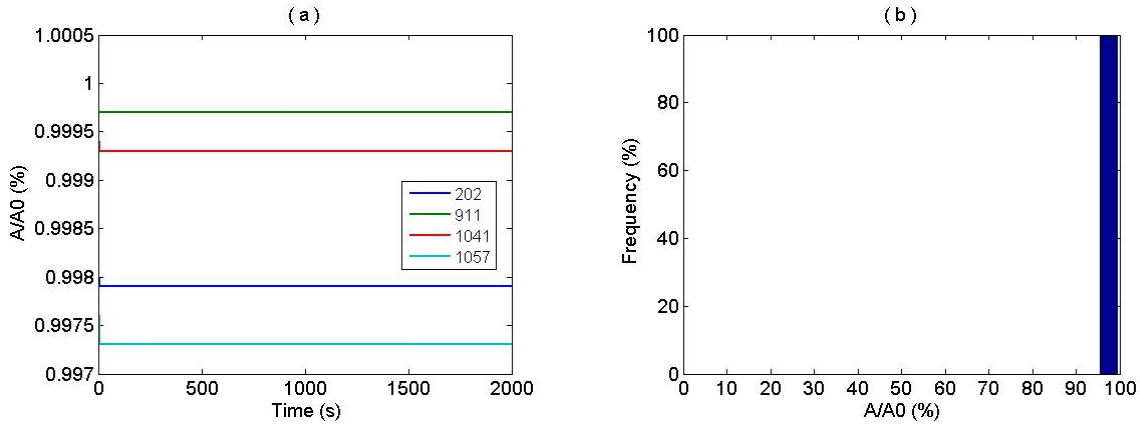


Figure 6.4 (a) Time courses for sample vessel behaviours under pathological condition with high hydraulic conductivity; (b) Histogram of the cross section area for the whole network, non-dimensionalised by the initial value, in the network at steady state.

The low value of the hydraulic conductivity for ISF passage represents the difficulty of the flow transport in the interstitial matrix, so that local flow cannot efficiently move around in tissue. This impairment of flow passage leads to fluid accumulation in the interstitial space and the local interstitial pressure builds up easily. The lower the hydraulic conductivity is for the tissue, the more vessels tend to collapse when the buckling threshold is reached.

As the hydraulic conductivity drops to 1/1000 of the baseline value (from 1.3×10^{-13} to 1.3×10^{-16} $m^4/N\cdot s$), the system behaves very differently from the baseline case in many ways. The vessels respond differently depending on their locations. As shown in Figure 6.5(a), vessel 911 undergoes a contraction from 100% to 92% of its initial cross sectional area, settling down after 400s whilst the cross sectional area of the vessel 1041 experiences a larger deformation, finally reaching about 83% of its initial area.

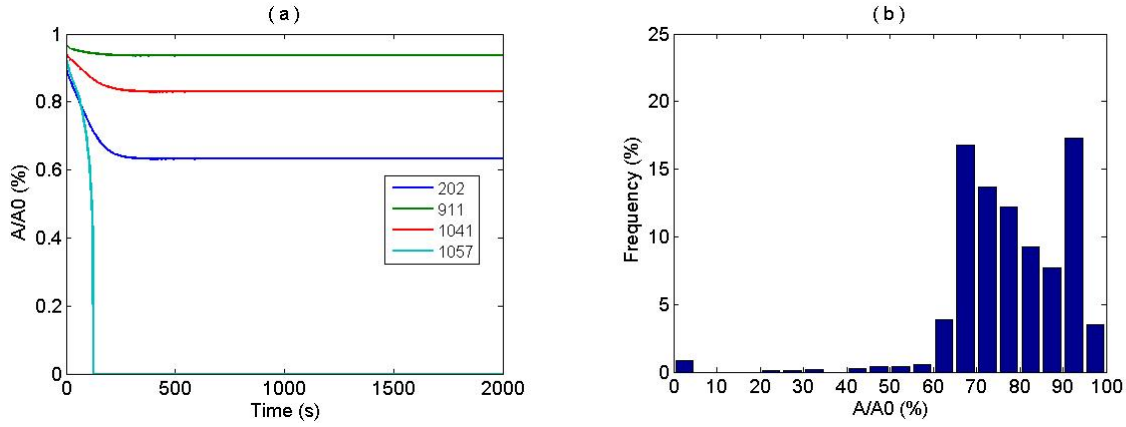


Figure 6.5 (a) Time courses for sample vessel behaviours under pathological conditions with low hydraulic conductivity; (b) Histogram of the cross sectional area for the whole network in the network at steady state.

On the other hand, vessels 202 and 1057 undergo similar contractions initially, but then their time courses bifurcate after 100s. It takes about 130s for vessel 1057 to collapse completely but vessel 202 doesn't experience further contraction after 130s. Vessel collapse occurs in the regions where there is higher interstitial pressure. Due to the very low value of the hydraulic conductivity, flow passage is highly impaired. More fluid will be retained in local regions rather than being moved away, leading to localised pressure build-up at certain sites in the space. This distribution of pressure is irregular, and the interstitial space may have some local sites with high pressure, where surrounding vessel transmural pressures become more negative, potentially even reaching the buckling limit for some vessels. That is why only some vessels tend to collapse.

Figure 6.5(b) illustrates the frequency of area ratios in terms of percentages of their initial values for the network in steady state. 1.1% of the vessels in the network have a final area less than 10% of their original values, and all of these vessels completely collapse. The histogram is essentially flat between 10% to 50% of the initial values and it shows a step increase as the ratio becomes higher than 60%. There are 81% of the vessels with an area ratio between 50% to 90% of their initial values, and 22% of the vessels deform less than 10% (A/A_0>90%). The distribution of the contraction frequency shows a two grouped pattern, 0-60% group with roughly uniform frequency with frequency less than 2% whereas a 60%+ group with frequency variations in the contraction ratios.

As mentioned in Chapter 2, the infarctions are commonly found in many cerebral vascular diseases, and this leads to the hypothesis that the initial infarction in tissue can interfere with the flow passage in the cerebral extracellular space, thereby causing a further pressure build-up in interstitial space. In the third case of the model simulations, an initial spherical infarction, of a radius of 100μm, is placed in the centre of the tissue to investigate the resultant changes in the pressure/flow patterns and their influence on the network contraction patterns in the network.

In practice, to mimic the blood flow impairment resulting from the infarction, the blood flow inside the vessels must be stopped in the simulation, which is done by setting the flow conductances of vessels crossing the infarction boundary to be 10^{-10} of their baseline values. The capillary blood inside the infarction is thus assumed to be static and the pressure should be homogenous through the network embedded by the brain infarction region. The average of the pressure in all vessels before infarction occurs is taken to be the typical capillary pressure in the damaged region and the filtration flux through those vessels is set as zero.

Figure 6.6 illustrates the flow patterns without infarction in (a) and with infarction in (b), with the same arrangement for the two flow inlet-outlet pairs in the network as above. Once the infarction has developed in the centre of the cube, the blood flow patterns tend to rearrange themselves, leaving a flow deficit (red lines) in the central region of the network.

(a) (b)

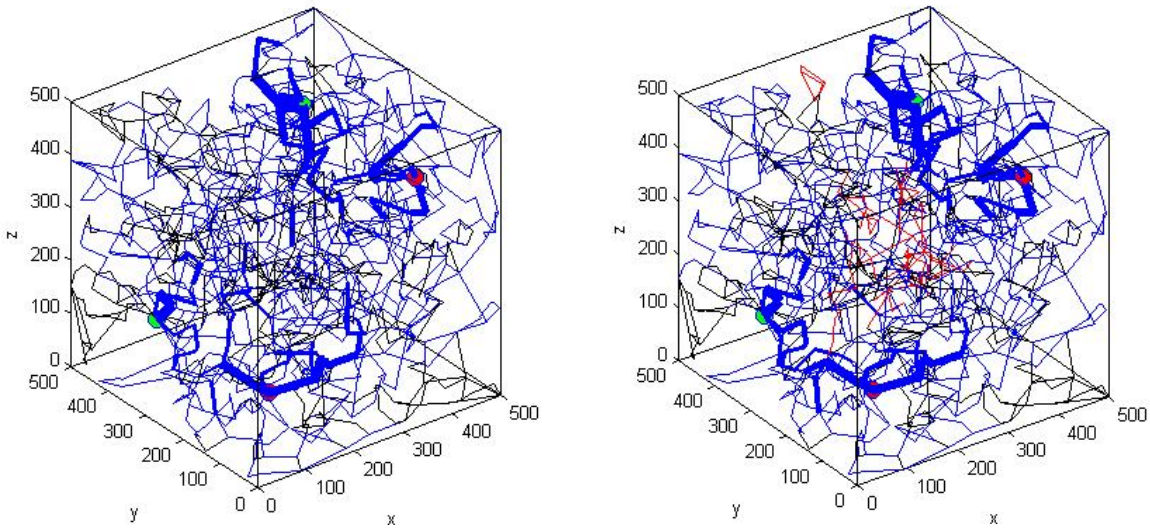


Figure 6.6 Flow distribution in the network with the line thickness representing the flow rate for (a) inflammatory network without infarction; (b) inflammatory network with core infarction (length unit: μm).

The flow is stopped in the infraction region and the flow paths outside undergo a redistribution, creating a new capillary pressure field, and hence new transmural pressures. These changes make some of the vessels more likely to contract. For instance, as seen in Figure 6.7(c), some vessels contract more rapidly than the case without infarction and both vessels eventually collapse at around 80s. Compared to the time course of the area ratio for vessel 1057 without a damaged core, the curve shows a more rapid decline (130 s seen in (a) and 80 s in (c)), suggesting that the transmural pressure distribution in the network with an infarction core facilitates the occurrence of vessel collapse.

Vessel 1041, which was very robust in the case without infarction, now fully collapses at around 190s. However, vessel 202 becomes more robust to the infarction condition, with an area ratio of 73% of its initial value compared to the old steady state value 62%. In this way, the infarction can cause a decrease in transmural pressures in most of the vessels in the network, but few vessels still exhibit an increase in transmural loadings.

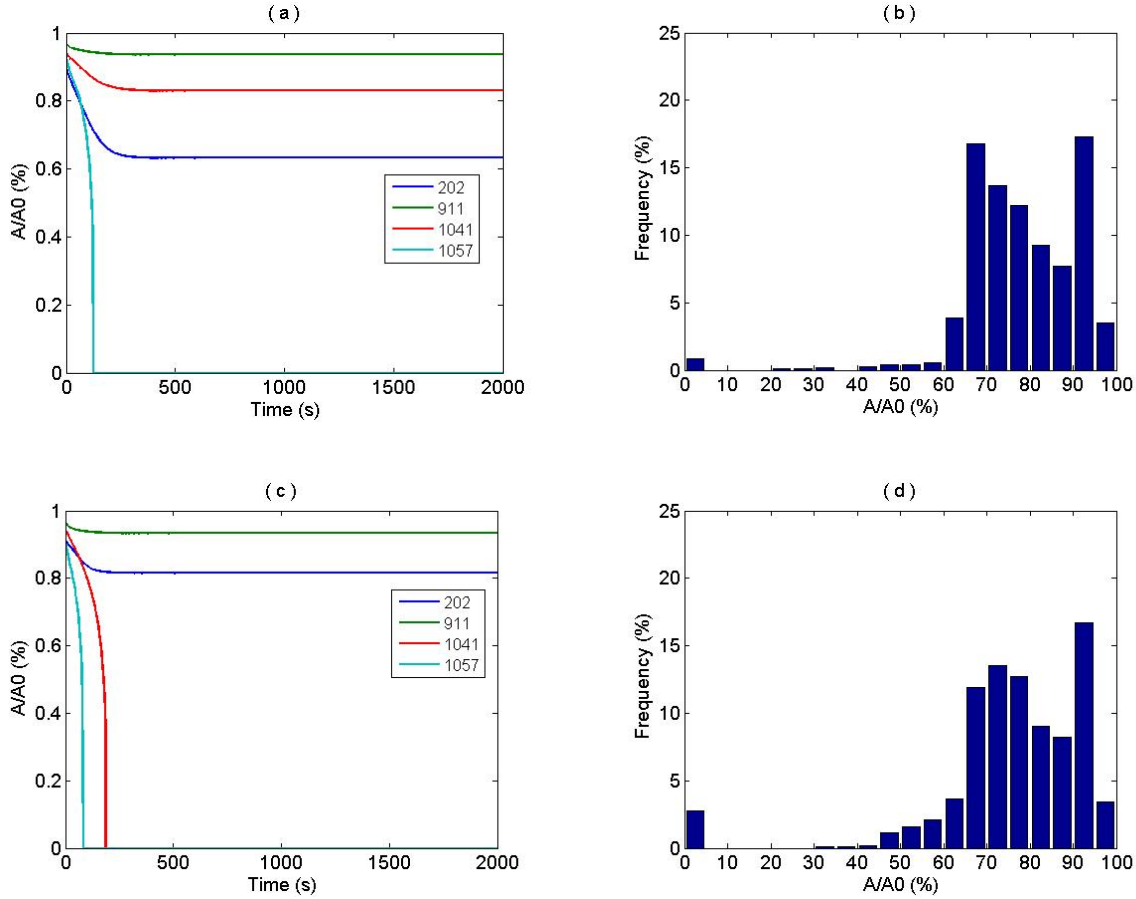


Figure 6.7 Time courses for sample vessel behaviours under pathological conditions with low hydraulic conductivity: (a) without infarction; (c) with infarction. Histogram of the cross sectional area for the whole network at steady state: (b) without infarction; (d) with infarction.

The histogram of the area ratio in the initial infarction setting shows a similar distribution pattern with the previous case. In the steady state, the vessel proportion that undergoes full

collapse increases from around 1.1% to 2.8% and likewise for other modes with a deformation ratio under 50%. The number of vessels with 60%-70% deformation ratio tends to decrease a bit, from about 25% to 19% of the total population whilst vessels with more than 70% of their initial areas seem relatively unchanged. Transmural pressures in some vessels with severe stenosis (with the stenosis ratios A/A_0 less than 65%), undergo a further decrease, hence the shrinkage.

For one particular network, the initial infarction in the tissue is able to increase the number of collapsing vessels but the effect of network variability is not well identified. It is thus of interest to know the role that the initial infarction plays on vessel collapse amongst different networks. The histograms shown in Figure 6.8 clearly illustrate that the stenosis population changes with the existence of the initial infarction and the differences between these two cases are notable in some modes of contraction ratios.

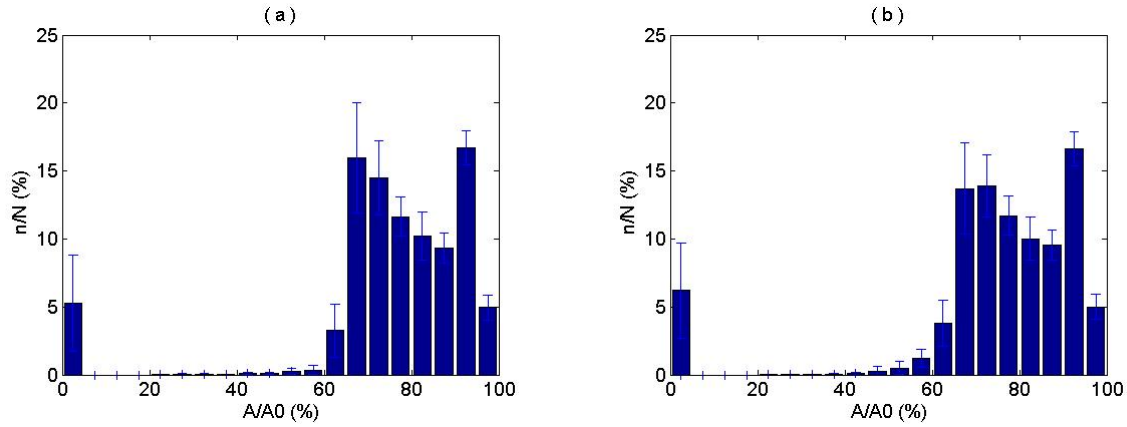


Figure 6.8 Histogram of the cross sectional area at steady state for the whole 10 networks, with the mean value as bars and the standard deviations as error bars: (a) without infarction; (b) with infarction.

For example, the vessel population with deformation ratios between 65% and 70% decreases from 16.6±4.5% to 14.2±3.1%. these number reduction being accompanied by population increases in the modes for area ratios of 60%-65% and of 0%-5%, where 5.2±3.6% of

vessels collapse for the case without infarction and 6.1±3.5% of those for the case with an initial infarction. In all, this shows that the infarction increases the total number of collapsing vessels, possibly further impairing the flow supply in non-infarcted tissue. As shown in Chapter 4, the flow shortage can cause local tissue hypoxia, and hence the lesion is very likely to expand leading to a larger infarction.

6.5-3 Simulation results for continuum model

Since the constant pressure condition is applied in this simulation, the pressure distribution will be affected by the boundary if the model domain is too small or by the volumetric source density accumulation if the model domain is too large. As shown in Figure 6.9, it is found that a 100 fold enlargement of the tissue size can only produce a very limited increase in the interstitial pressure for both cases. As shown in Figure 6.9(a), due to the no flux condition at origin, the pressure profile is very flat in the core region. The interstitial pressure then rises with time unevenly over space, with a maximum value of 672 Pa at the core region and a minimum value of 667 Pa at the boundary.

When the tissue size becomes larger, the pressure distribution still has a maximum value at the core region at different time points, similar to Figure 6.9(a), as shown in Figure 6.9(b). The flat portion of the pressure profile continues to the region next to the boundary, taking up about 95% of R_0. The finial interstitial pressure is 688 Pa: higher than 672 Pa in the baseline volume case, but not high enough to create a significant transmural pressure for vessel contraction. The tissue dimension can modify the pressure profile as the volume increase enlarges the core flat region and maximum values due to the fact that the pressure source effect outweighs the boundary quenching effect, under the setting conditions given here.

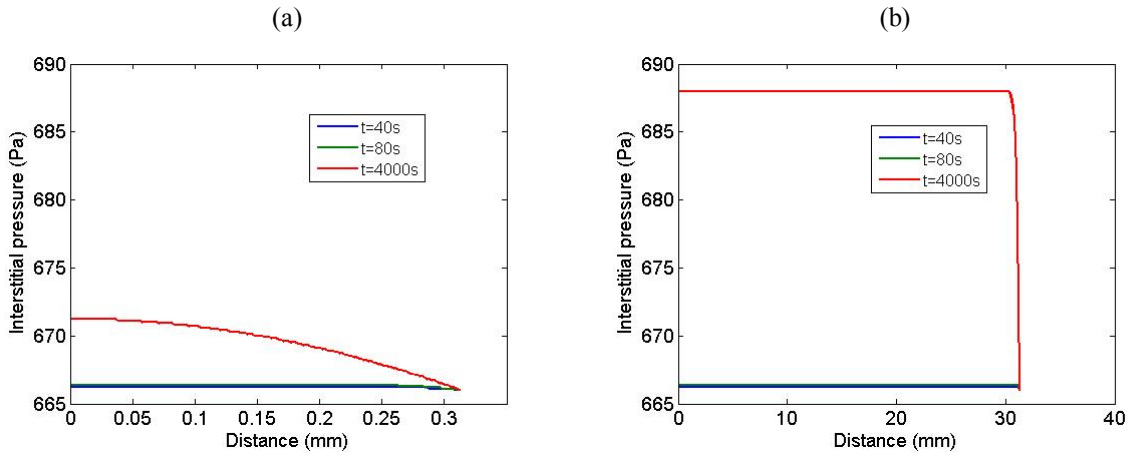


Figure 6.9 Distribution curve of interstitial pressure distribution curve at steady state for cases (a) R=312μm; (b) R=31.2mm under normal condition.

As shown in the 3D discretised model, the hydraulic conductivity of tissue is also an important factor governing the dynamics of the filtration pressure interaction. If the hydraulic conductivity is low enough, the flow passage through the interstitium would be highly impaired, enhancing the local pressure built-up and thus helping vessel collapse. The hydraulic conductivity dependency is thus tested here. The smaller the hydraulic conductivity for tissue is, the larger is the region with a flat profile. This spatial transition is relevant to the profiles for the area ratio.

The three plots in the left column of Figure 6.10 illustrate how the cross sectional area changes for different values of the hydraulic conductivity. Different values of tissue hydraulic conductivity do result in some differences in the time responses. However, the steady states are reached very rapidly for these three cases, which is reflected in the pressure and area ratio profiles. For these two variables, the departure from the initial values and the settling time required are the largest in the case of the lowest hydraulic conductivity. As shown in Figure 6.10(a), the ratio of the cross sectional area changes more in the core region, with a ratio of

96%, this change decaying with distance. Similarly, the pressure undergoes a decay with distance from 1320 Pa at the core to 667 Pa at the boundary.

When the value of the hydraulic conductivity is 1/10 of the baseline value, as shown in Figure 6.10(c)(d), the interstitial pressure becomes more sensitive to the value change of hydraulic conductivity the as the maximum has a significant value increase from 1320 Pa to about 3350 Pa. Such a large increase in the interstitial pressure can result in a large degree of vessel contraction, from the baseline case with 96 % at the core to 77%. The qualitative features in terms of the distribution curve are very similar to the first case since the change decays with the distance.

In the case with the smallest value of hydraulic conductivity, the pressure rises rapidly and reaches a steady state at around 100s, which is close to the settling time for the 3D model. In Figure 6.10(f), the region having the flat profile is largest amongst these three cases with different values of the hydraulic conductivity, which results from the flow accumulation due to the fact that pressure accumulation than the boundary dispassion effect. This feature is consistent with the results from the 3D model.

In the steady state, the interstitial pressure of the third case is nearly uniform and equal to the capillary pressure, 4000Pa. Only in the boundary region does the pressure drop to the baseline value of 667 Pa. Interestingly, in this case, the vessels are far from collapse but have a deformation of about 63%. This contrasts with the predictions of the 3D discretised model with the same values for the hydraulic conductivity, and the reason is explained below.

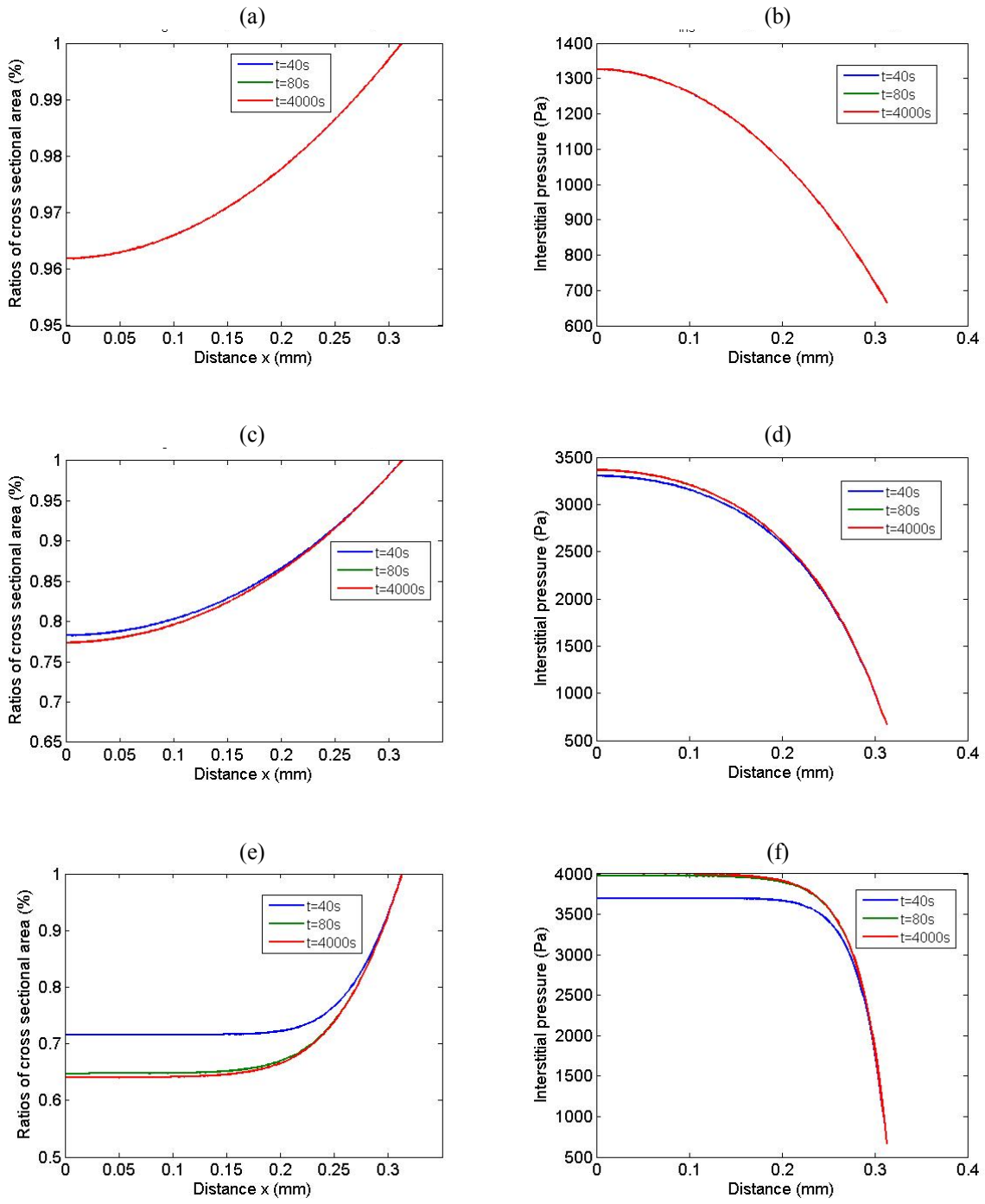


Figure 6.10 Area ratios of vessels at different locations with different values of hydraulic conductivity: (a) h=1.3×10^{-14} m^4/N·s; (c) h=1.3×10^{-15} m^4/N·s; (e) h=1.3×10^{-16} m^4/N·s; in pathological state. Distribution curve of interstitial pressure distribution curve in inflamed tissue at steady state (b) h=1.3×10^{-14} m^4/N·s ; (d) h=1.3×10^{-15} m^4/N·s ; (g) h=1.3×10^{-16} m^4/N·s; in pathological state.

In the discretised model, vessels in a particular voxel behave differently, and some vessels can always create a net vessel flux into the tissue when others fully collapse; however, there is a different story for the continuum model. In order to import the discretised information to a continuum model, the vascular variations are eliminated because a group of vessels in a particular voxel in 3D model is now replaced mathematically by a group of uniformly behaving vessels in the present continuum model. In this way, vessel variables such as capillary pressure, filtration flux, vessel ratio of vessels, which showed inter-vessel variations among vessels before, are here converted to single value variables in the continuum model. Once the local transmural pressure starts to approach zero, the fluxes from all vessels are thus stopped and there is no net flow into the local tissue space.

The core region, having the maximum interstitial pressure, is the first place to reach zero transmural pressure. The local interstitial pressure profile is flat, and the resulting Darcy flow is forced to stop. No further fluid accumulation in this region is expected. In addition, the cross sectional area and blood volume remain unchanged at the origin, as shown in Figure 4.10(e). Consequently, there are no further fluid accumulation or blood volume changes when the zero transmural pressure condition has been reached. The transmural pressure condition can never be negative enough to collapse the vessel completely. As time progresses, other tissue regions will experience the same saturation of interstitial pressure. By the end, no vessel collapse events are predicted by the continuum model. This clearly shows the limitation of the continuum model when applied directly to deal with interactions between over-filtration and vessel collapse.

6.5 Discussion

As discussed in Chapter 2, the GJB model can be applied to model water and small solute transport across the BBB (Li, Yuan, Fu 2010). However, pore theory is preferred here for two reasons. First, Li and co-workers only provide a model to quantify the hydraulic permeability and diffusion permeability for molecule movement across the BBB. They do not analyse the dynamic interactions between all Starling forces and the filtration flux because the ion exclusion by the BBB for the GJB model has not been fully investigated. Secondly, there is very limited information available for transvascular exchange modelling of inflamed capillaries, and one of the papers regarding this issue (Levick and Michel 2010) is based on the pore theory. Although it is not directly relevant to the BBB, it is adopted here as the foundation, with some modifications especially for the BBB filtration behaviour.

The involvement of the large pore system here is qualitative based on the observation of re-opening during inflammation (Preston and Foster 1997). The pore re-opening events in other peripheral microvessels during inflammation seems to be physiologically relevant to the damage of the glycocalyx layer, breaks appearing in the tight junction strands, or higher activity of the vesicle transcytosis but the detailed mechanisms require further experimental investigation (Michel and Curry 1999) (Curry 2005). The emerging breaks at the tight junction strands, which were rarely found in intact intercellular clefts, may also correlate with the increase in hydraulic permeability due to increasing the density of the small pores.

In an intact capillary, the plasma salts are highly restricted by the high resistance of the BBB (Abbott and others 2010) to enter brain tissue. In other words, such molecules are osmotically active and exert a greater osmotic pressure than do proteins on the vessel wall to counter-balance the hydraulic pressure drop. Therefore, restrictions to ion passage across the normal BBB are necessary in order to keep the filtration flux as small as possible.

Results from the lumped model show that the dynamics of the system responses to physiological and pathological states are quite different. The time courses in the former condition are essentially stationary and the interstitial pressure, although with some small variations between the two vessels, is largely invariant. On the contrary, the inflamed vessels behave very differently, with a rapid response and a large filtration flux into the tissue. These dramatic changes in the dynamic response as well as the differences in the magnitudes of the filtration flux, suggest a correlation of the local build-up of interstitial pressure and the break-down of the BBB.

During inflammation, the filtration flux via large pores dominates the transvascular transport of water, creating approximately a 10^6 fold rise in the flux from the intact state, despite a relatively small change in hydraulic permeability (150 fold larger). This very large increase in transvascular filtration results partially from the non-linearity of the Starling equation and partially from the introduction of the large pores into the model used here. Whether the break-down of the BBB is a gradual event or step-like, as in the current model, is still unclear. It could become still more complex if the degree of dysfunction of the BBB is related to the physiological status of the endothelium cell and its surrounding cellular structures. Understanding this would require a detail knowledge of cell death and a more detailed mechanism of the molecular structure of the tight junction, so doing this is far beyond the scope of the work presented here.

Since the lumped model is only time dependent, it cannot offer information regarding the spatial variations for the variables of interest. In more realistic 3D simulations, a low value of the hydraulic conductivity of brain tissue of order $O(10^{-16})$ seems to be a necessary condition for vessel collapse to occur. In brain tissue, the interstitial fluid is allowed to pass through torturous flow pathways in the interstitial space. Local tissue fluid accumulation can always

be compromised by flow passage at local boundaries, and hence the larger the hydraulic conductivity the smaller the local fluid accumulation.

Hydraulic conductivity of intact grey matter brain tissue is about an order of $O(10^{-12}\text{-}10^{-14})$, as used in other theoretical studies, (Linninger and others 2008) (Netti and others 1995) (Chen and Sarntinoranont 2007) but no measurements on tissue in the inflamed state have yet been made. Moreover, tissue vascular edema is always accompanied by an increase in the BBB permeability (Unterberg and others 2004), which may result in cell swelling, compressing the rest of the extracellular space, i.e. the interstitium. The volume shrinkage of the interstitial space should be relevant to decreases in the tissue hydraulic conductivity, but a quantitative description remains unknown.

Based on the model predictions, an initial infarction does seem to increase the rate of change of the vessel collapse event. The blockage caused by the core damage does change the flow patterns in the new available flow paths, altering the interstitial pressure distribution in the network. A new pattern of transmural pressure, and thereby of filtration flux in the network, is established. Not only speeding up collapse, the infarction can also increase the number of collapsed vessels, which may imply that infarction is a key factor in vessel collapse events. Since further vessel collapse causes more flow shortage sites in the network, tissue infarction volume can be further expanded. So far, however, this effect has not been investigated in current work.

In the first two models presented above, vessel collapse does occur but the time response is too rapid, about 200-300s, compared with the value of about 1 to 2 hrs, obtained from experiments on rat brain (del Zoppo and Mabuchi 2003). In our simulations, the non-linear intracranial compliance is pressure dependent, and would become much smaller with the pressure rises. This non-linear change in the intracranial compliance creates a further

elevation in the interstitial pressure locally and hence the transmural pressure is further reduced, leading to a change in the time response of the vessels.

In addition, the lack of consideration for local autoregulation here may also cause a discrepancy between the model prediction and the experimental observations. In the circulation system, autoregulation would tend to redistribute the flow by raising local arterial pressure when a flow shortage occurs. This dynamic modulation of the capillary pressure is not considered in the current model, so the transmural pressures will be under-estimated here, leading to a speeding-up in the collapse events when compared to experimental studies.

The best collapse time obtained from the lumped model is 160s, being much smaller than the typical value (3600-7200s) found in the experiments. To give a better match to this time characteristic, a sensitivity test has been performed and two parameters, wall hydraulic permeability, L_p, and the elastance, k_e, can individually lead to the results (1650s and 800s) approaching experimentally based collapse time by reducing their values by a factor of 0.1. It could be possible to physiologically fit the experimental values by merely adjusting both parameters to increase the accuracy of the simulations.

Although the continuum approach is a good way to simplify the flow and transport model in the tissue, it seems to be unable to replicate the vessel collapse post inflammation after an ischemic attack. Under the assumption of locally uniform behaviour in the model, dynamic variations among capillary vessels cannot be modelled, and hence no collapse events are predicted. To remedy this, a new statistically based sub-model which can account for the filtration flux in each individual vessel is thus required. However, this needs further investigation and is one of the suggested directions of future study.

It should be noted here all computations are run on a computer with Intel Core 2 6420 CPU, on a single core and with 2G bytes of memory in Windows XP environment. The computation for filtration/ICP dynamics by the lumped model was executed, for 200,000 timesteps ($\Delta t = 0.01$s), which was completed in 1min. For the 1D continuum model, 200 elements and 200,000 timesteps ($\Delta t = 0.01$s), were used for the filtration/ICP dynamics computation time, which is finished within 25 min. As for the 3D discrete model simulation, the filtration/ICP dynamics computation was executed, using a grid of 40×40×40 elements, for 200,000 timesteps ($\Delta t = 0.01$s), and was completed in 20 hours.

6.6 Conclusion

Vessel collapse is widely found in experiments conducted after reperfusion in the period post ischemic attacks and is regarded as an obstacle to restoration of normal tissue function. Two well known phenomena: the build-up of intracranial pressure and an increase in transvascular transport have been considered together here to investigate if their interaction could lead to the occurrence of vessel collapse during inflammation. The discretised and continuum models have been used to predict the dynamics of the filtration flux and intracranial pressure. Results from the discretised filtration model show that vessel collapse can occur during inflammation when flow movement in the interstitial space is highly impaired. An initial infarction seems to be a risk factor for further collapse. On the contrary, the continuum model is not able to replicate the collapse events due to its inability to capture the localised variability of vessel behaviour, which is the key to providing further fluid accumulation as the transmural pressure approaches its buckling limit.

Chapter 7 Conclusion

7.1 Summary

Directly reconstructing a cerebral microvascular network from real brain tissue involves sample preparation, section scanning, image processing and many other procedures. Using this approach to create networks is accurate but extremely labour intensive and time consuming. Such an approach is impracticable when there is a need for an analysis covering a large number of networks. It is thus very valuable to have an algorithm based model that can create a set of statistically based networks to bypass the complexities required in the direct reconstruction method. To implement this, statistical characteristics such as vessel length and diameter distribution obtained from experimental observations are required to constrain the algorithm, making the resulting artificial network physiologically relevant to small regions of the cerebral microvasculature. To construct and to analyse such networks has been the primary aim of this thesis.

As the kernel of the algorithm proposed here in Chapter 3, the spanning tree method selects connections between existing nodes to form a tree with a minimum total length. Merging two of these trees forms a web-like structure with minimum material cost; this network structure is found to capture the main features of the target length distribution curve. Extra procedures required in this algorithm such as the length filters for regulating arc adding or removing operations and a node planting procedure for new nodes can further refine the length distribution of the resulting network as desired. The artificial network is taken to be a good approximation to cerebral microvascular networks, and can be used in flow and oxygen transport simulations.

Following a similar rationale, given any statistically-based vessel characteristics for any other microvasculature, a set of virtual networks could always be generated through adjustments to

the algorithm (e.g. from MST to SAM) and the tuning of the length filters (e.g. the regulation range and the operation probability) to fit the desired length distribution whereas the vessel diameters can directly be assigned. This shows the flexibility of the basic concept of the present network generation method.

The resulting networks can be used for simulations of a small volume of brain tissue, as the blood flow and tissue oxygen transport patterns were presented and discussed in Chapter 4. In these simulations, different settings in blood viscosity and approximations for wall blood oxygen level have been tested. Only the model with variable viscosity and plasma oxygen level approximation can give the best match in tissue oxygen field to other relevant theoretical and experimental studies although this model would require extra numerical treatments for the flow viscosity interactions and the nonlinear saturation approximation. This confirms the validities and feasibilities of the flow/transport coupled model and of the network generation method when simulating the complex nature of flow-transport in brain network-tissue systems.

The resulting oxygenation field in tissue is irregular due to inhomogeneous distributions of blood oxygen caused by haematocrit variations in the network. By disabling one of the flow source nodes in the network, a flow shortage event can be created to mimic local ischemia. According to the predictions, the oxygen level in the region surrounding the flow shortage network will experience a decrease, after one of the flow sources is turned off, and some of the downstream regions can have a very low oxygen level with values close to hypoxia conditions. Although the surrounding tissue can supply oxygen to the model tissue, the total oxygen input to the model tissue is not sufficient after source removal, reflecting the essential role of blood perfusion in highly localised microvascular oxygen transport.

Flow and oxygen distribution variations amongst different networks are found to be significant at both local and overall scales. Local flow patterns are thus network dependent. One local region in tissue being poorly perfused in one network can be well supplied with sufficient blood flow due to the changes in network patterns, vessel geometry, haematocrit distributions and likewise the oxygenation due to these factors. Similarly, the overall scale features in blood flow and oxygen transport vary from one network to another as predictions for 10 networks exhibit the ratios of the maximum to the minimum values for net flow rate and mean tissue oxygen level are about 8.2 and 3.7 respectively. The oxygenation and blood flow patterns are thus highly influenced by the localised network structures, whose variations lead to substantial variability in the resulting flow and oxygen transport patterns in large scale.

On the other hand, the overall flow features and tissue oxygenation field of a discretised model can be accurately captured by an isotropic porous media model. With a proper estimation of the tissue permeability and other parameters, the proposed continuum model can provide a good large scale approximation to the discretised model in the resulting flow and transport features. Owing to this analogy with a network based model, scale-up of the simulations becomes feasible by conversion of the network information into the lumped parameters required in a continuum model.

Microvessel collapse is widely found in experiments conducted after reperfusion brain tissue post ischemic attacks and is hypothesised here to correlate to two simultaneous events: the build-up of intracranial pressure as well as an increase in transvascular filtration. The discretised and continuum models have both been used to predict the dynamics of the filtration flux and intracranial pressure field. The discretised model can replicate the vessel collapse events when the interstitial fluid movement is highly impaired. An initial infarction seems to promote collapse events. However, the continuum model is not able to replicate the

collapse events due to the inability to capture the variability in vessel properties, which are shown here to be the key to collapse as the transmural pressure approaches the buckling limit.

The final conclusions of this thesis are thus:

1. Networks created by the modified spanning tree method can capture the statistical characteristics deduced from a real microvasculature sample in the temporal lobe of the cerebral cortex. Based on these networks, a flow model with variable viscosity coupled with an oxygen transport model with plasma PO_2 approximation, is able to provide a reasonable estimate for haemodynamics features in the brain tissue. Haematocrit variations in the network play a crucial role in the formation of the irregular flow and oxygenation maps in the brain tissue and vasculature.

2. If the tissue hydraulic conductivity, porosity and wall exchange area can be well estimated from the network based discretised model, a porous media based continuum model can give a good match at a larger length scale to the discretised model predictions in terms of the flow and oxygen transport patterns. The same conversion, however, does not allow the continuum model to replicate the vessel collapse events predicted by the discretised model since its assumption of uniform vessel response fails to account for the variations in the network transvascular filtrations.

3. Flow perfusion is found to be of great importance in the local tissue oxygenation, as predicted by both the discretised and the continuum models. Once one flow source in the network is shut down, the tissue in the flow shortage region immediately suffers from oxygen depletion, the severity of which is dependent on the network oxygen distribution. Some tissue regions have only a very low oxygen level, being close to the threshold of hypoxia, providing a local environment for potential infarction development.

7.2 Future work

The attempt to replace a network by a porous media model can work well for flow and oxygen transport simulations as the resulting predictions are close to those in the available literature. However, the present continuum model cannot describe the individual vessel behaviours in blood space, and hence only a uniform response is predicted as expected. It could be remedied in the future by introducing a vessel-wise statistical sub-model into the blood phase to account for the blood phase haemodynamic changes caused by vessel structure variations. For example, multi-groups of vessel behaviours based on the vessel diameter distribution can be included and hence the vessel variations can be better modelled.

The haemodynamic models proposed here are based on the assumption that the capillary vessel wall is rigid and the flow inside the vessel is steady. In fact, flow and pressure in the capillary are both functions of space and time. To resolve the time varying behaviour for vessel wall and flow, two kinds of 1D model approaches could be considered afterwards. One attempt would be to extend the haemodynamic relationship for each vessel element by replacing a single flow resistance with a compliance, inductance, and resistance. By using simple network analysis, the time response of each vessel could then be resolved in more detail .

On the other hand, vessel deformations can be described by change in cross sectional area, and the continuity and Navier-Stokes equations can then be combined into a wave equation for flow rate or the cross sectional area with a source term affected by pressure gradient and viscous force. With a proper boundary condition at junction nodes in the network, this transient problem is in a closed form and could be solved numerically. For both approaches suggested here, the corresponding fluctuations in oxygen transport in the blood and tissue

space due to the wall vibrations need to be considered, and it would be an interesting topic for future investigations.

The present flow and oxygenation model offers haemodynamic features for the cerebral capillary bed but not for complete vasculature trees because large vessels are not included in this model. With the help of the continuum model, the capillary network can be replaced by a flow phase in a porous media model and large scale simulations for the capillary bed then become feasible. To further analyse the complete vasculature, flow features found in large vessels such as Fahraeus effect and venous compliance must be properly formulated and incorporated into this microvasculature model. This will expand the dimension of the simulation network up to the resolution limit of *in vivo* neural imaging techniques and the simulation results can be directly compared to functional imaging data.

Meanwhile, the network's influences on haemodynamics have been well described in this work but the opposite directional coupling is not considered in this model, in other words, the flow or oxygenation induced vessel structure adaption, like remodelling or autoregulation, which have been investigated theoretically and experimentally elsewhere, could be included in the present model fully to resolve the dynamic interaction between haemodynamics, metabolism and the network geometric and mechanical structure in brain tissue.

Finally, in the ischemic conditions, neurons and astrocytes may undergo certain transitions in cellular states, leading to alterations in the transport properties in the vascular or tissue level. The present model can offer a 3D flow and oxygen supply for a volume of brain tissue but lacks the means to estimate local oxygen metabolism related to cell physiological states after a localised flow shortage has been induced. Therefore the final oxygenation map could be better resolved if the cell death model due to ischemia can be included. Further modelling to

bridge the gap between cellular dynamics and vascular level dynamics will require more detailed physiological knowledge of the underlying.

Overall, both a discretised and continuum statistical based models have been proposed here for modelling the flow and oxygen transport in small volumes of cerebral tissue. Despite their limitations, they have been shown to have a good capability to capture the microvascular level haemodynamics and oxygenation features for the human cerebral cortex and can thus be further used as analytical tools for gaining better knowledge and understanding of cerebral microcirculation.

Appendix A: Discretisations and numerical solutions

In general, the mass transport of a substance, with concentration Φ, in a fluid can be described by the following equation:

$$\frac{\partial \Phi}{\partial t} + \mathbf{V} \cdot \nabla \Phi = \nabla \cdot (D_t \nabla \Phi) + G_S - M_S, \tag{A-1}$$

where $\mathbf{V}$ is the flow field, D_t is the diffusion coefficient for the substance (m^2/s). G_S and M_S are the rates of generation and consumption of the substance respectively ($mM/s/m^3$). Rewriting the equation in an integral form over an infinitesimal volume, gives:

$$\int_V \frac{\partial \Phi}{\partial t} dV + \int_V \mathbf{V} \cdot \nabla(\Phi) dV = \int_V \nabla \cdot (D_t \nabla \Phi) dV + \int_V G_S dV - \int_V M_S dV, \tag{A-2}$$

When using the continuity equation, the mass transport equation can be expressed in conservation form, which can be utilised more easily via discretisation with the Finite Volume Method (Patankar 1980), due to its computational efficiency. In addition, the use of the FVM can preserve the conservative features of the equation, and that is why FVM has been widely adopted in computational fluid dynamics (CFD).

$$\int_V \frac{\partial \Phi}{\partial t} dV + \int_V \nabla \cdot (\mathbf{V}\Phi) dV = \int_V \nabla \cdot (D_t \nabla \Phi) dV + \int_V G_S dV - \int_V M_S dV. \tag{A-3}$$

In this method, the field is divided into many small volumes, which are the calculation units when solving the discretised equation. The volume integrals in a partial differential equation containing a divergence term are converted to surface integrals using the divergence theorem. Thus adjacent finite volumes share the same boundary fluxes guaranteeing the conservation of concentration throughout the volume under simulation.

Either structured or unstructured grids can be used to represent the discretised field using the finite volume method. However, a uniform Cartesian grid system and the MAC (Harlow and Welsh 1965) variable arrangement are chosen here, where the variables of interest are located in a stagger manner with flow field variables, as shown in Figure A-1.

$$\int_V \frac{\partial \Phi}{\partial t} dV = \int_A -(\mathbf{V}\Phi)\mathbf{n}dA + \int_A D_t(\nabla\Phi)\mathbf{n}dA + \int_V G_S dV - \int_V M_S dV \tag{A-4}$$

The three dimensional computation domain with dimension $L_x \times L_y \times L_z$ can be divided into a number of small uniform voxels, with dimension $\Delta V = \Delta x \times \Delta y \times \Delta z$. Concentration, generation/consumption terms, and diffusion coefficient are thus sampled by a set of grids in space which are located at the centre of each finite volume element, being located at $X_C(i,j,k) = \left((i-0.5)\Delta x, (j-0.5)\Delta y, (k-0.5)\Delta z\right)$.

On the other hand, the flow field $\mathbf{V} = (u, v, w)$ is represented in grids which are staggered with the grids representing the pressure or concentration field. For a given voxel, flow passing the six surfaces of the volume is stored at the surface centre. For example, the coordinate systems $X_u(i,j,k) = \left((i)\Delta x, (j-0.5)\Delta y, (k-0.5)\Delta z\right)$, $X_v(i,j,k) = \left((i-0.5)\Delta x, (j)\Delta y, (k-0.5)\Delta z\right)$ and $X_w(i,j,k) = \left((i-0.5)\Delta x, (j-0.5)\Delta y, (k)\Delta z\right)$ are applied for the flow velocity in the *x*, *y*, and *z* directions respectively.

To resolve the temporal and spatial oxygen field, Eq.A-4 can be directly used, giving the oxygen transport equation for oxygenation in tissue:

$$\int_V \frac{\partial C}{\partial t} dV = \int_A \left[-VC + D_t(\nabla C)\right]\mathbf{n}dA + \int_V G_S dV - \int_V M_S dV \tag{A-5}$$

The grid arrangements for the scalar fields and the velocity fields are shown in Figure A.1.

(a) (b)

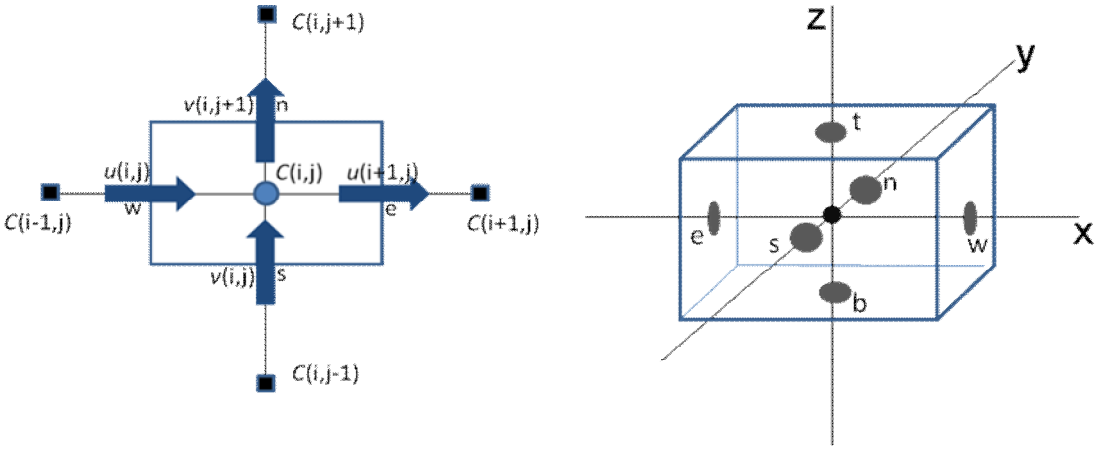


Figure A.1 Spatial arrangement of grids for flow field and concentration (a) 2D ; (b) 3D

For example, the oxygen concentration at $X_C(i,j,k)=\left((i-0.5)\Delta x,(j-0.5)\Delta y,(k-0.5)\Delta z\right)$ is the spatial average of the concentration field for the entire voxel, and the oxygen concentration is stored in the $N_x \times N_y \times N_z$ matrix with element $C(i,j,k)$. Similarly, $G_S(i,j,k)$, $M_S(i,j,k)$ and $\dfrac{\partial C(i,j,k)}{\partial t}$ can be expressed as follows:

$$G_S(i,j,k) \cong \int_{\Delta V(i,j,k)} G_S dV = \int_w^e \int_s^n \int_b^t G_S dV ,$$

$$M_S(i,j,k) \cong \int_{\Delta V(i,j,k)} M_S dV = \int_w^e \int_s^n \int_b^t M_S dV , \qquad \text{(A-6)}$$

$$\frac{\partial C(i,j,k)}{\partial t} \cong \int_{\Delta V(i,j,k)} \frac{\partial C}{\partial t} dV = \int_w^e \int_s^n \int_b^t \frac{\partial C}{\partial t} dV .$$

Under the assumption of the FVM, the surface integral can be approximated by the surface average flux multiplied by cross sectional area and the closed area integrals are simply the summation of the surface integral for the 6 surfaces, with the indices *m*= *e, w, n, s, t, b*:

$$\int_A [-\mathbf{V}C]\mathbf{n}dA \cong \sum_m -(\mathbf{V}C)_m n\Delta A,$$
$$\int_A [D_t(\nabla C)]\mathbf{n}dA \cong \sum_m (D_t(\nabla C))_m n\Delta A. \quad \text{(A-7)}$$

For a given voxel, the mass transport equation (A-5) can be discretised as follows:

$$\frac{\partial C(i,j,k)}{\partial t}\Delta V = \sum_m -(\mathbf{V}C)_m n\Delta A + \sum_m (D_t(\nabla C))_m n\Delta A + G_S(i,j,k)\Delta V + M_S(i,j,k)\Delta V, \quad \text{(A-8)}$$

where the first and second terms in the RHS of Eq. A-8 are the convection and the diffusion terms respectively. The convection terms can be expanded as follows:

$$\sum_m -(\mathbf{V}C)_m n\Delta A_m = -[uC]_w^e \Delta y\Delta z - [vC]_s^n \Delta x\Delta z - [wC]_b^t \Delta x\Delta y, \quad \text{(A-9)}$$

which can be further expressed as:

$$\begin{aligned}&\sum_m -(\mathbf{V}C)_m n\Delta A_m \\ &= -[u(i+1,j,k)\cdot C_e - u(i,j,k)\cdot C_w]\Delta y\Delta z \\ &\quad -[v(i,j+1,k)\cdot C_n - v(i,j,k)\cdot C_s]\Delta x\Delta z \\ &\quad -[w(i,j,k+1)\cdot C_s - w(i,j,k)\cdot C_b]\Delta y\Delta x\end{aligned}. \quad \text{(A-10)}$$

The concentration at the surface centre can be approximated by the upwind scheme for numerical stability. The value of the surface concentration is taken as the value in the upwind direction, i.e. giving the concentration expression at the east and west surfaces of voxel with centre at $X_C(i,j,k)$ as follows, likewise for other term:.

$$\begin{aligned}C_e &= \max(0,u(i+1,j,k))\cdot C(i,j,k) - \min(0,u(i+1,j,k))\cdot C(i+1,j,k) \\ C_w &= \max(0,u(i,j,k))\cdot C(i-1,j,k) - \min(0,u(i,j,k))\cdot C(i,j,k)\end{aligned}, \quad \text{(A-11)}$$

The diffusion terms are evaluated by the central difference method, giving:

$$\begin{aligned}\sum_m \left(D_t(\nabla C)\right)_m n\Delta A &= \sum_x \left(D_t(\nabla C)\right)_w^e \Delta A_x + \sum_y \left(D_t(\nabla C)\right)_s^n \Delta A_y + \sum_z \left(D_t(\nabla C)\right)_b^t \Delta A_z \\ &= \sum_x \left((D_t \frac{\partial C}{\partial x})_e - (D_t \frac{\partial C}{\partial x})_w \right) \Delta A_x \\ &+ \sum_y \left((D_t \frac{\partial C}{\partial y})_n - (D_t \frac{\partial C}{\partial y})_s \right) \Delta A_y \\ &+ \sum_z \left((D_t \frac{\partial C}{\partial z})_t - (D_t \frac{\partial C}{\partial z})_b \right) \Delta A_z \end{aligned} , \quad \text{(A12)}$$

where:

$$\begin{aligned}(D_t \frac{\partial C}{\partial x})_e \Delta A_x &= 0.5(D_t(i+1,j,k) + D_t(i,j,k)) \cdot \frac{C(i+1,j,k) - C(i,j,k)}{\Delta x} \Delta y \Delta z \\ (D_t \frac{\partial C}{\partial x})_s \Delta A_x &= 0.5(D_t(i,j,k) + D_t(i-1,j,k)) \cdot \frac{C(i,j,k) - C(i-1,j,k)}{\Delta x} \Delta y \Delta z \\ (D_t \frac{\partial C}{\partial x})_n \Delta A_y &= 0.5(D_t(i,j+1,k) + D_t(i,j,k)) \cdot \frac{C(i,j+1,k) - C(i,j,k)}{\Delta y} \Delta x \Delta z \\ (D_t \frac{\partial C}{\partial x})_s \Delta A_y &= 0.5(D_t(i,j,k) + D_t(i,j-1,k)) \cdot \frac{C(i,j,k) - C(i,j-1,k)}{\Delta y} \Delta x \Delta z \\ (D_t \frac{\partial C}{\partial x})_t \Delta A_z &= 0.5(D_t(i,j,k+1) + D_t(i,j,k)) \cdot \frac{C(i,j,k+1) - C(i,j,k)}{\Delta z} \Delta x \Delta y \\ (D_t \frac{\partial C}{\partial x})_b \Delta A_z &= 0.5(D_t(i,j,k) + D_t(i,j,k-1)) \cdot \frac{C(i,j,k) - C(i,j,k-1)}{\Delta z} \Delta x \Delta y \end{aligned} . \quad \text{(A-13)}$$

Now that one can express the derivatives and the values at any given time through the FVM, the next step is to march through time to solve the time dependent partial differential equations numerically. The time derivatives are approximated by the second order Crank-Nicholson scheme for the diffusion terms, Adams-Bashforth scheme for the convection terms, giving the following equation for variable $C(i,j,k)$ at time step *n* and time step *n*+1:

$$\begin{aligned}&\frac{C^{n+1}(i,j,k) - C^n(i,j,k)}{\Delta t} \Delta V \\ &= \sum_m -\left(1.5\mathbf{V}^n C^n - 0.5\mathbf{V}^{n-1} C^{n-1}\right)_m n\Delta A \\ &+ \sum_m 0.5\left(D_t(\nabla C^n) + D_t(\nabla C^{n+1})\right)_m n\Delta A \\ &+ G_S^n(i,j,k)\Delta V + M_S^n(i,j,k)\Delta V \end{aligned} . \quad \text{(A-14)}$$

Eq.A-14 can be re-arranged by moving the terms with the variables at time step n+1 onto the LHS and those at time steps n and n-1 onto the RHS. Therefore, it transforms to Eq. A-15, where the terms on the RHS are the values at the time step n and n-1, all of which are known:

$$\begin{aligned}
&(\Delta V/\Delta t)C^{n+1}(i,j,k) - \sum_m \left(D_t(\nabla C^{n+1})\right)_m n\Delta A \\
&= (\Delta V/\Delta t)C^{n}(i,j,k) \\
&+ \sum_m -\left(1.5\mathbf{V}^n C^n - 0.5\mathbf{V}^{n-1}C^{n-1}\right)_m n\Delta A \\
&+ \sum_m \left(D_t(\nabla C^n)\right)_m n\Delta A \\
&+ G_S^n(i,j,k)\Delta V + M_S^n(i,j,k)\Delta V
\end{aligned} \quad . \tag{A-15}$$

To obtain C^{n+1}, or in other words, the vector of N unknowns, **u**, it is necessary to solve the linear equations for N unknowns based on the collective terms f^n from the previous time steps. Arranging Eq.A-15 leads to the linear system **Tu=f**, where **T** is a $N \times N$ matrix ($N = N_x \times N_y \times N_z$) with 7 diagonals, **u** is the unknown vector for concentration at intermediate time step n+1, and **f** is the source term vector at time step n:

$$\begin{bmatrix} & & & & & & \\ & & & & & & \\ & & & & & & \\ & & & & & & \\ & & & & & & \\ & & & & & & \\ & & & & & & \end{bmatrix} \begin{bmatrix} C_1^{n+1} \\ C_2^{n+1} \\ : \\ C_{N-1}^{n+1} \\ C_N^{n+1} \end{bmatrix} = \begin{bmatrix} f_1^n \\ f_2^n \\ : \\ f_{N-1}^n \\ f_N^n \end{bmatrix}. \tag{A-16}$$

Although the **T** matrix is a sparse matrix, unlike the conductance matrix **B** used in the flow calculation, it is well structured with a seven-diagonal matrix structure. For pure diffusion problems, as encountered in the oxygen transport equation in Chapter 4 and the pressure Poisson equation in Chapter 6, the systems can be solved by a Poisson solver, such as a conjugate gradient method (CG) (Vandervorst 1992), due to the symmetric matrix structure.

If the flow effect is considered in the mass transport equation, the matrix is no longer symmetric, so as used in the continuum model, a biconjugate gradient stabilised method (BCGSTAB) (Vandervorst 1992) is adopted here to solve the linear system. The matrix is solved in a non-stationary manner where the approximate solutions and the errors are updated in each iteration until the error in the final solution is minimised.

Once the variable field of n+1 step is solved, the computation advances to the next time step. To continue this way, the dynamics of the oxygen field can be resolved. It should be noted that all of the numerical procedures in this thesis were all implemented in FORTRAN 77 and run in XP environment.

In 3D simulations for mass transport equations, grid refinement test were performed to investigate the accuracy dependence on the grid number (or size). As shown in Fig.A2(a), the time courses of the spatial averaged tissue oxygenation for the first discretised transport model (Chapter 4) shows that the prediction values converges as the grid number increases. The central voxel oxygen level, Fig.A2(b), shares a similar characteristics of grid size effect on the predictions. The 20×20×20 grid system creates the predictions with over-estimation (<5%) but as the grid size is refined further to half of its original size (40×40×40), the resulting values become overlap with the most accurate values in the test. Based on these two plots, the refined grid system with 40×40×40 grids is sufficient to provide the values very close to the best results (<3%) obtained from 80×80×80 grids and we thus take 40×40×40 as the standard grid setting for the other 3D simulations.

(a) (b)

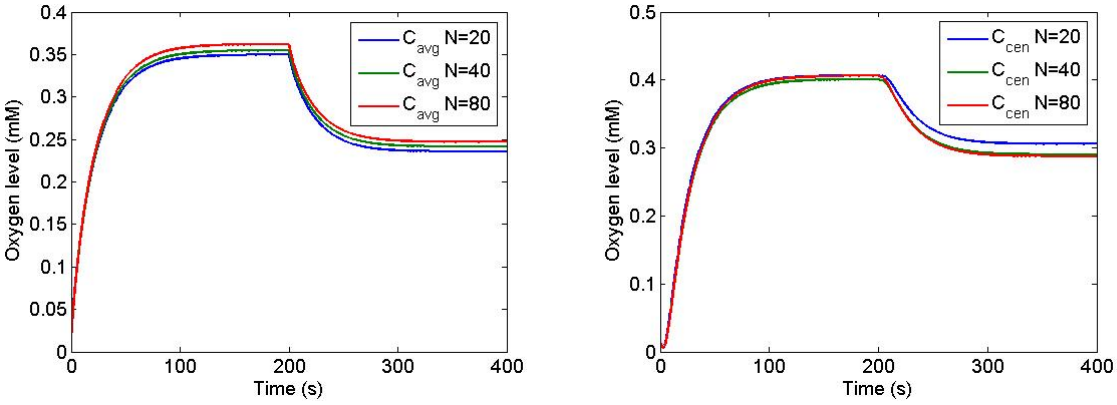


Figure A.2 Time courses for different grid systems for (a) averaged tissue oxygenation; (b) centre voxel oxygenation.

Appendix B: Filtration

B-1 Solute transport across the capillary membrane

Changes in the wall transport properties may be accompanied by changes in the physiological state of the tissue. Abnormal Starling forces can cause the development of certain pathological states. For example, edema may result from excessive fluid filtration into the interstitial space when the endothelium is inflamed.

Consider blood and interstitial fluid separated by a capillary membrane of thickness L, the solutes being passively carried by the filtration bulk flow (convection) and moving directly through molecular collision (diffusion). The solute transport across the capillary can be described by the O.D.E. for the solute concentration $C(x)$ across the capillary wall (Zhang and others 2006):

$$-P_d \frac{d^2C}{dx^2} + u(1-\sigma)\frac{dC}{dx} = 0, \tag{B-1}$$

where x is the location inside the vessel wall, P_d is the diffusion permeability of solute, u is the average flow velocity and σ is the osmotic reflection coefficient. The term $u(1-\sigma)$ represents the effective velocity of the solute convection. By introducing a new variable $X = x/L$, Eq.B-1 can be transformed to give:

$$\frac{d^2C}{dX^2} - Pe\frac{dC}{dX} = 0, \tag{B-2}$$

where $X = 0$ is the location of the membrane-lumen interface and $X = 1$ is the location of the interface of membrane-interstitial space. The modified Peclet number, $Pe = u(1-\sigma)L/P_d$,

represents the ratio of the advection to diffusion transport driving forces for the solute. The solution to this equation is of the form:

$$C = c_1 + c_2 \exp(PeX), \tag{B-3}$$

subject to two boundary conditions:

$$C(0) = C_c, \tag{B-4}$$

$$C(1) = C_i,.$$

The solute concentration at the lumen side is set to be the capillary concentration, C_c, which is a constant. However, the concentration at the albumen side, C_i, takes the form $C_i = J_S / J_V$, as the ratio of solute flow rate to water flow rate. Because in the steady state, the filtration continuously drives water and solute into the tissue space, the amounts of those materials occupying the local region at the ablumen side are estimated by $J_S \cdot dt$ (for the solute), and $J_V \cdot dt$ (for the water) for a small time interval *dt*, and hence the ratio of these two terms is the solute concentration at the albumen side. Here the solute flow rate is simply the flux, obtained by taking derivative of Eq. B-1, multiplied by the exchange area:

$$\begin{aligned} J_S &= A\left(-\frac{P_d}{L}\frac{dC}{dX} + u(1-\sigma)C \right) \\ &= A\left(-\frac{P_d}{L}\left[Pe \cdot c_2 \exp(PeX)\right] + u(1-\sigma)\left[c_1 + c_2 \exp(PeX)\right] \right). \\ &= Au(1-\sigma)c_1 \end{aligned} \tag{B-5}$$

Also, the water flow rate across the capillary membrane is equal to:

$$J_V = Au. \tag{B-6}$$

Thus, the boundary conditions can be rewritten as follows:

$$C(0) = C_c, \tag{B-7}$$

$$C(1) = (1-\sigma)c_1.$$

Thus determining the solution:

$$C(X) = C_c e^{Pe}/(e^{Pe}-\sigma) - \sigma C_c/(e^{Pe}-\sigma)\cdot e^{(PeX)}. \tag{B-8}$$

According to the Morse equation, for a dilute solution, the osmotic pressure, Π, is linearly proportional to the solute concentration:

$$\Pi = iCRT, \tag{B-9}$$

where i is the Van't Hoff factor, C is the solute molarity, R is the gas constant and T is the temperature in Kelvin. The osmotic pressure drop across the capillary wall can also be expressed as a function of the osmotic pressure at the lumen side:

$$\begin{aligned}\Delta\Pi &= (C_c - C_i)\cdot iRT \\ &= \left[\sigma C_c \frac{1-e^{-Pe}}{1-\sigma e^{-Pe}}\right]\cdot iRT. \\ &= \sigma\Pi_c \frac{1-e^{-Pe}}{1-\sigma e^{-Pe}}\end{aligned} \tag{B-10}$$

Substituting Eq.B-10 into Starling's equation, gives the following form, reproduced as Eq.6-4:

$$J_{VA} = L_P\left[(P_c - P_i) - \sigma^2\Pi_c \frac{1-e^{-Pe}}{1-\sigma e^{-Pe}}\right]. \tag{B-11}$$

B-2 The parameters in pore theory

Based on pore theory, wall hydraulic permeability, L_P, can be defined as a function of pore population and pore radius through use of Poiseuille's law:

$$L_P = \frac{\pi r^4 N}{\Delta x 8 \mu}, \tag{B-12}$$

where r is the pore radius, N is the number of the pores per unit area of the membrane, Δx is the length of the pathway and μ is the fluid viscosity in the pores. Since both small and large pore systems can transport the water and the solute in parallel, the total wall hydraulic permeability is the sum of the effective wall hydraulic permeability for each individual pore system. Once the wall hydraulic permeability, $(L_P)_S$, and pore radius, $(r)_S$, for small pathways have been determined, the small pore number density, $(N/\Delta x)_S$, can be calculated accordingly, likewise $(L_P)_L$ and $(N/\Delta x)_L$, for the large pore system. The partition coefficient, λ_P, is a measure of the area available for cross membrane transport when the pore pathways are occupied by the solute particle. It is a function of the ratio of the solute radius, a, to pore radius:

$$\lambda_P = \left(1 - \frac{a}{r}\right)^2. \tag{B-13}$$

According to the model (Levick and Michel 2010), the reflection coefficient for each pore pathway has the form:

$$\sigma = (1 - \lambda_P)^2. \tag{B-14}$$

The diffusion permeability of a solute can thus be determined for each set of pores from a function of solute-pore size ratio, *a/r*, and the diffusion coefficient, *D*, for the solute in an aqueous solution:

$$P_d = \frac{\pi r^2 N}{\Delta x} f\left(\frac{a}{r}\right) \lambda_P D, \tag{B-15}$$

where the function $f\left(\frac{a}{r}\right)$ is a polynomial of $\left(\frac{a}{r}\right)$:

$$f\left(\frac{a}{r}\right)=1-2.1\left(\frac{a}{r}\right)+2.09\left(\frac{a}{r}\right)^{3}-0.95\left(\frac{a}{r}\right)^{5}. \quad \text{(B-16)}$$

It should be noted that Eq.B-13 – B-16, adopted in the present filtration model, are also quoted by (Levick and Michel 2010).

Appendix C: Publications

Journal papers:

Su, S.-W., and Payne, S.J. Modelling the no-reflow phenomenon in the human cerebral microvasculature. (submitted).

Su, S.-W., and Payne, S.J. Investigating blood flow patterns in the human cerebral microvasculature through discretised and continuum models. (submitted).

Su, S.-W., Catherall, M.G.F. and Payne, S.J. The influence of network structure on the transport of blood in the human cerebral microvasculature, *Microcirculation*, 2012 (in press)

Conference papers:

Su, S.-W. and Payne, S.J. A two phase model of oxygen transport in cerebral tissue. Proceedings of 31st IEEE EMBS conference, Minneapolis, USA, September 2009.

Su, S.-W. and Payne, S.J. Influence of the microvasculature on oxygen transport in human brain tissue. Proceedings of 2nd Micro and Nano Flows conference, London, UK, September 2009.

References

Abbott NJ, Patabendige AA, Dolman DE, Yusof SR, Begley DJ. 2010. Structure and function of the blood-brain barrier. Neurobiol Dis 37(1):13-25.

Acker T and Acker H. 2004. Cellular oxygen sensing need in CNS function: Physiological and pathological implications. J Exp Biol 207(Pt 18):3171-88.

Adamson RH and Michel CC. 1993. Pathways through the intercellular clefts of frog mesenteric capillaries. J Physiol 466:303-27.

Alarcon T, Byrne HM, Maini PK. 2003. A cellular automaton model for tumour growth in inhomogeneous environment. J Theor Biol 225(2):257-74.

Assad F, Schultheiss R, Leniger-Follert E, Wullenweber R. 1984. Measurement of local oxygen partial pressure (pO2) of the brain cortex in case of brain tumors. Adv Neurosurg (12):263-70.

Baish JW, Netti PA, Jain RK. 1997. Transmural coupling of fluid flow in microcirculatory network and interstitium in tumors. Microvasc Res 53(2):128-41.

Beard DA. 2001. Computational framework for generating transport models from databases of microvascular anatomy. Ann Biomed Eng 29(10):837-43.

Beard DA and Bassingthwaighte JB. 2000. Advection and diffusion of substances in biological tissues with complex vascular networks. Ann Biomed Eng 28(3):253-68.

Beard DA, Schenkman KA, Feigl EO. 2003. Myocardial oxygenation in isolated hearts predicted by an anatomically realistic microvascular transport model. Am J Physiol Heart Circ Physiol 285(5):H1826-36.

Bolognese P, Miller JI, Heger IM, Milhorat TH. 1993. Laser-doppler flowmetry in neurosurgery. J Neurosurg Anesthesiol 5(3):151-8.

Bowler JV and Hachinski V. 2003. Vascular cognitive impairment: Preventable dementia. Oxford: Oxford University Press.

Buxton RB. 2005. Quantifying CBF with arterial spin labeling. J Magn Reson Imaging 22(6):723-6.

Buxton RB, Wong EC, Frank LR. 1998. Dynamics of blood flow and oxygenation changes during brain activation: The balloon model. Magn Reson Med 39(6):855-64.

Carmeliet P. 2005. Angiogenesis in life, disease and medicine. Nature 438(7070):932-6.

Cassot F, Lauwers F, Fouard C, Prohaska S, Lauwers-Cances V. 2006. A novel three-dimensional computer-assisted method for a quantitative study of microvascular networks of the human cerebral cortex. Microcirculation 13(1):1-18.

Cenic A, Nabavi DG, Craen RA, Gelb AW, Lee TY. 2000. A CT method to measure hemodynamics in brain tumors: Validation and application of cerebral blood flow maps. AJNR Am J Neuroradiol 21(3):462-70.

Chandler R and Northrop P. 2003. FORTRAN Random number generation **(**PROGRAM) http://www.homepages.ucl.ac.uk/~ucakarc/work/software/randgen.f [computer program]. .

Chaplain MAJ, McDougall SR, Anderson ARA. 2006. Mathematical modeling of tumor-induced angiogenesis. Annu Rev Biomed Eng 8:233-57.

Chen X, Buerk DG, Barbee KA, Jaron D. 2007. A model of NO/O2 transport in capillary-perfused tissue containing an arteriole and venule pair. Ann Biomed Eng 35(4):517-29.

Chen XM and Sarntinoranont M. 2007. Biphasic finite element model of solute transport for direct infusion into nervous tissue. Ann Biomed Eng 35:2145-58.

Chui HC, Victoroff JI, Margolin D, Jagust W, Shankle R, Katzman R. 1992. Criteria for the diagnosis of ischemic vascular dementia proposed by the state of california alzheimer's disease diagnostic and treatment centers. Neurology 42(3 Pt 1):473-80.

Cope M and Delpy DT. 1988. System for long-term measurement of cerebral blood and tissue oxygenation on newborn infants by near infra-red transillumination. Med Biol Eng Comput 26(3):289-94.

Curry FE and Michel CC. 1980. A fiber matrix model of capillary permeability. Microvasc Res 20(1):96-9.

Curry FR. 2005. Microvascular solute and water transport. Microcirculation 12(1):17-31.

Curry FR and Adamson RH. 2010. Vascular permeability modulation at the cell, microvessel, or whole organ level: Towards closing gaps in our knowledge. Cardiovasc Res 87(2):218-29.

Dawant B, Levin M, Popel AS. 1986. Effect of dispersion of vessel diameters and lengths in stochastic networks .1. modeling of microcirculatory flow. Microvasc Res 31(2):203-22.

Deb P, Sharma S, Hassan KM. 2010. Pathophysiologic mechanisms of acute ischemic stroke: An overview with emphasis on therapeutic significance beyond thrombolysis. Pathophysiology 17(3):197-218.

del Zoppo GJ and Mabuchi T. 2003. Cerebral microvessel responses to focal ischemia. J Cereb Blood Flow Metab 23(8):879-94.

Dunn JF and Swartz HM. 2003. In vivo electron paramagnetic resonance oximetry with particulate materials. Methods 30(2):159-66.

Duvernoy HM, Delon S, Vannson JL. 1981. Cortical blood vessels of the human brain. Brain Res Bull 7(5):519-79.

Fahraeus R. 1929. The suspension stability of the blood. Physiol Rev 9(2):241-74.

Fahraeus R and Lindqvist T. 1931. The viscosity of the blood in narrow capillary tubes. Am J Physiol 96(3):562-8.

Fraser PA, Dallas AD, Davies S. 1990. Measurement of filtration coefficient in single cerebral microvessels of the frog. J Physiol 423:343-61.

Fu B, Curry FR, Adamson RH, Weinbaum S. 1997. A model for interpreting the tracer labeling of interendothelial clefts. Ann Biomed Eng 25(2):375-97.

Fu BM, Curry FE, Weinbaum S. 1995. A diffusion wake model for tracer ultrastructure-permeability studies in microvessels. Am J Physiol 269(6 Pt 2):H2124-40.

Fu BM, Weinbaum S, Tsay RY, Curry FE. 1994. A junction-orifice-fiber entrance layer model for capillary permeability: Application to frog mesenteric capillaries. J Biomech Eng 116(4):502-13.

Gaehtgens P. 1980. Flow of blood through narrow capillaries - rheological mechanisms determining capillary hematocrit and apparent viscosity. Biorheology 17(1-2):183-9.

Gafiychuk VV and Lubashevsky IA. 2001. On the principles of the vascular network branching. J Theor Biol 212(1):1-9.

Gold G, Kovari E, Herrmann FR, Canuto A, Hof PR, Michel JP, Bouras C, Giannakopoulos P. 2005. Cognitive consequences of thalamic, basal ganglia, and deep white matter lacunes in brain aging and dementia. Stroke 36(6):1184-8.

Grote J, Laue O, Eiring P, Wehler M. 1996. Evaluation of brain tissue O2 supply based on results of PO2 measurements with needle and surface microelectrodes. J Auton Nerv Syst 57(3):168-72.

Grotte G. 1956. Passage of dextran molecules across the blood-lymph barrier. Acta Chir Scand Suppl 211:1-84.

Guibert R, Fonta C, Plouraboue F. 2010. Cerebral blood flow modeling in primate cortex. J Cereb Blood Flow Metab 30(11):1860-73.

Guyton AC and Hall JE. 2006.
Textbook of medical physiology. 11th ed. Philadelphia, Pa.: Saunders/Elsevier.

Hakamata Y, Ito U, Hanyu S, Yoshida M. 1995. Long-term high-colloid oncotic therapy for ischemic brain edema in gerbils. Stroke 26(11):2149-53.

Harrison RV, Harel N, Panesar J, Mount RJ. 2002. Blood capillary distribution correlates with hemodynamic-based functional imaging in cerebral cortex. Cereb Cortex 12(3):225-33.

Heiss WD. 2000. Ischemic penumbra: Evidence from functional imaging in man. J Cereb Blood Flow Metab 20(9):1276-93.

Hoffman WE, Charbel FT, Edelman G. 1996. Brain tissue oxygen, carbon dioxide, and pH in neurosurgical patients at risk for ischemia. Anesth Analg 82(3):582-6.

Hogg, R., Craig, A. 1978. *Introduction to mathematical statistics*. 4th ed. New York: Macmillan Publishing Co., Inc.

Hsu R and Secomb TW. 1989. A green's function method for analysis of oxygen delivery to tissue by microvascular networks. Math Biosci 96(1):61-78.

Hyde JS, Biswal BB, Jesmanowicz A. 2001. High-resolution fMRI using multislice partial k-space GR-EPI with cubic voxels. Magn Reson Med 46(1):114-25.

Iadecola C. 2010. The overlap between neurodegenerative and vascular factors in the pathogenesis of dementia. Acta Neuropathol 120(3):287-96.

Iadecola C. 2004. Neurovascular regulation in the normal brain and in alzheimer's disease. Nat Rev Neurosci 5(5):347-60.

Iadecola C and Nedergaard M. 2007. Glial regulation of the cerebral microvasculature. Nat Neurosci 10(11):1369-76.

Jellinger KA. 2008. Morphologic diagnosis of "vascular dementia" - A critical update. J Neurol Sci 270(1-2):1-12.

Jiang C, Agulian S, Haddad GG. 1991. O2 tension in adult and neonatal brain slices under several experimental conditions. Brain Res 568(1-2):159-64.

Jones EA, le Noble F, Eichmann A. 2006. What determines blood vessel structure? genetic prespecification vs. hemodynamics. Physiology (Bethesda) 21:388-95.

Kandel ER, Schwartz JH, Jessell TM. 2000. Principles of neural science. 4th ed. New York: McGraw-Hill.

Kassab GS, Rider CA, Tang NJ, Fung YC. 1993. Morphometry of pig coronary arterial trees. Am J Physiol 265(1 Pt 2):H350-65.

Khaled ARA and Vafai K. 2003. The role of porous media in modeling flow and heat transfer in biological tissues. Int J Heat Mass Transfer 46(26):4989-5003.

Khanafer K, Vafai K, Kangarlu A. 2003. Computational modeling of cerebral diffusion-application to stroke imaging. Magn Reson Imaging 21(6):651-61.

Kimelberg HK. 2004. Water homeostasis in the brain: Basic concepts. Neuroscience 129(4):851-60.

King's College London, London School of Economics. 2007. Dementia UK the full report. Alzheimer's Society 2007.

Kohling R, Greiner C, Wolfer J, Wassmann H, Speckmann EJ. 1998. Optical monitoring of PO2 changes and simultaneous recording of bioelectric activity in human and animal brain slices. J Neurosci Methods 85(2):181-6.

Kolev NI. 2007. Multiphase flow dynamics 1. 3rd ed. Springer.

Kovari E, Gold G, Herrmann FR, Canuto A, Hof PR, Michel JP, Bouras C, Giannakopoulos P. 2004. Cortical microinfarcts and demyelination significantly affect cognition in brain aging. Stroke 35(2):410-4.

Krogh A. 1921. Studies on the physiology of capillaries: II. the reactions to local stimuli of the blood-vessels in the skin and web of the frog. J Physiol 55(5-6):412-22.

Kudomi N, Hayashi T, Watabe H, Teramoto N, Piao R, Ose T, Koshino K, Ohta Y, Iida H. 2009. A physiologic model for recirculation water correction in CMRO2 assessment with 15O2 inhalation PET. J Cereb Blood Flow Metab 29(2):355-64.

Kurth CD, Steven JM, Benaron D, Chance B. 1993. Near-infrared monitoring of the cerebral circulation. J Clin Monit 9(3):163-70.

Kwong KK, Belliveau JW, Chesler DA, Goldberg IE, Weisskoff RM, Poncelet BP, Kennedy DN, Hoppel BE, Cohen MS, Turner R. 1992. Dynamic magnetic resonance imaging of human brain activity during primary sensory stimulation. Proc Natl Acad Sci U S A 89(12):5675-9.

Landis HR. 1927. Laboratory and clinical methods. Trans Am Climatol Clin Assoc 43:134-43.

Lauwers F, Cassot F, Lauwers-Cances V, Puwanarajah P, Duvernoy H. 2008. Morphometry of the human cerebral cortex microcirculation: General characteristics and space-related profiles. Neuroimage 39(3):936-48.

Lee RM. 1995. Morphology of cerebral arteries. Pharmacol Ther 66(1):149-73.

Levick JR. 1987. Flow through interstitium and other fibrous matrices. Q J Exp Physiol 72(4):409-37.

Levick JR and Michel CC. 2010. Microvascular fluid exchange and the revised starling principle. Cardiovasc Res .

Levin M, Dawant B, Popel AS. 1986. Effect of dispersion of vessel diameters and lengths in stochastic networks .2. modeling of microvascular hematocrit distribution. Microvasc Res 31(2):223-34.

Ley K, Pries AR, Gaehtgens P. 1986. Topological structure of rat mesenteric microvessel networks. Microvasc Res 32(3):315-32.

Li G, Yuan W, Fu BM. 2010. A model for the blood–brain barrier permeability to water and small solutes. J Biomech 43(11):2133-40.

Linninger AA, Somayaji MR, Mekarski M, Zhang LB. 2008. Prediction of convection-enhanced drug delivery to the human brain. J Theor Biol 250(1):125-38.

Lipowsky HH and Zweifach BW. 1974. Network analysis of microcirculation of cat mesentery. Microvasc Res 7(1):73-83.

Lipton P. 1999. Ischemic cell death in brain neurons. Physiol Rev 79(4):1431-568.

Liu KJ, Gast P, Moussavi M, Norby SW, Vahidi N, Walczak T, Wu M, Swartz HM. 1993. Lithium phthalocyanine: A probe for electron paramagnetic resonance oximetry in viable biological systems. Proc Natl Acad Sci U S A 90(12):5438-42.

Lo LW, Koch CJ, Wilson DF. 1996. Calibration of oxygen-dependent quenching of the phosphorescence of pd-meso-tetra (4-carboxyphenyl) porphine: A phosphor with general application for measuring oxygen concentration in biological systems. Anal Biochem 236(1):153-60.

Logothetis NK and Wandell BA. 2004. Interpreting the BOLD signal. Annu Rev Physiol 66:735-69.

Lorthois S, Cassot F, Lauwers F. 2011a. Simulation study of brain blood flow regulation by intra-cortical arterioles in an anatomically accurate large human vascular network. part II: Flow variations induced by global or localized modifications of arteriolar diameters. Neuroimage 54(4):2840-53.

Lorthois S, Cassot F, Lauwers F. 2011b. Simulation study of brain blood flow regulation by intra-cortical arterioles in an anatomically accurate large human vascular network: Part I: Methodology and baseline flow. Neuroimage 54(2):1031-42.

Mandeville JB, Marota JJ, Ayata C, Zaharchuk G, Moskowitz MA, Rosen BR, Weisskoff RM. 1999. Evidence of a cerebrovascular postarteriole windkessel with delayed compliance. J Cereb Blood Flow Metab 19(6):679-89.

Mantzaris NV, Webb S, Othmer HG. 2004. Mathematical modeling of tumor-induced angiogenesis. J Math Biol 49(2):111-87.

McDougall SR, Anderson ARA, Chaplain MAJ, Sherratt JA. 2002. Mathematical modelling of flow through vascular networks: Implications for ibmour-induced angiogenesis and chemotherapy strategies. Bull Math Biol 64(4):673-702.

Meixensberger J, Dings J, Kuhnigk H, Roosen K. 1993. Studies of tissue PO2 in normal and pathological human brain cortex. Acta Neurochir Suppl (Wien) 59:58-63.

Michel CC and Curry FE. 1999. Microvascular permeability. Physiol Rev 79(3):703-61.

Murray CD. 1926. The physiological principle of minimum work: I. the vascular system and the cost of blood volume. Proc Natl Acad Sci U S A 12(3):207-14.

Ndubuizu O and LaManna JC. 2007. Brain tissue oxygen concentration measurements. Antioxid Redox Signal 9(8):1207-19.

Nemani VM and Manley GT. 2004. Brain tissue oxygen monitoring: Physiologic principles and clinical application. Operative Techniques in Neurosurgery 7(1):2-9.

Netti PA, Baxter LT, Boucher Y, Skalak R, Jain RK. 1995. Time-dependent behavior of interstitial fluid pressure in solid tumors: Implications for drug delivery. Cancer Res 55(22):5451-8.

Nicholson C. 2001. Diffusion and related transport mechanisms in brain tissue. Reports on Progress in Physics 64(7):815-84.

Noble F, Fleury V, Pries A, Corvol P, Eichmann A, Reneman RS. 2005. Control of arterial branching morphogenesis in embryogenesis: Go with the flow. Cardiovasc Res 65(3):619-28.

Nolte D, Steinhauser P, Pickelmann S, Berger S, Hartl R, Messmer K. 1997. Effects of diaspirin-cross-linked hemoglobin (DCLHb) on local tissue oxygen tension in striated skin muscle: An efficacy study in the hamster. J Lab Clin Med 130(3):328-38.

Nordberg J and Arner ES. 2001. Reactive oxygen species, antioxidants, and the mammalian thioredoxin system. Free Radic Biol Med 31(11):1287-312.

Ogawa S, Lee TM, Kay AR, Tank DW. 1990. Brain magnetic resonance imaging with contrast dependent on blood oxygenation. Proc Natl Acad Sci U S A 87(24):9868-72.

Painter PR, Eden P, Bengtsson HU. 2006. Pulsatile blood flow, shear force, energy dissipation and murray's law. Theor Biol Med Model 3:31.

Pardridge WM. 1999. Blood-brain barrier biology and methodology. J Neurovirol 5(6):556-69.

Patankar SV. 1980. Numerical heat transfer and fluid flow. Hemisphere Pub Corp.

Paulson OB, Hasselbalch SG, Rostrup E, Knudsen GM, Pelligrino D. 2010. Cerebral blood flow response to functional activation. J Cereb Blood Flow Metab 30(1):2-14.

Peppiatt CM, Howarth C, Mobbs P, Attwell D. 2006. Bidirectional control of CNS capillary diameter by pericytes. Nature 443(7112):700-4.

Phillips CG, Parker KH, Wang W. 1994. A model for flow through discontinuities in the tight junction of the endothelial intercellular cleft. Bull Math Biol 56(4):723-41.

Popel AS and Johnson PC. 2005. Microcirculation and hemorheology. Annu Rev Fluid Mech 37:43-69.

Preston E and Foster DO. 1997. Evidence for pore-like opening of the blood-brain barrier following forebrain ischemia in rats. Brain Res 761(1):4-10.

Pries AR and Secomb TW. 2008. Modeling structural adaptation of microcirculation. Microcirculation 15(8):753-64.

Pries AR and Secomb TW. 2005a. Control of blood vessel structure: Insights from theoretical models. Am J Physiol Heart Circ Physiol 288(3):H1010-5.

Pries AR and Secomb TW. 2005b. Microvascular blood viscosity in vivo and the endothelial surface layer. Am J Physiol Heart Circ Physiol 289(6):H2657-64.

Pries AR, Reglin B, Secomb TW. 2003. Structural response of microcirculatory networks to changes in demand: Information transfer by shear stress. Am J Physiol Heart Circ Physiol 284(6):H2204-12.

Pries AR, Neuhaus D, Gaehtgens P. 1992. Blood viscosity in tube flow: Dependence on diameter and hematocrit. Am J Physiol 263(6 Pt 2):H1770-8.

Pries AR, Secomb TW, Gaehtgens P, Gross JF. 1990. Blood flow in microvascular networks. experiments and simulation. Circ Res 67(4):826-34.

Pries AR, Ley K, Claassen M, Gaehtgens P. 1989. Red cell distribution at microvascular bifurcations. Microvasc Res 38(1):81-101.

Pries AR, Secomb TW, Gessner T, Sperandio MB, Gross JF, Gaehtgens P. 1994. Resistance to blood flow in microvessels in vivo. Circ Res 75(5):904-15.

Rapoport SI. 2000. Osmotic opening of the blood-brain barrier: Principles, mechanism, and therapeutic applications. Cell Mol Neurobiol 20(2):217-30.

Reed BR, Eberling JL, Mungas D, Weiner M, Jagust WJ. 2001. Frontal lobe hypometabolism predicts cognitive decline in patients with lacunar infarcts. Arch Neurol 58(3):493-7.

Reichold J, Stampanoni M, Lena Keller A, Buck A, Jenny P, Weber B. 2009. Vascular graph model to simulate the cerebral blood flow in realistic vascular networks. J Cereb Blood Flow Metab .

Reina-De La Torre F, Rodriguez-Baeza A, Sahuquillo-Barris J. 1998. Morphological characteristics and distribution pattern of the arterial vessels in human cerebral cortex: A scanning electron microscope study. Anat Rec 251(1):87-96.

Renkin EM and Curry FE. 1982. Endothelial permeability: Pathways and modulations. Ann N Y Acad Sci 401:248-59.

Rippe B and Haraldsson B. 1994. Transport of macromolecules across microvascular walls: The two-pore theory. Physiol Rev 74(1):163-219.

Risau W. 1997. Mechanisms of angiogenesis. Nature 386(6626):671-4.

Rodriguez-Baeza A, Reina-De La Torre F, Ortega-Sanchez M, Sahuquillo-Barris J. 1998. Perivascular structures in corrosion casts of the human central nervous system: A confocal laser and scanning electron microscope study. Anat Rec 252(2):176-84.

Rubin MJ and Bohlen HG. 1985. Cerebral vascular autoregulation of blood flow and tissue PO2 in diabetic rats. Am J Physiol 249(3 Pt 2):H540-6.

Sarin H. 2010. Physiologic upper limits of pore size of different blood capillary types and another perspective on the dual pore theory of microvascular permeability. J Angiogenes Res 2:14.

Sarty G. 2007. Computing brain activity maps from fMRI time-series images. Cambridge: Cambridge University Press.

Secomb TW and Hsu R. 1994. Simulation of O2 transport in skeletal muscle: Diffusive exchange between arterioles and capillaries. Am J Physiol 267(3 Pt 2):H1214-21.

Secomb TW, Hsu R, Park EY, Dewhirst MW. 2004. Green's function methods for analysis of oxygen delivery to tissue by microvascular networks. Ann Biomed Eng 32(11):1519-29.

Secomb TW, Hsu R, Beamer NB, Coull BM. 2000. Theoretical simulation of oxygen transport to brain by networks of microvessels: Effects of oxygen supply and demand on tissue hypoxia. Microcirculation 7(4):237-47.

Sharan M, Vovenko EP, Vadapalli A, Popel AS, Pittman RN. 2008. Experimental and theoretical studies of oxygen gradients in rat pial microvessels. J Cereb Blood Flow Metab 28(9):1597-604.

Shiga T, Maeda N, Kon K. 1990. Erythrocyte rheology. Crit Rev Oncol 10(1):9-48.

Simoens P, De Schaepdrijver L, Lauwers H. 1992. Morphologic and clinical study of the retinal circulation in the miniature pig. A: Morphology of the retinal microvasculature. Exp Eye Res 54(6):965-73.

Sims DE. 1991. Recent advances in pericyte biology--implications for health and disease. Can J Cardiol 7(10):431-43.

Speck O, Chang L, DeSilva NM, Ernst T. 2000. Perfusion MRI of the human brain with dynamic susceptibility contrast: Gradient-echo versus spin-echo techniques. J Magn Reson Imaging 12(3):381-7.

Starling EH. 1896.
On the absorption of fluids from the connective tissue spaces. J Physiol 19:312-26.

Steiner LA and Andrews PJD. 2006. Monitoring the injured brain: ICP and CBF. British Journal of Anaesthesia 97(1):26-38.

Stewart GN. 1897. Researches on the circulation time and on the influences which affect it. J Physiol 22(3):159-83.

Sugihara-Seki M and Fu BMM. 2005. Blood flow and permeability in microvessels. Fluid Dyn Res 37(1-2):82-132.

Szirmai I, Vastagh I, Szombathelyi E, Kamondi A. 2002. Strategic infarcts of the thalamus in vascular dementia. J Neurol Sci 203-204:91-7.

Tiraboschi P, Hansen LA, Thal LJ, Corey-Bloom J. 2004. The importance of neuritic plaques and tangles to the development and evolution of AD. Neurology 62(11):1984-9.

Tran-Son-Tay R, Kan HC, Udaykumar HS, Damay E, Shyy W. 1998. Rheological modelling of leukocytes. Med Biol Eng Comput 36(2):246-50.

Tsai AG, Friesenecker B, Mazzoni MC, Kerger H, Buerk DG, Johnson PC, Intaglietta M. 1998. Microvascular and tissue oxygen gradients in the rat mesentery. Proc Natl Acad Sci U S A 95(12):6590-5.

Tsai AG, Cabrales P, Intaglietta M. 2010. The physics of oxygen delivery: Facts and controversies. Antioxid Redox Signal 12(6):683-91.

Tsai AG, Johnson PC, Intaglietta M. 2003. Oxygen gradients in the microcirculation. Physiological Reviews 83(3):933-63.

Unterberg AW, Stover J, Kress B, Kiening KL. 2004. Edema and brain trauma. Neuroscience 129(4):1019-27.

Ursino M and Lodi CA. 1997. A simple mathematical model of the interaction between intracranial pressure and cerebral hemodynamics. J Appl Physiol 82(4):1256-69.

Ursino M and Giannessi M. 2010. A model of cerebrovascular reactivity including the circle of willis and cortical anastomoses. Ann Biomed Eng 38(3):955-74.

Vandervorst HA. 1992. Bi-cgstab - a fast and smoothly converging variant of bi-cg for the solution of nonsymmetric linear-systems. Siam Journal on Scientific and Statistical Computing 13(2):631-44.

Vink H and Duling BR. 2000. Capillary endothelial surface layer selectively reduces plasma solute distribution volume. Am J Physiol Heart Circ Physiol 278(1):H285-9.

Vovenko E. 1999. Distribution of oxygen tension on the surface of arterioles, capillaries and venules of brain cortex and in tissue in normoxia: An experimental study on rats. Pflugers Arch 437(4):617-23.

Wallis WD. 2007. A beginner's guide to graph theory. Second Edition ed. Birkhauser Boston.

Wang ZH, Wang CY, Chen KS. 2001. Two-phase flow and transport in the air cathode of proton exchange membrane fuel cells. J Power Sources 94(1):40-50.

Weinbaum S, Tarbell JM, Damiano ER. 2007. The structure and function of the endothelial glycocalyx layer. Annu Rev Biomed Eng 9:121-67.

Weishaupt D, Köchli VD, Marincek B. 2006. How does MRI work?: An introduction to the physics and function of magnetic resonance imaging. 2nd ed. Berlin ; New York: Springer.

Weller RO, Djuanda E, Yow HY, Carare RO. 2009. Lymphatic drainage of the brain and the pathophysiology of neurological disease. Acta Neuropathol 117(1):1-14.

Wilson DF, Lee WM, Makonnen S, Finikova O, Apreleva S, Vinogradov SA. 2006. Oxygen pressures in the interstitial space and their relationship to those in the blood plasma in resting skeletal muscle. J Appl Physiol 101(6):1648-56.

Wolburg H, Noell S, Mack A, Wolburg-Buchholz K, Fallier-Becker P. 2009. Brain endothelial cells and the glio-vascular complex. Cell Tissue Res 335(1):75-96.

Wu J, Xu S, Long Q, Collins MW, Koenig CS, Zhao G, Jiang Y, Padhani AR. 2008. Coupled modeling of blood perfusion in intravascular, interstitial spaces in tumor microvasculature. J Biomech 41(5):996-1004.

Yankner BA, Duffy LK, Kirschner DA. 1990. Neurotrophic and neurotoxic effects of amyloid beta protein: Reversal by tachykinin neuropeptides. Science 250(4978):279-82.

Zekry D, Duyckaerts C, Belmin J, Geoffre C, Herrmann F, Moulias R, Hauw JJ. 2003. The vascular lesions in vascular and mixed dementia: The weight of functional neuroanatomy. Neurobiol Aging 24(2):213-9.

Zhang X, Adamson RH, Curry FR, Weinbaum S. 2006. A 1-D model to explore the effects of tissue loading and tissue concentration gradients in the revised starling principle. Am J Physiol Heart Circ Physiol 291(6):H2950-64.